Dissertation zur Erlangung des Doktorgrades
der Fakultät für Chemie und Pharmazie
der Ludwig-Maximilians-Universität München

Synthetic Investigations into Main Group and Transition Metal Borates at Extreme Conditions

Dipl. Chem. Johanna S. Knyrim
aus
Regensburg

2008

Erklärung:

Diese Dissertation wurde im Sinne von § 13 Abs. 3 bzw. 4 der Promotionsordnung vom 31. Mai 2002 von Herrn Univ.-Prof. Dr. Hubert Huppertz betreut.

Ehrenwörtliche Versicherung:

Diese Dissertation wurde selbständig, ohne unerlaubte Hilfe erarbeitet.

München, den 24. Juli 2008

Johanna S. Knyrim

Dissertation eingereicht am	25.07.2008
1. Gutachter	Prof. Dr. Wolfgang Schnick
2. Gutachter	Univ.-Prof. Dr. Hubert Huppertz
Mündliche Prüfung am	02.09.2008

To my beloved parents

First and foremost my especial thank goes to Univ.-Prof. H. Huppertz, who offered me a very interesting and promising research project. Further on, I would like to express my gratefulness due to his confidence, the amicable atmosphere in his research group, and his consistent cross-border support.

I am much obliged to Prof. W. Schnick for the acceptance in his group, even as "discontinued-model", the nice working atmosphere, and the perfect research conditions.

Special thanks go to Prof. D. Johrendt, Priv.-Doz. K. Müller-Buschbaum, Prof. K. Karaghiosoff, and Prof. A. Hartschuh for their attendance in my *vivavoce*.

Loads of thanks are due to C. Löhnert, who was so kind to assume the circular of my PhD Thesis.

My thank goes to Prof. R. Glaum and his staff member V. Dittrich for recording as well as evaluating several UV/Vis/NIR spectra and the standing power in finding appropriate crystals.

I. Kinski and her PhD student C. Zvoriste I like to thank for the recording and analysis of a couple of single crystal Raman spectra.

I am indebted to Prof D. Johrendt for his DFT studies, as well as the evaluation of magnetic measurements carried out by Dr. S. Jakob and D. Bichler, whom I want to thank as well.

In the same way I am thankful to Prof. R. Pöttgen and his coworker F. M. Schappacher for Mössbauer studies.

I'd like to thank Dr. J. Schmedt auf der Günne and C. Minke for the solid state NMR measurements and interpretation of the collected data.

A big thank goes to Dr. O. Oeckler for his continouos and excellent support in matters of every crystallographic or chemical problem.

Dr. M. Döblinger I like to thank for electron diffraction investigations as well as the elevation and preparation of the obtained data.

To R. Römer I express my gratitude for her DFT studies and the good teamwork concerning this topic.

Special thanks go to C. Minke, T. Miller, J. Kechele, A. Sattler, Dr. P. Mayer, Dr. O. Oeckler, I. Peters, R. Eicher, W. Kinkelin, and W. Wünschheim for carrying out innumerous other measurements.

W. Wünschheim I want to thank for his consistant help in all PC- or other technical problems, but also for his assistance concerning any other issue.

For loads of fun I thank my Solid State Girls J. Kechele, R. Römer, Dr. S. Jakob, C. Hecht, P. Jakubcová, S. Neumair, and A. Haberer. Cheers!

My laboratory mates Dr. G. Heymann, A. Haberer, and S. Neumair I am very thankful for the nice and friendly working atmosphere in laboratory D2.102. Especially I thank Dr. G. Heymann, for his continous help and a great many of funny undertakings. Have a good time in Innsbruck!

I say thanks a lot to my research students B. Körner, J. Friedrichs, F. Roeßner, S. Neumair, Y. Floredo, R. Tandon, and last but not least S. Rauh. Especially to Steffi, Yvi, and Basti, who became my dear friends: Thank you so much and all the best for your subsequent careers! Further on I thank all our HiWis, S. Christian, Y. Floredo, J. Friedrichs, S. Neumair, M. Pitscheider, S. Rauh, and Th. Soltner who provided countless assembly particles.

A lot of thank goes to the press team Dr. G. Heymann, C. Braun, S. Hering, F. Pucher, S. Sedlmaier, S. Neumair, and W. Wünschheim for the good and pleseant working atmosphere. In this connection I also want to thank the technicians S. Landerer, M. Kutschka, H. Ober, and H. Ober for the manufacturing of our assembly particles. Especially I like to thank Dr. G. Heymann and F. Pucher for all the organization and managing!

I also like to thank all my present and past colleagues, who were not mentioned above and everybody I may have forgotten.

My best friend N. Rehorik always gave me encouragement and accompanied me during my hole study. Thanks a lot!

Further on I want to thank to my brother J. Knyrim, not only for his constitutive words when I was stressed out from writing this thesis.

To my partner B. Strube I express my thankfulness, because he was always able to stand all my moods and helped me to solve all my LaTex problems. Without you I became desperate! Thanks a million - I love you!

Above all I am deeply grateful to my parents, for their belief in me, their continuous support in every circumstance, and for making a secure study possible to me.

„Man merkt nie, was schon getan wurde.
Man sieht immer nur, was noch zu tun bleibt.“
(Madame Marie Curie)

Contents

1 Introduction

In nature, boron mainly can be found in the form of the borate minerals borax ($Na_2B_4O_5(OH)_4 \cdot 8\,H_2O$), kernite ($Na_2B_4O_6(OH)_2 \cdot 3\,H_2O$), ulexite ($NaCaB_5O_6(OH)_6 \cdot 5\,H_2O$), as well as colemanite ($Ca_2B_6O_8(OH)_6 \cdot 2\,H_2O$) (see Figure 1.1). Most borates are found in California (Boron or Death Valley) and Turkey, with the rest coming from Russia, China, and the Andean regions of South America [1].

Figure 1.1: From left to right: borax [2], kernite [3], ulexite [4], and colemanite [5].

The use of borates presumably goes back to the ancient Egyptians, who utilized borax in metallurgy, medicine, and mummification. In two salt samples, one from the embalming material of Tutankhamen (18th dynasty, 1336 – 1327 B.C.) and the second one from Deir el-Bahari (25th dynasty, 700 – 600 B.C.) borate salts were found. Arab physicians used the salts of boric acid as early as 857 A.D. for internal medicine. Known as *sal sedativum*, borates were used in the 18th century to soothe the skin. Even before this time, borates were used as cleansing agents [7]. Since then borates were much valued as gemstones, such as tourmaline. Figure 1.2 shows a colourfull specimen of tourmaline ($AD_3G_6(BO_3)_3[Si_6O_{18}]Y_3Z$ with $A = Ca^{2+}$, Na^+, K^+ or hole, $D = Al^{3+}$, Fe^{2+}, Fe^{3+}, Li^+, Mg^{2+}, Mn^{2+}, $G = Al^{3+}$, Cr^{3+}, Fe^{3+}, V^{3+}, $Y = O^{2-}$, OH^-, $Z = F^-$, O^{2-}, OH^-) [8].

Figure 1.2: Tourmaline [6].

Today, borates find application in the fields of analytical chemistry for example, as borax bead. Borax $Na_2B_4O_5(OH)_4 \cdot 8\,H_2O$ or tincal turns into water free $Na_2B_4O_7$ when heated above 400 °C, whereas the glassy melt dissolves metal oxides by forming characteristic coloured borates [10]. Figure 1.3 shows different borax beads for qualitative analysis of Cu, Ni, Co, Cr, Mn, and Fe (from left to right).

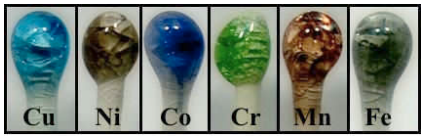

Figure 1.3: Borax beads of some metal oxides. [9]

Borates also find use in a wide range of industrial applications with an annual consumption of estimated 1.25×10^6 metric tons of B_2O_3. More than half of all boron used in industry is accounted by the manufacture of various types of vitreous materials, particularly fibreglass (*e.g.* for thermal insulation), ceramic glazes, enamel, and specialty borosilicate glasses (*e.g.* Pyrex®). Detergent manufacturers, who use peroxoborates as bleaching agents, form the second largest market for borates. Furthermore, borax and some other borates are used in fertilizers as important micronutrient. Figure 1.4 demonstrates the estimated total borate use by major industrial applications in B_2O_3 equivalents in the year 2001 [1].

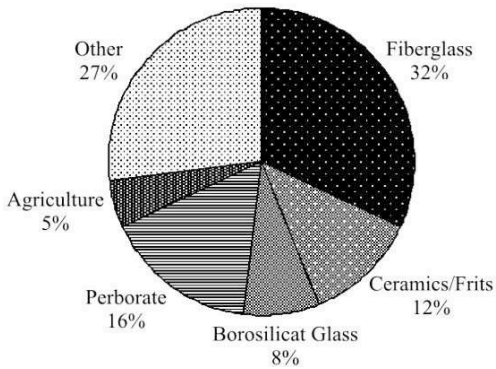

Figure 1.4: Schematic illustration of the consumption of main industrial applications of borates in 2001. [1]

Beneath the naturally occuring borate minerals, the number of synthetic borates steadily increased during the last years. To date, more than 1800 [11] borates can be found in the ICSD (Inorganic Crystal Structure Database). One of the primary applications of borates is in the fields of optics as phosphors or nonlinear optical components in laser tasks. For example, SrB_4O_7:Eu is used in UV-emitting medical lamps, $GdMgB_5O_{10}$:Ce,Tb as green luminescent material in fluorescent lamps, or $(Y,Gd)BO_3$:Eu as the red emitting component in plasma display panels (Figure 1.5).

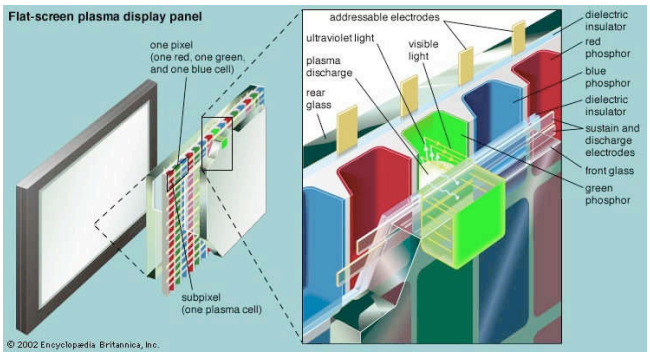

Figure 1.5: Schematic illustration of a plasma display panel. [12]

In the application area of nonlinear optics, borates like β-BaB_2O_4 (BBO) [13–15], LiB_3O_5 (LBO) [16–19], α-BiB_3O_6 (BIBO) [20–22], and $CsLiB_6O_{10}$ (CLBO) [23–26] are the most common compounds.

Efforts regarding the application of new materials were not only made in the fields of crystalline borates. In the range of rechargeable batteries, tin borate glasses came into the focus of research activities. Numerous studies showed that glasses in the system Sn-B-O are appropriate electrode materials for rechargeable Li batteries [27–35]. These electrode materials are characterized by higher capacities as the carbon based materials, which are used conventionally.

The major part of research activities concerning borates are conducted under normal-pressure conditions. The few results of high-pressure studies come from the area of geological research, investigating borate containing minerals, but these studies are limited to a pressure of 5 GPa. Therefore the enlargement of this branch of research appeared to be very promising. Due to this a short insight into the variety of high-pressure chemistry is given in the following.

Current research in high-pressure chemistry takes place *e.g.* in the system P-N. A binary high-pressure phosphorous nitride was realized within the compound γ-P_3N_5, which was synthesized in 2001 at 11 GPa and ∼1530 °C [36]. The high-pressure phase crystallizes in a network structure composed of corner-sharing PN_4-tetrahedra and distorted trans-edge-sharing PN_5-pyramids. Figure 1.6 shows the crystal structure of γ-P_3N_5 along [010], whereas green polyhedra represent PN_4-tetrahedra and yellow ones show tetragonal PN_5-pyramids. These PN_5-pyramids represent a novel building block, which was not known in solid-state chemistry before. Contemplating ternary P-N-compounds, one has to mention the first nitride clathrate $[P_4N_4(NH)_4](NH_3)$ [37], synthesized at 11 GPa and 600 °C in a multi-anvil device. NH_3, generated *in situ* during the high-pressure/high-temperature reaction, acts as a template molecule for the growing PN(NH) framework and is incorporated into the structure. Figure 1.7 right shows the crystal structure of the new cubic clathrate. Recently, another fascinating oxonitridophospate $Sr_3P_6O_6N_8$ was discovered by S. Sedlmaier [38]. The compound was synthesized under conditions of 6 GPa and ∼920 °C crystallizing in a highly consensed layer structure, consisting of corner-sharing PON_3-tetrahedra with threefold coordinated nitrogen atoms. The compound shows analogy to layer silicates, which was not observed in

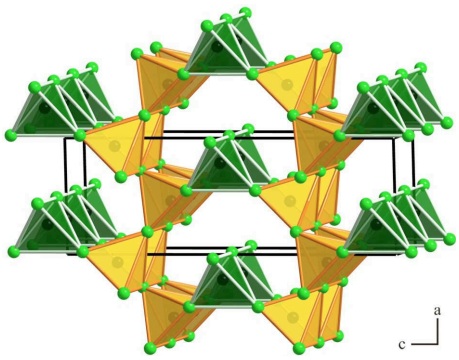

Figure 1.6: Crystal structure of γ-P_3N_5 with a view along [010].

phosphate chemistry before. Figure 1.7 (left) demonstrates a view on one layer of $Sr_3P_6O_6N_8$, exhibiting "Sechser" and "Vierer" [39] rings.

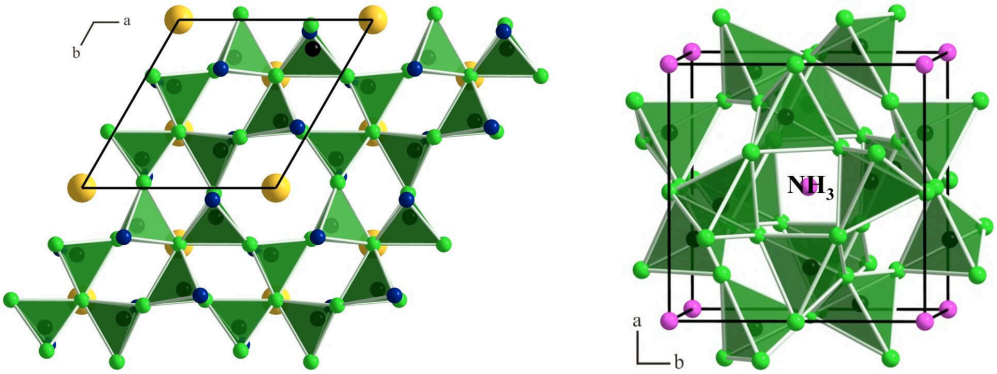

Figure 1.7: Left: Crystal structure of $Sr_3P_6O_6N_8$ with a view along [001]. Yellow spheres represent Sr^{2+}, black spheres P^{5+}, blue spheres O^{2-}, and green spheres N^{3-}. **Right**: Crystal structure of $[P_4N_4(NH)_4](NH_3)$ with a view along [001]. Pink spheres represent NH_3, black spheres P^{5+}, and green spheres N^{3-}.

Another outstanding nitride, synthesized under high-pressure/high-temperature conditions, can be found among the Si_3N_4-modifications. As the normal-pressure modifications α- and β-Si_3N_4 are composed of SiN_4-tetrahedra, the high-pressure modification γ-Si_3N_4, crystallizing in the cubic spinel structure, shows Si in fourfold and even sixfold coordination [40, 41] (see figure 1.8). β-Si_3N_4 is an important ceramic material, due to which the new cubic high-pressure modification attracted widespread interest as well. γ-Si_3N_4 represents a superhard material, comparable to stishovite [42], which is probably the third hardest material after diamond and c-BN [43], and even the hardest known oxide [40]. The cubic phase can be synthesized with yields of 80% *via* shock-wave experiments in large volumes [44]. In 2001, Kroll and Appen predicted a post-spinel phase of silicon nitride, δ-Si_3N_4, appearing at pressures about 160 GPa, built up from SiN_6-octahedra and SiN_6-prisms [45].

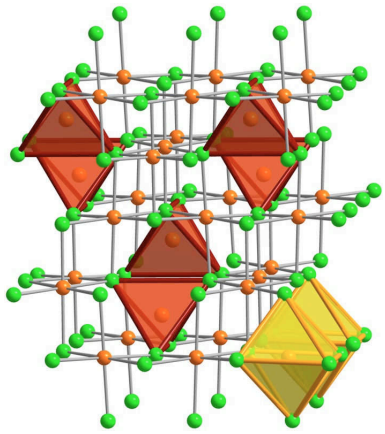

Figure 1.8: Crystal structure of the high-pressure modification γ-Si_3N_4. Red tetrahedra: SiN_4-groups; yellow polyhedra: SiN_6-octahedra.

The application of high pressures in combination with high temperatures also provides remarkable results in the wide fields of intermetallic phases. In the last years, several interesting high-pressure phases could be synthesized by G. Heymann. For example, the normal-pressure stannides NP-*RE*PtSn (*RE* = La – Nd, Sm) [46–51], NP-*RE*PdSn (*RE* = La, Ce, Pr, Nd) [51, 52], and NP-*RE*NiSn (*RE* = La – Nd, Sm) [51–54] crystallize in the orthorhombic TiNiSi type structure

[55], while those with the smaller rare-earth elements adopt the hexagonal ZrNiAl type [56–58]. By means of the parameter pressure, it was possible to stabilize the ZrNiAl type structure even for the larger rare-earth atoms [59–62]. In the case of the stannide ErAgSn, the normal-pressure phase NP-ErAgSn adopts the NdPtSb structure type [63–69], whereas the high-pressure modification HP-ErAgSn shows the hexagonal ZrNiAl type as well [51, 70]. Figure 1.9 demonstrates the connection between the mentioned structure types.

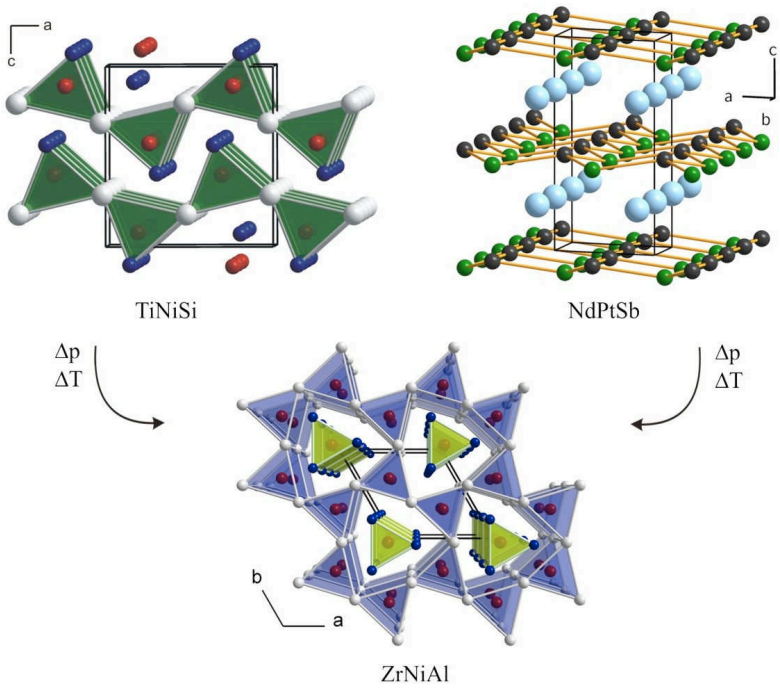

Figure 1.9: Comparison of TiNiSi, NdPtSb, and ZrNiAl type structures. [51]

Due to these interesting results of high-pressure investigations in diverse chemical systems, the question concerning the high-pressure behaviour of borates came up. From the chemical point of view, boron is closer related to silicon than to its following group-members Al, Ga, In, and Tl. Boron and silicon are both found in nature covalently bound to oxygen. Boron oxide and silicon oxide reveal similar acidities and both oxides tend to form glasses by cooling melts, containing other metal oxides as well. Therefore it was presumed that borates under pressure may act similar to silicates under normal-pressure with referrence to the pressure-homologous rule. With the synthesis of the semenovite-analogous rare-earth borate $RE_3B_5O_{13}$ (RE = Tm – Lu) [72] (Figure 1.10) and several other silicate analogous borates, which are described in detail in the following sections, this assumption was proved to be true.

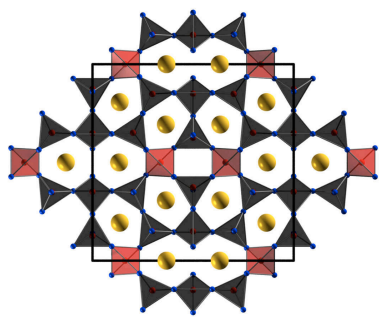

Figure 1.10: Crystal structure of the high-pressure borate $RE_3B_5O_{12}$ (RE = Tm – Lu). [71]

However, borates show an even bigger structural diversity than silicates. This is due to the occurrence of trigonal BO_3- and tetrahedral BO_4-units. These units can exist isolated, or can be linked *via* one, two, or three common corners, forming groups, rings, chains, bands, layers, or networks. It became evident that boron under high-pressure/high-temperature conditions favours fourfold coordination. On the example of the compound $Dy_4B_6O_{15}$ [73] and the isotypic phase $Ho_4B_6O_{15}$ [74, 75], Huppertz *et al.* showed that it is even possible, to realize borates with the faszinating element of edge-sharing BO_4-tetrahedra under extreme conditions. In the following years, another borate structure, comprising edge-sharing tetrahedra was discovered in our group, namely the rare-earth borate α-$RE_2B_4O_9$ (RE = Sm – Tb, Ho) [75–78]. Figure 1.11 compares the two mentioned compounds. By contrast, silicates are exclusively composed of corner-sharing tetrahedral SiO_4-groups,

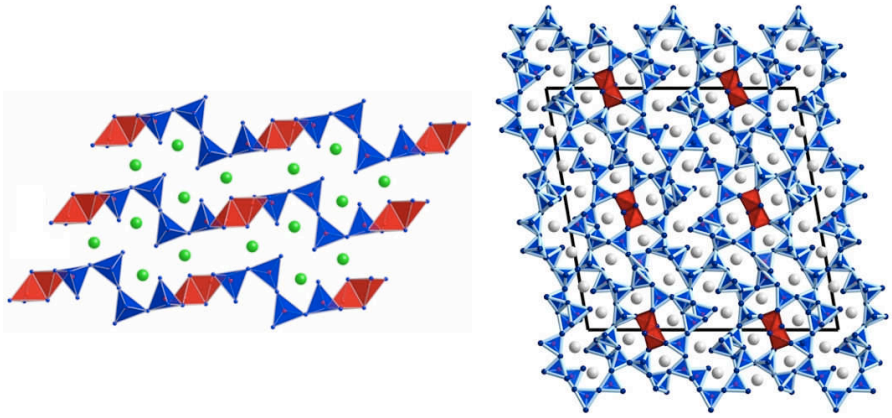

Figure 1.11: Crystal structures of the two borates exhibiting edge-sharing BO_4-tetrahedra. **Left**: $RE_4B_6O_{15}$ (RE = Dy, Ho) , **right**: α-$RE_2B_4O_9$ (RE = Sm –Tb, Ho).

connected to different polyanions. The supposed appearance of edge-sharing SiO_4-tetrahedra in fibrous SiO_2 [79] seems to be most doubtful.

According to the pressure-coordination rule [80], high pressures lead to boron in fourfold coordination. This can also be translated to oxygen: high-pressure borates often exhibit threefold coordinated oxygen atoms. In silicate chemistry this can only be observed in the silicon oxide modification stishovite. The normal-pressure modification of boron oxide B_2O_3-I [81] (Figure 1.12, left) solely consists of

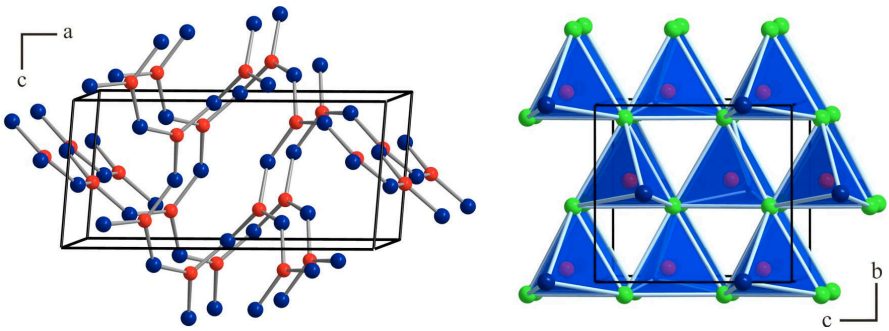

Figure 1.12: Left: Crystal structure of trigonal B_2O_3-I. **Right**: Crystal structure of orthorhombic B_2O_3-II. Blue spheres represent $O^{[2]}$, green spheres $O^{[3]}$, and red spheres B^{3+}.

trigonal BO_3-groups, whereas the high-pressure modification B_2O_3-II [82] (Figure 1.12, right) reveals only BO_4- tetrahedra and additionally threefold coordinated O^{2-} ions.

Because of the structural variety of borates, many new structure types can be expected in this field of solid-state chemistry. Recently, A. Haberer could synthesize a new high-pressure borate with the formula $Ti_5B_{12}O_{26}$ exhibiting a new structure type [83]. The tetragonal structure can be described as a kind of superstructure of the Zintl-phase NaTl, which consist of two interpenetrating diamond lattices (Figure 1.13, left). Instead of Na and Tl atoms, the positions are occupied by $B_{12}O_{26}$-clusters, which are displayed in Figure 1.13 (right).

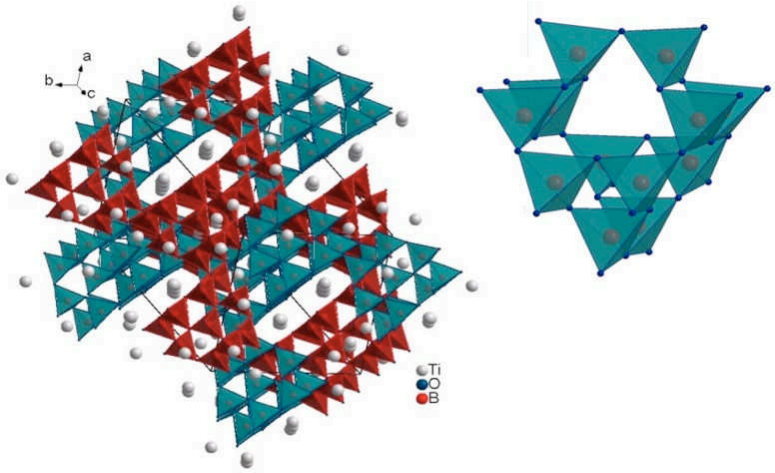

Figure 1.13: Crystal structure of the high-pressure phase $Ti_5B_{12}O_{26}$ along the space diagonal (left) and $B_{12}O_{26}$-cluster (right). [83]

As already mentioned above, a search in the ICSD database with B, O, and optional other elements, delivers more than 1800 hits [11]. Among this variety of borate crystal structures, only the fewest can be credited to high-pressure phases. This is due to the rather difficult accessibility to preparative high-pressure synthesis. Hitherto, high-pressure investigations were mainly performed from the geological point of view. By means of the multianvil technique, which will be described in the following, high-pressure syntheses can be carried out routinely. Since 1999, Huppertz *et al.* conduct systematic high-pressure experiments, while the main interest of these investigations was focused on rare-earth borates. The aim of this thesis was to enlarge the family of high-pressure borates into the fields of transition metal and main group borates, because there were known only very few compounds. Additionally, many normal-pressure phases in this area show interesting properties. In the following, a description of the used multianvil techique as well as the performed analytical methods is given. Afterwards the classes of transition metal and main group borates are introduced, whereon the analytical investigations and results of this thesis are discussed in detail. The research activities done in this work were executed within the scope of the DFG projects HU 966/2-2 and -3.

2 Experimental Methods

2.1 High-Pressure Synthesis

All syntheses presented in this thesis were carried out *via* the high-pressure/high-temperature route. Therefore a 1000 t press and a modified Walker-type module (both devices from Voggenreiter, Mainleus, Germany) were utilized, whereby a nearly hydrostatic pressure could be applied to the samples. A detailed description of the high-pressure facility, preparation of experiments and a short introduction into calibration methods are given in the following sections (2.1.1 – 2.1.7).

2.1.1 The 1000 t Press

The employed hydraulic downstoking press, with maximum load of 1000 t, was constructed and set up by the company Voggenreiter (Mainleus, Germany). The hydraulic system (shown in Figure 2.1) consists of three parts:

1. the main pressure cylinder (CCR-10002, Enerpac, Columbus, WI, USA)
2. an additional regulation cylinder with a worm gear screw jack driven by a servomotor
3. the main engine with the oil reservoir

Figure 2.1 shows a schematic side view of the 1000 t press including photographs of the three parts of the hydraulic system. The main valve for the main pressure cylinder and the lock valves for the regulation cylinder are housed under the top covering above the top plate. Figure 2.2 shows a picture of the valves and pipes and a diagram of the oil circuit divided in the three mentioned hydraulic parts by a red line.

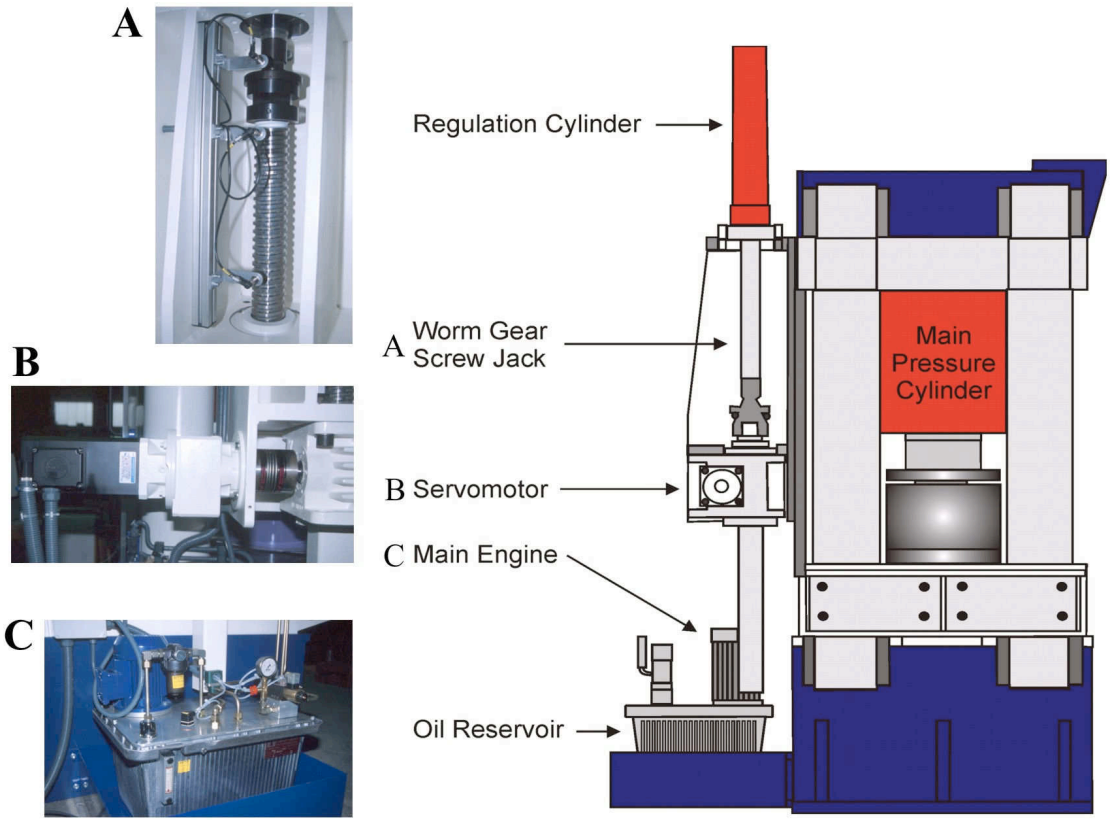

Figure 2.1: Schematic side view of the press with the hydraulic unit. **A**: Worm gear screw jack; **B**: Servomotor for slow pressure changes; **C**: Main hydraulic unit and oil reservoir. [84]

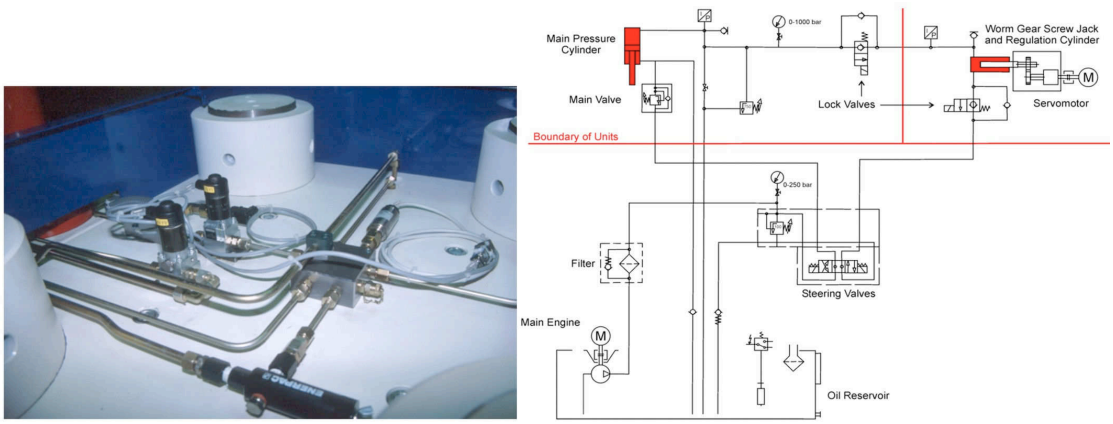

Figure 2.2: Left: Hydraulic valves and oil pipes on the top plate of the 1000 t press. **Right**: Oil circuit diagram of the press. [84]

After moving the Walker-type module underneath the main pressure cylinder, the ram is driven onto the top plate in 20 seconds using the main engine with high velocity. Figure 2.3 shows the induction switches, which avoid a hard put down by stopping the driving of the ram just before the distance piece touches the top pressure-distribution plate of the module. In the next step the oil pressure in the main cylinder is regulated by the servomotor moving the worm gear screw jack into the outer regulation cylinder. As the servomotor enables us to regulate the oil

pressure in a much more precise way, further compression and decompression is exclusively performed by the servomotor. Up to an oil pressure of 10 bar, which corresponds to a load of 14.3 t, the compression of the module takes place in a relatively fast time of approximately 20 min, closing all gaps between the wedges, cubes, and the octahedral cavity. Further compression is predetermined by the pressure program given for the experiment. Typically, the compression rate has a maximum value of 100 t per hour, whereas the decompression requires the threefold time.

Figure 2.3: Induction switches. [84]

The main engine, servomotor, and the valves are controlled by a SPS (Speicherprogrammierbare Steuerung, engl. Programmable Logic Controller, PLC) (Simatic S7-300) equipped with a serial RS232C interface. This has to be provided with the essential informations concerning the experimental profile, accomplished by a second control unit (Windows PC) which transfers the pressure ramps to the SPS, reads out the current system pressure, and controls all actions of the SPS. Since no commercial program was available to manage this, a special program with the name "PRESSCONTROL" was developed and programmed with Borland Delphi 4.0 for communication, calibration, and surveillance of the 1000 t press and the heating unit [85]. Figure 2.4 shows the graphical surface of the program. After starting the program, the experimental parameters have to be entered, *e.g.* type and size of the octahedron, type of furnace, the heating, and pressure ramp. For heating, the

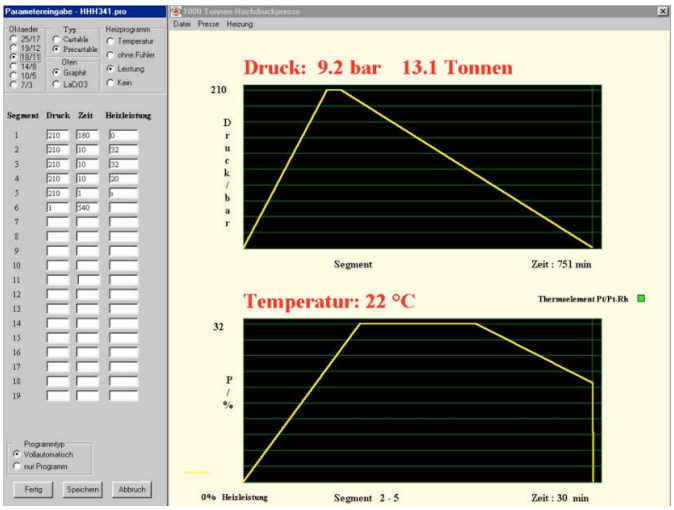

Figure 2.4: Graphical surface of the program "PRESSCONTROL". [85]

program distinguishes between temperature-controlled heating *via* a thermocouple or using predetermined power/temperature curves for the corresponding assembly without thermocouple. Next, the pressure/temperature ramp has to be entered including the intended times for each step, whereby the oil pressure is used as

input parameter for the intended load (700 bar correspond to the maximum load of 1000 t). Furthermore, the user has to decide, if the press is closed and opened automatically or by separate orders. After entering the experimental details, the program can be saved, and the pressure ramp as well as the temperature ramp are shown as yellow lines in two diagrams (Figure 2.4). The start of the press is performed *via* the task line of the program, sending the parameters to the SPS. During the experiment, the actual oil pressure and temperature given by the thermocouple are continuously read out and displayed on the screen. The actual pressure and heating values are dotted as a red line into the diagram to have a view of the advance of the experiment. In order to stop the experiment in the case of a rapid loss of pressure (blowout), security functions were implemented. Also routines for recording calibration curves were integrated in the program "PRESSCONTROL" [85].

2.1.2 The Walker-type Module

The press is operated with a multianvil-apparatus, whereby a nearly hydrostatic pressure can be applied to the samples. To realize high pressures and high temperatures combined with a large sample volume at reasonable costs, the best agreement is the system developed by Walker *et al.* in 1990 [86]. This Walker module was enhanced by Frost *et al.* [87] in 1998 at the Bayerisches Geoinstitut (Bayreuth, Germany), finally scaled up to a maximum load of 1000 t and fabricated in cooperation with the company Voggenreiter (Mainleus, Germany). Figure 2.5 demonstrates the setup of the module: the six tool steel wedges (C1-6; outer anvils) including the tungsten carbide cubes (D; inner anvils) plus the octahedral pressure medium (highlighted in red) are positioned in the containment ring (B). The latter is surrounded by a safety ring (A). The loading of the module is accomplished through pressure-distribution plates (E). The stability of the containment ring was scaled up by 2.5 for security reasons (containment ring, HSM, 1.2343, $R_c = 52$: 17.8 cm inner distance, 33.8 cm outer distance, total length 19.4 cm, surrounded by a safety ring (Höver, 1.4541): 33.8 cm inner distance, 37.8 cm outer distance, identical length). This means the module should stand a load of 2500 t without any failure.

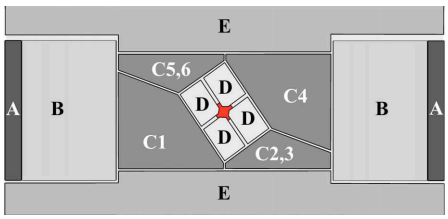

Figure 2.5: Schematic setup of the Walker module. [84]

The wedges are made from tool steel (HSM, 1.3343) hardened to $R_c = 62$ exhibiting a square face side, with dimensions of 6.00 cm × 6.00 cm (for 32 mm

tungsten carbide cubes) with an angle of 35° 26' to the axis of the module. The lowest corner of the square face has a distance of 2.00 cm from the basis. The three wedges with a height of 98 mm are assembled with a gap of approximately 1 mm in the cylindrical cavity of the containment ring (diameter 17.8 cm). Figure 2.6 shows a photograph of one tool steel wedge with the square face in front and wiring channels on both sides. The massive containment ring surrounded by the safety ring and incorporating three wedges with wiring ports is demonstrated in Figure 2.7.

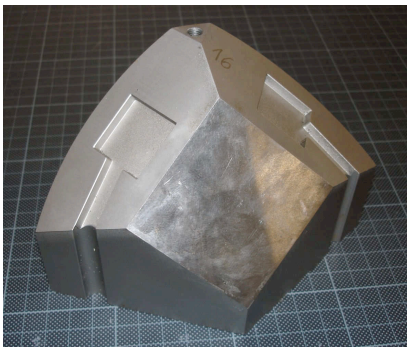

Figure 2.6: Single tool steel wedge with wiring channels for calibrations.

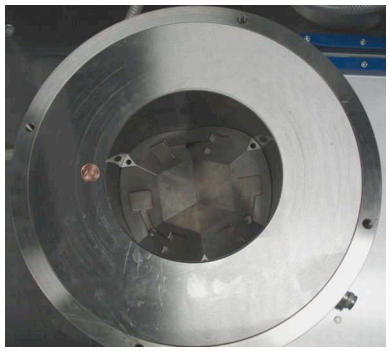

Figure 2.7: Containment ring with three of six wedges included.

The containment ring is covered by two pressure-distribution plates at its top and bottom (37.8 cm in diameter, 3.9 cm thick). These plates are made from an Al alloy (Alimex, AMP 8000) except the raised part of the plate, which directly lays on the wedges. This is substituted by tool steel (Höver, 1.4548.4) in order to avoid deformations of the plates. Figure 2.8 shows the spiral cooling, that was applied to the pressure-distibution plates, sealed by the tool steel plates (Figure 2.9). Additionally, several tunnels and shafts are added to the pressure-distribution plates and wedges, which is necessary for pressure and temperature calibrations.

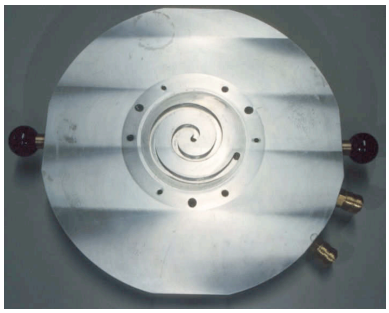

Figure 2.8: Cooling spiral inside of the pressure-distribution plates. [84]

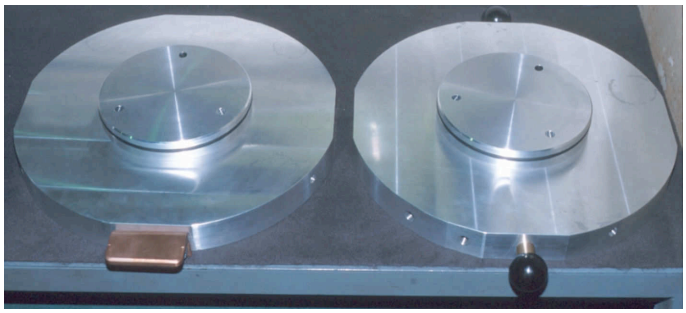

Figure 2.9: Pressure-distribution plates (left: bottom; right: top). [84]

2.1.3 The Preparation of High-Pressure Experiments

The Walker-type multianvil module (section 2.1.2) works with six wedges compressing a cubic arrangement of eight inner anvils. These consist of tungsten carbide cubes with an edge length of 32 mm and truncated corners forming triangular faces. By arranging these eight cubes with the truncated corners pointing to the middle of the formed cubic array, an octahedral cavity is generated, wherein the octahedral pressure cell can be located. There exist several different assemblies, which are clearly defined by their octahedral edge length (OEL) and truncation edge length (TEL) of the corresponding tungsten carbide cubes. For instance, an 18/11 assembly describes an octahedron with an edge length of 18 mm, including eight tungsten carbide cubes exhibiting truncated triangular faces with an edge length of 11 mm. In this work only 18/11 and 14/8 assemblies were used. Furthermore the assembly 10/5 can be used as a matter of routine. The sample volume and therewith the size of the octahedron determine the maximum achievable pressure. These values range typically from ∼35 mm^3 at a maximum pressure of 10 GPa (18/11), ∼9 mm^3 at a maximum pressure of 13 GPa (14/8), and ∼4 mm^3 at a maximum pressure of 16 GPa (10/5). As pressure-transmitting medium prefab-

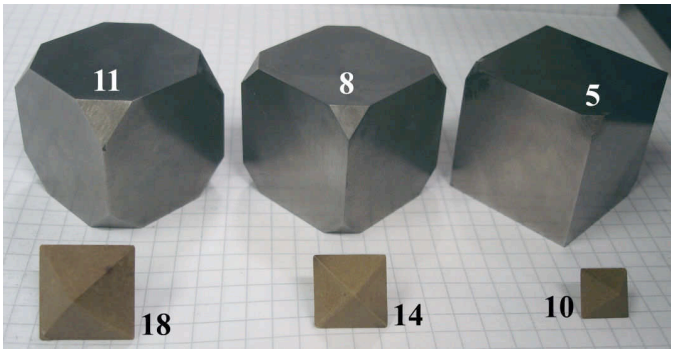

Figure 2.10: Different sizes (/mm) of tungsten carbide cubes with the corresponding octahedral pressure medium.

ricated, sintered magnesium oxide octahedra (Ceramic Substrates & Components Ltd., Newport, Isle of Wight) doped with 5 % magnesium chromite, are used. Figure 2.10 shows the octahedra with edge lenghts of 18 mm (left) and 14 mm (right). To bring in the sample, a hole is drilled into the octahedron along its $\overline{3}$ axis. All pieces used to built up the assembly are shown in Figure 2.11. The sample is located directly in the centre of the octahedron inside of a crucible made from hexagonal boron nitride (Henze BNP GmbH, HeBoSint® S10, Kempten, Germany) (d) and closed with a h-BN plate (e). This material reveals the advantage of its chemical inertness under high-pressure/high-temperature conditions. Of course, it is possible to use different capsule materials like copper, molybdenum, platinum, or gold in this assembly, but due to the oxoborate system, hexagonal boron nitride was a good choice for experiments. For reasons of heating, cylindrical graphite tubes (RW403, SGL Carbon, Bonn, Germany) are used as resistant heaters (a,b)

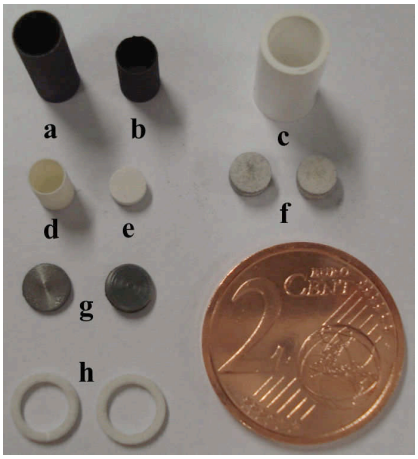

Figure 2.11: Survey about the assembly parts; **a**: long graphite tube, **b**: short graphite tube, **c**: zirconia sleeve, **d**: h-BN crucible, **e**: h-BN plate, **f**: MgO-rods, **g**: Mo-plates, **h**: MgO-rings.

surrounding the h-BN capsule. Up to pressures of 10 GPa and temperatures of 1500 °C, graphite can be used as the heater material without any problems. Above these conditions, the material starts to convert to diamond and its performance collapses. As an alternative $LaCrO_3$ (Cherry-O, Amagasaki-City, Japan) or tantalum can be used as a heater material to generate temperatures up to 3000 K. Two telescoped furnaces, with a stepped wall thickness, are used to reduce the thermal gradient along the sample [88]. The sample capsule is centred inside the furnaces utilizing MgO-rods (f) (Magnorite MN399CX, Saint-Gobain Industrial Ceramics, Worcester, MA, USA) at the bottom and the top of the furnaces. For thermal isolation of the furnace against the MgO octahedron, an additional zirconia sleeve (c) (Ceramic Substrates & Components Ltd., Newport, Isle of Wight) surrounds the inner part. The furnace is contacted *via* molybdenum plates (Mo007905, Goodfellow, Bad Nauheim, Germany) (g) at the bottom and at the top, fitting directly into the MgO-rings (h). Figures 2.12 and 2.13 demonstrate the dimensions of the described pieces of an 18/11 and an 14/8 assembly, which were used in this thesis.

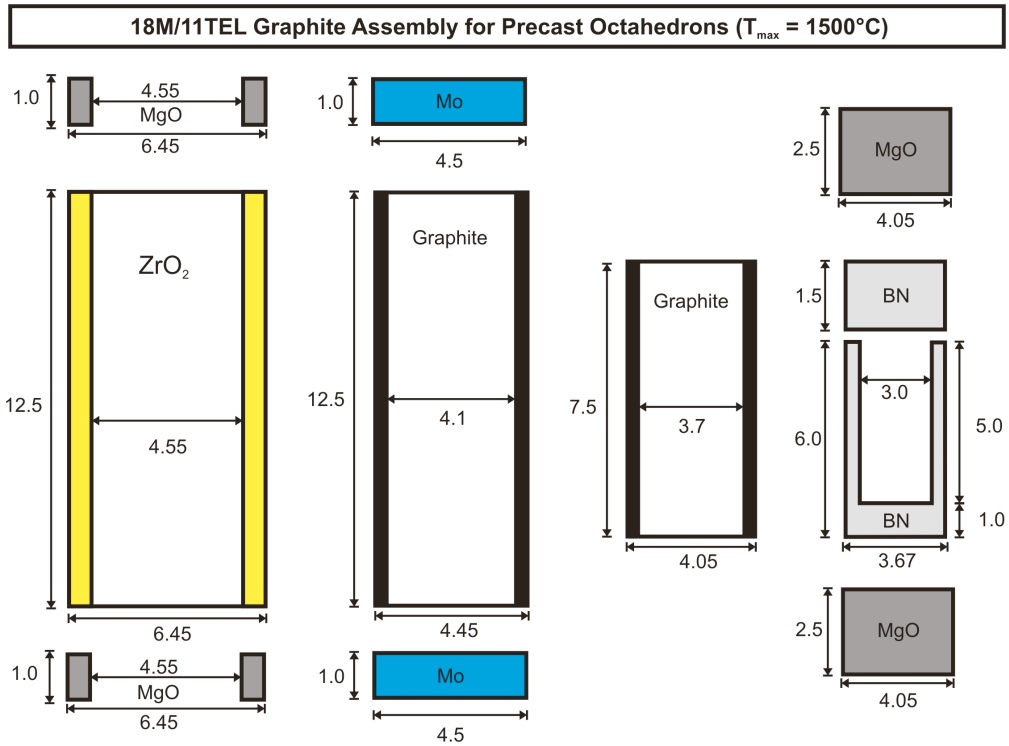

Figure 2.12: Dimensions/mm of the pieces used for an 18/11 assembly (precast MgO-octahedron, pyrophyllite gaskets).

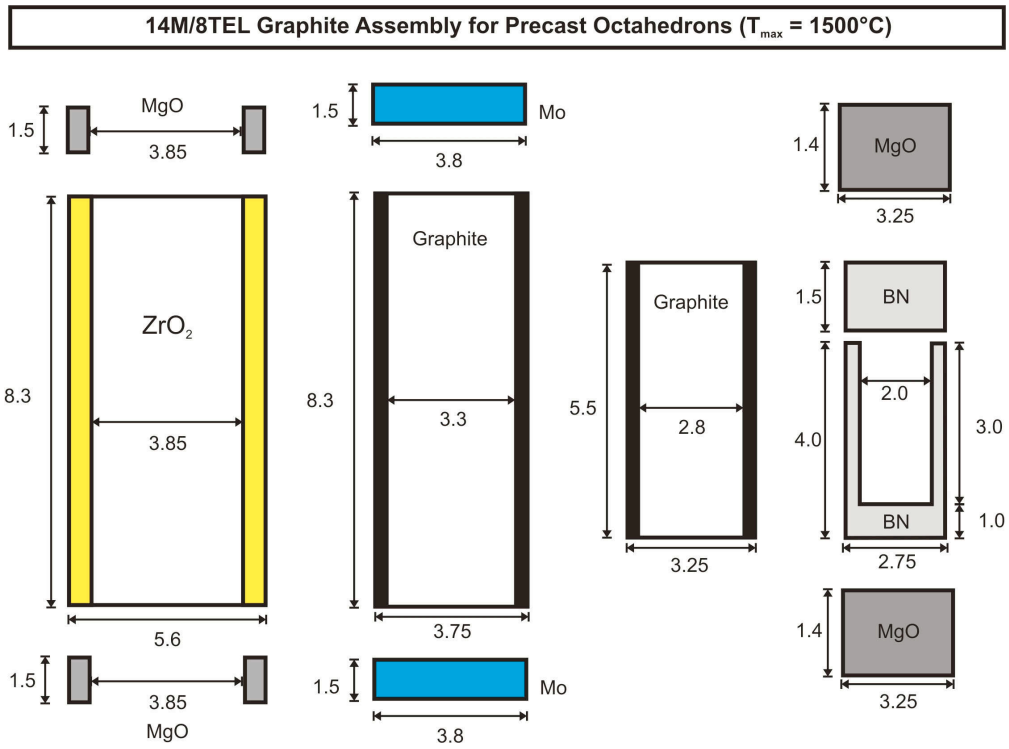

Figure 2.13: Dimensions/mm of the pieces used for an 14/8 assembly (precast MgO-octahedron, pyrophyllite gaskets).

Figure 2.14 shows a schematic cross section of an assembled octahedron. All mentioned h-BN, graphite, and MgO pieces were made by ourselves using a lathe (Opti D480, Collrep GmbH, Maintal, Germany) shown in Figure 2.15.

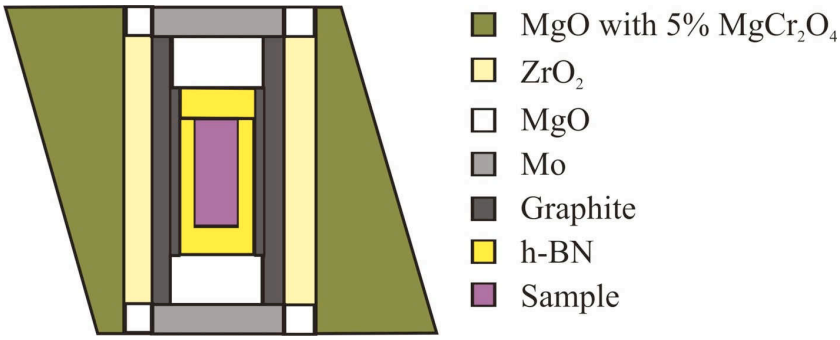

Figure 2.14: Schematic cross section of the octahedral pressure medium. [84]

Figure 2.15: Lathe for manufacturing of the assembly pieces.

After inserting the inner assembly pieces into the octahedron, the eight tungsten carbide cubes are arranged around it as seen schematically in Figure 2.17. The triangular faces of the truncated cubes fit onto the faces of the octahedron, keept on distance *via* pyrophyllite gaskets. To seal the octahedral cavity (this is necessary to built up pressure) the gaskets are arranged as shown in Figure 2.16. The truncated corners of the tungsten carbide cubes are surrounded by even three

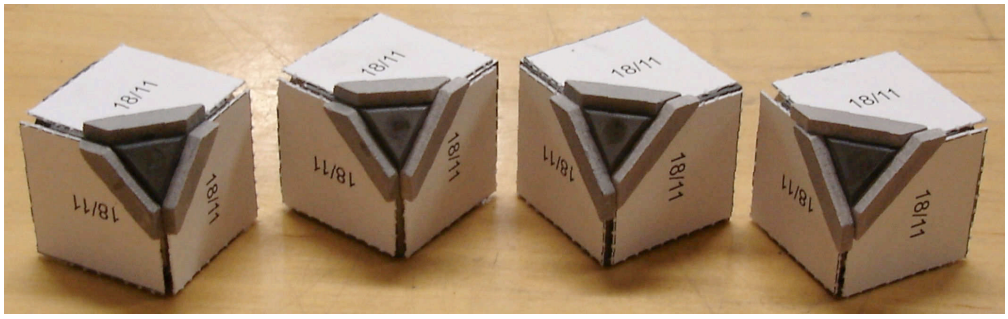

Figure 2.16: Arrengement of the pyrophyllite gaskets.

gaskets in the following way: three short gaskets, two short and one long gaskets, one short and two long gaskets, and three long gaskets. The gaskets are fixed at the cubes with small dots of UHU instant adhesive (UHU GmbH & Co KG, Bühl, Germany). Thereby it is important not to use too much glue, as it acts as lubricant at elevated temperatures. Behind the gaskets cardboards (Bristolkarton, 369 g/m^3) are applied by UHU instant adhesive to inhibit the gaskets from sliding. One half of the cubes is covered with gaskets and cardboards, the other half is laminated with PTFE-tape (SKAP 130, Beichler & Grünwald GmbH, Löchgau, Germany). The cubes are arranged in an alternating way, so that each cube pasted with gaskets and cardboards is positioned adjacent to a cube laminated with PTFE-tape and *vice versa*. This is to slow down and inhibit the extruding of crushed gaskets. In Figure 2.17 left, four tungsten carbide cubes are shown with the half octahedral cavity in the centre of it, Figure 2.17 further demonstrates, how the octahedron and the other cubes are arranged.

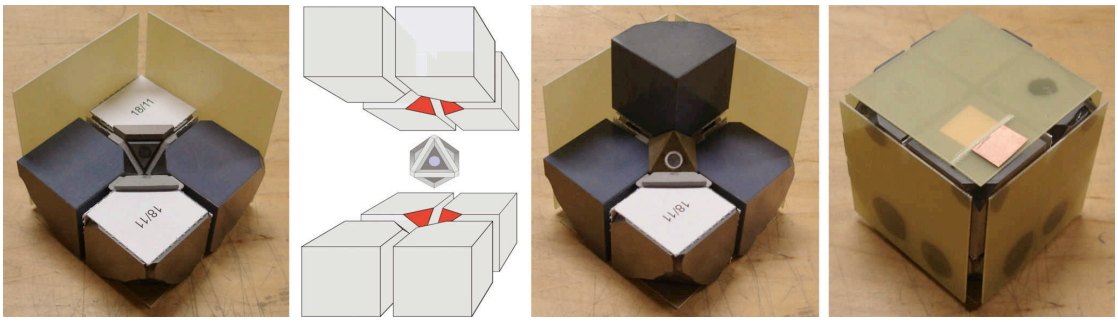

Figure 2.17: Insertion of the octahedral pressure medium into the inner anvils (tungsten carbide cubes).

The quality, technical specifications, and suitability of the tungsten carbide used for the inner anvils, produced by different manufactures, are highly variable [89]. Currently, the best qualities are Toshiba "F" grade (Langenfeld, Germany), Kennametal "THM-U", "THM-F" (Mistelgau, Germany), and Ceratizit "TSM10" (Reutte, Austria). Cubes applied in this work were Kennametal "THM-U", "THM-F", and Ceratizit "TSM10". For stabilisation the cubes are sticked to pads of fiber glass (Type 2372.4, Menzel & Seyfried, Gröbenzell, Germany) with a thickness of 0.8 mm (see Figure 2.17). The top (Figure 2.17 right) and bottom pads of the completely assembled cube, have incisions with threaded copper stripe (about 1.5 cm $\times$ 3.0 cm, thickness: 0.1 mm) ensuring a current flow from the pressure-distibution plates to the wedges, *via* the copper stripes to the tungsten carbide cubes. The truncated trigonal faces contact the Mo-plates directly.

Figure 2.18 demonstrates the positioning of the assembled cubes into the Walker-type module. On the left three wedges are shown, building a nest in which the cubic arrangement is placed along its $\overline{3}$ axis. After this, the top wedges take their

positions on top of the cube, leaving a gap between top and bottom wedges (Figure 2.18 middle). Because of stability reasons the complete assembly is placed in the containment ring (Figure 2.18 right).

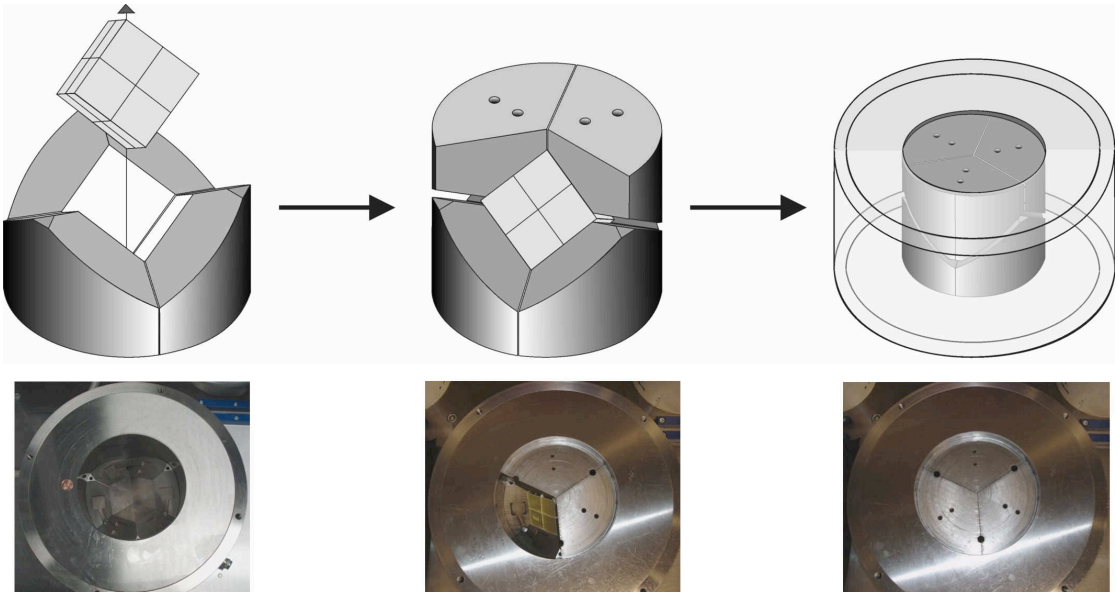

Figure 2.18: Illustration of the assemblage of the anvils in the Walker-type module. [84]

Figure 2.18 gives a view inside the containment ring. Between the wedges and the ring, two layers of PET-foil (BO-PET IA, D-K Kunststoff-Folien GmbH, Dessau, Germany) are positioned to fill the gap of 0.125 mm. One outer, large sheet (thickness: 0.75 mm) covers the complete inner side of the containment ring and sticks out 1.5 cm above the containment ring. The outer surface of this foil is covered with PTFE-spray, which acts as a lubricant. The inner, small sheets of foil (thickness: 0.50 mm) cover the outside of each wedge, whereas the foil is fixed by a thin film of PTFE-spray as well.

The PET-sheets fulfil several functions: The lubricated interfaces between containment ring, wedges, and PET-sheets allow the motion of the wedges. Additionally the PET-sheets provide electrical insulation of the containment ring from the wedges. Furthermore, the sheets absorb stress concentrations and compensate surface flaws and roughness of the inner side of the containment ring. Figure 2.18 shows the mounting of the cube of inner anvils into the Walker-type module. After inserting the last wedge, the pressure distribution plate is lifted on the flat top created by the top three wedges. This has to be done very carefully so that the sticking out PET-sheet is not damaged. Having closed the Walker-type module, it has to be moved from the preparation table directly under the hydraulic ram of the 1000 t press. Figure 2.19 left shows the complete press with the module under load and a second module on the left side of the table.

Figure 2.19: Left: Front view of the press with heating controll (left) and press controll (right). [51] **Right**: Walker-type module under the ram.

On the right side of Figure 2.19 one can see the Walker-type module under the ram. On the left side of the pressure distribution plates, the adapters for the cooling are visible. Electrical contact, in order to heat the sample, is enabled *via* a small metal extension at the right side of the bottom pressure-distribution plate, which moves directly into a small shoe connecting the plate with one pole of the electrical circuit. The second pole is fixed on the backside of the distance piece (aluminum) between the ram and the top pressure distribution plate.

2.1.4 Pressure Calibration

Due to a multitude of factors, that collude in a multianvil setup, it is nearly impossible to calculate the exact pressure that dominates inside the sample. Therefore, calibrating measurements were carried out with systems, that show phase transitions at known pressures. These points are established from diamond anvil cell investigations, where actual pressures can be easily detected through the shift of the fluorescence lines of ruby. Commonly used transitions for calibrating the assemblies up to a pressure of 13 GPa are the I-II, II-III, and III-V transitions in Bi (at 2.55, 3.15, and 7.70 GPa, respectively) representing one of the most studied elements at high-pressure [90–101] and semiconductor to metal transitions in ZnTe (6 GPa - anomaly-, LPP-HPP1 at 9.6 GPa, and HPP1-HPP2 at 12.1 GPa) [102–105]. To accomplish the Bi investigations, a hole was drilled along the $\overline{3}$ axis of the octahedral pressure medium with a diameter of

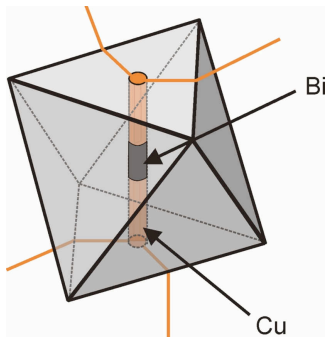

Figure 2.20: Schematic bismuth calibration octahedron. [84]

1.7 mm stuffed with a 3.8 mm long cylinder of Bi metal. The remaining space was filled with copper electrodes on either side of the octahedron, each provided with two cable connections of copper wire to allow electrical communication between the bismuth and the resistance measuring circuit outside the press. Figure 2.20 gives a schematic view of the prepared octahedron for calibration. This setup permits a current free detection of the resistance in dependence of the ram oil pressure. Figure 2.21 shows a typical diagram for the relative resistance of Bi in a 14/8 precast octahedron. The graph exhibits three sharp resistance changes due to the phase transformations I-II, II-III, and III-V. The structures transform from rhombohedral Bi-I (isotypic to As) into Bi-II with a monoclinic structure, followed by Bi-III being composed of a tetragonal host structure and an interpenetrating guest component, which is incommensurate with the host [101]. Further increase in pressure results in a phase transformation to the body-centred cubic phase Bi-V above 7.7 GPa.

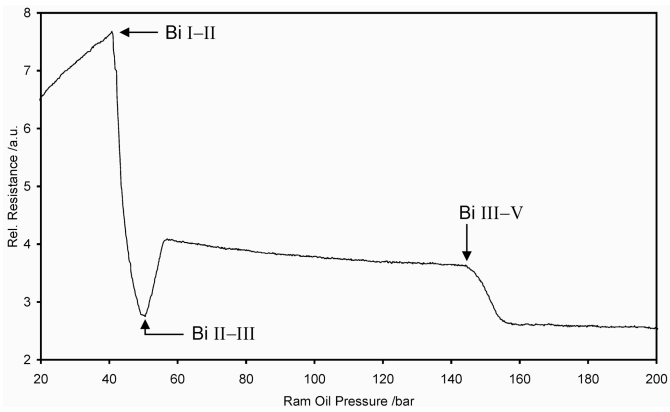

Figure 2.21: Typical relative resistance of Bi against ram oil pressure diagram (14/8 assembly).

For calibrations with ZnTe, a powdered sample (99.998 %, Alfa Aesar) with a thickness of 1.9 mm and a diameter of 1.6 mm in the centre of the octahedron, contacted analogously to the Bi calibration, was used. Since the resistance of the semi-conductor ZnTe is much larger than the resistance of tungsten carbide, the cubes were part of the circuit. Figure 2.22 demonstrates the resistance changes in ZnTe in dependence on the hydraulic oil pressure, showing three anomalies (around 6, 9.6 and 12 GPa). The first anomaly at ∼6 GPa can be explained by a change of the band gap in the zinc blende type ZnTe, followed by a transformation into a semiconducting cinnabar-type phase at ∼9 GPa [104, 105]. The last anomaly describes a transition to a metallic orthorhombic (*Cmcm*) phase at ∼12.0 GPa [106], which can be regarded as a distorted rocksalt lattice.

Other systems, which can be utilized for pressure calibrations, are the metals Ce (phase transition at 0.77 GPa [107–109]), Tl (phase transition at 3.65 GPa [110]), and Ba (phase transition at 5.5 GPa [111–113]).

Figure 2.23 shows the pressure calibration curves for Bi and ZnTe measurements

for the 18/11 and 14/8 assemblies.

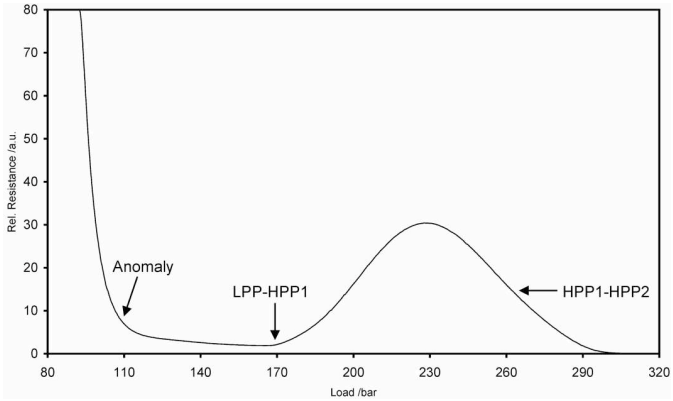

Figure 2.22: Typical relative resistance of ZnTe against ram oil pressure diagram (14/8 assembly).

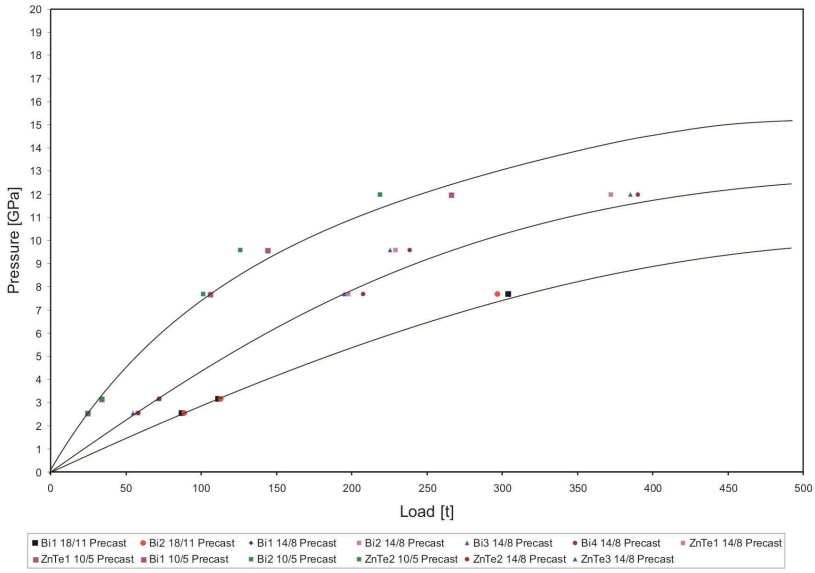

Figure 2.23: Pressure calibration curves for 18/11, 14/8, and 10/5 assemblies. [51]

2.1.5 Temperature Calibration

For an exact knowledge of the applied pressure, temperature calibrations are just as important. The temperature is measured using a thermocouple (Figure 2.24, left), which can be inserted perpendicular to the heater or along the axis as shown in Figure 2.24 right. The thermocouple is connected directly to an Eurotherm 2404 temperature controller (Limburg a. d. Lahn, Germany).

As thermocouple, Pt-$Pt_{87}Rh_{13}$ was used for temperatures up to 1500 °C, and W_3Re_{97}-$W_{25}Re_{75}$ above 1500 °C (SPPL-010, SP13RH-010, W3W25-010, Newport Omega, Deckenpfronn, Germany). For the insertion of a thermocouple the assembly setup has to be changed. On one side the MgO and Mo plate are replaced by corresponding rings, to put in the wiring. The measurement along the heater axis

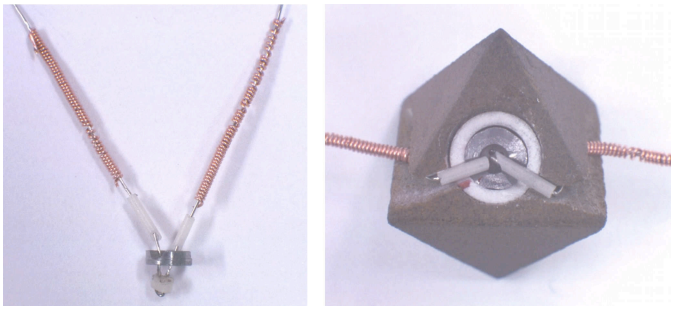

Figure 2.24: Left: Thermocouple with copper coils, alumina sleeves, and Mo ring. **Right**: Thermocouple inserted in an octahedron. [84]

allows the use of a thermocouple in combination with the sample. But this offers a source of uncertainty, because of the thermal gradient existing primarily along the sample axis. Other insecurities concerning the accuracy of the measurements arise from the pressure effect on the thermocouple electromotive force (emf) [114], but this effect can not be interpreted up to now. Recorded temperatures are therefore affected by several effects. Diagrams of the recorded temperatures in dependence of the heating power were established for every assembly. Therefore it is possible to perform synthesis in a roughly estimated temperature range without fitting a thermocouple into the assembly during every experiment.

2.1.6 Recovering the Sample

After the pressure is released, the Walker-type module is moved out from the hydraulic ram to the preparation table. The top pressure-distribution plate is lifted, the upper three wedges removed, and the cube comprising the inner anvils carefully raised out of the nest. Figure 2.25 gives a view of the opened cube after an experiment revealing the octahedral pressure medium. This clearly demonstrates the function of cardboards, PTFE-tape, and gaskets. The recovered octahedron was cracked with the help of a centre punch.

Figure 2.25: Left: Cube of inner anvils opened after a high-pressure/high-temperature program. **Right, top**: Hammer and centre punch to open the octahedron. **Right, bottom**: Opened octahedral pressure medium.

The sample was carefully separated from surrounding graphite and boron ni-

tride. Figure 2.26 shows typically looking crucibles containing different transition metal borates (from left to right: red: β-CoB_4O_7, green: HP-NiB_2O_4, yellow: β-NiB_4O_7, blue: β-CuB_4O_7). The left sample shows a beginning reaction with the

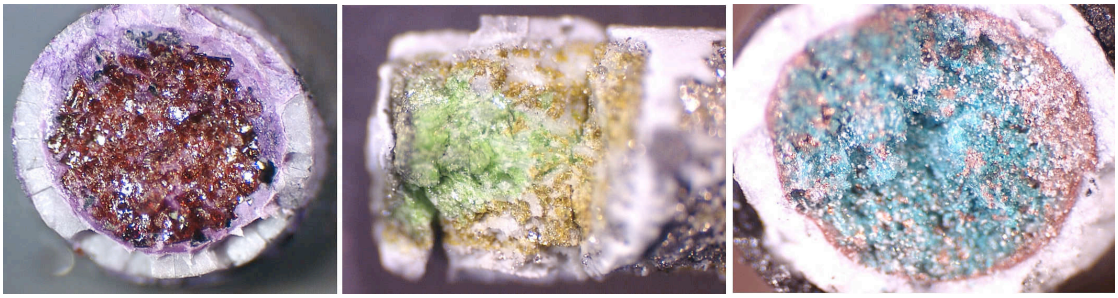

Figure 2.26: Crucibles containing different transition metal borates. From left to right: red: β-CoB_4O_7, green: HP-NiB_2O, yellow: β-NiB_4O_7, blue: β-CuB_4O_7.

BN-crucible (violet region). Figure 2.27 shows more advanced reactions with the crucibles. This can lead to new interesting materials.

Figure 2.27: Left: Beginning reaction; **Middle**: Nearly complete reaction with the BN-crucible; **Right**: Complete reaction. [84]

2.1.7 Experimental Dangers

Due to the robustness of the two Walker-type modules, with containment rings scaled up to a 2.5× stability (up to 2500 t), there exists no reason for experimental dangers with regard to ruptures. Nevertheless, during the heating phase of an experiment, it is required to wear ear protectors owing to the risk of a blow-out (aprupt loss of pressure). A blow-out can be caused by the failure of a gasket or by too much glue, which can act as a lubricant. Figure 2.28 represents an octahedron after a blow-out.

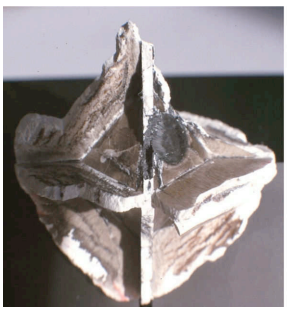

Figure 2.28: Recovered octahedron after a blow-out. [84]

A second danger arises from the eight inner tungsten carbide anvils. Especially, when the cubes were used at high-temperature and high-pressure, they start to built up tensions, which can lead to cracks or even explosive destructions

(Figures 2.29) under normal pressure conditions. Therefore, it is necessary to wear goggles while working with used cubes, and to keep the cubes under a protective shield, if not in use.

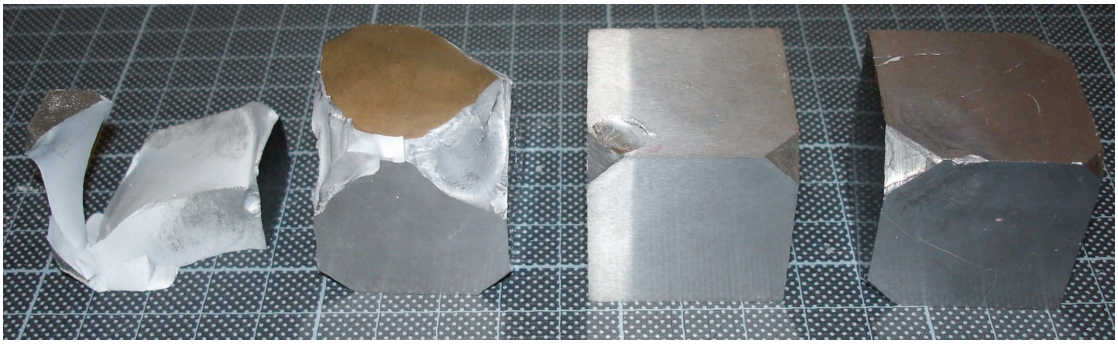

Figure 2.29: Destroyed or cracked tungsten carbide cubes.

3 Analytical Methods

3.1 X-Ray Diffraction Methods

X-Ray powder diffraction was performed for the purpose of phase analysis, determination of crystal parameters, and control of reaction products. For structure determination single crystal diffraction was accomplished.

3.1.1 Basic Principles of X-Ray Diffraction

In order to observe diffraction phenomena at a crystal lattice, the utilized radiation has to be in the dimensions of the interplanar spacing (0.03 – 0.5 nm) [115]. The appropriate radiation therefore is X-ray radiation, for powder measurements preferrable $CuK_{\alpha 1}$ (λ = 154.18 pm) and $MoK_{\alpha 1}$ (λ = 71.073 pm), for single crystal diffraction MoK_{α} (λ = 71.073 pm). The periodically arranged atoms or ions in a crystal build up a three dimensional diffraction grating, on which the incoming X-rays are dispersed. To achieve constructive interference, the retardation between two waves must be an integer multiple of the wavelength. Due to the three dimensional periodicity in a crystal, the dispersed waves show angle-dependend intensity maxima, which cause sharp reflections. These can be described *via* the three Laue-equations (Equation 3.1), which all have to be fulfilled to observe a reflection.

$$\begin{aligned} a\ cos\ \mu_a + a\ cos\ \nu_a &= n_1\ \lambda \\ b\ cos\ \mu_b + b\ cos\ \nu_b &= n_2\ \lambda \\ c\ cos\ \mu_c + c\ cos\ \nu_c &= n_3\ \lambda \end{aligned} \tag{3.1}$$

a, b, c: lattice period (x-, y-, z-direction)
μ_a, μ_b, μ_c: angle of incidence
ν_a, ν_b, ν_c: diffraction angle
n_1, n_2, n_3: diffraction order

The atoms or ions can be assigned as parts of lattice planes. As a result of periodicity there exists a family of parallel planes to every lattice plane. The

Bragg equation (Equation 3.2) describes the diffraction of X-rays as a partial reflection (angle of incidence = diffraction angle) of the waves at the lattice planes of a crystal, belonging to the same family.

$$2\, d_{hkl}\, sin\, \theta_{hkl} = n\, \lambda \tag{3.2}$$

d_{hkl}: interplanar spacing
θ_{hkl}: angle of incidence (= diffraction angle)
n: diffraction order
λ: wavelength

It correlates the interplanar spacing d_{hkl} of lattice planes belonging to the same family with the diffraction angle θ_{hkl} (Figure 3.1).

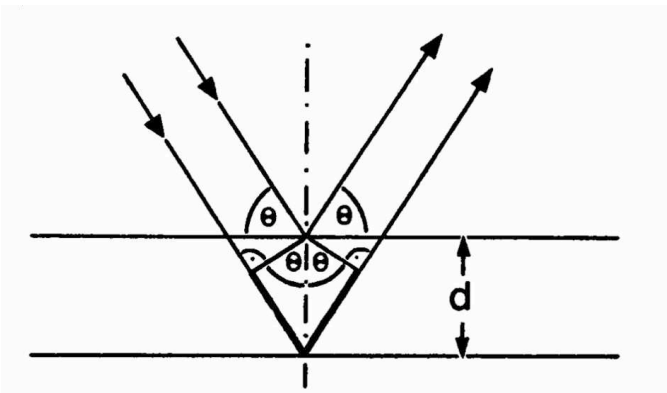

Figure 3.1: *Bragg* reflection: Reflection of X-rays at two parallel lattice planes.

Due to the interaction of X-rays with the electron sheath of atoms and ions, the intensity of a reflection is dependend on the number of electrons and therefore dependend on the chemical element. The scattered total intensities I_{hkl} (Equation 3.3) are proportional to the square of the structure amplitude, taking into account several correction terms during data reduction.

$$I_{hkl} \propto L \cdot P \cdot |F_{hkl}|^2 \tag{3.3}$$

L: Lorentz factor
P: polarisation factor
F_{hkl}: structure amplitude

The structure amplitude F_{hkl} depends both on the atom position and on its scattering factor f_j. This allows a summation over all j atoms included in the cell (Equation 3.4).

$$F_{hkl} = \sum_j f_j\, e^{2\pi i(hx_j + ky_j + lz_j)} \tag{3.4}$$

x_j, y_j, z_j: atomic positions

From Equation 3.3 it appears that F_{hkl} is directly proportional to the total intensities I_{hkl}. If the structure factors are known in modulus and phase, the

atomic positions are uniquely determinable. According to Equation 3.5 the electron density function ρ_{xyz} and therefore finally the crystal stucture, can be calculated by a Fourier Transformation of F_{hkl}.

$$\rho_{hkl} = \frac{1}{V}\sum_{hkl} F_{hkl} \cdot e^{-2\pi i(hx+ky+lz)} \tag{3.5}$$

As follows from Equation 3.3, only the moduli of F_{hkl} can be obtained from diffraction intensities, because the corresponding phase information is lost (crystallographic phase problem). The problem of identifying the atomic positions, starting only from $|F_{hkl}|$, can be solved by means of the *Direct methods* or the *Patterson method* [116, 117]. The refinement is carried out *via* optimization of the model on full-matrix least-squares on F^2. Additional atoms are assigned to residual peaks by difference Fourier synthesis with associated refinement until no significant residual peaks remain.

3.1.2 Powder Diffractometric Methods

X-Ray powder diffraction was principally used for a fast identification of the synthesized samples. Further on crystal parameters could be determined from powder measurements.

Powder diffractometry was carried out *via* two STOE Stadi P diffractometers (STOE & Cie, Darmstadt, Germany). They are constructed in focussing geometry using Ge(111)-monochromatized $CuK_{\alpha 1}$ (λ = 154.18 pm) and $MoK_{\alpha 1}$ (λ = 71.073 pm) radiation. Measurements were performed in transmission geometry, placing the powder sample between acetate films. The intensities were collected by a PSD (position sensitive detector) with an opening angle of $2\theta = 5°$.

Temperature-programmed *in situ* X-ray diffraction experiments were carried out on a STOE Stadi P diffractometer (STOE & Cie, Darmstadt, Germany) with Ge(111)-monochromatized $MoK_{\alpha 1}$ radiation (λ = 71.073 pm) with a computer controlled STOE furnace. All measurements were performed in Debeye-Scherrer geometry (silica capillary, Fa. Hilgenberg, Malsfeld, Germany, $\varnothing_{ext} = 0.2 - 0.5$ mm). An electrically heated graphite tube held the sample capillary vertical with respect to the scattering plane. Borings in the tube permitted unobstructed pathways for the primary beam, as well as for the scattered radiation. The temperature was recorded by a thermocouple.

3.1.3 Single Crystal Diffractometric Methods

Small single crystals were isolated by mechanical fragmentation utilizing a polarization microscope (MZ12, Leica, Bensheim, Germany). Therefore a crop of crystals

was placed on a glass carrier which was covered by a thin film of paraffine oil. Small crystals were fixed on thin glass fibers by means of beeswax. The quality of the selected crystals was checked using a Buerger precession camera in Laue mode (Buerger precession camera 205, Huber Diffraktionstechnik GmbH, Rimsting, Germany) operating with white Mo radiation (Röntgengenerator Kristalloflex 760, Siemens, Germany). The camera was equipped with an image plate system consisting of imaging plates [118] coated with a photosensitive material (BaBrF:Eu^{2+}) for recording the dispered X-rays, and a laser scanner (BAS-2500 Bio Imaging Analyser, Fuji Photo Film Corporation, Japan) for readout.

Single crystal intensity data were measured by use of a STOE IPDS-I diffractometer equipped with an area detector (STOE & Cie GmbH, Darmstadt, Germany) or on a Kappa CCD diffractometer (BRUKER AXS/Enraf-Nonius, Karlsruhe, Germany) equipped with a rotating anode (small or weak crystals). Both diffractometers act with MoK_{α} radiation (λ = 71.073 pm). Usually a raw data reduction was carried through with instrumental specific software, typically accounting for Lorentz-, polarisation-, and isotropic extinction corrections.

3.1.4 Computer Programs for X-Ray Diffraction Experiments

For scanning and viewing the Laue diagrams, the programs BASREAD [119] and TINA 2.10g [120] were used, respectively. By means of the STOE program package WinXPOW [121] the powder diagrams were recorded and handled. The included programs TREOR [122–124], ITO [125], DICVOL [126], and THEO [127] allowed indexing of recorded diffractograms, as well as simulation of powder patterns on the basis of single crystal data. Further on the integrated search routine "search-match", which referred to the JCPDS-database [128], was used for phase analysis.

The programs X-RED [129], X-RED32 [130], X-SHAPE [131], HABITUS [132], and SCALEPACK [133] were used for data reduction and absorption correction. The data sets were analysized by the program X-PREP [134], which was also used for the determination of possible space groups, as well as for semi-empirical absorption correction. Crystal structures were solved by *Direct methods* applying the program SHELXS-97 [135, 136] or SIR2004 (Semi-Invariants Representation) [137]. Structure refinement, based on F^2 (full-matrix least-square method), was carried out with the program SHELXL-97 [135, 136]. SHELXS-97 and SHELXL-97 are combined in the X-STEP32 [138] user interface. Structure evaluation and verification was carried out *via* the program PLATON, including the ADSYMM routine [139].

Crystal structure visualization was accomplished by the program DIAMOND

[140].

3.2 Electron Diffraction Experiments

Electron diffraction was carried out on a FEI Titan 80–300, equipped with a field emission gun, operating at 300 kV. Samples were ground in an agate mortar and dispersed in ethyl alcohol suspension. A small amount of the suspension was subsequently dispersed on a copper grid, coated with holey carbon film. The grids were mounted on a double tilt holder with a maximum tilt angle of 30° and subsequently transferred into the microscope. The diffraction patterns were recorded on a Gatan UltraScan 1000 P CCD camera.

3.3 Spectroscopic Methods

3.3.1 Vibrational Spectroscopy

Vibrational spectroscopy is a versatile tool for the characterization of molecular arrangements. Typical vibrations can be assigned to peaks in the measured spectra by means of databases, whereby the correlation between certain absorption bands and typical lattice vibrations in solid state compounds is not easy to verify. Nevertheless, vibrational spectroscopy is a useful method to distinguish between BO_3- and BO_4-groups.

Infrared spectra were recorded on a Bruker IFS66/v FTIR spectrometer (Bruker Analytik GmbH, Ettlingen, Germany) in an evacuated cell in a range of 400 – 4000 cm^{-1} (DLATGS detector). The samples were thoroughly mixed with dried KBr (5 mg sample, 500 mg KBr) in a glove box (MBraun, MB150-GI and UniLab, $O_2 < 1$ ppm, Garching, Germany) under dried argon atmosphere (purity grade 4.8, Messer Griesheim, Germany). Afterwards the KBr pellets were prepared by pressurizing, using a hand press with a press capacity of 10 kN.

Raman spectra were measured at single crystals with a Raman-microscope Horiba Jobin yvon HR800 (x50LWD), using a green laser (Melles Griot ion laser) with a wavelength of 514 nm.

Optical absorption spectroscopy is valuable in identifying the electronic states of matter. Single crystal measurements have the advantage of providing polarisation information as well [141]. Single crystal UV/Vis/NIR electronic spectra of arbitrary crystal faces of crystals smaller than 50 µm were measured using a strongly modified CARY 17 microcrystal spectrophotometer (Spectra Services, ANU Canberra, Australia) [142].

All spectra were handled and interpreted with the program Origin [143].

3.3.2 Mößbauer Spectroscopy

^{119}Sn Mößbauer investigations were performed with a Ca $^{119}SnO_3$ source at a powdered sample, that was dilluted with α-quartz. The sample was placed within a thin-walled PVC container at a thickness between 10 and 15 mg Sn/cm^2. A palladium foil of 0.05 mm thickness was used to reduce the tin K X-rays concurrently emitted by this source. The measurements were conducted in the usual transmission geometry at 77 K and room temperature.

3.3.3 Solid State NMR Spectroscopy

The NMR experiments were carried out on a Bruker Avance DSX spectrometer, equipped with standard 2.5 mm and 4.0 mm MAS NMR probe tubes. A commercially available pneumatic control unit was used to limit MAS frequency variations to a 2 Hz interval during the experiment. Samples were spun at 10 and 25 kHz, respectively. The powdered samples were filled into a ZrO_2 tube and sealed by means of Vespel and Kel-F caps, respectively.

The SOQE parameters and isotropic chemical shift values were determined from the moment analysis [144, 145] of the sheared MQMAS spectrum. Simulations of the chemical shift parameters were done by minimizing the squared difference between experiment and simulation, using the Simpson Minuit routines [146], and the chemical shift conventions implemented in Simpson [147]. The spectra were handeled and interpreted within the program Origin [143].

3.3.4 DTA/TG Investigations

For thermal investigation and evaluation of the metastable character of the synthesized compounds, combined DTA- (Difference Thermo Analysis) and TG- (Thermogravimetry) measurements were performed on a Setaram TGA 92-2400 DTA-TG-Thermobalance (Fa. Setaram, Calurie, France). The powdered samples were filled into a 100 µl corundum crucible. Measurements were carried out under He-atmosphere with a standard DTA-TG-sample carrier.

3.3.5 Scanning Electron Microscopy (SEM) and Energy Dispersive X-Ray Analysis (EDX)

Investigations concerning morphology and composition of crystals were conducted by a scanning electron microscope (SEM) (JEOL Ltd., JSM-6500F, Tokyo, Japan) with field emission source and maximum resolution of 1.5 nm. Energy dispersive X-ray analysis (EDX) enables a qualitative and semi-quantitative analysis of

chemical compositions on the basis of characteristic X-ray emissions of elements (EDX detector: model 7418, Oxford Instruments, Oxfordshire, UK). Crystals or an aggregation of several crystals placed on a brass sample carrier, fixed with hot-melt adhesive (Pattex, Henkel, Düsseldorf, Germany) or self-adhesive carbon plates (Plano, Wetzlar, Germany). For the purpose of conductivity, the samples were sputtered with carbon (Sputter device: BAL-TEC MED 020, BAL-TEC AG, Balzers, Netherlands).

Data collection and evaluation was carried through with aid of the INCA [148] program package.

3.4 Magnetic Investigations

Magnetic moments of the samples were measured using a SQUID magnetometer (Quantum Design, MPMS-XL5, San Diego, USA) between 1.8 and 300 K with magnetic flux densities as large as 5 Tesla. Samples of about 20 mg were loaded into gelatin capsules and fixed in straw as sample holder. Corrections for the sample holder and the core diamagnetism were applied to the data. Magnetic parameters were determined using an extended Curie-Weiss-law (Equation 3.6).

$$\chi = C/(T - \theta) + \chi_0 \tag{3.6}$$

3.5 DFT Calculations

In order to investigate conspicuous lone-pair behaviour of elements in the synthesized compounds, self-consistent DFT band structure calculations were performed by the LMTO-method in its scalar-relativistic version (program TB-LMTO-ASA) [149, 150]. Reciprocal space integrations were performed with the tetrahedron method [151].

For finding the position and the visualization of electrons, a three dimensional grid of the charge density and electron localization function (ELF) [152, 153] were calculated. In the density functional theory, ELF depends on the excess of local kinetic energy due to the Pauli principle as compared to a bosonic system. High values of ELF appear in regions of space, where the Pauli principle does not increase the local kinetic energy and thus pairing of electrons plays an important role. These regions can be assigned either to covalent bonds or to lone pairs.

For the investigation of the stability of different phases in a chemical system, structural optimizations, total energies, and properties were calculated within density functional theory (DFT) [154], for which the Vienna *ab-initio* Simulation Pack-

age (VASP) was used. It combines the total energy pseudopotential method with a plane-wave basis set [155–157]. The electron exchange and correlation energy is treated within the general gradient approximation (GGA) [158] to approximate the electron exchange and correlation energy. The utilized pseudopotentials were based on the projector-augmented-wave (PAW) method [159]. The cut-off energy for the expansion of the wave function into the plane wave basis set was 500 eV. Residual forces were converged below $5{\cdot}10^{-3}$ eV/Å. The Brillouin-Zone integration was carried out *via* the Monkhorst-Pack scheme [160].

The choice of the GGA functional is based on the experience that it significantly better describes relative energies of structures with different coordination of the atoms. Since our target is to study structures and structural transformations at high pressures, it is the better choice in comparison to the local density approximation (LDA). Therefore, though we controlled all our calculations within the LDA as well, all enthalpy differences and transition pressures given are based on GGA calculations.

3.6 Theoretical Calculations

3.6.1 Lattice Energy Calculations according to the Maple concept

MAPLE (Madelung Part of Lattice Energy) [161–163] calculations are an appropriate method to check crystal structures with respect to their plausibility. These computations exclusively consider the electrostatic interactions in an ionic crystal, depending on their distance, their charge, and their coordination. For every ion, partial MAPLE-values are computed, which are summed up to the total MAPLE value of the compound. MAPLE-values are additive with high accuracy, which means that the sum of the total MAPLE-values of the starting materials are comparable to the total MAPLE-value of the product.

3.6.2 The Bond-Length Bond-Strength Concept

In solid state compounds, the bond-length bond-strength concept allows the interpretation and evaluation of bond distances. The concept is historically founded on Pauling's defined bond-grade Pauling, mainly applied on metals or intermetallic phases. Brown [164], as well as Breese and O'Keeffe [165] extended the concept for a multitude of compounds. The correlation of bond lengths and bond valences allows a prediction of bond distances in solid state compounds with known valences. Contrary, it is possible to calculate valence sums from bond distances

derived from crystal structure determinations as well and therefore to check crystal structures on their plausibility. Bond valences ν_{ij} of bonds between atoms i and j are calculated according to Equation 3.7.

$$\nu_{ij} = exp\left[\frac{(R_{ij}-d_{ij})}{b}\right] \tag{3.7}$$

ν_{ij}: bond valence
R_{ij}: bond valence parameter
d_{ij}: bond distance
b: constant (= 37 pm)

The constant b was determined to 37 pm by Brown and Altermatt [165]. R_{ij} is characteristic for each elemental combination and was determined from known compounds [165, 166]. The total valence sum V_i sums up the bond valences ν_{ij} of all bonds starting from atom i (Equation 3.8).

$$V_1 = \sum_j \nu_{ij} \tag{3.8}$$

3.6.3 Calculation of the Charge Distribution according to the Chardi Concept

The CHARDI (Charge Distribution in Solids) concept [167, 168] is a combination of Pauling's [169] bond-grade and the effective coordination number (ECoN). In contrast to the MAPLE concept, CHARDI considers anion-anion- and cation-cation-interactions as well. The ECoN contribution $\Delta E(ij \rightarrow k)$ is based on the average distance $d(ij \rightarrow k)$ between the cations K_{ij} (crystallographic site j) and anions A_k. The summation of these contributions provides a partial effective coordination number Δ(ECoN) for every anion A_k as ligand of cation K_{ij}. In consideration of the number of the anions A_k surrounding K_{ij}, a part of the charge distribution $\Delta q(ij \rightarrow k)$ is obtained. According to Equations 3.9 and 3.10 the charges Q of the cations K_{ij} and anions A_k are calculated, respectively.

$$Q_{cation} = -\sum_i \sum_j \Delta q(ij \rightarrow k)_{cation} \tag{3.9}$$

$$Q_{anion} = -\sum_k \Delta q(ij \rightarrow k)_{anion} \tag{3.10}$$

4 Experimental Part

4.1 Transition Metal Borates

4.1.1 Introduction

Among the transition metal borates some very interesting materials with extraordinary characteristics can be found. One of those is represented by the compound $FeBO_3$, which is one of the extremly rare materials, that combine partial transparency in the visible and spontaneous magnetization at room-temperature. Therefore, it is suitable for the modulation of light [170].

Up to now many compounds are known in the field of transition metal borates, but only very few high-pressure phases. Recent interesting high-pressure studies of our group on phase formation and crystal chemistry of the transition metal borates revealed the compounds β-ZnB_4O_7 [171], β-HgB_4O_7 [172], and basic investigations on CdB_2O_4 [71] (Figure 4.1).

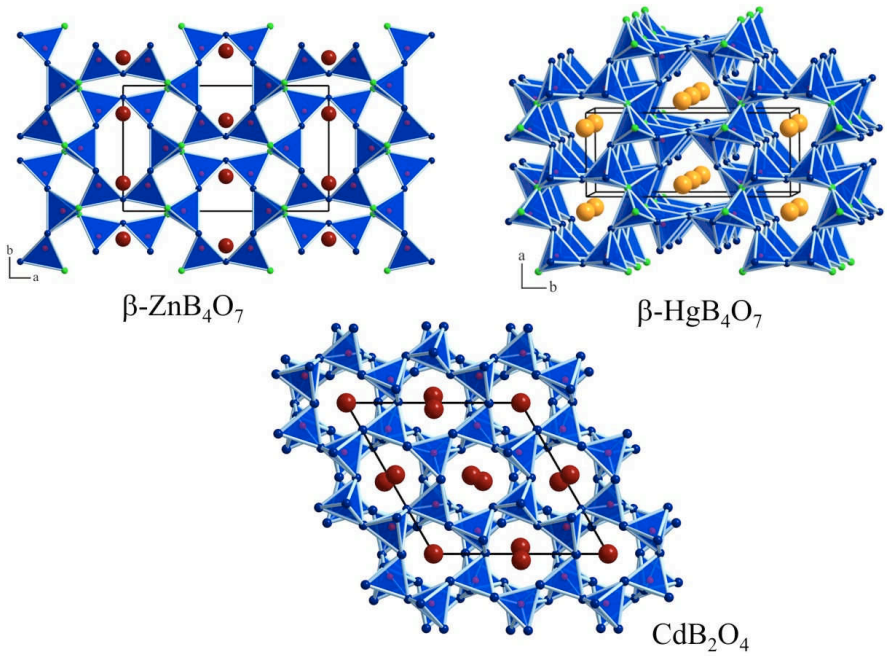

Figure 4.1: Crystal structures of the high-pressure borates β-ZnB_4O_7 (top, left), β-HgB_4O_7 (top, right), and CdB_2O_4 (bottom).

β-ZnB_4O_7 was synthesized by Huppertz and Heymann in 2003 crystallizing in

the orthorhombic space group *Cmcm* (see Figure 4.1 left). The network structure is exclusively composed of tetrahedral BO_4-groups, that share common corners *via* twofold ($O^{[2]}$) and even threefold coordinated oxygen atoms ($O^{[3]}$). The structure shows channels of "Vierer" and "Sechser" rings (rings consisting of four and six tetrahedra, respectively) [39]. The cations are positioned inside the "Sechser" ring channels coordinated in a sqare pyramidal way. β-HgB_4O_7 [172], which was discovered in our group in 2005, is isotypic to the orthorhombic ($Pmn2_1$) high-pressure phase β-CaB_4O_7 [173], as well as to the ambient-pressure phases SrB_4O_7 [174, 175], PbB_4O_7 [175, 176], and EuB_4O_7 [177]. The non-centrosymmetric crystal structure (Figure 4.1 middle) is solely assembled of corner-sharing BO_4-tetrahedra, exhibiting a network structure partially built up by threefold coordinated oxygen atoms $O^{[3]}$. Along [001] the structure is crisscrossed by channels composed of "Vierer" and "Sechser" rings [39]. The Hg^{2+} cations lie in the "Sechser" ring channels, coordinated by 15 O^{2-} ions. Emme described the synthesis of CdB_2O_4 as well as the structure of a preliminary model within his PhD thesis [71]. The crystal structure of this model is exclusively composed of BO_4-tetrahedra, showing a condensed network structure, which is built up by layers consisting of "Sechser" rings (Figure 4.1 right).

Due to this promising investigations, we focussed on the high-pressure/high-temperature research of further transition metal borate systems.

In this thesis the first period of transition metal elements from Mn to Cu in combination with B_2O_3 was examined intensively. Additionally, the systems Zr–B–O, Hf–B–O, and Cd–B–O were investigated. In the following, a short summary of the compounds already known in the mentioned systems under ambient-pressure conditions is given.

Manganese borates show a variety of compositions, *e.g.* α-MnB_4O_7 [178] (Figure 4.2), which is isotypic to α-ZnB_4O_7 [179–181] and CdB_4O_7 [182], showing planar BO_3-groups and tetrahedrally coordinated metal cations. Additionally, there are the manganese(II,III) oxyborates $Mn_2^{II}Mn^{III}(BO_3)O_2$ [183] and Mn_2OBO_3 [184] with the metal cations in octahedral oxygen coordination and trigonal planar BO_3-units. From high-temperature experiments, the compositions $Mn_3B_2O_6$, MnB_2O_4, and $Mn_2B_6O_{11}$ are reported starting from MnO and B_2O_3 [185].

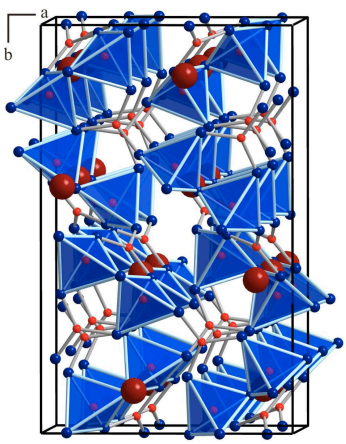

Figure 4.2: Crystal structure of α-MnB_4O_7.

Moving along to the element iron, five compositions can be found in the system Fe–B–O. It concerns $Fe^{II}Fe^{III}(BO_3)O$ (*Pmcn*: warwickite-structure [186, 187], $P2_1/c$: distorted warwickite-structure [186, 188]), $Fe_2^{II}Fe^{III}(BO_3)O_2$ (ludwigite [188, 189], vonsenite [190, 191] (Figure 4.3), hulsite [192]), $Fe^{II}Fe_2^{III}(BO_4)O_2$ (norbergite-structure, Figure 4.3) [193, 194], $FeBO_3$ (Figure 4.3) [170], and FeB_4O_7

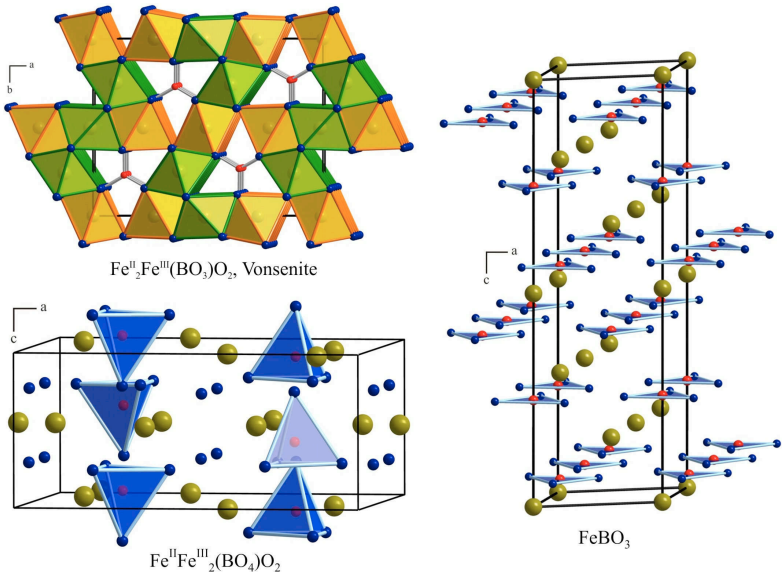

Figure 4.3: Crystal structures of the iron borates $Fe_2^{II}Fe^{III}(BO_3)O_2$ (vonsenite), $Fe^{II}Fe_2^{III}(BO_4)O_2$, and $FeBO_3$.

[195, 196]. $Fe^{II}Fe_2^{III}(BO_4)O_2$ consists of isolated BO_4-tetrahedra and, like $Fe^{II}Fe^{III}(BO_3)O$ and $Fe_2^{II}Fe^{III}(BO_3)O_2$, of isolated oxygen-atoms. In FeB_4O_7, both trigonal planar and tetrahedral building blocks can be found. All other compounds ($FeBO_3$ and the polymorphic phases of $Fe^{II}Fe^{III}(BO_3)O$ and $Fe_2^{II}Fe^{III}(BO_3)O_2$) are exclusively built up from trigonal planar BO_3-groups. In $FeBO_3$, an isostructural first-order phase transition under high-pressure conditions (diamond anvil cell; p = 53 ± 2 GPa), described in the same space group, is reported [197, 198].

In the system Co–B–O the compositions $Co_3(BO_3)_2$ (kotoite-type [199]), CoB_4O_7 (*Pbca* [200]), $Co_4B_6O_{13}$ ($I\bar{4}3m$ [200], Figure 4.4 left), $Co_2B_2O_5$ ($P\bar{1}$ [200, 201], Figure 4.4 right), $Co_3(BO_3)O_2$ (*Pbam*: ludwigite-structure [202]) are referred. While $Co_3(BO_3)_2$ and $Co_2B_2O_5$ consist of BO_3-groups, $Co_4B_6O_{13}$ and $Co_3(BO_3)O_2$

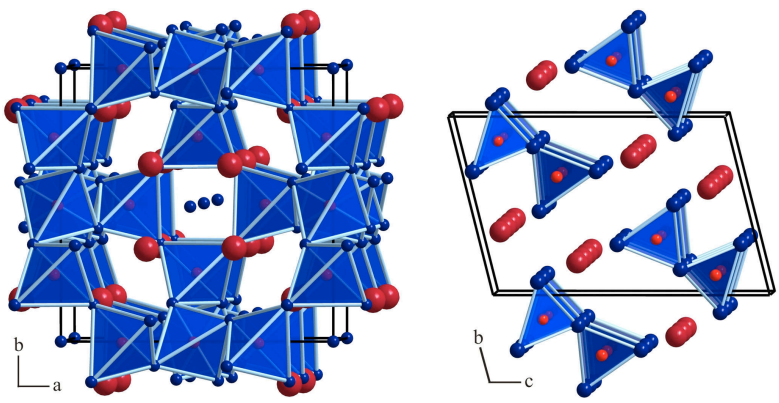

Figure 4.4: Crystal structures of the cobalt borates $Co_4B_6O_{13}$ and $Co_2B_2O_5$.

are built up from BO_4-tetrahedra, whereas the latter compound also possesses isolated oxygen atoms. In $Co_3(BO_3)O_2$ and CoB_4O_7 both BO_3- and BO_4-groups can be found.

Searching for nickel borates, only one nickel borate with the composition $Ni_3(BO_3)_2$ [180, 199, 203, 204] (Figure 4.5 left) could be found in the ternary system Ni–B–O, which shows trigonally coordinated boron atoms and Ni^{2+} ions in an octahedral coordination. In combination with the element sodium, the system Ni–B–O shows an interesting compound with composition $Na_2Ni_2B_{12}O_{21}$ [205] (Figure 4.5 right), possessing an isotypic structure to $Na_2Co_2B_{12}O_{21}$ [206]. Both structures show frameworks with one-dimensional channels along the crystallographic b-axis. In the case of $Na_2Co_2B_{12}O_{21}$, the authors suspected ionic conductivity along the channels, which was confirmed by Pompetzki and Albert in the case of $Na_2Ni_2B_{12}O_{21}$. Related compounds MCuB$_7$O$_{12}\cdot$nH$_2$O (M = Na, K) can also be found for the system Cu–B–O [207].

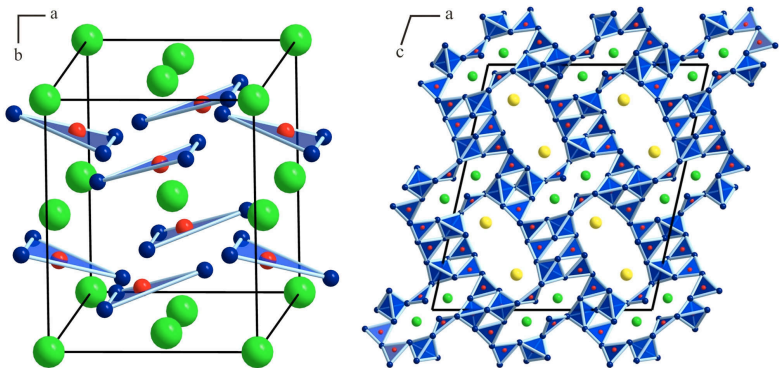

Figure 4.5: Crystal structures of the nickel borates $Ni_3(BO_3)_2$ (left) and $Na_2Ni_2B_{12}O_{21}$ (right).

Copper borates exhibit a few more compositions, namely CuB_2O_4 (tetragonal, $I\bar{4}2d$, Figure 4.6 left) [208, 209], exclusively showing BO_4-tetrahedra with copper in square-planar coordination and $Cu_3B_2O_6$ (also written as $Cu_{15}[(B_2O_5)_2(BO_3)_6O_2]$) (triclinic, $P\bar{1}$, Figure 4.6 middle) [210–212] exhibiting BO_3-groups and copper in square, square-pyramidal, and octahedral coordination. Further on the compositions $CuBO_2$ and $Cu_2B_4O_7$ were mentioned by Rza-Zade *et al.* in 1971 [213], whereas the latter compound was found to be CuB_2O_4 by Abdullaev and Mamedov in 1977 [209]. In 2007, Snure and Tiwari reported about the synthesis of bulk material and thin films of the transparent p-type Cu delafossite $CuBO_2$ [214] (the name refers to the mineral delafossite $CuFeO_2$, trigonal, $P\bar{3}m$, Figure 4.6). This transparent conductive oxide (TCO) could possibly find application in transparent light emitting diodes, UV detectors or solar cells [214]. The isotypy to the Cu delafossites CuMO$_2$ (M = Al, Ga, In, etc.) was postulated by only three concurrent reflexes of an X-ray powder diffraction pattern of $CuBO_2$ with the powder pattern of CuMO$_2$ delafossite structure. Therefore it is most doubtful, if $CuBO_2$

truly adopts this structure. The trigonal crystal structure of copper delafossite is composed of linear arranged Cu^+ and M^{3+} ions coordinated octahedrally by oxygen, while the octahedra build planar layers [215]. This would be a revolutionary discovery, because until today the maximum coordination number of boron in borates is four.

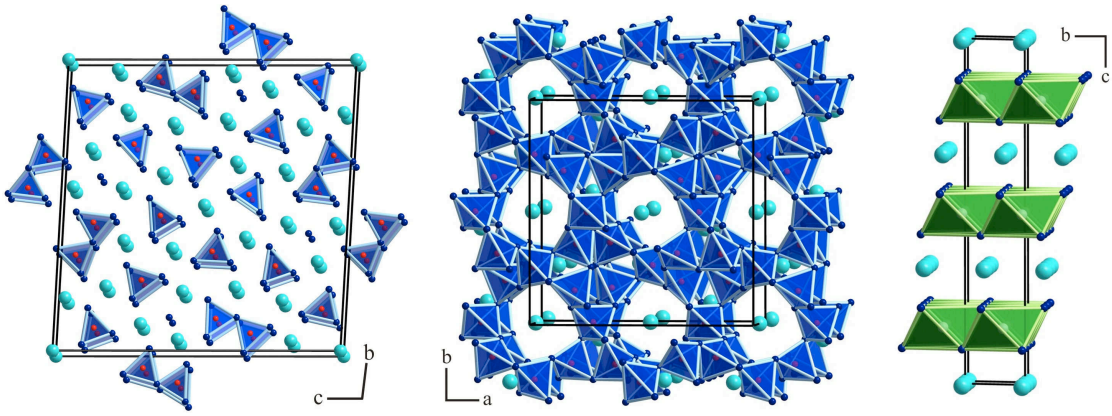

Figure 4.6: Crystal structures of the copper borates CuB_2O_4 (left), $Cu_3B_2O_6$ (middle), and the Cu delafossite $CuMO_2$ (M = Y) [216] (right).

In the systems Zr–B–O and Hf–B–O, no ternary phases could be found in literature, though several quaternary compounds. For zirconium the phases $Ni_5ZrO_4(BO_3)_2$ [217], $K_2Zr(BO_3)_2$ [218], $(Co_{1.5}Zr_{0.5})(BO_3)O$ [219], $BaZr(BO_3)_2$ [220], $Zr_3V_3B_{0.384}O_{0.576}$, and $Zr_3V_3B_{0.24}O_{0.36}$ [221] are known. In the case of the heavier homologue hafnium, only the composition $Ni_5HfB_2O_{10}$ [222], which is built up from Ni/HfO_6 octahedra and BO_3-groups, is described in the literature (Figure 4.7).

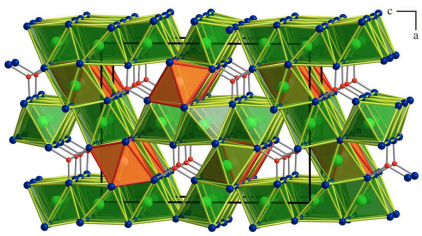

Figure 4.7: Crystal structure of $Ni_5HfB_2O_{10}$.

Concerning the second period of transition metal borates, we also investigated the system Cd–B–O. Up to now, three cadmium borates have been structurally well-characterized: the tetraborate CdB_4O_7 [182], which is a member of the isotypic MB_4O_7 family (orthorhombic, *Pbca*) with M = Mg [223], Mn [178], Co [200], Zn [179–181], and Hg [224] (see Figure 4.2)), the orthoborate $Cd_3(BO_3)_2$ (Figure 4.8) [225, 226], which adopts the kotoite ($Mg_3(BO_3)_2$) [199, 227] structure type (orthorhombic, *Pnnm*), and the diborate $Cd_2B_2O_5$ (see Figure 4.4 right) [228], which

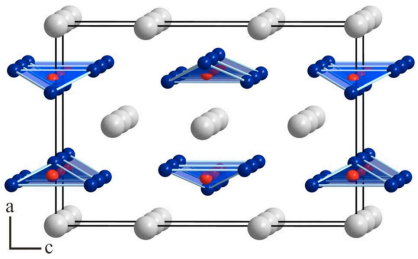

Figure 4.8: Crystal structure of $Cd_3(BO_3)_2$.

is isotypic to its Mg [229] and Co [200] analogues (triclinic, $P\overline{1}$).

Considering the structural characteristics of the mentioned normal-pressure phases, one finds BO_3-groups as the main building block and only few structures, composed of BO_4-tetrahedra. In this sense, the application of high-pressure conditions to borates with BO_3-groups could lead to new transition metal borates, exhibiting an increased portion of BO_4-tetrahedra, because conditions exceeding 7.5 GPa favour fourfold-coordinated boron atoms due to the pressure coordination rule [80]. Further on the coordination number of the metal cations should rise as well. This increase of coordination numbers could already be observed in the former described high-pressure phases, which are exclusively built up from tetrahedral BO_4-groups. In the same way, the coordination at the metal cations can be enlarged in comparison to the corresponding normal-pressure phases.

A second characteristic of the normal-pressure synthesis of borates is the aspect of forming glasses, which is presumably the reason why there exist no ambient pressure phases in the systems Hf–B–O and Zr–B–O. In this regard the question arose, if it is possible to force crystallisation by including the parameter pressure in the syntheses of borates belonging to systems, where only glasses are known.

In the following sections (4.1.3–4.1.9) our investigations in the borate systems of the transition metals Mn – Cu, Zr, Hf, and Cd are discussed. The syntheses, structural charactarization, and description of new high-pressure phases in the mentioned systems are reported.

4.1.2 Starting Materials

The starting materials for the adjacent syntheses were all air- and humidity-resistant. The characterization of the crystalline materials was carried out *via* powder diffraction followed by a comparison with the ICSD-database, whereas only crystalline impurities, with a concentration exceeding 3 %, can be detected. The used substances are listed in Table 4.1.

Table 4.1: List of used substances.

Substance	State	Source of Supply	Purity	ICSD-PDF
B_2O_3	Granulate	Strem Chemicals, Newburyport, USA	99.9	amorphous
MnO_2	Powder	–	–	[44-141]
Fe_2O_3	Powder	Sigma-Aldrich Chemie GmbH, Munich, Germany	99.9	[33-664], Hematite
Co_2O_3	Powder	Merck KGaA, Darmstadt, Germany	*p.a.*	[42-1467]
NiO	Powder	Avocado Research Chemicals Ltd., Shore Road, Heysham, Morecambe, Lancashire, UK	–	[44-1159]
CuO	Powder	–	–	[80-1268]
HfO_2	Powder	Strem Chemicals, Newburyport, USA	98	[74-1506]
ZrO_2	Powder	Strem Chemicals, Newburyport, USA	99.9	[37-1484], Baddeleyite
CdO	Powder	–	–	[5-640]

4.1.3 The Borates β-MB$_2$O$_5$ (M = Zr, Hf)

4.1.3.1 Syntheses

According to Equation (4.1) the two new phases β-MB$_2$O$_5$ (M = Hf [230], Zr [231]) were prepared *via* high-pressure/high-temperature syntheses from HfO_2 (Strem Chemicals, Newburyport, USA, 98%), ZrO_2 (Strem Chemicals, Newburyport, USA, 99.9%) and B_2O_3 (Strem Chemicals, Newburyport, USA, > 99.9%).

$$MO_2 + B_2O_3 \xrightarrow[1100\ ^\circ\mathrm{C}]{7.5\ \mathrm{GPa}} \beta\text{-}MB_2O_5 \quad (M = \mathrm{Hf,\ Zr}) \tag{4.1}$$

The stoichiometric mixtures of the according oxides were ground and each mixture filled into a boron nitride crucible of an 18/11-assembly, which was compressed up to 7.5 GPa during 3 h. The samples were heated to 1100 °C in 10 min, kept there for 5 min, and cooled down to 750 °C in 15 min. Afterwards, the samples were quenched to room temperature, followed by decompression over a period of 9 h. The recovered experimental octahedra were broken apart and the samples were carefully separated from the surrounding boron nitride crucibles, yielding the

colourless, crystalline compounds β-HfB_2O_5 and β-ZrB_2O_5. The powder patterns of the reaction products showed small amounts of unreacted HfO_2 and ZrO_2. The corresponding surplus boron oxide was not detectable in the powder XRD patterns (X-ray amorphous). Systematic variations of the experimental conditions showed that β-HfB_2O_5 can be synthesized in the pressure range of 6–11 GPa, applying temperatures of 800–1200 °C. The best results were obtained at the above mentioned conditions of 7.5 GPa and 1100 °C.

4.1.3.2 Crystal Structure Analyses

The powder diffraction patterns of the isotypic phases were collected on a STOE Stadi P powder diffractometer with monochromatized $CuK_{\alpha 1}$ (λ = 154.051 pm) radiation in transmission geometry from flat samples. The diffraction patterns were indexed with the program ITO [125] on the basis of monoclinic unit cells. Based on least-square fits of the powder data, the lattice parameters (see Table 4.2) were calculated. The correct indexing of the patterns was confirmed by intensity calculations [121], taking the atomic positions from the refined crystal structure data. The lattice parameters determined from the powder data and single crystal data fit well. Figure 4.9 shows the measured powder patterns of the isotypic phases (top) in comparison to the simulated patterns derived from the single crystal data (bottom). Additional reflections belong to unreacted metal oxide (marked with asterisks). Variation of temperature or pressure did not succeed in pure samples until now.

Small single crystals of β-MB_2O_5 (M = Hf, Zr) were isolated by mechanical fragmentation and examined by means of Laue photographs of a Buerger camera, equipped with an image plate system (Fujifilm BAS-2500). Single crystal intensity data of β-MB_2O_5 (M = Hf, Zr) were measured with a Kappa CCD diffractometer (Enraf-Nonius) (MoK_α radiation (λ = 71.073 pm)). A numerical absorption correction (HABITUS [132]) was applied to the data of β-HfB_2O_5. A multi-scan absorption correction was performed on the data of β-ZrB_2O_5 using the program SCALEPACK [133]. According to the systematic extinctions $h0l$ with $l \neq 2n$, $0k0$ with $k \neq 2n$, and $00l$ with $l \neq 2n$, the monoclinic space group $P2_1/c$ (No. 14) was derived. Structure solution and parameter refinement (full-matrix least squares against F^2) were carried out *via* direct methods, using the SHELX-97 software suite [135, 136]. Table 4.2 shows details of the data collection and structure refinement. The positional parameters, anisotropic displacement parameters, interatomic distances, and interatomic angles are listed in Tables 4.3, 4.4, 4.5, and 4.6.

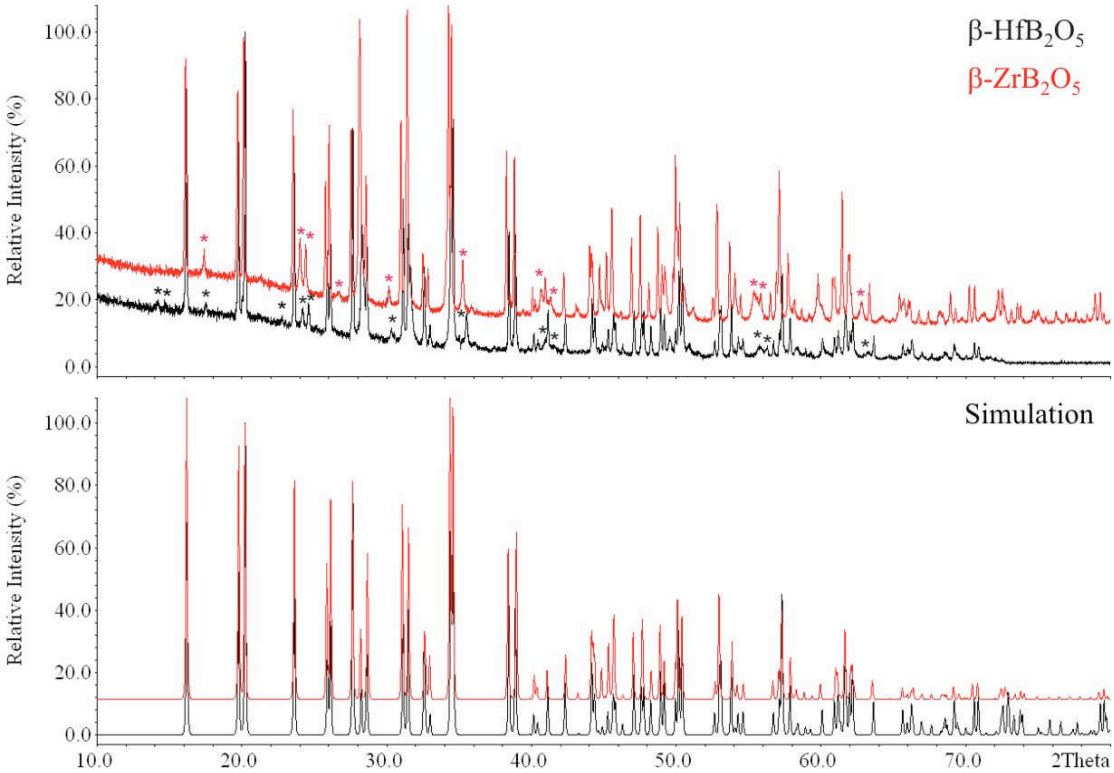

Figure 4.9: Recorded and simulated (single crystal data) powder diffraction patterns of β-MB_2O_5 (M = Hf, Zr). Reflections marked with asterisks belong to unreacted MO_2 (M = Hf, Zr).

Table 4.2: Crystal data and structure refinement of β-MB_2O_5 (M = Hf, Zr) (standard deviations in parentheses).

Empirical Formula	HfB_2O_5	ZrB_2O_5
Molar mass/g·mol^{-1}	280.11	192.84
Crystal system	monoclinic	
Space group	$P2_1/c$	
Powder diffractometer	STOE Stadi P	
Radiation	$CuK_{\alpha 1}$ (λ = 154.051 pm)	
Powder data		
a/pm	438.43(3)	440.21(2)
b/pm	690.48(6)	693.15(3)
c/pm	897.27(6)	899.24(3)
β/°	90.76(1)	90.93(1)
V/nm^3	0.2716(1)	0.27435(2)
Single crystal diffractometer	Enraf-Nonius Kappa CCD	
Radiation	MoK_α (λ = 71.073 pm)	
Single crystal data		
a/pm	438.48(9)	439.04(9)
b/pm	690.60(2)	691.2(2)
c/pm	897.60(2)	896.8(2)
β/°	90.76(3)	90.96(3)
V/nm^3	0.2718(2)	0.2721(2)
Formula units per cell	Z = 4	Z = 4
Temperature/K	293(2)	293(2)
Calculated density/g·cm^{-3}	6.847	4.71
Crystal size/mm^3	0.044 × 0.030 × 0.022	0.02 × 0.02 × 0.02
Detector distance/mm	50.0	30.0
Scan time per degree/min	80.0	80.0
Absorption coefficient/mm^{-1}	38.24	3.890
F (000)/e	488	360
θ range/°	3.1 – 35.0	3.7 – 34.8
Range in hkl	-7/+6, -11/+9, ±14	-6/+7, -11/+10, ±14
Total no. reflections	5887	2203
Independent reflections	1186 (R_{int} = 0.0372)	1166 (R_{int} = 0.0352)
Reflections with I > 2σ(I)	1144 (R_σ = 0.0352)	969 (R_σ = 0.0437)
Data/parameters	1186/74	1166/73
Absorption correction	numerical (HABITUS [132])	multi-scan (SCALEPACK [133])
Transm. ratio (min/max)	0.270/0.497	–
Goodness-of-fit (F^2)	1.165	1.027
Final R indices (I > 2σ(I))	R1 = 0.0201	R1 = 0.0262
	wR2 = 0.0498	wR2 = 0.0540
R indices (all data)	R1 = 0.0210	R1 = 0.0379
	wR2 = 0.0502	wR2 = 0.0576
Extinction coefficient	0.068(2)	–
Largest diff. peak, deepest hole/Å·e^{-3}	2.143/-2.432	0.79/-0.93

Table 4.3: Atomic coordinates and equivalent isotropic displacement parameters $U_{eq}/Å^2$ of β-MB_2O_5 (M = Hf, Zr) (space group $P2_1/c$; all Wyckoff sites $4e$). U_{eq} is defined as one third of the trace of the orthogonalized U_{ij} tensor (standard deviations in parentheses).

Atom	x	y	z	U_{eq}
Hf	0.00132(3)	0.11281(2)	0.67087(2)	0.00420(8)
B1	0.5267(8)	0.2286(6)	0.4232(4)	0.0046(6)
B2	0.4652(9)	0.0871(7)	0.1655(4)	0.0039(6)
O1	0.7874(6)	0.0898(4)	0.1790(3)	0.0050(4)
O2	0.3297(6)	0.8950(3)	0.1502(3)	0.0051(5)
O3	0.3456(5)	0.2215(4)	0.0547(3)	0.0048(4)
O4	0.3039(5)	0.1555(4)	0.3078(3)	0.0043(4)
O5	0.7685(6)	0.0963(4)	0.4679(3)	0.0048(4)
Zr	0.00127(5)	0.11284(3)	0.67103(2)	0.00605(7)
B1	0.5271(6)	0.2299(4)	0.4230(3)	0.0072(5)
B2	0.4641(6)	0.0868(4)	0.1656(3)	0.0072(5)
O1	0.7861(4)	0.0902(2)	0.1790(2)	0.0076(3)
O2	0.3307(4)	0.8955(2)	0.1504(2)	0.0077(3)
O3	0.3477(4)	0.2212(2)	0.0540(2)	0.0082(3)
O4	0.3055(4)	0.1549(3)	0.3077(2)	0.0074(3)
O5	0.7689(4)	0.0974(2)	0.4674(2)	0.0080(3)

Table 4.4: Anisotropic displacement parameters of β-MB_2O_5 (M = Hf, Zr) (standard deviations in parentheses).

Atom	U_{11}	U_{22}	U_{33}	U_{23}	U_{13}	U_{12}
Hf	0.0050(2)	0.0039(2)	0.0038(2)	0.00006(3)	-0.00011(6)	0.00006(3)
B1	0.007(2)	0.003(2)	0.004(2)	0.000(2)	-0.001 (2)	0.001(2)
B2	0.004(2)	0.005 (2)	0.002(2)	-0.001(2)	0.000(2)	-0.001(2)
O1	0.004(2)	0.005(2)	0.006(2)	0.0014(8)	0.0001(8)	0.0001(8)
O2	0.006(2)	0.003(2)	0.006(2)	-0.0010(7)	0.0011(8)	-0.0011(7)
O3	0.0048(9)	0.004(2)	0.0054(9)	0.0017(8)	0.0005(7)	0.0013(8)
O4	0.004(2)	0.004(2)	0.0044(9)	-0.0015(8)	0.0001(7)	-0.0005(8)
O5	0.004(2)	0.004(2)	0.006(2)	-0.0009(7)	-0.0014(8)	0.0008(7)
Zr	0.0064(2)	0.0059(2)	0.0059(2)	0.00001(7)	0.00026(7)	0.00003(8)
B1	0.008(2)	0.007(2)	0.007(2)	-0.0015(8)	-0.0002(9)	-0.0001(9)
B2	0.008(2)	0.007(2)	0.007(2)	-0.0003(8)	0.0016(9)	0.0008(9)
O1	0.0071(7)	0.0084(8)	0.0071(7)	0.0013(6)	0.0001(6)	0.0000(6)
O2	0.0084(7)	0.0065(8)	0.0083(7)	0.0003(6)	0.0016(6)	0.0005(6)
O3	0.0083(7)	0.0076(8)	0.0088(7)	0.0011(6)	0.0010(6)	0.0019(6)
O4	0.0080(7)	0.0076(7)	0.0065(7)	0.0003(6)	-0.0001(6)	-0.0003(6)
O5	0.0091(7)	0.0071(8)	0.0077(7)	0.0013(6)	0.0003(6)	0.0008(6)

4.1.3.3 Crystal Structure Description

The crystal structure of β-MB_2O_5 (M = Hf, Zr) is built up from corner-sharing BO_4-tetrahedra ($Q^{[3]}$), which are interconnected to layers, separated by the corresponding cations (Figure 4.10). These layers extend parallel to the bc-plane and are based on "Vierer"- and "Achter"- rings (rings consisting of four and eight tetrahedral centres, respectively; the expressions refer to the german words vier

and acht, which mean four and eigth, respectively [39]) of BO_4-tetrahedra (Figure 4.11). Figures 4.12 and 4.13 give a view of the M^{4+} (M = Hf, Zr) ions, which separate the borate sheets and are coordinated by eight oxygen atoms in a distorted square-antiprismatic way. In the two crystallographically distinguishable

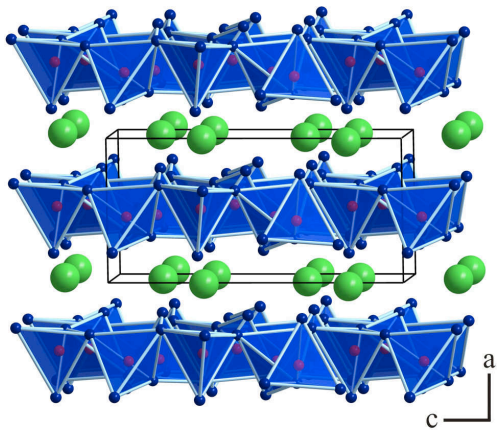

Figure 4.10: Crystal structure of β-MB$_2$O$_5$ (M = Hf, Zr) with view along [010], revealing layers of BO_4-tetrahedra separated by M^{4+}-ions.

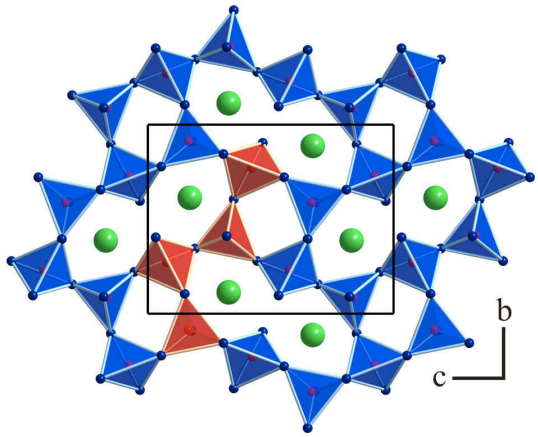

Figure 4.11: View on one borate layer in β-MB$_2$O$_5$ (M = Hf, Zr).

BO_4-tetrahedra, the B–O distances vary between 142 and 154 pm in both isotypic structures, with a mean value of 147.1 pm in β-HfB_2O_5 and 146.8 pm in β-ZrB_2O_5. This corresponds to the known average value of 147.6 pm for boron-oxygen bonds in BO_4-tetrahedra [232, 233]. The O–B–O angles range between 99.6 and 116.5° with a mean value of 109.5° and between 99.8 and 115.7° with a mean value of 109.4° for the Hf-phase and the Zr-phase, respectively. The Hf–O distances range from 208 to 241 pm with a mean value of 221.2 pm in β-HfB_2O_5, which is slightly higher than the average Hf–O distance of 218.8 pm found in $HfSiO_4$ [234] or β-$HfMo_2O_8$ [235] exhibiting hafnium in eightfold oxygen-coordination. In the case of β-ZrB_2O_5 the Zr–O distances vary from 208 to 241 pm with an average value of 221.7 pm. This is also slightly higher than the average Zr–O distance of 219.8 pm in zirconia ($ZrSiO_4$) [236] or 219.5 pm in $ZrMo_2O_8$ [237], which both exhibit zirconium in eight-fold coordination.

The application of Liebau's nomenclature for silicates [39] to the arrangement of tetrahedra in the structure of β-MB$_2$O$_5$ (M = Hf, Zr) leads to the formula $M\{\mathrm{uB}, 1^2_\infty\}[^4\mathrm{B}_2\mathrm{O}_5]$, representing an unbranched "Vierer" single layer. The term "Vierer" was coined by F. Liebau [39] and is derived from the german word vier, which means four. The whole borate-layer in β-MB$_2$O$_5$ (M = Hf, Zr) can be built up by an unbranched chain consisting of four tetrahedral centres by applying the symmetry element $\bar{1}$ followed by translation. Figure 4.11 shows one of these "Vierer" chains, highlighted in red.

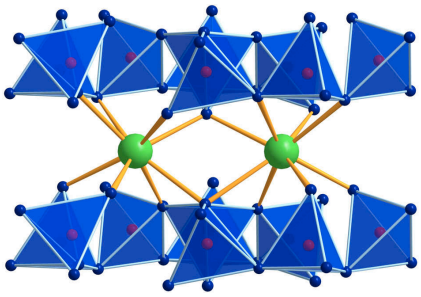

Figure 4.12: Distorted square-antiprismatic coordination of M^{4+} in β-MB$_2$O$_5$ (M = Hf, Zr).

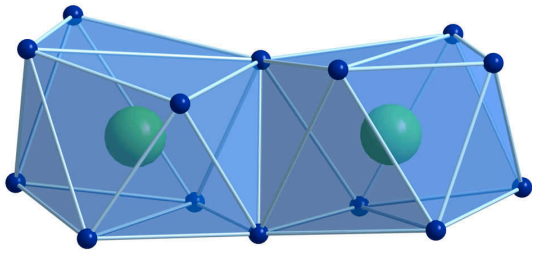

Figure 4.13: Coordination polyhedra in β-MB$_2$O$_5$ (M = Hf, Zr).

Table 4.5: Interatomic distances/pm in β-MB$_2$O$_5$ (M = Hf, Zr) (space group $P2_1/c$) calculated with the single crystal lattice parameters (standard deviations in parentheses).

β-HfB$_2$O$_5$				β-ZrB$_2$O$_5$			
Hf-O5a	207.9(3)	B1-O5	145.2(5)	Zr-O5a	207.9(2)	B1-O5	145.3(3)
Hf-O1a	214.4(3)	B1-O2	147.0(4)	Zr-O1a	214.6(2)	B1-O3	146.5(3)
Hf-O5b	216.5(3)	B1-O3	147.2(4)	Zr-O5b	217.1(2)	B1-O2	146.5(3)
Hf-O3	217.2(2)	B1-O4	150.1(4)	Zr-O2	218.4(2)	B1-O4	150.1(3)
Hf-O2	218.0(3)	Ø = 147.4		Zr-O3	218.7(2)	Ø = 147.1	
Hf-O1b	225.9(3)	B2-O1	141.7(5)	Zr-O1b	226.1(2)	B2-O1	141.7(3)
Hf-O4a	229.5(3)	B2-O3	145.3(5)	Zr-O4a	229.8(2)	B2-O2	145.2(3)
Hf-O4b	240.6(3)	B2-O2	145.9(5)	Zr-O4b	241.0(2)	B2-O3	145.2(3)
Ø = 221.2		B2-O4	154.2(4)	Ø = 221.7		B2-O4	153.6(3)
		Ø = 146.8				Ø = 146.4	

Table 4.6: Interatomic angles/° in β-MB$_2$O$_5$ (M = Hf, Zr) calculated with the single crystal lattice parameters (standard deviations in parentheses).

β-HfB$_2$O$_5$				β-ZrB$_2$O$_5$			
O2-B1-O4	103.4(2)	O2-B2-O4	99.6(3)	O2-B1-O4	103.7(2)	O2-B2-O4	99.8(2)
O3-B1-O4	106.2(3)	O3-B2-O4	101.9(3)	O3-B1-O4	106.3(2)	O3-B2-O4	102.5(2)
O5-B1-O2	107.4(3)	O3-B2-O2	111.9(3)	O5-B1-O2	107.5(2)	O2-B2-O3	112.4(2)
O5-B1-O3	109.0(3)	O1-B2-O4	113.1(3)	O5-B1-O3	109.0(2)	O1-B2-O3	112.8(2)
O2-B1-O3	114.5(3)	O1-B2-O3	113.6(3)	O2-B1-O3	114.8(2)	O1-B2-O4	113.0(2)
O5-B1-O4	116.5(3)	O1-B2-O2	115.1(3)	O5-B1-O4	115.7(2)	O1-B2-O2	115.0(2)
Ø = 109.5		Ø = 109.5		Ø = 109.5		Ø = 109.5	

A comparison of the isotypic phases shows that the bond-lengths and -angles of the two phases are nearly identical. This is in accord with the similar ionic radii of Zr^{4+} (98 pm) and Hf^{4+} (97 pm) in an eightfold oxygen-coordination [238]. Appropriate to that, the lattice parameters of β-HfB$_2$O$_5$ (a = 438.48(9), b = 690.60(2), c = 897.60(2) pm, and β = 90.76(3)°) are nearly equal to those of β-ZrB$_2$O$_5$ (a = 439.04(9), b = 691.2(2), c = 896.8(2) pm, and β = 90.96(3)°).

The arrangement of BO$_4$-tetrahedra in β-MB$_2$O$_5$ (M = Hf, Zr), exhibiting "Vierer"- and "Achter"- rings, reminds of the crystal structure of apophyllite KCa$_4$[Si$_4$O$_{10}$]$_2$(F,OH) · 8 H$_2$O [239] (Figure 4.14). This structure is also composed

of layers of rings (SiO_4-tetrahedra) with the same ring-sizes, but the tetrahedral sequence inside the rings shows a different topology.

A closer comparison of the orientation of tetrahedra leads to minerals of the gadolinite group, in which the topology of the tetrahedra is identical to the arrangement in β-MB_2O_5 (M = Hf, Zr). Figure 4.15 shows the structure of gadolinite-(Y) $Y_2Be_2FeSi_2O_8O_2$ [240, 241], exhibiting the same arrangement of tetrahedra as found in β-MB_2O_5 (M = Hf, Zr). The difference is that the tetrahedra in gadolinite-(Y) are centred alternately by beryllium (green polyhedra) and silicon atoms (orange polyhedra). Additionally, iron atoms are positioned in the origin of the unit cell beneath and above the four-membered rings. Several minerals and synthetic compounds belong to the gadolinite group (space group $P2_1/c$), which can be represented by the general chemical formula $A_2Z_2XSi_2O_8(O,OH)_2$. Demartin *et al.* [242] reviewed several members of this family, including datolite $CaBSiO_4(OH)$ [243–246] (Figure 4.16), homilite $Ca_2B_2FeSi_2O_8O_2$ [247], hingganite-(Y) $Y_2Be_2Si_2O_8(OH)_2$ [242], hingganite-(Yb) $Yb_2Be_2Si_2O_8(OH)_2$ [248], minasgeraisite-(Y) $Y_2Be_2CaSi_2O_8(OH)_2$ [249], and synthetic compounds like calcybeborosilelite-(Y) $(Y,Ca)_2(B,Be)_2Si_2O_8(OH,O)_2$ [250], calciogadolinite $CaYBe_2FeSi_2O_8O_2$ [251–253], and $NiYb_2Be_2Si_2O_{10}$ [254]. A common feature of all these compounds is the fact that at least half of the tetrahedral positions are occupied by silicon atoms. This is also expressed by the general formula $A_2Z_2XSi_2O_8(O,OH)_2$, in which Z stands for the atoms, that occupy the second half of tetrahedral positions. To include the replacement of silicon at the tetrahedral position against other suitable atoms, we modified the general formula of Demartin *et al.* to $A_2Z_2XT_2O_8(O,OH)_2$. This way, compounds like herderite $Ca_2Be_2P_2O_8(OH)_2$ [255], bakerite $Ca_4B_5Si_3O_{15}(OH)_5$ [256], $CuTm_2(B_2O_5)_2$ [257], $NiHo_2(B_2O_5)_2$ [258] and the diborates β-MB_2O_5 (M = Hf, Zr) → $M_2B_2B_2O_8O_2$ can be included into the systematic representation of this structure family. Table 4.7 gives a survey of the different compositions including cell parameters, volume, c/a-, b/a-ratio, density, and an assignment of the cations to their positions.

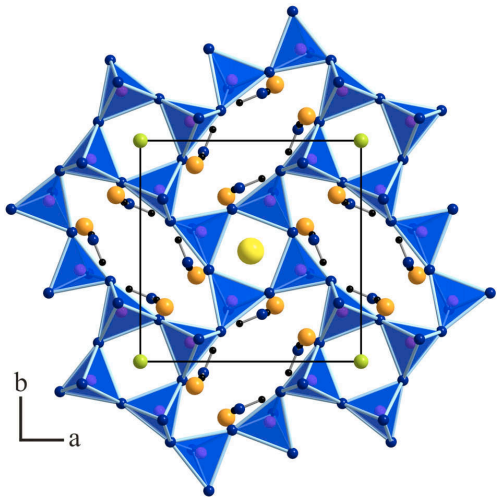

Figure 4.14: Crystal Structure of apophyllite $KCa_4[Si_4O_{10}]_2(F,OH) \cdot 8\ H_2O$ with view along $[00\bar{1}]$. K^+ is shown as yellow, Ca^{2+} as orange, Si^{4+} as pink, O^{2-} as blue, F^- as green, and H^+ as black spheres.

In the general formula $A_2Z_2XT_2O_8(O,OH)_2$, the A site is occupied by rare earth

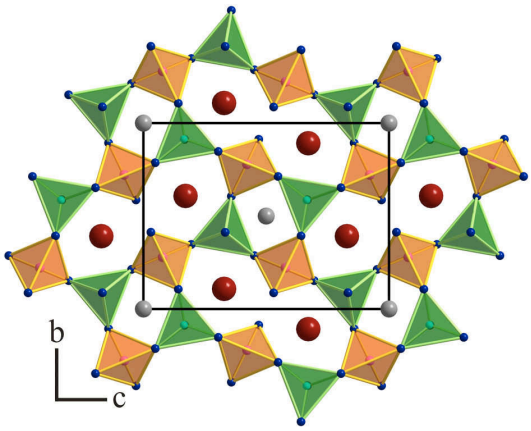

Figure 4.15: View of the crystal structure of gadolinite-(Y) along [100]. Y^{3+} ions are shown as red spheres, Fe^{2+} as gray spheres. Orange tetrahedra represent SiO_4-groups and green tetrahedra BO_4-groups.

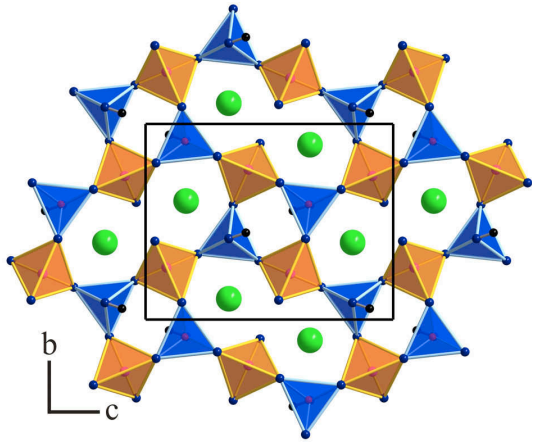

Figure 4.16: Projection of the structure of datolite in the bc-plane. Ca^{2+} ions are shown as gray spheres, protons as black spheres. Orange polyhedra represent SiO_4-groups and blue polyhedra BO_4-groups.

(*RE*) or calcium ions, Z includes boron or beryllium, the T site contains silicon, phosphorous, or boron, and the X site can be filled with Fe^{2+}, Ni^{2+}, and Cu^{2+} ions or remains empty. The occupation with Ca^{2+} or Fe^{3+}, as listed in the examples calciogadolinite and minasgeraisite-(Y), seems to be most doubtful. Often, vacancies on the X site are charge balanced by the substitution of oxygen ions for hydroxyl ions, *e.g.* $RE_2Be_2FeSi_2O_8O_2$ (gadolinite) $\rightarrow$ $RE_2Be_2Si_2O_8(OH)_2$ (hingganite). Burt described this substitution giving an operator $(OH)_2(FeO_2)_{-1}$, not involving real vacancies but favored on crystal-chemical reasons for balancing the charge variation [259]. Furthermore, the replacement of *RE* and Be by Ca and B, respectively, leads to the second operator $CaB(REBe)_{-1}$. Starting with gadolinite $RE_2Be_2FeSi_2O_8O_2$, the operator $(OH)_2(FeO_2)_{-1}$ leads to the end member hingganite, $CaB(REBe)_{-1}$ to the final compound homilite $Ca_2B_2FeSi_2O_8O_2$, and if both operators act together, datolite $Ca_2B_2Si_2O_8(OH)_2$ is the final end member of these substitutions. Figure 4.16 shows the structure of datolite, built up from BO_3OH (blue tetrahedra) and SiO_4-tetrahedra (orange polyhedra), in which the X site is empty. For compensation, the hydrogen atoms of the hydroxyl groups point to the X site. A detailed discussion of further variants of substitution can be found in Reference [242]. Also other variants can be realized by substitutions on the T site, *e.g.* herderite $Ca_2Be_2P_2O_8(OH)_2$, which is built up from sheets of corner-sharing PO_4- and BeO_3OH-tetrahedra (alternating). Even a total occupation of the tetrahedral positions by boron atoms was possible in the synthetic compounds $CuTm_2(B_2O_5)_2$ and $NiHo_2(B_2O_5)_2$.

In this structure family, the diborates β-MB_2O_5 (M = Hf, Zr) represent the first ternary compounds with M^{4+} on the A site, boron on the Z and T sites, and an empty position X corresponding to "$M_2B_2B_2O_8O_2$" $\rightarrow$ MB_2O_5. Hydrogen was

excluded by IR spectroscopic investigations, in which no absorptions of hydroxyl groups or water could be found. So, β-MB$_2$O$_5$ (M = Hf, Zr) can be considered as the simplest structural variant of all compounds belonging to the gadolinite family. Table 4.7 illustrates that the unit cell of β-MB$_2$O$_5$ (M = Hf, Zr) has the lowest extension (Hf: V = 0.2718(2) nm^3; Zr: V = 0.2721(2) nm^3) of all compounds given, while the c/a and b/a ratios correspond to the values of the other phases. This is caused by the fact that β-MB$_2$O$_5$ (M = Hf, Zr) are dense metastable high-pressure phases.

Table 4.7: Review of substances with the general formula $A_2Z_2XT_2O_8(O,OH)_2$ ·

Name	Formula	A	Z	T	X	a/pm	b/pm	c/pm	β/°	c/a	b/a	V/Å^3	ρ/g·cm^{-3}	Ref.
Gadolinite-(Y)	$Y_2Be_2FeSi_2O_8O_2$	Y	Be	Si	Fe^{2+}	476.8(1)	756.5(2)	1000.0(2)	90.31(2)	2.097	1.586	360.7(1)	4.307	[240, 241]
Datolite	$Ca_2B_2Si_2O_8(OH)_2$	Ca	B	Si	vac.	483.2(4)	760.8(4)	963.6(8)	90.40(7)	1.994	1.575	354.2	2.999	[243, 246]
Homilite	$Ca_2B_2FeSi_2O_8O_2$	Ca	B	Si	Fe^{2+}	477.6(1)	762.1(2)	978.6(2)	90.61(2)	2.049	1.596	356.2(1)	3.451	[247]
Hingganite-(Yb)	$Yb_2Be_2Si_2O_8(OH)_2$	Yb	Be	Si	vac.	474.0(2)	760.7(3)	988.8(5)	90.45(4)	2.086	1.605	356.5	5.424	[248]
Hingganite-(Y)	$Y_2Be_2Si_2O_8(OH)_2$	Y	Be	Si	vac.	474.4(7)	757.1(8)	981.1(11)	90.26(2)	2.068	1.596	352.4(8)	3.901	[242]
Minasgeraisite-(Y)[b]	$Y_2Be_2CaSi_2O_8(OH)_2$	Y	Be	Si	Ca^{2+}	470.2(1)	756.2(1)	983.3(2)	90.46(6)	2.091	1.608	349.6(2)	4.313	[249]
Bakerite	$Ca_4B_5Si_3O_{15}(OH)_5$	Ca	B	Si	vac.	480.0(1)	757.9(1)	954.3(1)	90.44(1)	1.988	1.579	347.2	2.982	[256]
Calcybeborosilelite-(Y)	$(Y,Ca)_2(B,Be)_2Si_2O_8(OH,O)_2$	Y,Ca	B,Be	Si	vac.[a]	476.6(2)	760.0(2)	984.6(4)	90.11(3)	2.066	1.595	356.6	3.408	[250]
Calciogadolinite[b]	$CaYBe_2FeSi_2O_8O_2$	Y,Ca	Be	Si	Fe^{3+}	469.6(1)	756.6(2)	998.8(2)	90.1(2)	2.127	1.611	354.0(2)	3.931	[251–253]
	$NiYb_2Be_2Si_2O_{10}$	Yb	Be	Si	Ni^{2+}	466.4(4)	738.5(4)	986.6(8)	90.02	2.115	1.583	339.8	6.244	[254]
Herderite	$Ca_2Be_2P_2O_8(OH)_2$	Ca	Be	P	vac.	480.4(1)	766.1(1)	978.9(2)	90.02(1)	2.038	1.595	360.3	2.969	[255]
	$CuTm_2(B_2O_5)_2$	Tm	B	B	Cu^{2+}	452.18(7)	720.0(2)	929.2(5)	90.16(5)	2.055	1.593	302.5(2)	6.638	[257]
	$NiHo_2(B_2O_5)_2$	Ho	B	B	Ni^{2+}	451.0(4)	724.8(3)	938.8(6)	91.39	2.082	1.607	306.8(3)	6.406	[258]
β-Hafnium-diborate	$HfB_2O_5 \rightarrow Hf_2B_2B_2O_8O_2$	Hf	B	B	vac.	438.48(9)	690.60(2)	897.60(2)	90.76(3)	2.047	1.575	271.8(2)	6.847	[230]
β-Zirconium-diborate	$ZrB_2O_5 \rightarrow Zr_2B_2B_2O_8O_2$	Zr	B	B	vac.	439.04(9)	691.2(1)	896.8(1)	90.96(3)	2.043	1.574	272.1(2)	4.708	[231]

vac. = vacant;

[a] nearly vacant;

[b] doubtful, redetermination of the crystal structure would be useful

4.1.3.4 Thermal Behaviour

Temperature-programmed X-ray powder diffraction experiments were performed on a STOE Stadi P powder diffractometer ($MoK_{\alpha 1}$) with a computer controlled STOE furnace. The samples were enclosed in a silica capillary and heated from room temperature to 500 °C in 100 °C steps and from 500 °C to 1100 °C in 50 °C steps. Afterwards, the samples were cooled down to 500 °C in 50 °C steps, and below 500 °C in 100 °C steps. At each temperature a diffraction pattern was recorded over the angular range $7° \leq 2\theta \leq 22°$. Figures 4.17 and 4.18 illustrate the temperature-programmed X-ray powder diffraction patterns of β-HfB_2O_5 and β-ZrB_2O_5 showing a decomposition of the high-pressure phase into the binary transition metal-oxides and supposed B_2O_3 after successive heating to 800 – 850 °C. Heating above 1000 °C caused a reaction with the quartz capillary, leading to $HfSiO_4$ [234].

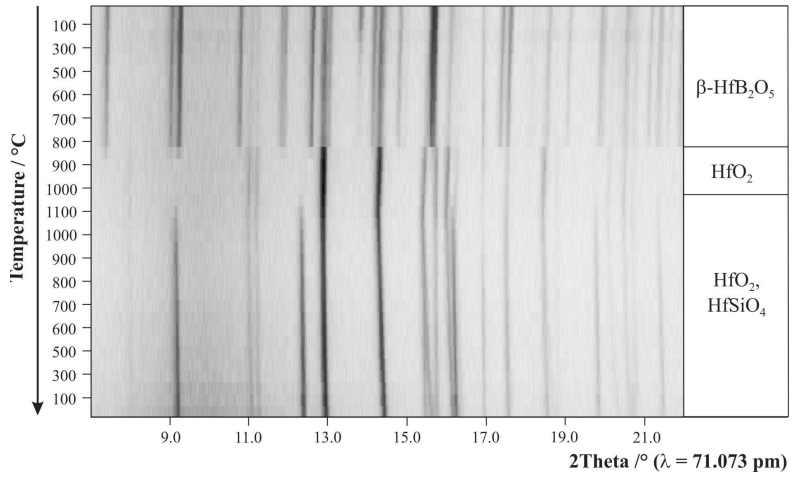

Figure 4.17: Temperature-programmed X-ray powder patterns of β-HfB_2O_5.

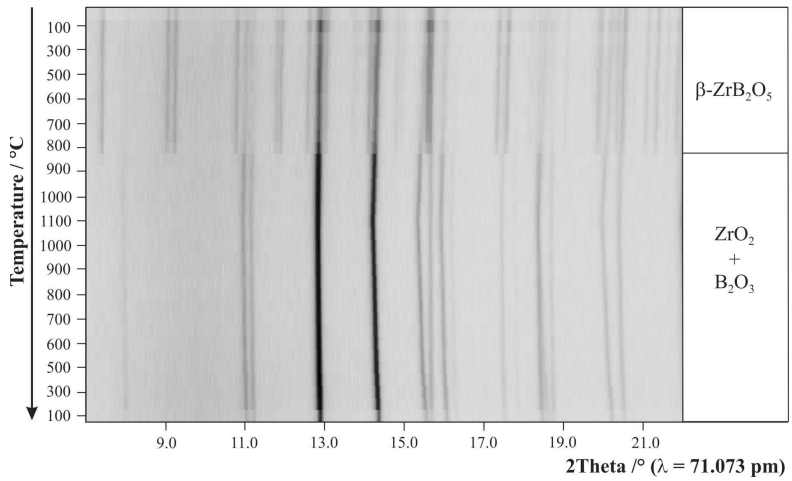

Figure 4.18: Temperature-programmed X-ray powder patterns of β-ZrB_2O_5.

4.1.3.5 Theoretical Calculations

The calculation of bond-valence sums for β-MB$_2$O$_5$ (M = Hf, Zr) with the help of bond-length/bond-strength (ΣV) [164, 165] and CHARDI (ΣQ) [167] concepts confirm the formal ionic charges of the atoms, acquired by the X-ray structure analysis. Table 4.8 shows the value of each atom.

Table 4.8: Charge distribution in β-MB$_2$O$_5$ (M = Hf, Zr) calculated with the bond-length / bond-strength concept (ΣV) and the CHARDI concept (ΣQ).

β-HfB$_2$O$_5$	Hf	B1	B2	O1	O2	O3	O4	O5
ΣQ	+4.01	+2.98	+3.02	-1.94	-2.08	-2.10	-1.81	-2.08
ΣV	+3.78	+3.03	+3.10	-1.84	-2.05	-2.07	-1.97	-1.98
β-ZrB$_2$O$_5$	Zr	B1	B2	O1	O2	O3	O4	O5
ΣQ	+3.87	+3.06	+3.13	-1.87	-2.09	-2.09	-2.00	-2.02
ΣV	+4.01	+2.97	+3.02	-1.93	-2.10	-2.09	-1.81	-2.07

Furthermore, we calculated the MAPLE values (Madelung Part of Lattice Energy) [161–163] for β-MB$_2$O$_5$ (M = Hf, Zr) in order to compare them with MAPLE values of the binary components MO$_2$ and the high-pressure modification B$_2$O$_3$-II [82]. For β-HfB$_2$O$_5$ we obtained a value of 34626 kJ·mol^{-1} in comparison to 34729 kJ·mol^{-1} (deviation: 0.3 %), starting from the binary oxides (1 × HfO$_2$ (12791 kJ·mol^{-1}) + 1 × B$_2$O$_3$-II (21938 kJ·mol^{-1})). In the case of β-ZrB$_2$O$_5$, the calculated value (34651 kJ·mol^{-1}) and the MAPLE value obtained from the sum of the binary oxides (1 × ZrO$_2$ [260] (12713 kJ·mol^{-1}) + 1 × B$_2$O$_3$-II (21938 kJ·mol^{-1}) = 34661 kJ·mol^{-1}) tally well (deviation 0.03 %).

4.1.4 The New Borates β-MB$_4$O$_7$ (M = Mn, Co, Ni, Cu)

4.1.4.1 Syntheses

The isotypic high-pressure phases β-MB$_4$O$_7$ (M = Mn, Co, Ni, Cu [261]) were synthesized under high-pressure/high-temperature conditions according to Equations 4.2 – 4.5. Starting materials for the syntheses were B_2O_3 (Strem Chemicals, Newburyport, USA, 99.9%) and the transition metal oxides MnO_2, Co_2O_3, NiO, and CuO. The stoichiometric mixtures were ground up and filled into boron nitride crucibles (Henze BNP GmbH, HeBoSint® S10, Kempten, Germany) (18/11 assemblies).

$$MnO_2 + 2\,B_2O_3 \xrightarrow[1000\ °C]{7.5\ GPa} \beta\text{-}MnB_4O_7 + \tfrac{1}{2}O_2 \tag{4.2}$$

$$Co_2O_3 + 4\,B_2O_3 \xrightarrow[1250\ °C]{7.5\ GPa} 2\,\beta\text{-}CoB_4O_7 + \tfrac{1}{2}O_2 \tag{4.3}$$

$$NiO + 2\,B_2O_3 \xrightarrow[1150\ °C]{7.5\ GPa} \beta\text{-}NiB_4O_7 \tag{4.4}$$

$$CuO + 2\,B_2O_3 \xrightarrow[550\ °C]{7.5\ GPa} \beta\text{-}CuB_4O_7 \tag{4.5}$$

For the syntheses of β-MB$_4$O$_7$ (M = Mn, Co, Ni, Cu), 18/11 assemblies were compressed within 180 min to 7.5 GPa and heated to 1000 °C (Mn)/ 1250 °C (Co)/ 1150 °C (Ni)/ 550 °C (Cu) at constant pressure in the following 10 minutes. After the crucibles had stayed at this temperature for 5 min, the samples were cooled down to 650 °C (Mn, Co)/ 520 °C (Ni)/ 300 °C (Cu) in another 15 min. Afterwards, the samples were quenched to room temperature by switching off the heating, followed by a decompression period of 540 minutes. Then, the recovered pressure media were broken and the samples carefully separated from the surrounding boron nitride crucibles. The compounds were gained as air- and water-resistant, crystalline solids. β-MnB_4O_7 was obtained as colourless, β-CoB_4O_7 as dichroic (red/grayish green), β-NiB_4O_7 as dichroic (orange/pale yellow), and β-CuB_4O_7 as blue crystals. Figure 4.19 shows the obtained high-pressure phases β-CoB_4O_7, β-NiB_4O_7, and β-CuB_4O_7 (from left to right) inside the BN-crucibles. The middle picture presents, next to crystals of the yellow β-NiB_4O_7, elemental Ni in the outer area of the crucible (hottest zone during the synthesis), whereas in the inner area the green phase HP-NiB_2O_4 (see section 4.1.6) appears. On the right picture, apart from blue β-CuB_4O_7 crystals, elemental Cu can be observed.

Recently Stephanie Neumair could synthesize another representative of the isotypic compounds β-MB$_4$O$_7$ (M = Mn, Co, Ni, Cu, Zn): β-FeB_4O_7. This compound was obtained by the use of a high-pressure/high-temperature conversion at 10.5 GPa and 1200 °C.

The reaction between MnO_2/Co_2O_3 and boron oxide did not succeed in a

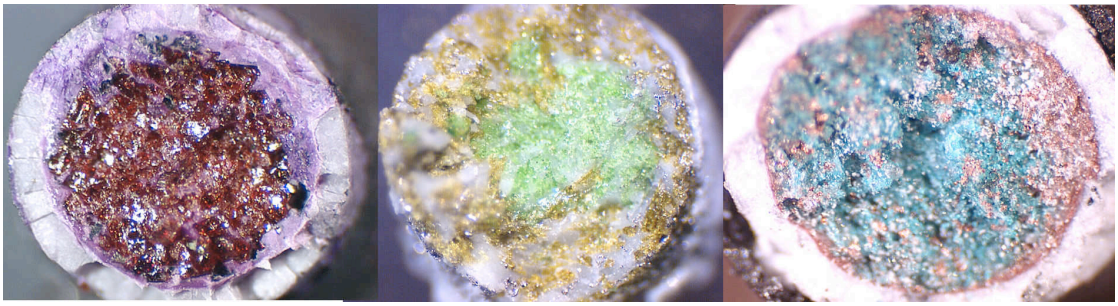

Figure 4.19: Samples of β-CoB_4O_7, β-NiB_4O_7, and β-CuB_4O_7 (from left to right).

Mn(IV)/Co(III) oxoborate but the metal cations were reduced to the oxidation state 2+. We often observe the reduction of the metal oxides to lower oxidation states or to the metals in the used high-pressure assembly. In the case of β-NiB_4O_7 and β-CuB_4O_7, we found tiny particles of elemental nickel and copper at the boundary layer between the h-BN crucible and the reaction mixture (hottest area during the syntheses) as shown in Figure 4.19. At higher temperatures, these small spheres of metal can also be observed as impurities in the inner part of the reaction product. Therefore, it is important to maintain exactly the optimized temperatures and heating times in order to get nearly phase pure samples. In the system Co_2O_3/B_2O_3, a decrease of the synthetic temperature leads to a new phase with the composition $Co_3B_{11}O_{19}OH$, which is described in section 4.1.8. Nevertheless, we often observe small impurities in the powder diffraction patterns even at these optimized conditions, which cannot be assigned to any known phase.

4.1.4.2 Crystal Structure Analyses

Powder diffraction experiments were performed on a STOE Stadi P powder diffractometer with monochromatized $MoK_{\alpha 1}$ (λ = 71.073 pm) radiation from a flat sample. The patterns were indexed with the program TREOR [122–124] on the basis of an orthorhombic unit cell. The lattice parameters (Table 4.9) were calculated from least-squares fits of the powder data. Intensity calculations, taking the atomic positions from the structure refinement [121], confirmed the correct indexing of the patterns of β-MB_4O_7 (M = Mn, Co, Ni, Cu). The lattice parameters, determined from the powder data and single crystal data, fit well. Figure 4.20 shows a comparison of the experimental powder patterns (top) to the patterns derived from single crystal data (bottom).

For the crystal structure analyses, small, irregularly shaped single crystals of the compounds β-MB_4O_7 (M = Mn, Co, Ni, Cu) were examined through a Buerger camera, equipped with an image plate system (Fujifilm BAS-2500) in order to establish both, symmetry and suitability for an intensity data collection. The single crystal intensity data were collected at room temperature by a STOE IPDS-I

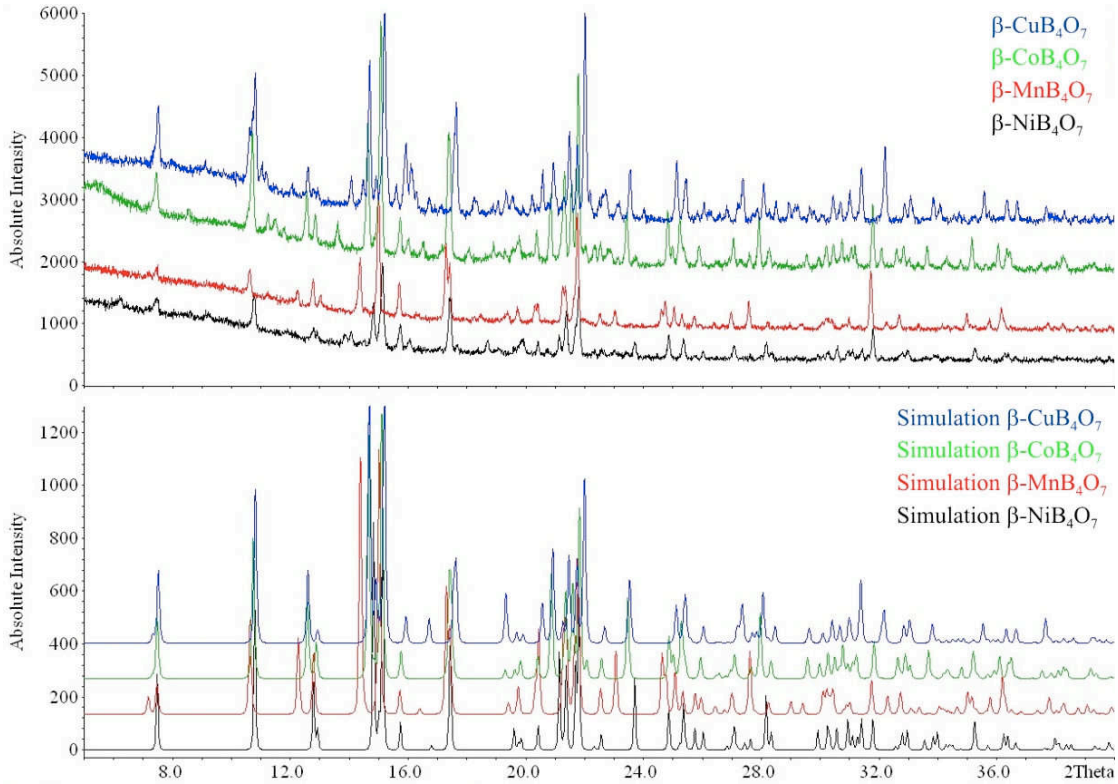

Figure 4.20: Powder diffraction patterns of β-MB$_4$O$_7$ (M = Mn, Co, Ni, Cu) (top) in comparison to the simulated powder data (bottom).

diffractometer (β-MnB$_4$O$_7$, β-CoB$_4$O$_7$, β-NiB$_4$O$_7$) with graphite monochromatized MoK$_\alpha$ radiation (λ = 71.073 pm). For β-CuB$_4$O$_7$ an Enraf-Nonius Kappa CCD with graded multilayer X-ray optics and MoK$_\alpha$ (λ = 71.073 pm) radiation was used. In the case of β-MnB$_4$O$_7$, β-CoB$_4$O$_7$, and β-NiB$_4$O$_7$, a numerical absorption correction was carried out (HABITUS [132]). To β-CuB$_4$O$_7$, a multi-scan absorption correction was applied (SCALEPACK [133]). All relevant details of the data collections and evaluations are listed in Table 4.9. The atomic parameters of β-ZnB$_4$O$_7$ were taken as starting values for all four borates, and the structures were refined by using SHELXL-97 (full-matrix least-squares on F^2) [135, 136] with anisotropic atomic displacement parameters for all atoms. The final difference Fourier syntheses did not reveal any significant residual peaks in all refinements. The positional parameters of the refinements, anisotropic displacement parameters, interatomic distances and angles are listed in Tables 4.10 – 4.15.

Table 4.9: Crystal data and structure refinement of β-MB$_4$O$_7$ (M = Mn, Co, Ni, Cu) (standard deviations in parentheses).

Empirical formula	MnB_4O_7	CoB_4O_7	NiB_4O_7	CuB_4O_7
Molar mass/ g·mol^{-1}	210.18	214.17	213.95	218.78
Crystal System		orthorhombic		
Space group		*Cmcm*		
Single crystal diffractometer	Stoe IPDS I	Stoe IPDS I	Stoe IPDS I	Enraf-Nonius Kappa CCD
Radiation		MoK$_\alpha$ (λ = 71.073 pm)		
Single crystal data				
a/pm	1088.5(2)	1087.0(2)	1087.5(2)	1082.0(2)
b/pm	663.3(2)	646.8(2)	636.8(2)	646.3(2)
c/pm	518.7(2)	517.4(2)	518.0(2)	512.0(2)
V/nm^3	0.3745(2)	0.3638(2)	0.3588(2)	0.3580(2)
Powder diffractometer		Stoe Stadi P		
Radiation		MoK$_{\alpha 1}$ (λ = 71.073 pm)		
Powder data				
a/pm	1089.6(2)	1089.2(2)	1086.3(3)	1080.7(3)
b/pm	664.2(2)	674.4(2)	635.8(2)	645.7(2)
c/pm	519.02(8)	518.08(8)	517.5(2)	511.20(9)
V/nm^3	0.3756	0.3654	0.3574	0.3567
Formula units per cell		Z = 4		
Calculated density/g·cm^{-3}	3.73	3.91	3.96	4.06
Crystal size/mm^3	0.03×0.03×0.02	0.19×0.09×0.052	0.094×0.056×0.01	0.03×0.03×0.02
Temperature/K	293(2)	293(2)	293(2)	293(2)
Detector distance/mm	50	40	40	35
Exposure time/min	15	12	26	75
Absorption coefficient/mm^{-1}	3.497	4.689	5.379	6.071
F (000)/e	404	412	416	420
θ range/°	3.6 – 30.4	3.7 – 32.9	3.7 – 32.9	3.7 – 46.3
Range in hkl	±15,-9/+7,±6	±16,±9,-7/+6	-15/+16,±9,±7	±21,-11/+12, -10/+9
Total no. reflections	1914	2506	2257	3111
Independent reflections	315 (R_{int} = 0.0231)	361 (R_{int} = 0.0268)	384 (R_{int} = 0.0688)	842 (R_{int} = 0.0690)
Reflections with I > 2σ(I)	299 (R_σ = 0.0134)	334 (R_σ = 0.0125)	285 (R_σ = 0.0475)	703 (R_σ = 0.0502)
Data/parameters	315/35	361/36	384/36	842/36
Absorption correction		numerical (Habitus [132])		multi-scan (Scalepack [133])
Transm. ratio (max/min)	0.9146/0.8373	0.7478/0.6372	0.9094/0.8031	–
Goodness-of-fit (F^2)	1.148	1.112	1.026	1.051
Final R indices (I > 2σ(I))	R1 = 0.0198 wR2 = 0.0550	R1 = 0.0207 wR2 = 0.0557	R1 = 0.0372 wR2 = 0.0853	R1 = 0.0346 wR2 = 0.0813
R indices (all data)	R1 = 0.0209 wR2 = 0.0553	R1 = 0.0224 wR2 = 0.0561	R1 = 0.0544 wR2 = 0.0894	R1 = 0.0508 wR2 = 0.0882
Extinction coefficient	–	0.018(5)	0.014(4)	0.012(3)
Largest diff. peak, deepest hole/Å·e^{-3}	0.419/-0.321	0.421/-0.669	0.765/-1.183	1.239/-1.238

Table 4.10: Atomic coordinates, equivalent isotropic displacement parameters $U_{eq}/\text{Å}^2$, and anisotropic displacement parameters/Å^2 of β-MnB_4O_7 (space group *Cmcm*). U_{eq} is defined as one third of the trace of the orthogonalized U_{ij} tensor (standard deviations in parentheses).

Atom	Wyckoff Position	x	y	z	U_{eq}	
Mn	4*c*	0	0.22327(6)	1/4	0.0051(2)	
B1	8*e*	0.2072(2)	1/2	0	0.0037(4)	
B2	8*g*	0.1194(2)	0.2032(3)	3/4	0.0041(4)	
O1	4*c*	0	0.9028(3)	1/4	0.0044(4)	
O2	8*g*	0.7844(2)	0.9744(2)	1/4	0.0035(3)	
O3	16*h*	0.13266(8)	0.3218(2)	0.9771(2)	0.0043(2)	
	U_{11}	U_{22}	U_{33}	U_{23}	U_{13}	U_{12}
Mn	0.0057(2)	0.0055(2)	0.0042(3)	0	0	0
B1	0.0047(8)	0.0040(8)	0.0025(9)	0.0000(6)	0	0
B2	0.0039(8)	0.0041(8)	0.0043(9)	0	0	0.0000(6)
O1	0.0034(8)	0.0033(8)	0.007(2)	0	0	0
O2	0.0039(5)	0.0040(5)	0.0026(7)	0	0	0.0005(4)
O3	0.0050(4)	0.0038(4)	0.0041(5)	-0.0008(3)	0.0006(3)	-0.0015(3)

Table 4.11: Atomic coordinates, equivalent isotropic displacement parameters $U_{eq}/\text{Å}^2$, and anisotropic displacement parameters/Å^2 of β-CoB_4O_7 (space group *Cmcm*). U_{eq} is defined as one third of the trace of the orthogonalized U_{ij} tensor (standard deviations in parentheses).

Atom	Wyckoff Position	x	y	z	U_{eq}	
Co	4*c*	0	0.24297(4)	1/4	0.00630(17)	
B1	8*e*	0.2035(2)	1/2	0	0.0051(3)	
B2	8*g*	0.1171(2)	0.1918(3)	3/4	0.0050(3)	
O1	4*c*	0	0.9224(2)	1/4	0.0053(3)	
O2	8*g*	0.7800(2)	0.97619(18)	1/4	0.0046(2)	
O3	16*h*	0.12830(7)	0.3165(2)	0.9779(2)	0.0054(2)	
	U_{11}	U_{22}	U_{33}	U_{23}	U_{13}	U_{12}
Co	0.0063(2)	0.0070(2)	0.0056(2)	0	0	0
B1	0.0057(6)	0.0046(6)	0.0050(8)	-0.0004(6)	0	0
B2	0.0063(7)	0.0045(7)	0.0041(9)	0	0	0.0002(6)
O1	0.0048(7)	0.0041(6)	0.007(2)	0	0	0
O2	0.0048(5)	0.0060(5)	0.0030(6)	0	0	0.0012(3)
O3	0.0066(3)	0.0052(4)	0.0044(5)	-0.0012(3)	0.0008(3)	-0.0017(3)

Table 4.12: Atomic coordinates, equivalent isotropic displacement parameters $U_{eq}/\text{Å}^2$, and anisotropic displacement parameters/Å^2 of β-NiB_4O_7 (space group *Cmcm*). U_{eq} is defined as one third of the trace of the orthogonalized U_{ij} tensor (standard deviations in parentheses).

Atom	Wyckoff Position	x	y	z	U_{eq}	
Ni	4*c*	0	0.2568(2)	1/4	0.0125(3)	
B1	8*e*	0.2021(4)	1/2	0	0.0128(8)	
B2	8*g*	0.1160(4)	0.1855(8)	3/4	0.0129(9)	
O1	4*c*	0	0.9333(6)	1/4	0.0120(9)	
O2	8*g*	0.7781(3)	0.9790(5)	1/4	0.0125(6)	
O3	16*h*	0.1262(2)	0.3138(4)	0.9778(5)	0.0123(5)	
Atom	U_{11}	U_{22}	U_{33}	U_{23}	U_{13}	U_{12}
Ni	0.0126(4)	0.0139(4)	0.0109(4)	0	0	0
B1	0.014(2)	0.015(2)	0.009(2)	-0.001(2)	0	0
B2	0.015(2)	0.010(2)	0.013(2)	0	0	-0.002(2)
O1	0.011(2)	0.011(2)	0.014(2)	0	0	0
O2	0.013(2)	0.013(2)	0.012(2)	0	0	0.001(2)
O3	0.0131(9)	0.0132(9)	0.011(2)	-0.0009(7)	0.0002(8)	-0.0004(6)

Table 4.13: Atomic coordinates, equivalent isotropic displacement parameters $U_{eq}/\text{Å}^2$, and anisotropic displacement parameters/Å^2 of β-CuB_4O_7 (space group *Cmcm*). U_{eq} is defined as one third of the trace of the orthogonalized U_{ij} tensor (standard deviations in parentheses).

Atom	Wyckoff Position	x	y	z	U_{eq}	
Cu	4*c*	0	0.27374(6)	1/4	0.0061(2)	
B1	8*e*	0.2032(2)	1/2	0	0.0055(3)	
B2	8*g*	0.1147(2)	0.1866(3)	3/4	0.0052(3)	
O1	4*c*	0	0.9254(3)	1/4	0.0047(3)	
O2	8*g*	0.7795(2)	0.09781(2)	1/4	0.0048(2)	
O3	16*h*	0.12673(9)	0.3161(2)	0.9802(2)	0.0054(2)	
	U_{11}	U_{22}	U_{33}	U_{23}	U_{13}	U_{12}
Cu	0.00530(14)	0.00765(15)	0.00540(16)	0	0	0
B1	0.0059(7)	0.0045(6)	0.0061(8)	-0.0003(6)	0	0
B2	0.0044(6)	0.0051(6)	0.0061(8)	0	0	0.0000(5)
O1	0.0043(6)	0.0037(6)	0.0059(7)	0	0	0
O2	0.0052(4)	0.0043(4)	0.0049(5)	0	0	0.0006(4)
O3	0.0059(3)	0.0043(3)	0.0059(4)	-0.0011(3)	0.0007(3)	-0.0015(2)

Table 4.14: Interatomic distances/pm calculated with the single crystal lattice parameters in β-MB$_4$O$_7$ (M = Mn, Co, Ni, Cu) (standard deviations in parentheses).

Mn–O1	212.5(2)	B1–O3	143.9(2) 2×	B2–O3	142.4(2) 2×	O2–B1	155.5(2) 2×
Mn–O3	212.5(2) 4×	B1–O2	155.5(2) 2×	B2–O1	147.8(2)	O2–B2	157.6(2)
			Ø = 149.7	B2–O2	157.6(2)		Ø = 156.2
					Ø = 147.6		
Co–O1	207.4(2)	B1–O3	144.6(2) 2×	B2–O3	143.4(2) 2×	O2–B1	154.5(2) 2×
Co–O3	203.79(9) 4×	B1–O2	154.5(2) 2×	B2–O1	147.2(2)	O2–B2	155.9(2)
			Ø = 149.6	B2–O2	155.9(2)		Ø = 155.0
					Ø = 147.5		
Ni–O1	206.0(4)	B1–O3	145.0(3) 2×	B2–O3	143.9(4) 2×	O2–B1	154.2(3) 2×
Ni–O3	200.1(2) 4×	B1–O2	154.2(3) 2×	B2–O1	147.1(5)	O2–B2	155.6(6)
			Ø = 149.6	B2–O2	155.6(6)		Ø = 154.7
					Ø = 147.6		
Cu–O1	225.1(2)	B1–O3	145.1(2) 2×	B2–O3	145.1(2) 2×	O2–B1	153.0(2) 2×
Cu–O3	196.6(2) 4×	B1–O2	153.0(2) 2×	B2–O1	143.7(2)	O2–B2	156.3(2)
			Ø = 149.1	B2–O2	156.3(2)		Ø = 154.1
					Ø = 147.6		

Table 4.15: Interatomic angles/° calculated with the single crystal lattice parameters in β-MB$_4$O$_7$ (M = Mn, Co, Ni, Cu) (standard deviations in parentheses).

		β-MnB$_4$O$_7$			
O3a-B1-O2a	106.50(6)	O1-B2-O2	103.2(2)	B1-O2-B1	113.0(2)
O3b-B1-O2b	106.50(6)	O3a-B2-O2	110.2(2)	B1-O2-B2 2×	116.15(7)
O3a-B1-O2b	109.01(6)	O3b-B2-O2	110.2(2)		Ø = 115.1
O3b-B1-O2a	109.01(6)	O3a-B2-O1	110.6(2)		
O3a-B1-O3b	111.4(2)	O3b-B2-O1	110.6(2)		
O2a-B1-O2b	114.5(2)	O3a-B2-O3b	111.7(2)		
	Ø = 109.5		Ø = 109.4		
		β-CoB$_4$O$_7$			
O3a-B1-O2a	106.77(5)	O1-B2-O2	105.7(2)	B1-O2-B1	113.7(2)
O3b-B1-O2b	106.77(5)	O3a-B2-O2	109.34(8)	B1-O2-B2 2×	117.08(6)
O3a-B1-O2b	108.66(6)	O3b-B2-O2	109.34(8)		Ø = 115.9
O3b-B1-O2a	108.66(6)	O3a-B2-O1	110.83(9)		
O3a-B1-O3b	111.1(2)	O3b-B2-O1	110.83(9)		
O2a-B1-O2b	114.9(2)	O3a-B2-O3b	110.7(2)		
	Ø = 109.5		Ø = 109.5		
		β-NiB$_4$O$_7$			
O3a-B1-O2a	107.5(2)	O1-B2-O2	106.7(3)	B1-O2-B2 2×	117.1(2)
O3b-B1-O2b	107.5(2)	O3a-B2-O2	109.0(2)	B1-O2-B1	114.2(3)
O3a-B1-O2b	108.0(2)	O3b-B2-O2	109.0(2)		Ø = 116.1
O3b-B1-O2a	108.0(2)	O3a-B2-O1	111.0(2)		
O3a-B1-O3b	110.6(3)	O3b-B2-O1	111.0(2)		
O2a-B1-O2b	115.1(3)	O3a-B2-O3b	110.1(4)		
	Ø = 109.5		Ø = 109.5		
		β-CuB$_4$O$_7$			
O3a-B1-O2a	106.87(7)	O1-B2-O2	106.8(2)	B1-O2-B1	113.6(2)
O3b-B1-O2b	106.87(7)	O3a-B2-O2	109.1(2)	B1-O2-B2 2×	117.29(7)
O3a-B1-O2b	108.96(7)	O3b-B2-O2	109.1(2)		Ø = 116.1
O3b-B1-O2a	108.96(7)	O3a-B2-O1	111.6(2)		
O3a-B1-O3b	110.5(2)	O3b-B2-O1	111.6(2)		
O2a-B1-O2b	114.7(2)	O3a-B2-O3b	108.6(2)		
	Ø = 109.5		Ø = 109.5		

4.1.4.3 Crystal Structure Description

The crystal structures of β-MB$_4$O$_7$ (M = Mn, Co, Ni, Cu) are isotypic to the structure of β-ZnB$_4$O$_7$ [171], which was also synthesized under high-pressure/high-temperature conditions (10.5 GPa, 1000 °C, multianvil assembly). Figure 4.21 gives a view of the structure of β-MB$_4$O$_7$ (M = Mn, Co, Ni, Cu, Zn), in which all boron atoms coordinate to four oxygen atoms in a distorted, tetrahedral way. These polyhedra are linked *via* common corners forming a three-dimensional network of BO$_4$-tetrahedra. 2/5 of the oxygen atoms bridge three boron atoms (O$^{[3]}$), while 3/5 connect two boron atoms (O$^{[2]}$). Along c, the structure shows channels of "Vierer" and "Sechser" rings (rings consisting of four and six tetrahedra, respectively) [39]. The metal cations are positioned inside the "Sechser" ring channels,

whereas the "Vierer" ring channels stay empty. Figure 4.22 shows the bigger ring

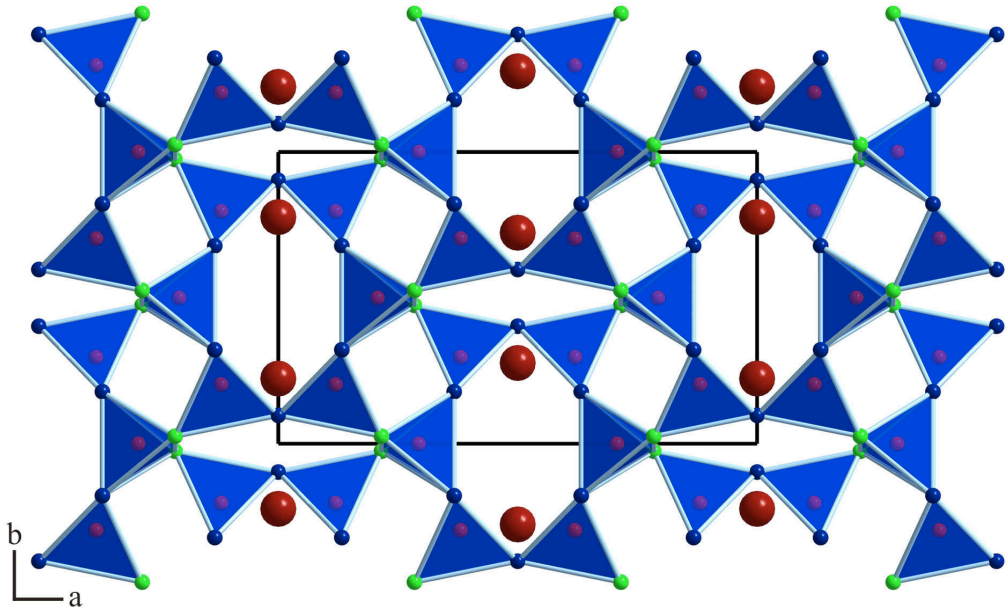

Figure 4.21: Crystal structure of β-MB$_4$O$_7$ (M = Mn, Co, Ni, Cu, Zn) with view along [001]. M is shown as dark red, B as red, O$^{[2]}$ as blue, and O$^{[3]}$ as green atoms.

channels along [100] (left) and [001] (right). The right figure shows the conjunction of the "Sechser" rings *via* two BO$_4$-tetrahedra. Thereby, other "Sechser" rings and additionally "Dreier" rings (consisting of three BO$_4$-groups) are built. All oxygen atoms inside of the "Sechser" ring channels bridge two tetrahedral BO$_4$-groups, the oxygen atoms outside of the channels connect three tetrahedral centres, linking the large channels to form a network structure. The external linkage of the "Sechser" rings results in the formation of empty "Vierer" ring channels.

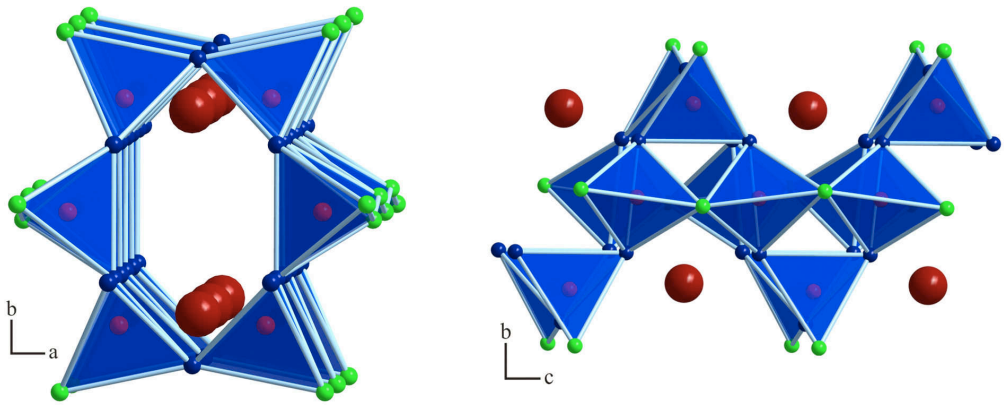

Figure 4.22: "Sechser" ring channels in β-MB$_4$O$_7$ (M = Mn, Co, Ni, Cu). Left: view along [00$\bar{1}$]; right: view along [100].

An investigation of boron-oxygen distances in β-MB$_4$O$_7$ (M = Mn, Co, Ni, Cu) reveals values of 142.4–157.6 (Mn), 143.4–155.9 (Co), 143.9–155.6 (Ni), and 143.7–156.3 (Cu) pm (Table 4.14). This fits well to the distance range found in β-ZnB$_4$O$_7$

(143.6–156.2 pm). The average B–O bond-lengths are 148.6 pm (β-MnB_4O_7, β-CoB_4O_7, β-NiB_4O_7), and 148.3 pm (β-CuB_4O_7), corresponding to the value of 148.7 pm for β-ZnB_4O_7. It should be mentioned that these values are slightly higher than the average B–O distance of 147.6 pm in tetrahedral BO_4-groups of oxoborates [232, 233]. This is caused by the linkage of the tetrahedra by threefold coordinated oxygen atoms resulting in an aplanar OB_3-group. The B–O$^{[3]}$ distances exhibit average values of 156.2 (Mn), 155.0 (Co), 154.7 (Ni), and 154.1 pm (Cu). These distances are distinctively larger than the average distances in other borates, revealing threefold coordinated oxygen atoms O$^{[3]}$ (*e.g.* β-$RE(BO_2)_3$ (RE = Nd, Sm, Gd–Lu) [262–264], γ-$RE(BO_2)_3$ (RE = La–Nd) [265, 266], and minerals like tunnelite ($SrB_6O_9(OH)_2{\cdot}3H_2O$), strontioginorite ($(Sr,Ca)_2B_{14}O_{20}(OH)_6{\cdot}6H_2O$) [267], aristarainite ($Na_2Mg[B_6O_8(OH)_4]_2{\cdot}4H_2O$) [268], and the high-pressure modification of B_2O_3 [82]).

The differences inside the structures of β-MB_4O_7 (M = Mn, Co, Ni, Cu, Zn) are due to the varying ionic radii and electronic configurations of the M^{2+} ions. Table 4.16 gives a survey of the ionic radii (M^{2+}), lattice parameters, and the corresponding volumes of the unit cells of β-MB_4O_7 (M = Mn, Co, Ni, Cu, Zn). In agreement with the different effective ionic radii of the M^{2+} ions, β-MnB_4O_7

Table 4.16: Comparison of the ionic radii M^{2+}/pm, lattice parameters/pm and volumes/nm^3 of β-MB_4O_7 (M = Mn, Co, Ni, Cu, Zn).

Compound	r(M^{2+})	a	b	c	V
β-MnB_4O_7	89	1088.5(2)	663.3 (2)	518.7(2)	0.3745(2)
β-CoB_4O_7	81	1087.0(2)	646.8(2)	517.4(2)	0.3638(2)
β-NiB_4O_7	77	1087.5(2)	636.8(2)	518.0(2)	0.3588(2)
β-CuB_4O_7	79	1082.0(2)	646.3(2)	512.0(2)	0.3580(2)
β-ZnB_4O_7	82	1083.31(3)	648.87(2)	516.80(2)	0.363(1)

has got the largest cell volume and β-NiB_4O_7 and β-CuB_4O_7 the smallest ones. A closer look at the extensions along the individual axes shows small variations along a (1082.0(2)–1088.5(2)pm) and c (512.0(2)–518.7(2)pm), but remarkable differences along the b axis (636.8(2)–663.3(2)pm). As the differences in the B–O distances of the BO_4-tetrahedra are insignificant, the reason can be found in the coordination of the M^{2+} ions. Figure 4.23 shows the square-pyramidal coordination sphere of the M^{2+} ions in β-MB_4O_7 (M = Mn, Co, Ni, Cu, Zn) and Table 4.17 gives detailed information about the distances inside the square-pyramidal coordination polyhedra.

The distortion of the OB_3-group and the increase of the B–O$^{[3]}$ distances are reasonable, because the metal atoms lie in the direct neighbourhood of the

OB_3-group with $O^{[3]}\cdots M^{2+}$ distances **g** of 286.9 (Mn), 286.9 (Co), 299.2 (Ni), 305.7 (Cu), and 291.7 pm (Zn) (Figure 4.23). This leads to a deflection of the oxygen atom O2 from the plane in the direction of the metal atom. Similar distortions can be found in the oxoborates SrB_4O_7 [174, 175] and PbB_4O_7 [175, 176], where the average B–$O^{[3]}$ distances of 155.0 pm and 155.4 pm in the OB_3-groups correspond to the average distance of 156.2 (Mn), 155.0 (Co), 154.7 (Ni), 154.1 (Cu), and 155.3 pm (Zn) found in β-MB_4O_7 (M = Mn, Co, Ni, Cu, Zn). The value **e** represents

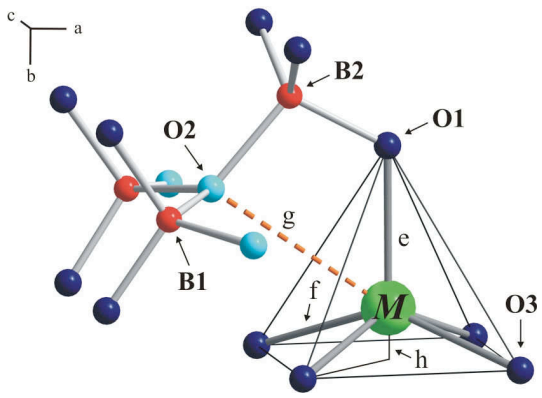

Figure 4.23: Coordination sphere of the M cations in β-MB_4O_7 (M = Mn, Co, Ni, Cu, Zn), including a view of the distortion of the OB_3-group.

Table 4.17: Comparison of the metal–oxygen distances **e**, **f**, **g**/pm and the deflection **h**/pm of the M^{2+} ion from the square plane in β-MB_4O_7 (M = Mn, Co, Ni, Cu, Zn) as shown in Figure 4.23 (standard deviations in parentheses).

M^{2+}	d^n	**e** (M–O1)	**f** (M–O3)	**g** (M–O2)	**h**
Mn	d^5	212.5(2)	212.5(2)	286.9(2)	65.3
Co	d^7	207.4(2)	203.79(9)	286.9(2)	47.5
Ni	d^8	206.0(4)	200.1(2)	299.2(4)	36.3
Cu	d^9	225.1(2)	196.6(2)	305.7(2)	27.4
Zn	d^{10}	202.1(2)	204.4(1)	291.7(2)	53.7

the apical M^{2+}–O bond-length and the value **f** the basal M^{2+}–O distance. The distance **g** designates the M^{2+}–$O^{[3]}$ bond-lenghth, whereas **h** denotes the deflection of the metal ion from the basal plane (Table 4.17). The regular coordination of the cation in β-MnB_4O_7 with identical apical and basal distances of 212.5(2)pm inside the square pyramid is noteworthy. This symmetric coordination corresponds to a square-pyramidal arrangement of Mn^{II}/Mn^{III} in $YBaMn_2O_5$ [269], where the apical and basal distances were nearly identical (200.0(2) (4 ×) and 200.4(2) pm (1 ×)). The coordination distorts in β-ZnB_4O_7 (apical: 202.1(2) pm, basal: 204.4(1) pm; for comparison: Zn–O bond-lengths in ZnO_5 square pyramids in $BiZn_2PO_6$ vary between 197(2) and 205(2) pm [270]), β-NiB_4O_7 (apical: 206.0(4) pm, basal: 200.1(2) pm; for comparison: Ni–O bond-lengths in NiO_5 square pyramids of $Y_8Ba_5Ni_4O_{21}$ [271]: 201.0(6) (2 ×), 200.5(9) (1 ×), and 206.4(6) pm (2 ×)) and β-CoB_4O_7 (apical: 207.4(2) pm, basal: 203.79(9) pm; for comparison: Co–O bond-lengths in CoO_5 square pyramids of $SrCoAs_2O_7$ [272]: 199.2(5), 201.2(5), 204.9(5), 210.3(5), 215.7(5) pm). The strongest distortion is found in β-CuB_4O_7 (apical: 225.1(2) pm, basal: 196.6(2) pm), resulting from

a typical Jahn-Teller effect due to the electronic configuration of the d^9 ion. A similar situation can be observed in the structure of $La_2Cu_2O_5$ [273], which also comprises CuO_5 square pyramids. Owing to the electronic configuration of the d^9 ion, the CuO_5 square pyramids show a Jahn-Teller distortion with four short Cu–O bonds (194.08(1), 194.08(1), 190.8(3), 196.5(2) pm) and a long apical Cu–O bond (227.9(3) pm). Generally, this is observed in a variety of valence mixed copper oxides, which possess much longer apical Cu–O bonds (230–250 pm) inside the CuO_5 pyramid than the four Cu–O distances in the basal plane (192–198 pm) [274]. The coordination of the copper ions in β-CuB_4O_7 corresponds to those examples. A much better comparison of the square pyramids $[M^{II}O_5]$ can be done with similarly oriented groups in the quaternary transition metal(II) diphosphates $SrMP_2O_7$ (M = Cr [275], Mn [275], Fe [276], Co [277], Ni [278], Cu [279], Zn [275]). As observed for the diphosphates $SrMP_2O_7$, the anisotropy in the anti-bonding of the various d-electronic configurations (Mn^{2+} d^5, Co^{2+} d^7, Ni^{2+} d^8, Cu^{2+} d^9, Zn^{2+} d^{10}) is nicely revealed by a comparison of the bond-length d(M–O_{basal}) and d(M–O_{apical}), and more indirectly, by a comparison of the lattice parameters.

4.1.4.4 Investigations into Magnetism

Magnetic moments of β-CuB_4O_7 and β-MnB_4O_7 were measured using a SQUID magnetometer (Quantum-Design MPMS-XL5) between 1.8 and 300 K with magnetic flux densities as large as 5 Tesla. Samples of about 20 mg were loaded into gelatin capsules and fixed in straw as sample holder. Corrections for the sample holder and the core diamagnetism were applied to the data. Magnetic parameters were determined using an extended Curie-Weiss-law $\chi = C/(T - \theta) + \chi_0$.

The inverse magnetic susceptibility of β-CuB_4O_7 (Figure 4.24) shows Curie-Weiss behaviour between room temperature and ~75 K. From the Curie-constant we determine an effective magnetic moment of 1.75(2) μ_B per copper atom in agreement with one unpaired electron as expected for a $3d^9$ configuration of Cu^{2+}. The paramagnetic Curie-temperature (Weiss-constant) of -91(2) K indicates antiferromagnetic interactions among these moments. The $\chi^{-1}(T)$ plot deviates increasingly above the Curie line below 75 K, which may be an onset of antiferromagnetic ordering. The drop of $\chi^{-1}(T)$ below T ≈ 20 K can probably be attributed to small traces of ferromagnetic impurities.

The magnetic susceptibility of β-MnB_4O_7 obeys the Curie-Weiss law down to 20 K, as depicted in Figure 4.25. A rather large temperature independent paramagnetic contribution ($\chi_0 = 3 \times 10^{-3}$ $cm^3 \cdot mol^{-1}$) corrects the small curvature of the $\chi^{-1}(T)$ plot. This may be due to traces of a ferromagnetic impurity. The resulting effective magnetic moment of 6.01(2) μ_B per manganese atom agrees well with the expected 5.92 μ_B for the spherical $3d^5$-shell of Mn^{2+}. A Weiss-constant of

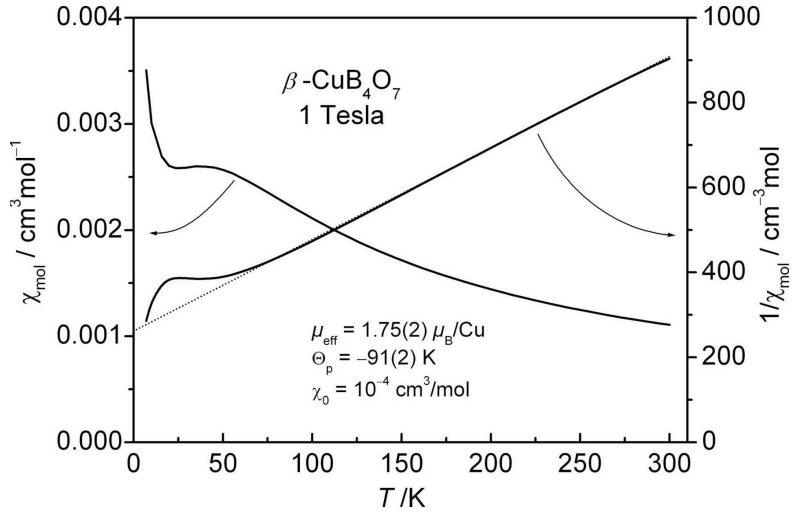

Figure 4.24: Magnetic and inverse magnetic susceptibility of β-CuB_4O_7.

26(1) K stands for weak antiferromagnetic interactions among the moments. We did not detect magnetic ordering in β-MnB_4O_7 at temperatures down to 2 K.

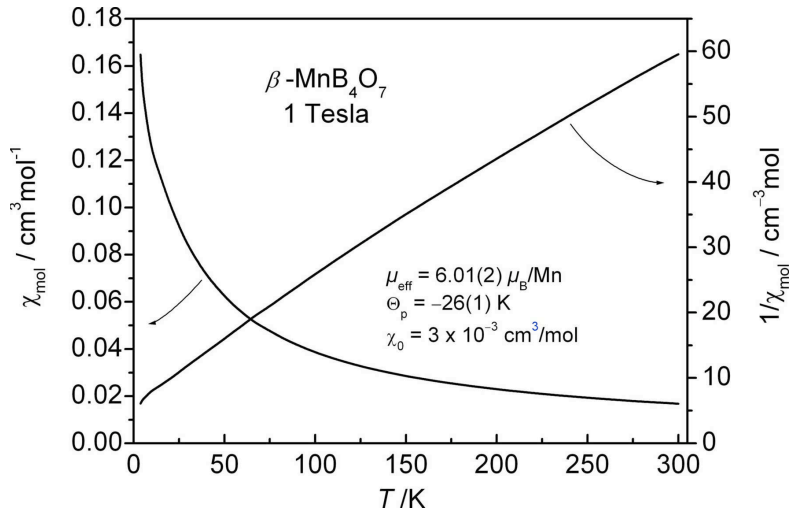

Figure 4.25: Magnetic and inverse magnetic susceptibility of β-MnB_4O_7.

4.1.4.5 Electronic Spectroscopic Investigations

Polarized single crystal electronic spectra of arbitrary faces of β-MnB_4O_7 (cross section: 0.3 × 0.3 mm^2, d = 0.05 mm, T = 80 K) and β-CuB_4O_7 (cross section: 0.08 × 0.2 mm^2, d = 0.01 mm, T = 298 K) crystals were measured by a strongly modified CARY 17 microcrystal spectralphotometer (Spectra Services, ANU Canberra, Australia). Attached to the spectrometer was a flow-tube, that allowed the cooling of the crystals with cold (77 K) $N_{2,g}$. Details of the spectrometer have already been described in literature [141, 142].

Crystals of β-NiB_4O_7 show dichroism (orange/pale yellow) for perpendicular

polarization directions. This behaviour is reflected by the absorption spectra in Figure 4.26 with rather strong absorption bands in one ("hpol" // a- or c-axis) and nearly vanishing bands in the other direction ("vpol" // b-axis). Almost iden-

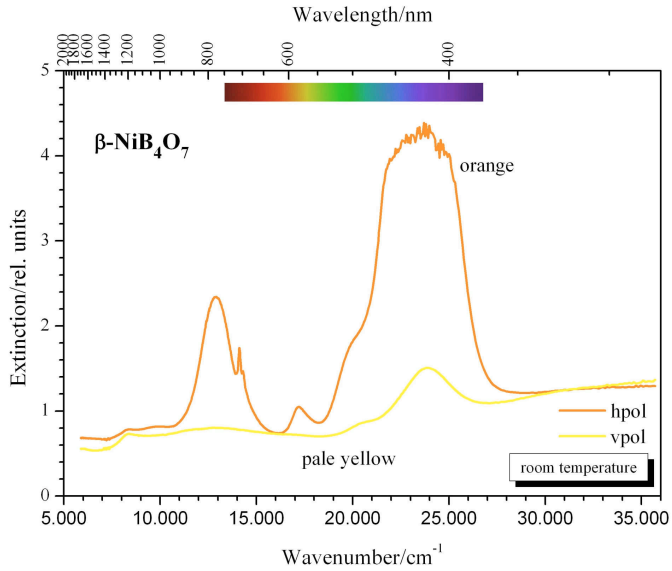

Figure 4.26: Polarized electronic spectra of β-NiB_4O_7.

tical polarized single-crystal spectra have been observed for the square-pyramidal chromophore $[Ni^{II}O_5]$ in $[(Ph_2MeAsO)_4Ni(NO_3)]^+(NO_3)^-$ [280]. With one exception, the assignment of the observed bands, given in Table 4.18, is the same as proposed in reference [280]. For the band around 20190 cm^{-1}, we prefer an assignment to the spin-forbidden transition $^3B_1 \rightarrow {}^1B_2(D)$, instead of relating it to the transition $^3B_1 \rightarrow {}^3A_2(P)$ as a result of a very large splitting of the excited $^3T_{1g}(P)$ state. The rather high absorbance of the spin-forbidden transitions in β-NiB_4O_7 follows from intensity stealing by spin-orbit coupling.

Pale blue crystals of β-CuB_4O_7 do not show a noticeable dichroism, though the spectra observed for two perpendicular polarization directions are distinctly different (Figure 4.27). The direction "hpol" refers to the dipole vector of the incident light beam within the basal plane of the chromophore (// crystallographic ac-plane), "vpol" describes the direction perpendicular to the basal plane (// crystallographic b-axis). The main absorption band around 14700 cm^{-1} is clearly split into two components. A third, weaker band, presumably located around 6000 cm^{-1}, is cut off due to the spectral limit of the used spectrometer. The proposed band assignment (Table 4.18) is in agreement with group theoretical considerations for point group C_{4v}. In addition to the strong absorption bands assigned to Cu^{2+} ions in square-pyramidal coordination, three very weak bands of unknown origin are found around 25000 cm^{-1}.

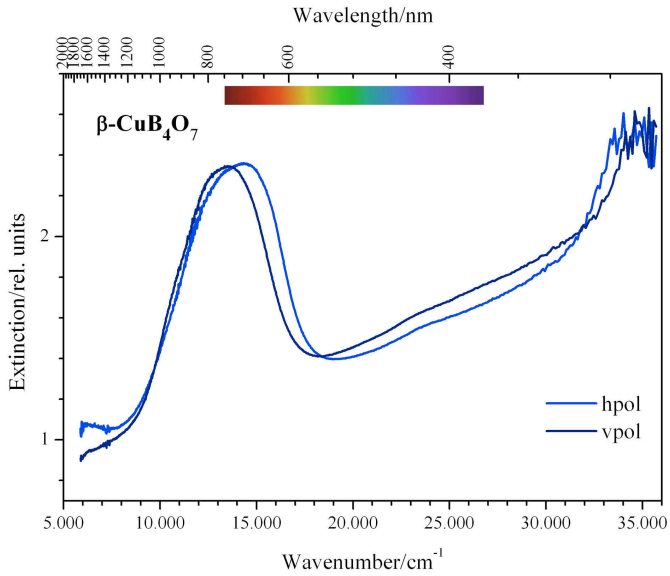

Figure 4.27: Polarized electronic spectra of β-CuB_4O_7.

In the case of β-CoB_4O_7 a close examination and evaluation of the spectra is still required. However the dichroism (red/greyish green) for perpendicular polarization directions of this phase is clearly visible in Figure 4.28 .

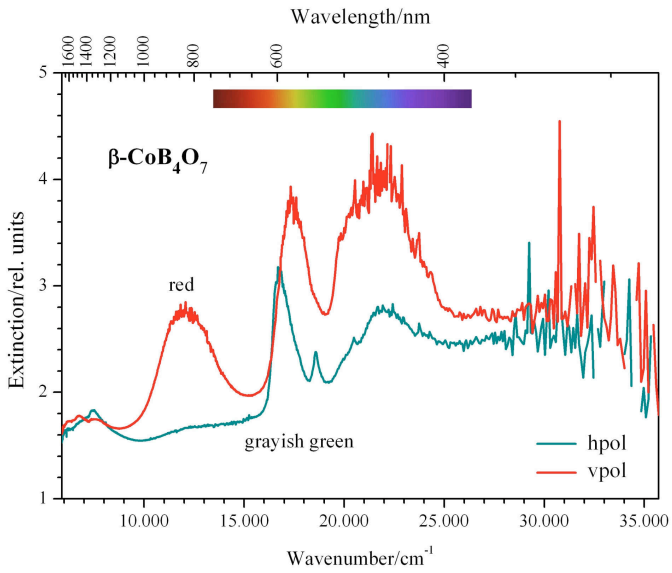

Figure 4.28: Polarized electronic spectra of β-CoB_4O_7.

Table 4.18: Electronic transitions observed for β-NiB_4O_7 and β-CuB_4O_7.

β-NiB_4O_7		β-CuB_4O_7	
Transition[a]	Energy/cm^{-1}	Transition[c]	Energy/cm^{-1}
$^3B_1 \rightarrow {}^3E(F)$	not obs.[b]		
$^3B_1 \rightarrow {}^3A_2(F)$, $^1A_1(D)$	8400	$^2B_1 \rightarrow {}^2A_1(E)$	< 6000
$^3B_1 \rightarrow {}^3B_2(F)$	9800	$^2B_1 \rightarrow {}^2B_2(T)$	13140
$^3B_1 \rightarrow {}^3E(F)$	12970	$^2B_1 \rightarrow {}^2E(T)$	14230
$^3B_1 \rightarrow {}^1B_1(D)$	14143	?	(23214)
$^3B_1 \rightarrow {}^1E(D)$	17270	?	(23747)
$^3B_1 \rightarrow {}^1B_2(D)$	20190	?	(26601)
$^3B_1 \rightarrow {}^3A_2(P)$	22200		
$^3B_1 \rightarrow {}^3E(P)$	23930		

[a] Band assignment for β-NiB_4O_7 according to [280], assuming C_{4v} symmetry for the chromophore [$Ni^{II}O_5$]. For a better understanding, the orbital degeneracies of the parental electronic states of the free ion are given in parentheses.

[b] Not observed due to limitations of the used spectrometer.

[c] Band assignment for β-CuB_4O_7, assuming C_{4v} symmetry for the chromophore [$Cu^{II}O_5$]. For a better understanding, the orbital degeneracies of the parental electronic states of the Cu^{2+} ion in a ligand-field of O_h symmetry are given in parentheses.

4.1.4.6 Thermal Behaviour

Temperature-programmed X-ray powder diffraction experiments were performed on a STOE Stadi P powder diffractometer ($MoK_{\alpha 1}$ radiation ($\lambda = 71.073$pm)) with a computer controlled STOE furnace. The sample was enclosed in a silica capillary and heated from room temperature to 500 °C in 100 °C steps, and from 500 °C to 1100 °C in 50 °C steps. The heating rate was set to 40 °C/min. Afterwards, the sample was cooled down to 500 °C in 50 °C steps, and from 500 °C to room temperature in 100 °C steps (heating rate: 50 °C/min). After each heating step, a diffraction pattern was recorded from 6° to 30° 2Θ.

In the case of β-NiB_4O_7, the starting powder in the capillary contained also traces of HP-NiB_2O_4, metallic Ni, and B_2O_3. Figure 4.29 shows that β-NiB_4O_7 is stable up to a temperature of 750 °C. Between 750 and 850 °C, a decomposition occurs into the normal-pressure phase $Ni_3B_2O_6$, elemental Ni, and presumably molten B_2O_3. There are also additional reflections, which can be assigned to a phase with the composition "$Ni_2B_2O_5$" (ICSD No. 22-1183). Except for this entry in the database, there does not exist any characterization of this phase to our knowledge. Therefore, heating of β-NiB_4O_7 into the temperature range 750–850 °C, followed by a slow reduction of the temperature to room temperature, could be a promising way for an isolation of the phase "$Ni_2B_2O_5$".

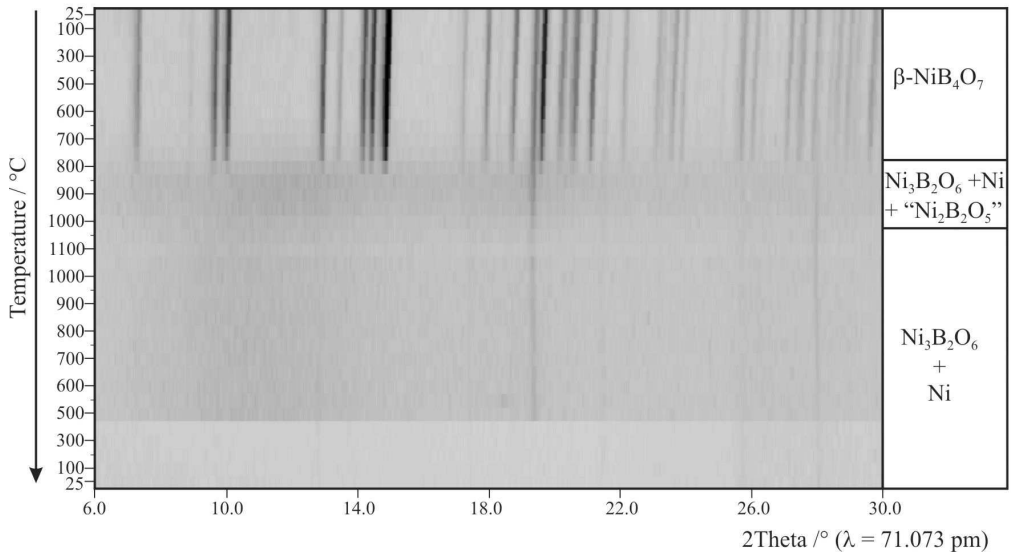

Figure 4.29: Temperature-programmed diffraction patterns of β-NiB_4O_7.

The patterns of β-CuB_4O_7 (Figure 4.30) show that the pure high-pressure phase remains stable up to a temperature of 600 °C. The increase of the temperature to 650 °C leads to a partial decomposition of the high-pressure phase into CuB_2O_4. After heating up to 850 °C, the decomposition of the phases to Cu_2O starts, whereas above 900 °C only Cu_2O and Cu can be detected in the diffraction pat-

terns.

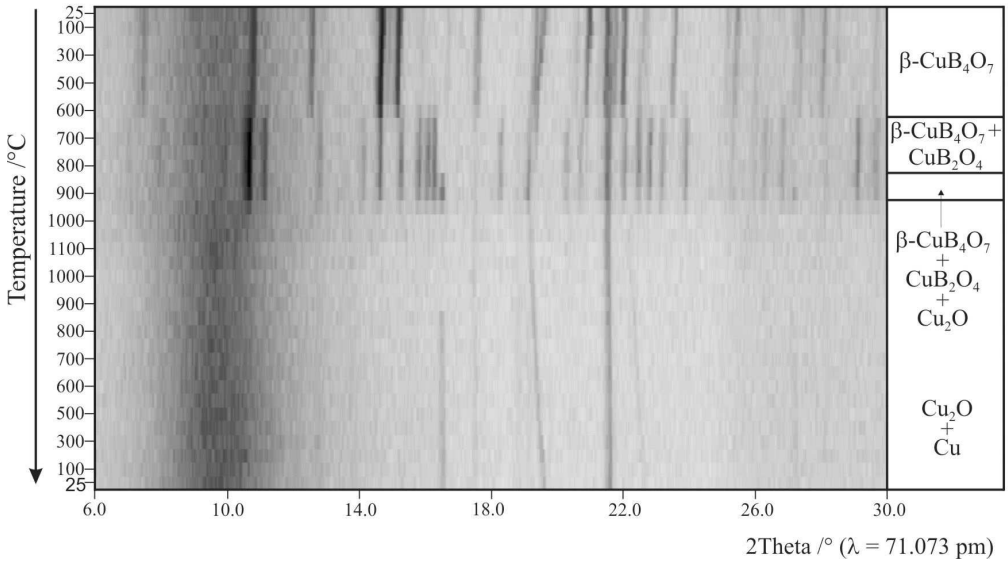

Figure 4.30: Temperature-programmed diffraction patterns of β-CuB_4O_7.

Figure 4.31 demonstrates the metastable character of β-MnB_4O_7, which transformes into the normal-pressure phase α-MnB_4O_7 above 650 °C. In the temperature range of 700–750 °C, both, the α- and the β-phase are stable. At a temperature of 1150 °C, the capillary broke, so no other transformation or decomposition could be recorded.

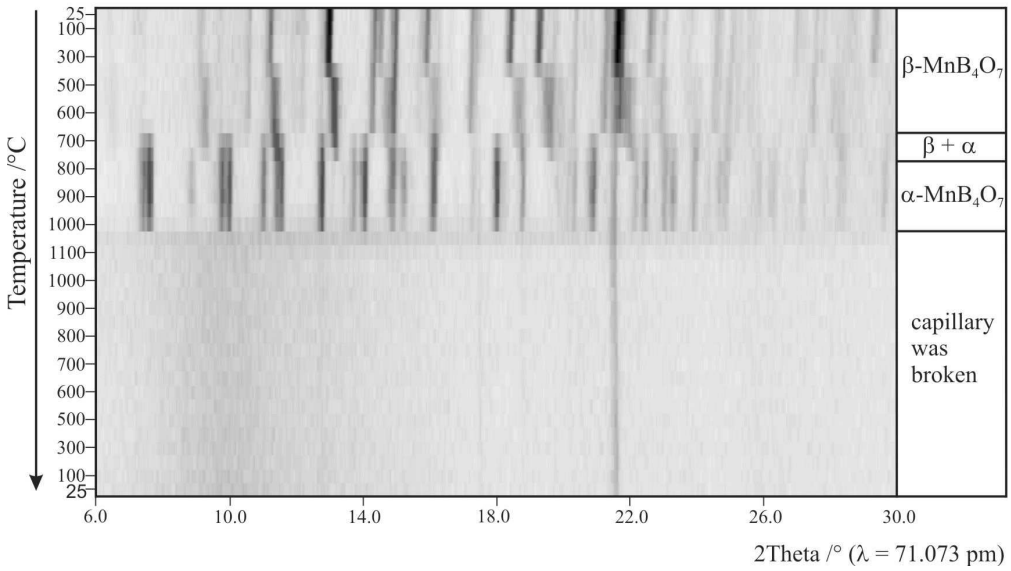

Figure 4.31: Temperature-programmed diffraction patterns of β-MnB_4O_7.

Figure 4.32 demonstrates the metastable character of β-CoB_4O_7, which is stable up to a temperature of 650 °C. Between 650 and 700 °C the transformation in unknown crystalline phases appears. Above 1000 °C and during cooling no crystalline phases could be recorded.

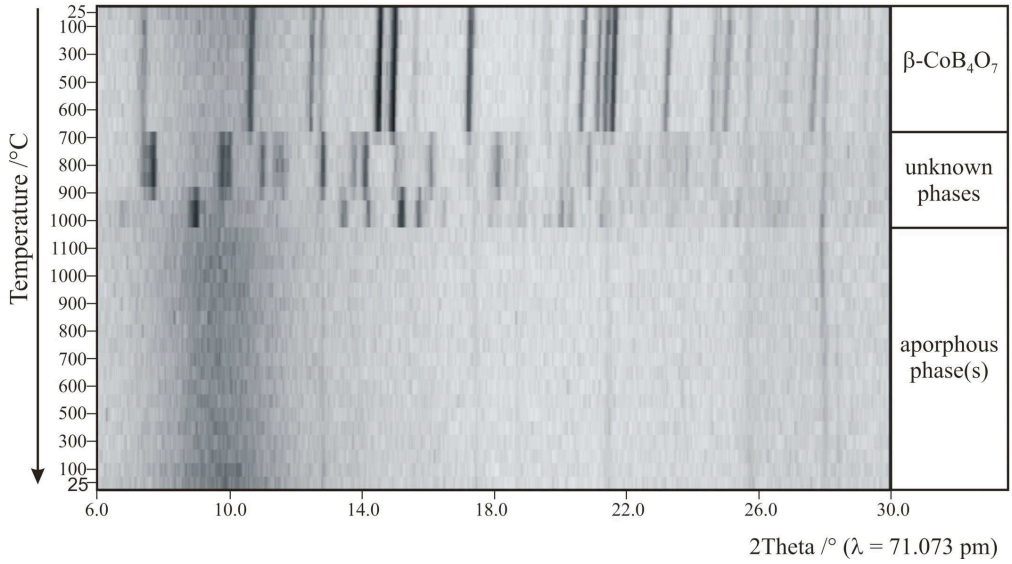

Figure 4.32: Temperature-programmed diffraction patterns of β-CoB_4O_7.

4.1.4.7 Theoretical Calculations

Bond-valence sums were calculated for all atoms, using the bond-length/bond-strength (ΣV) [164, 165] and the CHARDI concept (Charge Distribution in Solids) (ΣQ) [167]. A comparison of the charge distribution, calculated with both concepts, confirms the formal ionic charges of β-MB_4O_7 (M = Mn, Co, Ni, Cu), as shown in Table 4.19, exceptional the threefold coordinated oxygen atom O2, which shows reduced values in the CHARDI-concept. Similar deviating values for the $O^{[3]}$ atoms are obtained in β-CaB_4O_7 (-1.92 (ΣV); -1.77 (ΣQ))[173], β-HgB_4O_7 (-2.06 (ΣV); -1.83 (ΣQ))[172], and β-ZnB_4O_7 (-1.83 (ΣV); -1.67 (ΣQ)) [171]. Remarkably, in all these cases the deviation was only observed in the CHARDI-calculations (ΣQ), whereas the bond-length/bond-strength values (ΣV) corresponded to the expected values.

Table 4.19: Charge distribution in β-MB$_4$O$_7$ (M = Mn, Co, Ni, Cu) calculated with the bond-length/bond-strength concept (ΣV) and the CHARDI concept (ΣQ).

β-MnB$_4$O$_7$	Mn	B1	B2	O1	O2	O3
ΣV	+2.02	+2.88	+3.06	-1.90	-1.79	-2.10
ΣQ	+1.85	+3.10	+2.97	-1.87	-1.57	-2.25
β-CoB$_4$O$_7$	Co	B1	B2	O1	O2	O3
ΣV	+1.92	+2.88	+3.05	-1.88	-1.85	-2.05
ΣQ	+1.88	+3.07	+2.99	-1.87	-1.68	-2.19
β-NiB$_4$O$_7$	Ni	B1	B2	O1	O2	O3
ΣV	+1.90	+2.88	+3.03	-1.86	-1.86	-2.03
ΣQ	+1.89	+3.06	+3.00	-1.87	-1.72	-2.17
β-CuB$_4$O$_7$	Cu	B1	B2	O1	O2	O3
ΣV	+2.05	+2.91	+3.04	-1.89	-1.89	-2.07
ΣQ	+1.87	+3.06	+3.00	-1.88	-1.74	-2.16

Additionally, we calculated MAPLE values (Madelung Part of Lattice Energy) [161–163] for the isotypic compounds in order to compare the results with MAPLE values of the binary components. Table 4.20 shows the results of the calculation.

Table 4.20: Calculated MAPLE values/kJ·mol^{-1} of β-MB$_4$O$_7$ (M = Mn, Co, Ni, Cu) in comparison to the values achieved from the binary oxides.

	MO/Space group	MAPLE value from binary oxides	calculated MAPLE value	deviation/%
β-MnB$_4$O$_7$	MnO/$Fm\overline{3}m$ [281]	48244	48220	0.05
β-CoB$_4$O$_7$	CoO/$Fm\overline{3}m$ [282]	48436	48330	0.2
β-NiB$_4$O$_7$	NiO/$Fm\overline{3}m$ [283]	48525	48325	0.4
β-CuB$_4$O$_7$	CuO/$Fm\overline{3}m$ [284]	48450	48392	0.1

4.1.5 The Iron Borate α-FeB_2O_4

4.1.5.1 Synthesis

The new high-pressure phase α-FeB_2O_4 [285] was prepared *via* a high-pressure/high-temperature synthesis starting from the binary oxides Fe_2O_3 and B_2O_3 according to Equation 4.6. A mixture of Fe_2O_3 (Sigma-Aldrich Chemie GmbH, Munich, Germany, 99.9%) and B_2O_3 (Strem Chemicals, Newburyport, USA, >99.9%) at a ratio of 1:1 was ground up and filled into a boron nitride crucible (Henze BNP GmbH, HeBoSint® S10, Kempten, Germany) of an 18/11 assembly.

$$Fe_2O_3 + 2\,B_2O_3 \xrightarrow[1100\ ^\circ C]{7.5\ GPa} 2\,\alpha{-}FeB_2O_4 + \tfrac{1}{2}O_2 \tag{4.6}$$

The sample was compressed to 7.5 GPa during 3 h, then heated to 1100 °C in 10 minutes and kept there for 5 minutes. Subsequently, the sample was cooled down to 750 °C in 15 minutes followed by quenching to room temperature by switching off the heating. Decompression occurred during a period of 9 h. The recovered experimental MgO-octahedron was cracked and the sample carefully isolated from the surrounding boron nitride crucible. α-FeB_2O_4 was obtained as a colourless, crystalline compound, dispersed with black needles, which stem from the normal-pressure iron oxide borate vonsenite $Fe_2Fe(BO_3)O_2$. Interestingly, α-FeB_2O_4 could not be synthesized from a stoichiometric mixture of the starting materials (Fe_2O_3 and B_2O_3), or with FeO as starting material, until yet. Hitherto, all attempts in gaining a pure sample of α-FeB_2O_4 resulted in a mixture of several different phases (Figure 4.33). However, recent studies of Stephanie Neumair revealed that α-FeB_2O_4 can be synthesized nearly phase pure from FeO and B_2O_3 at temperatures of 960 °C and 7.5 GPa. Further experiments in order to define the stability area of α-FeB_2O_4 are currently in progress. Furthermore, Stephanie Neumair was able to synthesize a new polymorph of α-FeB_2O_4, designated as β-FeB_2O_4. β-FeB_2O_4 was synthesized at a pressure of 8 GPa and 1100 °C and is isotypic to HP-NiB_2O_4 [286], which is described in detail in section 4.1.6.

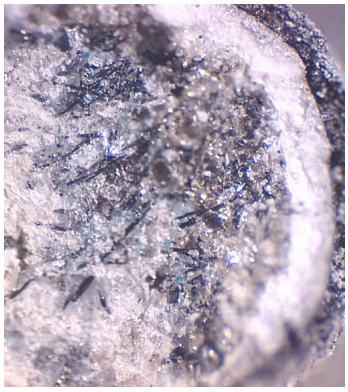

Figure 4.33: Typical picture of a mixture of different iron borates.

4.1.5.2 Crystal Structure Analysis

The powder diffraction pattern (Figure 4.34) was obtained in transmission geometry from a flat sample of the reaction product, using a STOE Stadi P powder

diffractometer with monochromatized $MoK_{\alpha 1}$ (λ = 71.073 pm) radiation. The diffraction pattern was indexed with the program ITO [125] on the basis of a monoclinic unit cell. The calculation of the lattice parameters (Table 4.21) was founded on least-square fits of the powder data. The correct indexing of the patterns of α-FeB_2O_4 was confirmed by intensity calculations, taking the atomic positions from the structure refinement. The lattice parameters, determined from the powder data and single crystal data, are in good agreement. Figure 4.34 shows the experimental powder pattern of a sample of α-FeB_2O_4 highlighted with the reflections of vonsenite (top). For comparability, the theoretical powder diffraction pattern derived from the single crystal data of α-FeB_2O_4 is displayed on the bottom of Figure 4.34. Due to the fact that α-FeB_2O_4 possesses iron in the oxidation state

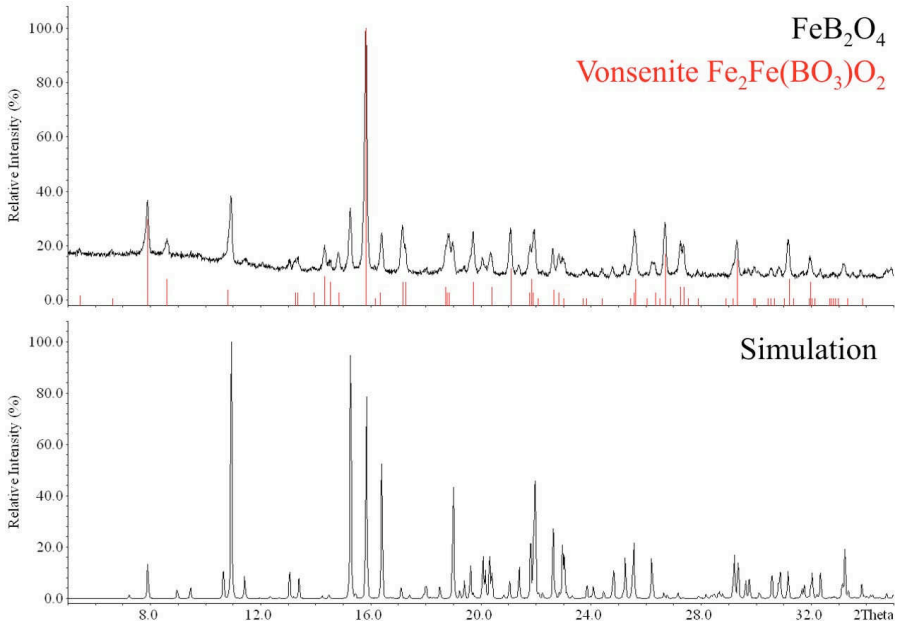

Figure 4.34: Recorded powder pattern of α-FeB_2O_4 (top) underlayed with reflections of vonsenite $Fe_2Fe(BO_3)O_2$ in comparison to the theoretical powder pattern derived from single crystal data of α-FeB_2O_4 (bottom).

+II, the iron cations from the starting material Fe_2O_3 must be reduced from +III to +II. From our experimental experience, we know about the reducing conditions in our high-pressure assembly, especially at high temperatures. We often observe metallic impurities (the corresponding metals of the oxides) at the border of the crucible and in the sample, when the temperature for the synthesis of a borate was too high. We suppose that the boron nitride of our crucible plays an important role in these reactions. Details about the reaction mechanisms are still unknown.

For the crystal structure analysis, a small single crystal of α-FeB_2O_4 was isolated and examined through a Buerger camera, equipped with an image plate system (Fujifilm BAS-2500) in order to establish symmetry and suitability for an intensity data collection. The single crystal intensity data were measured at room

temperature by a STOE IPDS-I diffractometer with graphite monochromatized MoK_α (λ = 71.073 pm) radiation. A numerical absorption correction was applied with the program HABITUS [132]. Table 4.21 shows all relevant details of the data collection and evaluation. Structure solution and parameter refinement (full-matrix least-squares against F^2) were successfully performed using the SHELX-97 software suite [135, 136] with anisotropic atomic displacement parameters for all atoms. The final difference Fourier syntheses did not reveal any significant residual peaks in all refinements. The positional parameters of the refinement, anisotropic displacement parameters, interatomic distances, and interatomic angles are listed in Tables 4.22-4.25.

Table 4.21: Crystal data and structure refinement of α-FeB_2O_4 (standard deviations in parentheses).

Empirical Formula	FeB_2O_4
Molar mass/g·mol^{-1}	141.47
Crystal system	monoclinic
Space group	$P2_1/c$ (No. 14)
Powder diffractometer	STOE Stadi P
Radiation	$MoK_{\alpha 1}$ (λ = 71.073 pm)
Powder data	
a/pm	715.2(2)
b/pm	745.8(4)
c/pm	861.7(3)
β/°	94.78(4)
V/nm^3	0.4580(3)
Single crystal diffractometer	STOE IPDS-I
Radiation	MoK_α (λ = 71.073 pm)
Single crystal data	
a/pm	715.2(2)
b/pm	744.5(2)
c/pm	862.3(2)
β/°	94.71(3)
V/nm^3	0.4576(2)
Formula units per cell	Z = 8
Temperature/K	293(2)
Calculated density/g·cm^{-3}	4.107
Crystal size/mm^3	0.096 × 0.052 × 0.026
Detector distance	50.0
Exposure time per plate/min	15.0
Number of exposures	151
Absorption coefficient/mm^{-1}	6.352
F (000)/e	544
θ range/°	2.7 – 30.5
Range in hkl	±10, ±10, -12/+10
Total no. reflections	4732
Independent reflections	1376 (R_{int} = 0.0293)
Reflections with I > 2σ(I)	1060 (R_σ = 0.0291)
Data/parameters	1376/128
Absorption correction	numerical (HABITUS [132])
Transm. ratio (min/max)	0.6218/0.7529
Goodness-of-fit (F^2)	0.909
Final R indices (I > 2σ(I))	R1 = 0.0226
	wR2 = 0.0509
R indices (all data)	R1 = 0.0350
	wR2 = 0.0532
Extinction coefficient	0.021(2)
Largest diff. peak, deepest hole/e·Å^{-3}	0.503/-0.621

Table 4.22: Atomic coordinates and equivalent isotropic displacement parameters $U_{\mathrm{eq}}/\mathrm{Å}^2$ of α-FeB_2O_4 (space group $P2_1/c$; all Wyckoff sites $4e$). U_{eq} is defined as one third of the trace of the orthogonalized U_{ij} tensor (standard deviations in parentheses).

Atom	x	y	z	U_{eq}
Fe1	0.02841(4)	0.22840(4)	0.10878(4)	0.0063(2)
Fe2	0.47421(4)	0.26064(4)	0.14062(4)	0.0076(2)
B1	0.7007(3)	0.1032(3)	0.8840(3)	0.0047(4)
B2	0.6798(3)	0.9036(3)	0.1207(3)	0.0040(4)
B3	0.1995(3)	0.4359(3)	0.8603(3)	0.0052(4)
B4	0.8193(3)	0.4290(3)	0.8581(3)	0.0044(4)
O1	0.2320(2)	0.2479(2)	0.2960(2)	0.0051(3)
O2	0.2355(2)	0.0583(2)	0.0267(2)	0.0052(3)
O3	0.5148(2)	0.1620(2)	0.9236(2)	0.0053(3)
O4	0.0038(2)	0.0174(2)	0.3061(2)	0.0069(3)
O5	0.8327(2)	0.2506(2)	0.9282(2)	0.0049(3)
O6	0.6832(2)	0.4344(2)	0.2157(2)	0.0051(3)
O7	0.6822(2)	0.0602(2)	0.2218(2)	0.0063(3)
O8	0.2370(2)	0.4319(2)	0.0286(2)	0.0061(3)

Table 4.23: Anisotropic displacement parameters of α-FeB_2O_4 (standard deviations in parentheses).

Atom	U_{11}	U_{22}	U_{33}	U_{23}	U_{13}	U_{12}
Fe1	0.0054(2)	0.0073(2)	0.0058(2)	-0.0002(2)	-0.0021(2)	0.0009(2)
Fe2	0.0054(2)	0.0104(2)	0.0069(2)	-0.0043(2)	-0.0005(2)	0.00075(9)
B1	0.005(2)	0.0051(9)	0.004(2)	0.0007(8)	-0.0003(8)	0.0004(7)
B2	0.003(2)	0.0052(9)	0.003(2)	-0.0002(8)	-0.0007(8)	0.0001(7)
B3	0.007(2)	0.0039(9)	0.004(2)	0.0000(7)	-0.0001(8)	-0.0002(7)
B4	0.004(2)	0.0048(9)	0.004(2)	-0.0001(7)	0.0005(8)	0.0010(7)
O1	0.0082(7)	0.0038(7)	0.0032(8)	-0.0001(5)	-0.0007(6)	-0.0007(4)
O2	0.0063(7)	0.0045(6)	0.0051(8)	0.0009(5)	0.0017(6)	0.0014(5)
O3	0.0032(7)	0.0056(6)	0.0072(8)	-0.0019(5)	-0.0001(5)	-0.0002(5)
O4	0.0041(7)	0.0080(6)	0.0087(8)	-0.0026(5)	0.0008(5)	-0.0002(5)
O5	0.0044(7)	0.0048(6)	0.0053(7)	0.0014(5)	-0.0009(5)	-0.0004(4)
O6	0.0044(7)	0.0064(6)	0.0044(8)	-0.0001(5)	-0.0002(6)	-0.0019(5)
O7	0.0061(7)	0.0067(6)	0.0057(8)	-0.0016(5)	-0.0010(6)	0.0015(5)

4.1.5.3 Crystal Structure Description

Figure 4.35 (left) gives a view of the crystal structure of α-FeB_2O_4 along [100]. The high-pressure phase is unexceptionally composed of corner-sharing BO_4-tetrahedra. These tetrahedral groups are interconnected to "Sechser" rings (consisting of six BO_4-tetrahedra) [39], which are condensed to borate layers. The layers are linked among each other in a staged way. This leads to channels composed of "Sechser" rings along [100], in which the iron cations are arranged. Considering the orientation of the tetrahedra, building up one ring, only one type of ring with the topology UUDUDD (U = up, D = down) is found (Figure 4.35). β-$SrGa_2O_4$ [287],

the high-pressure phase $CaAl_2O_4$-II [288, 289], and $CaGa_2O_4$ [290] reveal the analogous orientation of tetrahedra and connection of layers. α-FeB_2O_4 is isotypic to these compounds. The orthorhombic compound $BaFe_2O_4$ [291] shows the same topology as well, but the layers are interconnected in a different way, resulting in a different crystal structure.

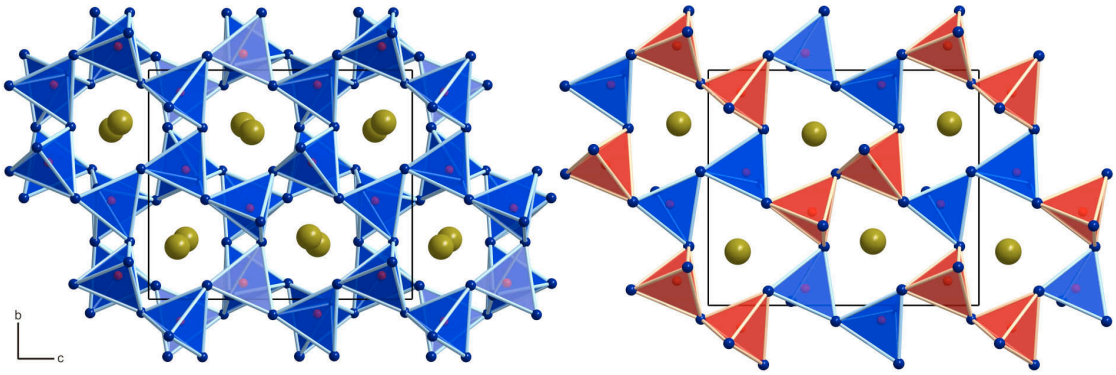

Figure 4.35: Left: Crystal structure of α-FeB_2O_4 along [100], consisting of corner-sharing BO_4-tetrahedra and Fe^{2+} ions. **Right**: Single layer of BO_4-tetrahedra built up from "Sechser" rings with the topology UUDUDD (red BO_4-tetrahedra face upwards, blue tetrahedra downwards).

Drawing a comparison to other network structures consisting of tetrahedra, a close relationship to the high-pressure borate CdB_2O_4 [292] can be discovered. The network-structure is built up from corner-sharing BO_4-tetrahedra, which are linked to condensed layers of "Sechser" rings as well. In CdB_2O_4, these rings show a staged adjustment in which one fourth of the rings reveal an UDUDUD topology and the remaining rings an UUUDDD topology (a close discussion of the crystal structure of CdB_2O_4 can be found in section 4.1.7). In contrast, α-FeB_2O_4 exhibits only one kind of "Sechser" rings with the topology UUDUDD. All the mentioned compounds can be understood as stuffed derivates of the tridymite (SiO_2) framework-structure. Figure 4.36 shows a view of the crystal structure of β-tridymite with an illustration of the topology of SiO_4-tetrahedra (blue tetrahedra point upwards, green ones downwards).

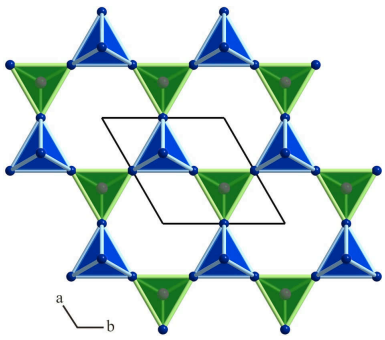

Figure 4.36: Crystal Structure of β-tridymite along [001]. Blue atoms represent O and pink atoms Si-atoms. Green tetrahedra point down, blue ones up.

The B–O bond-lengths in α-FeB_2O_4 (Table 4.24) vary between 145 and 150 pm with an average B–O bond-length of 146.3 pm, which agrees with the known average value of 147.6 pm for borates [232, 233]. The O–B–O angles in the four crystallographically independent BO_4-tetrahedra range between 102.7 and 114.4° (Table 4.25) with a mean value of 109.4°. The Fe–O distances for the sixfold coordi-

nated iron cations (Fe1) range from 201 to 233 pm with a mean value of 218.5 pm. This value is slightly higher than the average Fe–O distance of sixfold coordinated

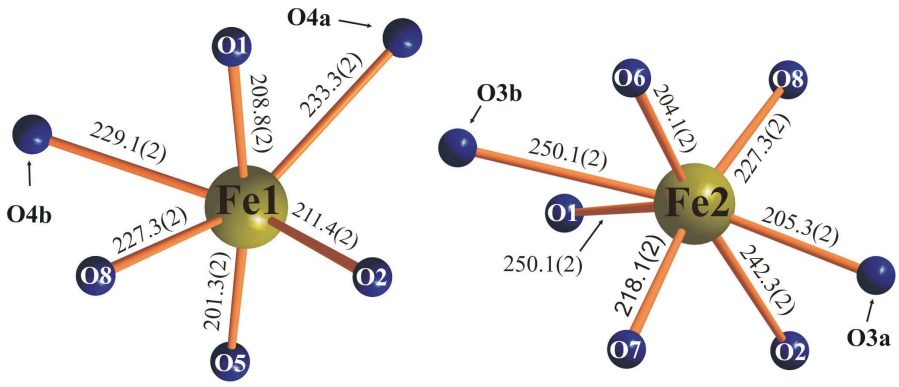

Figure 4.37: Coordination spheres of the Fe cations. Iron-oxygen distances are shown in pm.

iron atoms found in $Fe^{II}Fe_2^{III}(BO_4)O_2$ (203.8 pm) or in $FeBO_3$ (202.8 pm). For the sevenfold coordinated iron atoms (Fe2), the Fe–O bond-lengths range from 204 to 250 pm with a mean value of 225 pm, which is larger than the Fe–O distances for Fe1 due to the higher coordination number. Figure 4.37 shows the coordination spheres of both iron atoms.

Table 4.24: Interatomic distances/pm in α-FeB_2O_4 (space group $P2_1/c$) calculated with the single crystal lattice parameters (standard deviations in parentheses).

Fe1-O5	201.3(2)	Fe2-O6	204.1(2)	B1-O3	146.6(3)	B3-O8	145.4(3)
Fe1-O1	208.8(2)	Fe2-O3	205.3(2)	B1-O6	147.3(3)	B3-O6	146.9(3)
Fe1-O2	211.4(2)	Fe2-O7	218.1(2)	B1-O5	147.7(3)	B3-O4	148.0(3)
Fe1-O8	227.3(2)	Fe2-O8	227.3(2)	B1-O2	148.0(3)	B3-O1	150.2(3)
Fe1-O4a	229.1(2)	Fe2-O1	227.8(2)		Ø = 147.4		Ø = 147.6
Fe1-O4b	233.3(2)	Fe2-O2	242.3(2)				
	Ø = 218.5	Fe2-O3	250.1(2)	B2-O7	145.5(3)	B4-O5	145.9(3)
			Ø = 225.00	B2-O1	147.7(3)	B4-O7	147.0(3)
				B2-O2	148.0(3)	B4-O4	148.3(3)
				B2-O3	149.5(3)	B4-O8	150.1(3)
					Ø = 147.7		Ø = 147.8

Table 4.25: Interatomic angles/° in α-FeB_2O_4 calculated with the single crystal lattice parameters (standard deviations in parentheses).

O3-B1-O5	106.9(2)	O1-B2-O3	102.7(2)	O6-B3-O4	105.4(2)	O7-B4-O8	106.6(2)
O3-B1-O6	106.3(2)	O2-B2-O3	106.4(2)	O4-B3-O1	105.6(2)	O7-B4-O4	107.2(2)
O5-B1-O2	107.8(2)	O7-B2-O1	110.7(2)	O6-B3-O1	108.8(2)	O4-B4-O8	107.7(2)
O6-B1-O2	110.9(2)	O7-B2-O2	112.0(2)	O8-B3-O1	109.2(2)	O5-B4-O4	109.9(2)
O3-B1-O2	111.6(2)	O1-B2-O2	112.3(2)	O8-B3-O6	113.2(2)	O5-B4-O8	111.8(2)
O6-B1-O5	113.3(2)	O7-B2-O3	112.3(2)	O8-B3-O4	114.4(2)	O5-B4-O7	113.4(2)
	Ø = 109.5		Ø = 109.4		Ø = 109.4		Ø = 109.4

4.1.5.4 Theoretical Calculations

We calculated bond-valence sums for α-FeB_2O_4 with the help of the bond-length/bond-strength (ΣV) [164, 165] and the CHARDI concept (ΣQ) (Table 4.26) [167]. The formal ionic charges of the atoms, acquired by X-ray structure analysis, were confirmed within the limits of the concepts.

Table 4.26: Charge distribution in α-FeB_2O_4, calculated with the bond-length/bond-strength concept (ΣV) and the CHARDI concept (ΣQ).

	Fe1	Fe2	B1	B2	B3	B4		
ΣQ	+1.87	+1.90	+3.03	+3.01	+3.01	+3.00		
ΣV	+1.99	+1.99	+2.96	+2.98	+3.02	+3.05		
	O1	O2	O3	O4	O5	O6	O7	O8
ΣQ	-2.07	-2.00	-2.05	-1.90	-2.01	-1.96	-1.86	-1.97
ΣV	-2.10	-2.01	-2.02	-1.88	-2.07	-2.01	-1.93	-1.98

We calculated the MAPLE values (Madelung Part of Lattice Energy) [161–163] for α-FeB_2O_4 in order to compare them with MAPLE values of the binary components FeO (Wuestit) and the high-pressure modification B_2O_3-II. The foundation is the additive potential of the MAPLE values, by which it is possible to calculate hypothetical values for α-FeB_2O_4, starting from the binary oxides. Resultant we obtained a value of 26474 kJ·mol^{-1} in comparison to 26427kJ·mol^{-1} (deviation: 0.2 %), starting from the binary oxides (1 × FeO (4489 kJ·mol^{-1}) + 1 × B_2O_3-II (21938 kJ·mol^{-1})).

4.1.6 The Borate HP-NiB_2O_4

4.1.6.1 Synthesis

HP-NiB_2O_4 [286] was synthesized using a high-pressure/high-temperature reaction according to Equation 4.7, starting from the binary oxides NiO (Avocado Research Chemicals Ltd., Shore Road, Heysham, Morecambe, Lancashire, UK) and B_2O_3 (Strem Chemicals, Newburyport, USA, 99.9%). The stoichiometric mixtures were ground together and filled into a boron nitride crucible (Henze BNP GmbH, HeBoSint® S10, Kempten, Germany) of an 18/11 assembly.

$$NiO + B_2O_3 \xrightarrow[680\ °C]{7.5\ GPa} HP\text{-}NiB_2O_4 \tag{4.7}$$

For the synthesis of HP-NiB_2O_4, the assembly was compressed to 7.5 GPa within 180 min. After reaching this pressure, the sample was heated up to 680 °C (constant pressure) during the following 10 minutes. Having stayed at this temperature for 5 min, the sample was cooled down to ca. 350 °C in another 15 min. After that the sample was quenched to room temperature by switching off the heating, followed by a decompression period of 540 minutes. Afterwards, the recovered MgO-octahedron was broken apart and the sample carefully separated from the surrounding boron nitride crucible. The compound HP-NiB_2O_4 was gained as an air- and water-resistant, light green crystalline solid. Figure 4.38 shows a sample of HP-NiB_2O_4, with yellow β-NiB_4O_7 (see section 4.1.4) in the outer zone (hottest zone during the synthesis). This leads to the conclusion that the two phases can be synthesized under different reaction temperatures, although it is very difficult to remain phase pure samples.

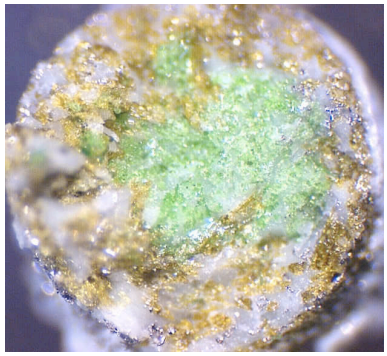

Figure 4.38: Sample of green HP-NiB_2O_4 with yellow crystals of β-NiB_4O_7 in the outer region of the crucible.

4.1.6.2 Crystal Structure Analysis

The powder diffraction pattern of HP-NiB_2O_4 was obtained in transmission geometry from a flat sample using a STOE Stadi P powder diffractometer with monochromatized $MoK_{\alpha 1}$ (λ = 71.073 pm). The diffraction pattern was indexed with the program ITO [125] on the basis of a monoclinic unit cell. The lattice parameters (Table 4.27) were calculated from least-squares fits of the powder data. The correct indexing of the pattern of HP-NiB_2O_4 was confirmed by intensity calculations, taking the atomic positions from the structure refinement [121]. The lattice pa-

rameters, determined from the powder data and single crystal data, fit well. Figure 4.39 shows the experimental (top) and the simulated powder diagram (bottom). Reflections not belonging to HP-NiB_2O_4 and which could not be assigned to any phase in the system Ni-B-O, are marked with asterisks.

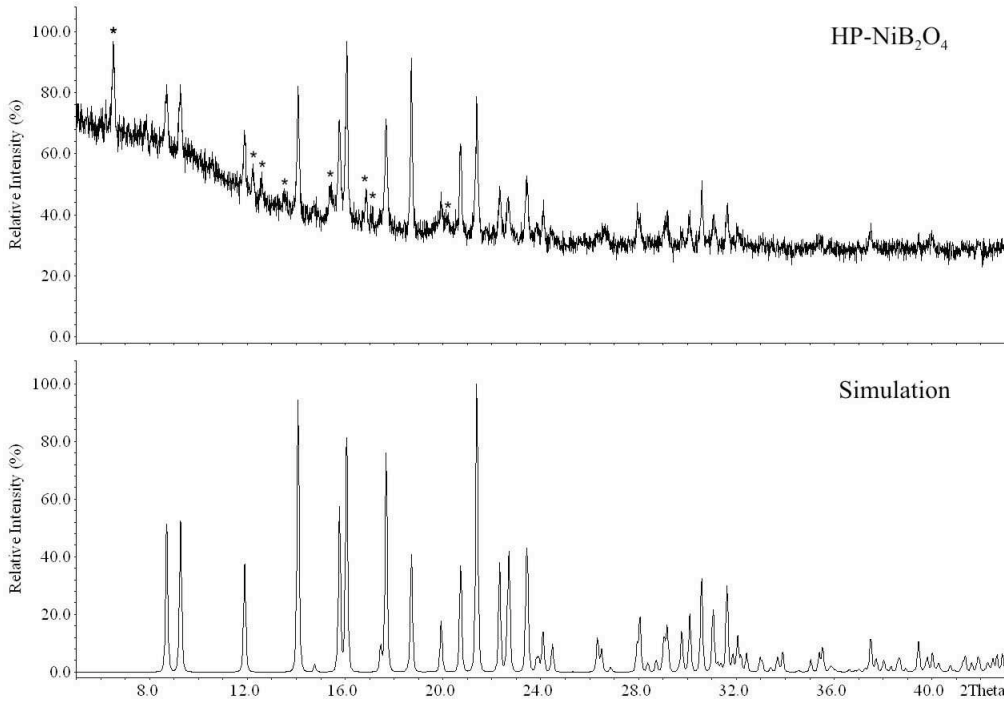

Figure 4.39: Measured (top) and simulated (single crystal data) (bottom) powder diffraction patterns of HP-NiB_2O_4.

Small single crystals of HP-NiB_2O_4 were isolated by mechanical fragmentation and examined through a Buerger camera, equipped with an image plate system (Fujifilm BAS-2500). Single crystal intensity data of HP-NiB_2O_4 were measured with an Enraf-Nonius Kappa CCD with a graded multilayer monochromatized MoK_α (λ = 71.073 pm) radiation. Afterwards, a multi-scan absorption correction was applied to the data (SCALEPACK [133]). Structure solution and parameter refinement (full-matrix least squares against F^2) were successfully performed using the SHELX-97 software suite [135, 136]. Details of the data collection and structure refinement are listed in Table 4.27. The positional parameters, anisotropic displacement parameters, interatomic distances, and interatomic angles are given in Tables 4.28–4.31.

Table 4.27: Crystal data and structure refinement of HP-NiB_2O_4 (standard deviations in parentheses).

Empirical Formula	NiB_2O_4
Molar mass/g·mol^{-1}	144.33
Crystal system	monoclinic
Space group	$C2/c$
Powder diffractometer	STOE Stadi P
Radiation	$MoK_{\alpha 1}$ (λ = 71.073 pm)
Powder data	
a/pm	922.2(2)
b/pm	551.16(6)
c/pm	441.60(4)
β/°	108.3(1)
V/nm^3	0.21307(3)
Single crystal diffractometer	Enraf-Nonius Kappa CCD
Radiation	MoK_α (λ = 71.073 pm)
Single crystal data	
a/pm	924.7(2)
b/pm	552.3(2)
c/pm	442.88(9)
β/°	108.30(3)
V/nm^3	0.21474(7)
Formula units per cell	Z = 4
Temperature/K	293(2)
Calculated density/g·cm^{-3}	4.464
Crystal size/mm^3	0.05 × 0.04 × 0.02
Detector distance	35.0
Scan time per degree/min	25.0
Absorption coefficient/mm^{-1}	8.780
F (000)/e	280
θ range/°	4.36 – 46.57
Range in hkl	±18, -9/+11, ±9
Total no. reflections	2648
Independent reflections	939 (R_{int} = 0.0362)
Reflections with I > 2σ(I)	851 (R_σ = 0.0358)
Data/parameters	939/34
Absorption correction	multi-scan (SCALEPACK [133])
Goodness-of-fit (F^2)	1.070
Final R indices (I > 2σ(I))	R1 = 0.0260
	wR2 = 0.0520
R indices (all data)	R1 = 0.0314
	wR2 = 0.0542
Extinction coefficient	0.008(2)
Largest diff. peak, deepest hole/e·Å^{-3}	1.223/-1.287

Table 4.28: Atomic coordinates and equivalent isotropic displacement parameters $U_{eq}/Å^2$ of HP-NiB_2O_4 (space group $C2/c$). U_{eq} is defined as one third of the trace of the orthogonalized U_{ij} tensor (standard deviations in parentheses).

Atom	Wyckoff Position	x	y	z	U_{eq}
Ni	4*e*	1/2	0.84699(4)	1/4	0.00489(6)
B1	8*f*	0.3151(2)	0.6077(2)	0.6283(3)	0.0048(2)
O1	8*f*	0.64364(9)	0.8509(2)	0.9805(2)	0.0046(2)
O2	8*f*	0.36336(9)	0.5911(2)	0.9713(2)	0.0048(2)

Table 4.29: Anisotropic displacement parameters of HP-NiB_2O_4 (standard deviations in parentheses).

Atom	U_{11}	U_{22}	U_{33}	U_{23}	U_{13}	U_{12}
Ni	0.00482(8)	0.00479(8)	0.00519(9)	0.000	0.00177(6)	0.000
B1	0.0048(4)	0.0048(4)	0.0049(4)	0.0000(3)	0.0018(3)	-0.0004(3)
O1	0.0038(2)	0.0046(3)	0.0053(3)	-0.0006(2)	0.0014(2)	-0.0001(2)
O2	0.0058(3)	0.0047(3)	0.0037(3)	0.0001(2)	0.0011(2)	-0.0010(2)

4.1.6.3 Crystal Structure Description

HP-NiB_2O_4 is composed of distorted tetrahedral BO_4-groups, which are linked to planar borate layers. These layers are based on B_2O_6 dimer building blocks consisting of two edge-sharing BO_4-tetrahedra. The dimers are interconnected among each other *via* common corners. Figure 4.40 gives a view of the crystal structure along $[00\bar{1}]$, displaying the planar layers, which are connected by strings of edge-sharing NiO_6-octahedra. The layers spread out in the bc-plane, while the strings of

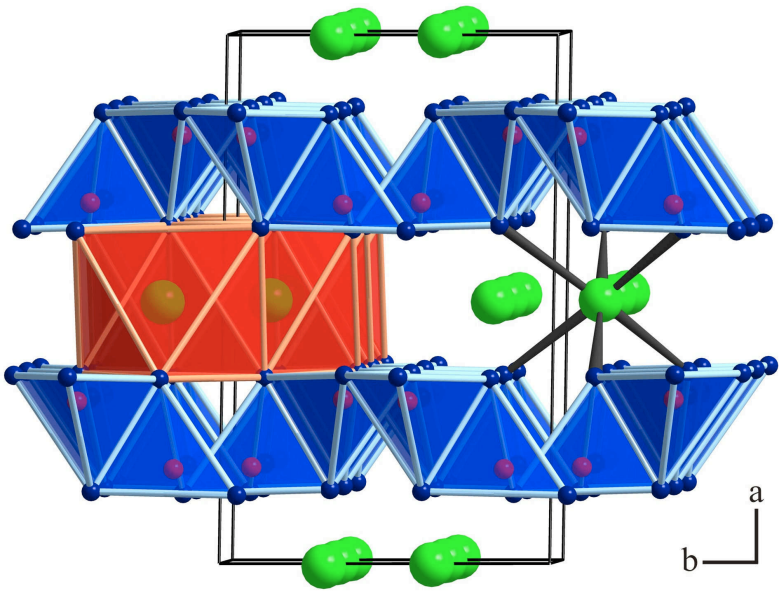

Figure 4.40: Crystal structure of HP-NiB_2O_4, view along $[00\bar{1}]$. Green spheres: Ni^{2+}, blue spheres: O^{2-}, blue polyhedra: BO_4-tetrahedra, red polyhedra: NiO_6-octahedra.

NiO_6-octahedra run along the c-direction. Figure 4.41 shows a single layer of BO_4-tetrahedra, with one B_2O_6-dimer highlighted in yellow. Inside the layer, "Sechser" rings (a ring consisting of six tetrahedral units) [39] are formed by four B_2O_6-

dimers. Therewith, each dimer is part of four "Sechser" rings. Similar layers composed of edge-sharing tetrahedra were observed in the compounds β-$Ca_3[Al_2N_4]$ [293], $Ca_3[Al_2As_4]$ [294], $Sr_3[Al_2P_4]$ [295], $Ba_3[In_2P_4]$ [296], and α-$Ca_3[Ga_2N_4]$ [297].

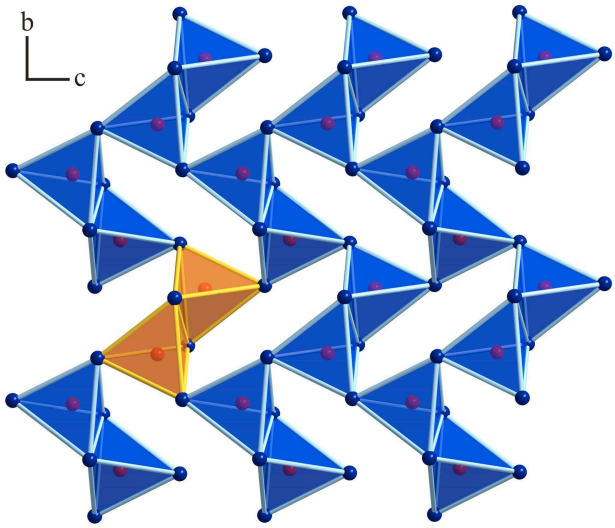

Figure 4.41: Layer of edge-sharing BO_4-tetrahedra in HP-NiB_2O_4, view along [100]. One B_2O_6-dimer is highlighted in yellow.

In contrast, the layers in all these compounds are corrugated and the metal content between the layers is three times as high as in HP-NiB_2O_4, leading to a different crystal structure (see Figure 4.42). Figure 4.43 illustrates the linkage of the distorted NiO_6-octahedra, in which the Ni^{2+} ions are coordinated by six oxygen atoms in the range of 203–218 pm. These distances correspond to the known Ni–O distances of octahedrally coordinated Ni, as in $Ni_3(BO_3)_2$ (202–213 pm [204]) and $Na_2Ni_2B_{12}O_{21}$ (197–233 pm [205]). At the bottom of Figure 4.43, the bond lengths and angles inside the B_2O_6-dimers in HP-NiB_2O_4 are shown. Obviously, the B–O distances inside the B_2O_2-ring are larger (151.6(2) pm and 153.1(2) pm) than the distances outside of the rings (144.3(2) pm and 144.5(2) pm). The average B–O distance of 148.4 pm is slightly higher than the average B–O bond length of 147.6 pm in tetrahedral BO_4-groups of borates [232, 233]. The B···B distance inside the edge-sharing tetrahedra of HP-NiB_2O_4 has a value of 208.8(2) pm. This corresponds to the values found in the other two structure types, which exhibit the structural motive of edge-sharing BO_4-tetrahedra, namely

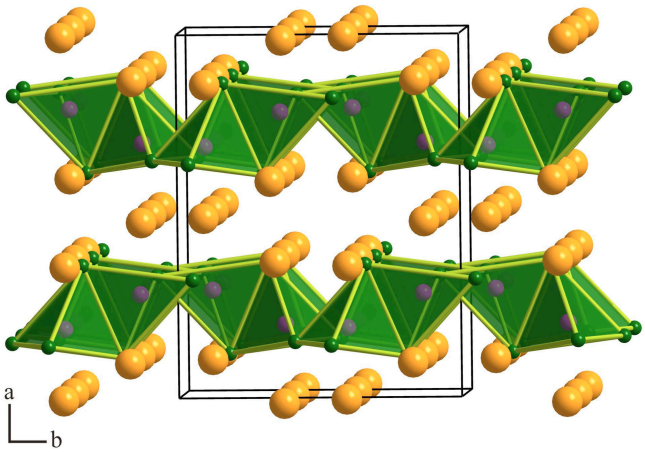

Figure 4.42: Crystal structure of β-$Ca_3[Al_2N_4]$ along [001] showing the corrugated layers of AlN_4-tetrahedra (green).

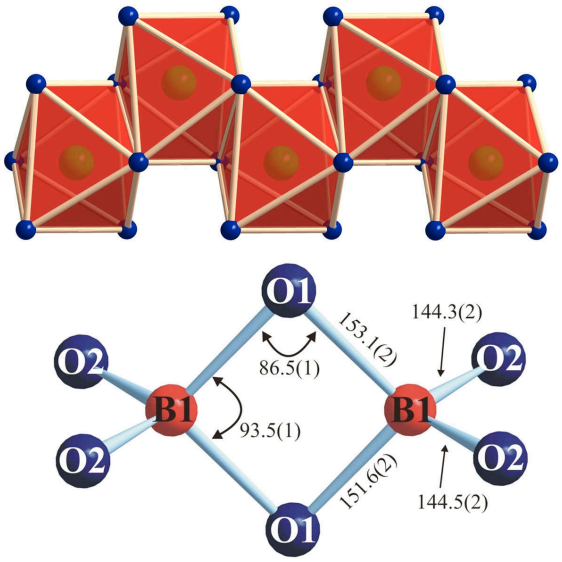

Figure 4.43: Top: String of NiO_6-octahedra linked *via* common edges along [001]. **Bottom**: Distances/pm and angels/° inside of the edge-sharing BO_4-tetrahedra of HP-NiB_2O_4.

$RE_4B_6O_{15}$ (RE = Dy: 207.2(8) pm; Ho: 207(1) pm) [73–75] and α-$RE_2B_4O_9$ (RE = Sm: 207.1(9) pm; Gd: 204(2) pm; Eu: 205.3(9) pm; Tb: 205.5(9) pm; Ho: 204(3) pm) [76–78].

Table 4.30: Interatomic distances/pm in HP-NiB_2O_4 (space group $C2/c$) calculated with the single crystal lattice parameters (standard deviations in parentheses).

Ni-O2	2×	203.4(2)	B1-O2a	144.3(2)	O1-B1a	151.6(2)
Ni-O1b	2×	204.55(9)	B1-O2b	144.6(2)	O1-B1b	153.0(2)
Ni-O1a	2×	217.70(9)	B1-O1a	151.6(2)		Ø = 152.3
		Ø = 208.6	B1-O1b	153.0(2)		
				Ø = 148.4		

Table 4.31: Interatomic angles/° in HP-NiB_2O_4 calculated with the single crystal lattice parameters (standard deviations in parentheses).

O2a-B1-O2b	114.69(9)	B1a-O1-B1b 2×	86.43(8)
O2a-B1-O1b	113.30(9)		
O2b-B1-O1a	111.95(9)		
O2a-B1-O1a	111.40(9)		
O2b-B1-O1b	110.09(9)		
O1a-B1-O1b	93.57(8)		
	Ø = 109.17		

4.1.6.4 Investigations into Magnetism

Magnetic moments of HP-NiB_2O_4 were measured using a SQUID magnetometer (Quantum-Design MPMS-XL5) between 1.8 and 300 K with magnetic flux densities as large as 5 Tesla. Samples of about 15 mg were loaded in gelatin capsules and fixed in straw as sample holder. Corrections for the sample holder, the core diamagnetism and for traces of ferromagnetic impurities (Ni-metal) were applied to the data. Magnetic parameters were determined using the Curie-Weiss-law

$\chi = C/(T - \theta)$. The inverse magnetic susceptibility of HP-NiB_2O_4 showed Curie-Weiss behaviour between room temperature and ~150 K (Figure 4.44). From the Curie-constant we determined an effective magnetic moment of 3.50(1) μB per nickel atom. This is at the upper limit of values, expected for Ni^{2+} (2.80–3.50 μB) [298], which may be due to crystal field effects or to an incomplete correction for ferromagnetic impurities (traces of metallic Ni). The paramagnetic Curie-temperature (Weiss-constant) of –83.3(1) K indicated antiferromagnetic interactions among the moments. A sharp upward bend of $\chi^{-1}(T)$ at $T \approx 32$ K is most likely the onset of antiferromagnetic ordering. This is also supported by a linear magnetization isotherm down to 2 K.

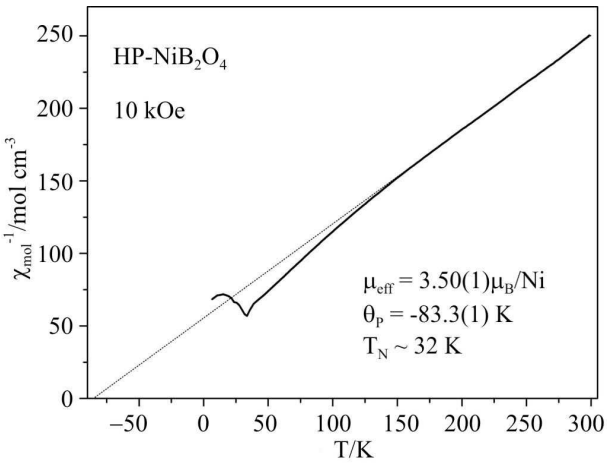

Figure 4.44: Inverse magnetic susceptibility of HP-NiB_2O_4.

4.1.6.5 Vibrational Spectroscopic Investigations

The Raman-spectrum of HP-NiB_2O_4 was measured at a single crystal with a Raman-microscope Horiba Jobin yvon HR800 (x50LWD), using a green laser (Melles Griot ion laser) with a wavelength of 514 nm. In former works, we tried to determine the Raman-active modes of the new B_2O_6 unit from the Raman spectra of $Dy_4B_6O_{15}$ [74] and α-$Gd_2B_4O_9$ [77]. These spectra revealed several peaks in the range of 1200–1450 cm^{-1}, that are normally correlated to BO_3-groups. As both compounds do not contain boron in threefold coordination, these bands were probably Raman-active modes of the B_2O_6 unit of the edge-sharing BO_4-tetrahedra.

Figure 4.45 gives a view of the Raman spectra of $Dy_4B_6O_{15}$ [74] (blue line), α-$Gd_2B_4O_9$ [77] (red line), HP-NiB_2O_4 (black line), and β-NiB_4O_7 [261] (green line). As HP-NiB_2O_4 possesses only BO_4-tetrahedra with a common edge to a second tetrahedron, a comparison of the intensities of all three compounds should lead to an agreement about those peaks, which exclusively belong to Raman-active modes of the B_2O_6-group. Figure 4.45 shows that the peaks, which are marked with an arrow, occur in all three spectra of the compounds with edge-sharing tetrahedra. These peaks do not occur in a spectrum of β-NiB_4O_7 [261], which exhibits only corner-sharing BO_4-tetrahedra. So, the intensities at 1262 and 1444 cm^{-1} (HP-NiB_2O_4), 1253 and 1431 cm^{-1} (α-$Gd_2B_4O_9$), and 1271 and

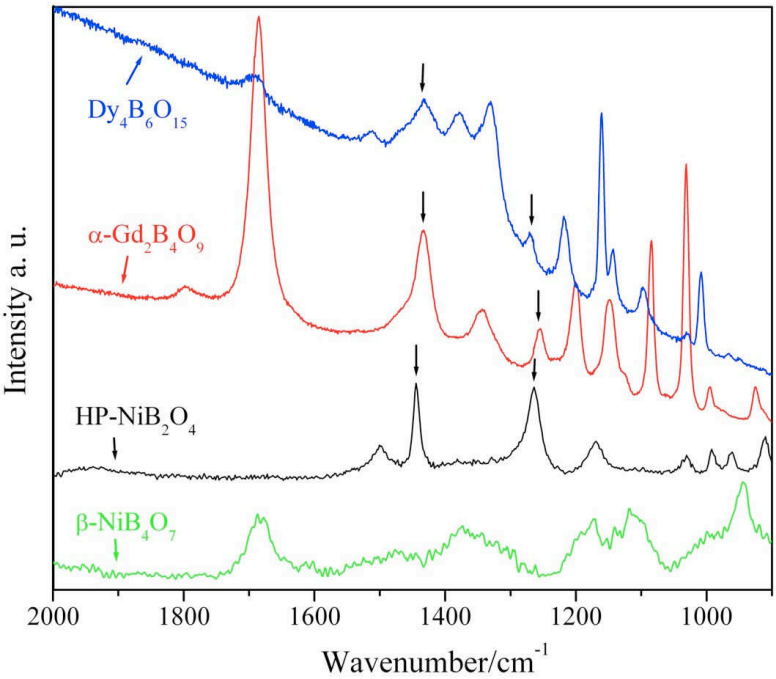

Figure 4.45: Raman-spectra of $Dy_4B_6O_{15}$ (blue), α-$Gd_2B_4O_9$ (red), HP-NiB_2O_4 (black), and β-NiB_4O_7 (green).

1435 cm^{-1} ($Dy_4B_6O_{15}$) can presumably be assigned to Raman-active modes of the edge-sharing BO_4-tetrahedra.

A single crystal electronic spectrum of an arbitrary face of a crystal of HP-NiB_2O_4 (cross section: 0.1 × 0.2 mm^2, d = 0.05 mm; T = 298 K) was measured using a strongly modified CARY 17 microcrystal spectralphotometer (Spectra Services, ANU Canberra, Australia. For details on the spectrometer see Reference [142]). The UV/Vis/NIR spectrum of pale-green HP-NiB_2O_4 shows three absorption bands, as expected for Ni^{2+} ions in octahedral coordination ($E[^3A_{2g}\rightarrow{}^3T_{2g}(F)]$ = 8620 cm^{-1}, $E[^3A_{2g}\rightarrow{}^3T_{1g}(F)]$ = 13940 cm^{-1}, $E[^3A_{2g}\rightarrow{}^3T_{1g}(P)]$ = 24600 cm^{-1}). As a consequence of low-symmetric components in the ligand-field ($[Ni^{II}O_6]$ chromophores with C_2 symmetry), the second and third absorption bands are split. The observed transition energies Δ_o = 8620 cm^{-1} and B = 845 cm^{-1} (β = B/B_0 = 0.81) were estimated according to a procedure described by Lever [299]. It is quite remarkable that the ligand-field splitting Δ_o = 7300 cm^{-1}, observed for yellow $Ni_2P_4O_{12}$, is significantly smaller, despite a very similar geometric structure of the $[Ni^{II}O_6]$ chromophore therein [300]. We attribute this difference to stronger π-donating oxygen ligands in the phosphate than in the borate. The basically negligible π-bonding of the oxygen ligands in HP-NiB_2O_4, a typical second-sphere ligand field effect [301], is a consequence of the higher coordination number of the oxygen atoms in the borate (C.N.(O^{2-}) = 4 (2 B^{3+} + 2 Ni^{2+})) in contrast to the coordination in the phosphate (C.N.(O^{2-}) = 2 (2×) and 3 (4×)). With the transition energy Δ_o = 8620 cm^{-1}, the nephelauxetic ratio β = 0.81, and the spin-orbit coupling parameter for the free ion ($\xi_0(Ni^{2+})$ = 630 cm^{-1}), a magnetic

moment of 3.16 μB per nickel atom can be calculated [302].

4.1.6.6 Thermal Behaviour

Due to the synthetic conditions of 7.5 GPa and 680 °C, we investigated the assumed metastable character of the high-pressure phase HP-NiB_2O_4. These investigations were performed on a STOE Stadi P powder diffractometer ($MoK_{\alpha 1}$; λ = 71.073 pm) with a computer controlled STOE furnace. The sample was enclosed in a silica glass capillary and heated from room temperature to 500 °C in steps of 100 °C, and from 500 °C to 1100 °C in steps of 50 °C. Afterwards, the sample was cooled down to 500 °C in steps of 50 °C, and further on to room temperature in steps of 100 °C. At each temperature, a diffraction pattern was recorded. The temperature-programmed X-ray powder diffraction patterns of HP-NiB_2O_4 revealed that the compound is remarkably stable up to 750 °C in ambient pressure conditions (Figure 4.46). At higher temperatures, HP-NiB_2O_4 decomposes into the normal pressure nickel borate $Ni_3(BO_3)_2$ and presumably boron oxide. Further heating (up to 1100 °C) and subsequent cooling to room temperature did not succeed in obtaining any other crystalline phase than $Ni_3(BO_3)_2$.

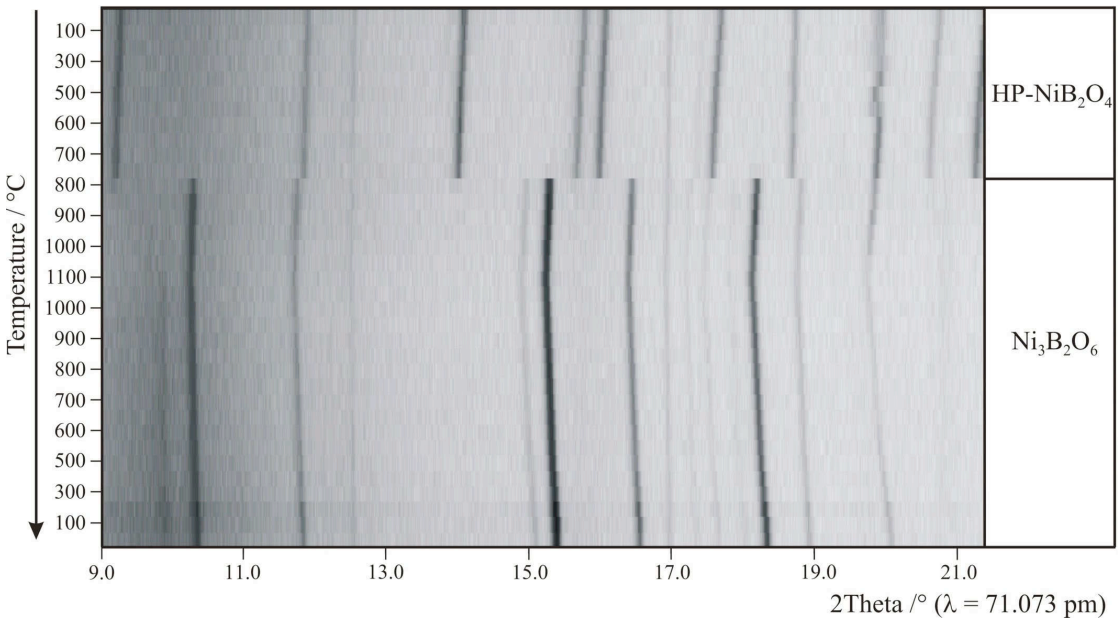

Figure 4.46: Temperature-programmed X-ray powder patterns of HP-NiB_2O_4.

4.1.6.7 Theoretical Calculations

The bond-valence sums were calculated for all atoms, using the bond-length/bond-strength (ΣV) [164, 165] and the CHARDI concept (Charge Distribution in Solids) (ΣQ) [167]. A comparison of the charge distribution, calculated with both concepts, confirms the formal ionic charges of Ni^{2+} ($\Sigma V = +1.90$; $\Sigma Q = +2.04$), B^{3+}

(ΣV = +2.97; ΣQ = +2.98), and O^{2-} (O1: ΣV = -1.91; ΣQ = -1.87, O2: ΣV = -2.00; ΣQ = -2.13).

Further on, we computed MAPLE values (Madelung Part of Lattice Energy) [161–163] for HP-NiB_2O_4 in order to compare the results with MAPLE values of the binary components NiO and the high-pressure modification B_2O_3-II [82]. The calculated value (26363 kJ·mol^{-1}) for HP-NiB_2O_4 and the MAPLE value obtained from the sum of the binary oxides (1 × NiO ($Fm\overline{3}m$ [303]) (4649 kJ·mol^{-1}) + 1 × B_2O_3-II (21938 kJ·mol^{-1}) = 26587 kJ·mol^{-1}) fit well (deviation: 0.008 %).

4.1.7 The Borate CdB_2O_4

4.1.7.1 Synthesis

The compound CdB_2O_4 [292] was synthesized under high-pressure/high-temperature conditions of 7.5 GPa and 1100 °C. As starting reagents, CdO and B_2O_3 (Strem Chemicals, Newburyport, USA, 99+%) were ground together in the stoichiometric ratio $CdO : B_2O_3 = 1 : 1$ (Equation 4.8). The mixture was filled into a boron nitride crucible (Henze BNP GmbH, HeBoSint® S10, Kempten, Germany) of an 18/11-assembly.

$$CdO + B_2O_3 \xrightarrow[1100\ °C]{7.5\ GPa} CdB_2O_4 \tag{4.8}$$

For the synthesis of CdB_2O_4, the sample was compressed to 7.5 GPa within 3 h. After reaching constant pressure, the sample was heated to 1100 °C in the following 10 minutes. After holding this temperature for 5 min, the sample was cooled down to 650 °C in another 15 min. Afterwards, the sample was quenched to room temperature by switching off the heating, followed by decompression over a period of 9 h. The recovered pressure medium was cracked and the sample carefully separated from the surrounding boron nitride crucible, gaining the air- and water-resistant, colourless, crystalline compound CdB_2O_4. A powder diffraction pattern showed no crystalline impurities, and EDX measurements confirmed the chemical composition of CdB_2O_4.

4.1.7.2 Crystal Structure Analysis

The powder diffraction pattern of CdB_2O_4 was obtained in transmission geometry from a flat sample, using a STOE STADI P powder diffractometer with monochromatized $CuK_{\alpha 1}$ radiation (λ = 154.051 pm). The diffraction pattern was indexed with the program TREOR [122–124] on the basis of a hexagonal unit cell. Table 4.32 lists the lattice parameters, which were obtained from the least-square fits of the powder data. The correct indexing of the pattern was confirmed by intensity calculations [121], taking the atomic positions from the structure refinement (Table 4.33). The lattice parameters, determined from the powder and the single crystal data agree well. Figure 4.47 shows the experimental powder pattern compared to the pattern simulated from single crystal data.

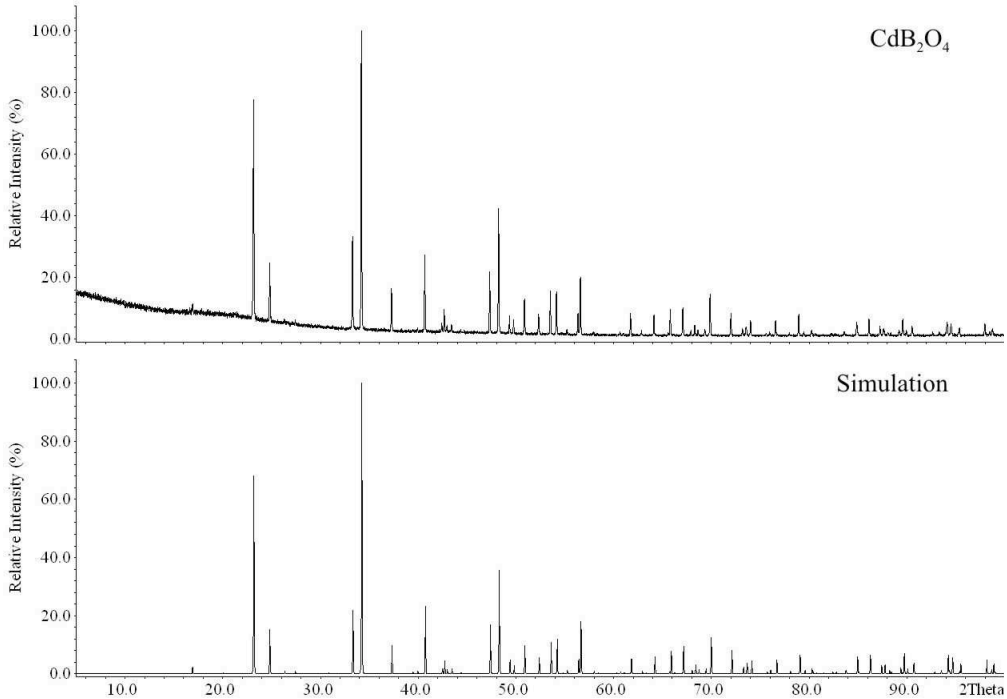

Figure 4.47: Experimental (top) and simulated (single crystal data) (bottom) powder diffraction patterns of CdB_2O_4.

Prior to single crystal measurements, the quality of selected crystals was checked under a polarizing microscope. For the data collection, a colourless fragment (0.23 × 0.18 × 0.14 mm) was used. Intensity data were measured on a CAD4 diffractometer (Nonius) in the $\omega/2\theta$ technique, scanning the whole reciprocal sphere up to $90°/2\theta$. A numerical absorption correction, based on an optimization of the crystal shape, was applied using the program HABITUS [132]. The crystal structure of CdB_2O_4 was solved by *Direct methods* in space group $P6_3$ (No. 173), according to the systematic extinction $000l \neq 2n$, and refined with the SHELXTL program package [136, 304]. First, the structure refinement of CdB_2O_4 converged with residuals of R1 = 6.9% and wR2 = 19%. Additionally, a high electron density close to one oxygen atom remained. The consideration of twinning by merohedry and the introduction of a twofold rotation axis according to the twin matrix $\begin{pmatrix} 0 & 1 & 0 \\ 1 & 0 & 0 \\ 0 & 0 & 1 \end{pmatrix}$ led to a twin ratio of 0.55 : 0.45 with satisfactory residuals (R1 = 1.8%, wR2 = 3.9%) without any significant electron density. The checking of a possible higher symmetry, using the program PLATON [139], did not reveal any additional symmetries. Further details of the data collection and refinement are summarized in Table 4.32, atomic coordinates, isotropic and anisotropic displacement parameters, interatomic distances and angles can be found in Tables 4.33 to 4.36.

Table 4.32: Crystal data and structure refinement of CdB_2O_4 (standard deviations in parentheses).

Empirical Formula	CdB_2O_4
Molar mass/g·mol^{-1}	198.02
Crystal system	hexagonal
Space group	$P6_3$
Powder diffractometer	STOE Stadi P
Radiation	$CuK_{\alpha 1}$ (λ = 154.051 pm)
Powder data	
a/pm	886.64(3)
c/pm	717.38(3)
Volume/nm^3	0.488(1)
Single crystal diffractometer	CAD4 (Nonius)
Radiation	MoK_α (λ = 71.073 pm)
Single crystal data	
a/pm	885.2(2)
c/pm	716.72(8)
Volume/nm^3	0.486(1)
Formula units per cell	Z = 8
Temperature/K	293
Calculated density/g·cm^{-3}	5.408
Crystal size/mm^3	0.23 × 0.18 × 0.14
Absorption coefficient/mm^{-1}	8.756
F (000)/e	720
θ range /°	2.66 – 44.88
Range in hkl	±17, ±17, ±14
Total no. reflections	16090
Independent reflections	2691 (R_{int} = 0.0365)
Reflections with I > 2σ(I)	2598 (R_σ = 0.0167)
Data/parameters	2691/87
Absorption correction	numerical (HABITUS [132])
Transm. ratio (max./min.)	0.4572/0.2449
Goodness-of-fit (F^2)	1.154
Final R indices (I > 2σ(I))	R1 = 0.0163
	wR2 = 0.0383
R indices (all data)	R1 = 0.0178
	wR2 = 0.0388
Extinction coefficient	0.0600(9)
Largest diff. peak, deepest hole/e·Å^{-3}	0.985/-2.349

Table 4.33: Atomic coordinates and equivalent isotropic displacement parameters $U_{eq}/Å^2$ of CdB_2O_4 (space group $P6_3$). U_{eq} is defined as one third of the trace of the orthogonalized U_{ij} tensor (standard deviations in parentheses).

Atom	Wyckoff Position	x	y	z	U_{eq}
Cd1	6*c*	0.48061(3)	0.95729(2)	0.54204(2)	0.00703(2)
Cd2	2*a*	0	0	0.56427(2)	0.00740(3)
B1	2*b*	2/3	1/3	0.7548(5)	0.0047(4)
B2	2*b*	2/3	1/3	0.3653(4)	0.0042(4)
B3	6*c*	0.3273(2)	0.1522(4)	0.7318(3)	0.0045(4)
B4	6*c*	0.1514(4)	0.8227(4)	0.8454(3)	0.0042(4)
O1	2*b*	2/3	1/3	0.5612(3)	0.0098(3)
O2	6*c*	0.3289(2)	0.0899(2)	0.5378(2)	0.0053(2)
O3	6*c*	0.1846(2)	0.0034(2)	0.8284(2)	0.0056(2)
O4	6*c*	0.4927(2)	0.2048(2)	0.8307(2)	0.0051(2)
O5	6*c*	0.2934(2)	0.2986(2)	0.7198(2)	0.0055(2)
O6	6*c*	0.3069(2)	0.8106(2)	0.7942(2)	0.0041(2)

Table 4.34: Anisotropic displacement parameters of CdB_2O_4 (standard deviations in parentheses).

Atom	U_{11}	U_{22}	U_{33}	U_{23}	U_{13}	U_{12}
Cd1	0.00838(5)	0.00923(4)	0.00613(4)	-0.00063(3)	0.00003(9)	0.00639(4)
Cd2	0.00797(4)	0.00797(4)	0.00626(6)	0.000	0.000	0.00399(2)
B1	0.0038(6)	0.0038(6)	0.006(2)	0.000	0.000	0.0019(3)
B2	0.0033(6)	0.0033(6)	0.0061(9)	0.000	0.000	0.0017(3)
B3	0.0025(6)	0.006(2)	0.0053(7)	0.0006(6)	-0.0007(4)	0.0021(6)
B4	0.0037(9)	0.0046(9)	0.0040(6)	0.0012(6)	0.0007(6)	0.0019(8)
O1	0.0128(4)	0.0128(4)	0.0037(7)	0.000	0.000	0.0064(2)
O2	0.0077(4)	0.0057(4)	0.0042(4)	0.0002(4)	0.0001(4)	0.0045(3)
O3	0.0041(4)	0.0042(4)	0.0086(4)	0.0015(5)	0.0027(4)	0.0022(4)
O4	0.0026(4)	0.0059(4)	0.0056(4)	0.0008(4)	-0.0007(4)	0.0011(4)
O5	0.0057(5)	0.0056(5)	0.0061(4)	0.0007(4)	0.0022(4)	0.0035(4)
O6	0.0041(5)	0.0034(6)	0.0051(5)	0.0017(3)	0.0014(3)	0.0021(4)

4.1.7.3 Crystal Structure Description

CdB_2O_4 consists of corner-sharing BO_4-tetrahedra, linked to layers, which are interconnected to a three-dimensional network. The layers spread out perpendicularly to [001] and consist of "Sechser" rings (a ring with six tetrahedral centres) [39] (Figure 4.48 left). These rings show two types of topologies with respect to the orientation of the containing tetrahedra (U = up, D = down): one fourth of the rings reveals an UDUDUD topology, and the remaining rings adopt an UUUDDD topology. Figure 4.48 right gives a view of the two arrangements inside of a layer. The layers are interconnected *via* the atoms O1 and O2, building further B_6O_6-"Sechser", as well as B_4O_4-"Vierer"-rings.

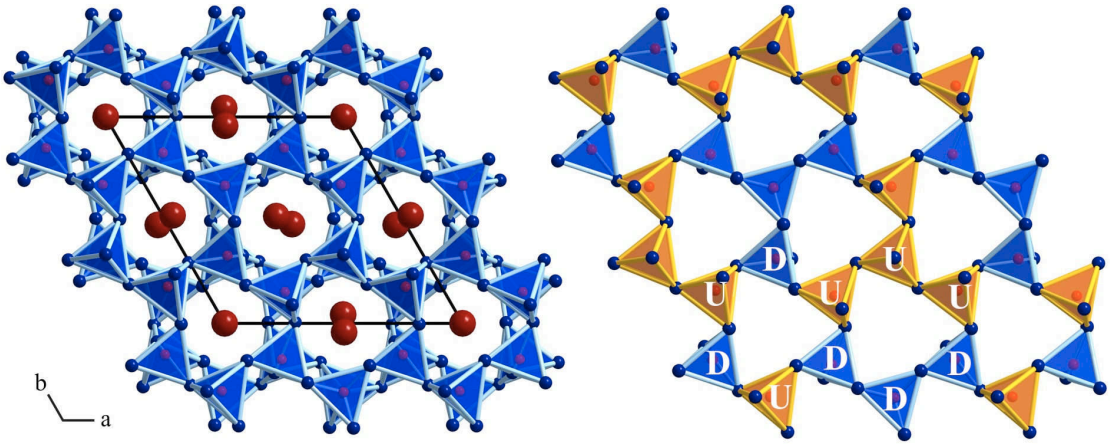

Figure 4.48: Left: Crystal structure of CdB_2O_4 with a view along $[00\bar{1}]$. Red spheres represent Cd-atoms, blue spheres O-atoms; blue polyhedra show BO_4-groups. **Right**: One layer of CdB_2O_4 consists of two different types of "Sechser" rings [39] (topology: UUUDDD, UDUDUD). Blue spheres represent O-atoms. Blue BO_4-polyhedra face downwards (D), yellow polyhedra face upwards (U) (view along $[00\bar{1}]$).

Figure 4.49 shows the connection of the borate layers, whereas adjacent layers are marked in blue and orange for better demonstration. The layers are equivalent and can be transformed into one another by a rotation of 60° along [001] and a translation of $[00\frac{1}{2}]$.

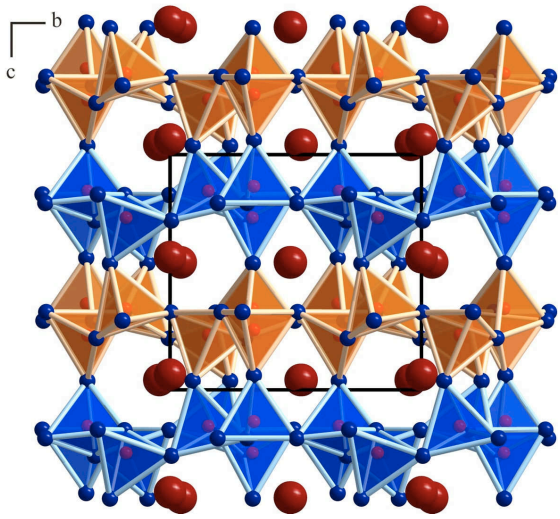

Figure 4.49: Crystal structure of CdB_2O_4 with a view along [100]. Adjacent layers are shown in different colours. Red spheres represent Cd-atoms, blue spheres O-atoms.

Cd1 is surrounded by six oxygen atoms in the range of 218–277 pm with an average value of 223.4 pm (Figure 4.50 left). This value is smaller than the average Cd–O distance of 231.9 pm in $Cd_2B_2O_5$ [228] or 232.9 pm in $Cd_3(BO_3)_2$ [305], which both exhibit cadmium in a six-fold coordination as well. However, Cd2 possesses 12 (9+3) next-near neighbors with Cd–O distances from 234–285 pm with a mean distance of 257.4 pm (Figure 4.50 right). As far as we know, no cadmium borate with a comparably high coordination-sphere at a Cd^{2+}-ion was described up to now. Within the BO_4-network, the B–O lengths reach from 139 to 150 pm with a

mean value of 147.3 pm, which corresponds to the known average value of 147.6 pm for B–O distances in BO_4-tetrahedra [232, 233]. The O–B–O bond angles range from 107.4(2) to 112.8(2)° with a mean value of 109.5°.

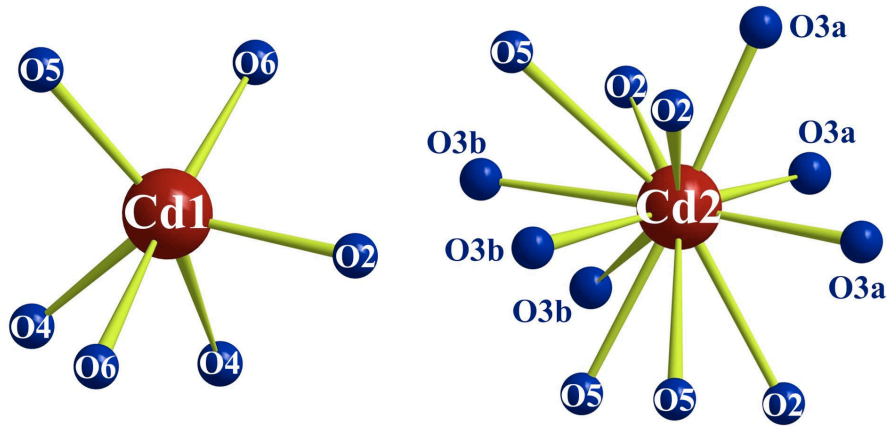

Figure 4.50: Coordination spheres of Cd1 and Cd2 in CdB_2O_4.

Table 4.35: Interatomic distances/pm in CdB_2O_4 (space group $P6_3$) calculated with the single crystal lattice parameters (standard deviations in parentheses).

Cd1-O4a	217.9(2)	Cd2-O3a 3×	234.1(2)
Cd1-O2	218.2(2)	Cd2-O3b 3×	249.1(2)
Cd1-O5	221.5(2)	Cd2-O2 3×	261.3(2)
Cd1-O6a	230.6(2)	Cd2-O5 3×	284.8(2)
Cd1-O6b	265.5(2)		Ø = 257.3
Cd1-O4b	276.9(2)		
	Ø = 223.4		
B1-O1	138.7(4)	B2-O1	140.4(3)
B1-O4 3×	148.6(2)	B2-O6 3×	149.5(2)
	Ø = 146.1		Ø = 147.2
B3-O3	146.5(3)	B4-O3	148.0(3)
B3-O5	147.2(4)	B4-O6	148.0(3)
B3-O4	147.7(3)	B4-O2	148.2(3)
B3-O2	149.9(3)	B4-O5	148.7(3)
	Ø = 147.8		Ø = 148.2

Table 4.36: Interatomic angles/° in CdB_2O_4 calculated with the single crystal lattice parameters (standard deviations in parentheses).

O4-B1-O4	107.4(2)	O6-B2-O6	109.0(2)
O4-B1-O4	107.4(2)	O6-B2-O6	109.0(2)
O4-B1-O4	107.4(2)	O6-B2-O6	109.0(2)
O1-B1-O4	111.5(2)	O1-B2-O6	109.9(2)
O1-B1-O4	111.5(2)	O1-B2-O6	109.9(2)
O1-B1-O4	111.5(2)	O1-B2-O6	109.9(2)
	Ø = 109.5		Ø = 109.5
O3-B3-O2	105.7(2)	O2-B4-O5	106.0(2)
O5-B3-O2	108.3(2)	O3-B4-O2	108.2(2)
O3-B3-O4	109.3(2)	O6-B4-O5	108.6(2)
O3-B3-O5	110.8(2)	O3-B4-O5	109.4(2)
O5-B3-O4	110.9(2)	O3-B4-O6	111.7(2)
O4-B3-O2	111.8(2)	O6-B4-O2	112.8(2)
	Ø = 109.5		Ø = 109.5

The structure of CdB_2O_4 is closely related to the structure-type of the compounds $BaGa_2O_4$ [306], $KAlSiO_4$ [307], $KGeAlO_4$ [308, 309], $KCoPO_4$ [310], CaP_2N_4 [311], and SrP_2N_4 [312]. Both structure types consist of layers of tetrahedra, forming "Sechser" rings [39] with an identical orientation of the tetrahedra. Except CdB_2O_4, all other compounds form a superstructure, which means that CdB_2O_4 is the first representative, showing a threefold smaller basic cell. Table 4.37 lists the lattice parameters of CdB_2O_4 in comparison to the related compounds. The superstructure can be obtained from the basic structure by the

Table 4.37: Lattice parameters of CdB_2O_4 and related structures, all in space group $P6_3$.

	a/pm	c/pm	V/nm^3
CdB_2O_4	885.2(2)	716.72(8)	0.486(1)
$BaGa_2O_4$	1864.03(7)	868.01(2)	2.6119(2)
$KAlSiO_4$	1811.11(8)	846.19(4)	2.4037(2)
$KGeAlO_4$	1841.3(1)	859.0(1)	2.5222(2)
$KCoPO_4$	1820.6(1)	851.35(8)	2.4438(2)
CaP_2N_4	1684.66(4)	785.5(2)	1.9307(1)
SrP_2N_4	1710.29(8)	810.318(5)	2.05270(2)

following lattice transformation: $a_{super} = 2a_{basic} + b_{basic}$; $b_{super} = -a_{basic} + b_{basic}$; $c_{super} = c_{basic}$. This corresponds to an isomorphic transition of index 3. Figure 4.51 shows the crystal structure of SrP_2N_4 (view along [001]) with the position of the according subcell of CdB_2O_4 drawn in thick black lines.

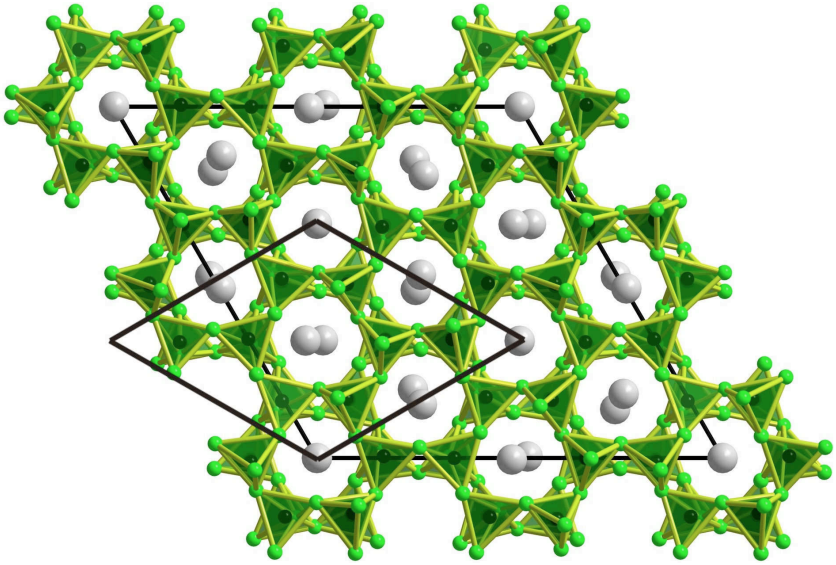

Figure 4.51: Structure of SrP_2N_4 [312] with a view along [001]. Polyhedra represent PN_4-tetrahedra, white spheres show Sr^{2+} ions. The according basic unit cell of CdB_2O_4 is drawn in thick black lines.

In SrP_2N_4 [312], this superstructure is caused by avoiding one P–N–P-angle of 180° at nitrogen atom N15 (see Figure 4.52). The isotypic compounds $BaGa_2O_4$ [306], $KAlSiO_4$ [307], $KGeAlO_4$ [308, 309], $KCoPO_4$ [310], and CaP_2N_4 [311] do not show the linear arrangement at the corresponding position as well. By con-

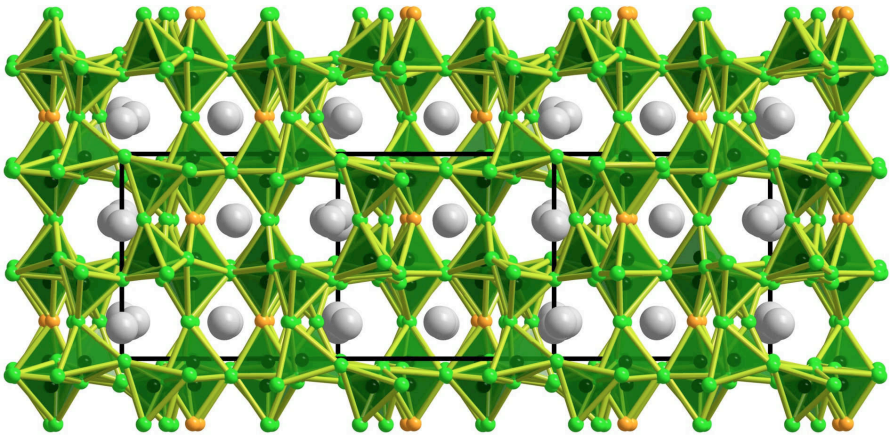

Figure 4.52: Structure of SrP_2N_4 [312] with a view along [120]. Polyhedra represent PN_4-tetrahedra, white spheres show Sr^{2+} ions. Orange spheres represent nitrogen-atoms N15.

trast, the associated B–O–B-angle in CdB_2O_4 adopts a value of 180° at oxygen O1 on thermal average (Figure 4.53). From our knowledge, this is the first example of a linear
B–O–B arrangement in the structural chemistry of borates. There exists a molecular compound, divinylborinic anhydride $[(CH_2{=}CH)_2B]_2O$, in which the vibrational data indicate that the molecule possesses C_1 symmetry and a linear B–O–B angle [313]. In a theoretical work, Geisinger *et al.* investigated the potential energy curves for molecules, containing a B–O–B group [314]. These results showed that a linear arrangement is energetically unfavourable. In other solids, comparable linear arrangements with different atoms could be found in silicates as zunyite

$Al_{13}Si_5O_{16}(OH,F)_{15}O_4Cl$ [315], thortveitite $Sc_2Si_2O_7$ [316], or $(AgSiO_4) \cdot Ag_{10}Si_4O_{13}$ [317] and in the nitridosilicate $Ba_2Nd_7Si_{11}N_{23}$ [318]. Liebau examined the influence of thermal vibrations on the Si–O–Si bond-angles [39] with the following observation: the stronger the displacement at the bridging atom, the smaller the deviation from linearity [39, 319]. Further analysis of the thermal displacement parameters at the bridging atom showed that the oscillation amplitude, perpendicular to the Si–Si-vector, is considerably larger. Figure 4.53 gives a view of the linear B–O–B arrangement in CdB_2O_4, drawn with 90% thermal probability ellipsoids. It also shows that the thermal displacement parameter at oxygen O1 has the largest value perpendicular to the B–B-vector, which corresponds to Liebau's observations. The existence of the basic cell in CdB_2O_4 is confirmed by electron diffraction.

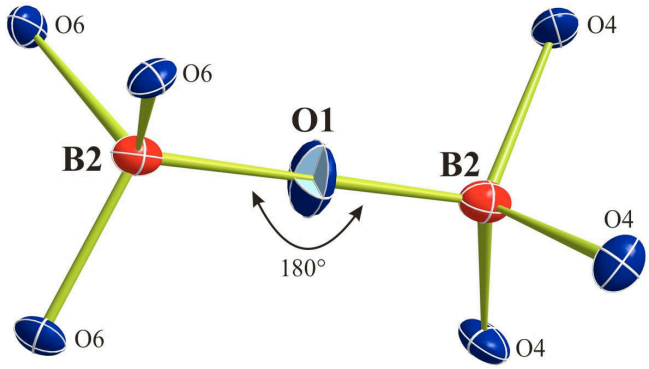

Figure 4.53: Linear environment of O1 in CdB_2O_4, drawn with 90% thermal probability ellipsoids.

4.1.7.4 Electron Diffraction Experiments

Figure 4.54 shows the electron diffraction patterns (along zone axis [001]) of CdB_2O_4 (left) in comparison to that of SrP_2N_4 (right). The reciprocal unit cells of both phases are shown in solid lines. The dashed line in the right pattern (SrP_2N_4) designates the basic cell. In contrast to the pattern of CdB_2O_4, where no additional reflections can be found, the pattern of SrP_2N_4 clearly exhibits the supercell reflections.

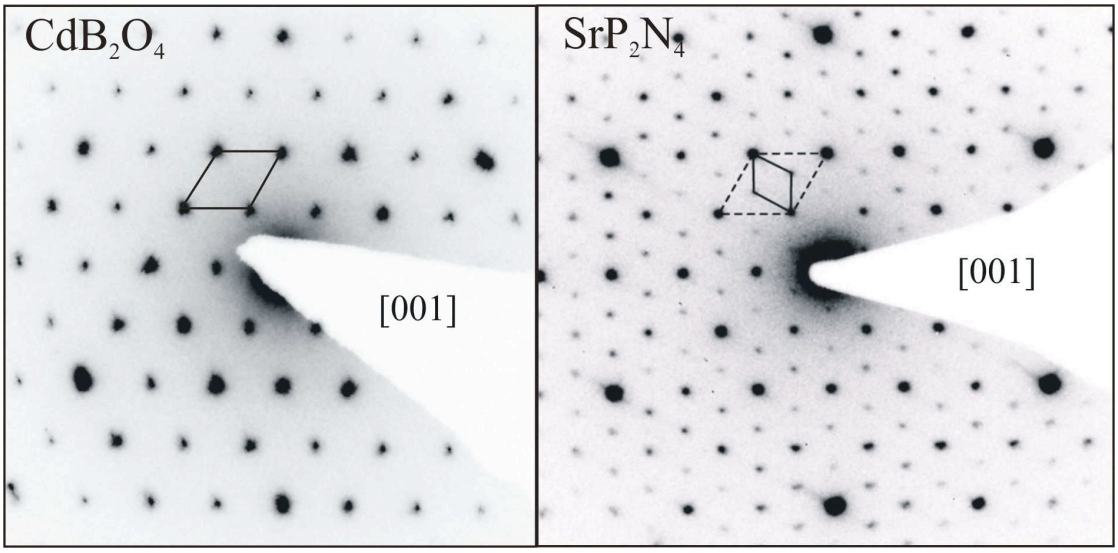

Figure 4.54: Electron diffraction patterns (zone axis [001]) of CdB_2O_4 (left) and SrP_2N_4 (right) [312]. The reciprocal unit cells are drawn in black solid lines. In dashed lines (right picture) the basic unit cell is drawn.

4.1.7.5 Thermal Behaviour

Temperature-programmed X-ray powder diffraction experiments were performed on a STOE STADI P powder diffractometer ($MoK_{\alpha 1}$ radiation, $\lambda = 71.073$ pm) with a computer controlled STOE furnace in order to study the thermal stability and the metastable character of CdB_2O_4. The sample was enclosed in a silica capillary and heated from room temperature to 500 °C in 100 °C steps, and from 500 °C to 1100 °C in 50 °C steps. Afterwards, the sample was cooled down to 500 °C in 50 °C steps, and from 500 °C to room temperature in 100 °C steps. After each heating step, a diffraction pattern was recorded over the angular range $8° < 2\theta < 16°$.

The temperature-programmed X-ray powder diffraction patterns (Figure 4.55) show that the compound remains stable up to a temperature of 600 °C. Between 600 and 650 °C, decomposition occurs into the normal-pressure borates $Cd_2B_2O_5$ and CdB_4O_7, and above 850 °C only an amorphous phase can be detected, which remains during and after cooling to room temperature.

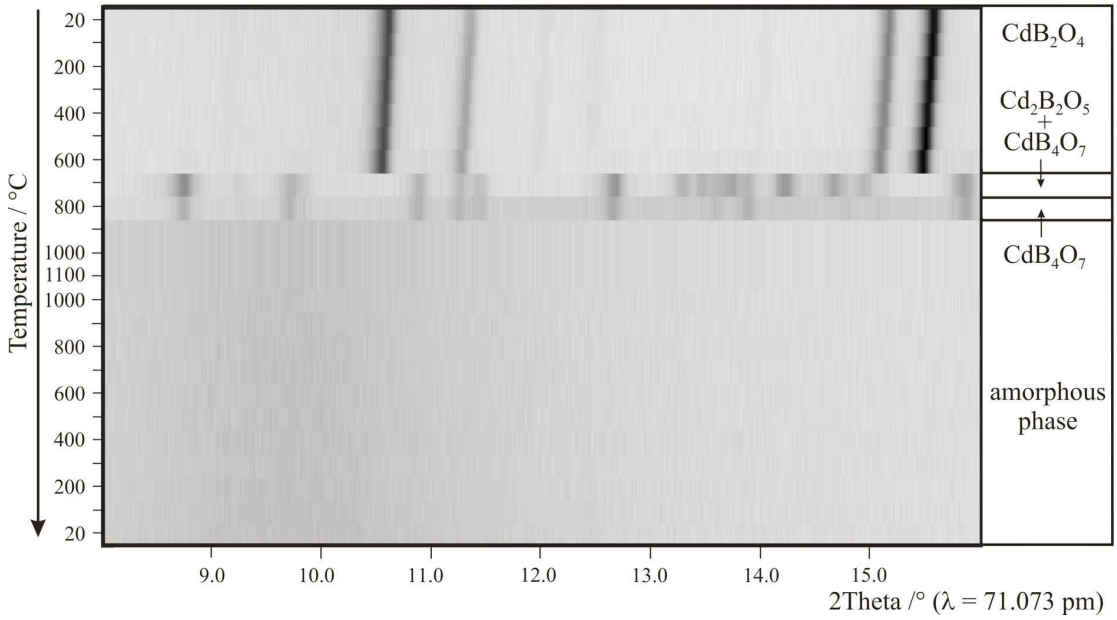

Figure 4.55: *In situ* X-ray powder patterns of CdB_2O_4.

4.1.7.6 Theoretical Calculations

We calculated bond-valence sums for CdB_2O_4 with the bond-length/bond-strength (ΣV) [164, 165] and CHARDI (ΣQ) [167] concepts (Table 4.38). The formal ionic charges of the atoms, as calculated from the results of the X-ray structure analysis, were in agreement within the limits of both concepts.

Table 4.38: Charge distribution in CdB_2O_4 calculated with the bond-length/bond-strength concept (ΣV) and the CHARDI concept (ΣQ).

	Cd1	Cd2	B1	B2	B3	B4
ΣV	+1.94	+2.21	+3.16	+3.06	+3.00	+2.96
ΣQ	+2.00	+1.96	+3.04	+3.15	+2.95	+2.99
	O1	O2	O3	O4	O5	O6
ΣV	-1.87	-2.07	-2.03	-2.06	-2.00	-1.93
ΣQ	-1.96	-2.10	-2.02	-1.98	-2.04	-1.88

Additionally, we calculated the MAPLE values (Madelung Part of Lattice Energy) [161–163] for CdB_2O_4 in order to compare the results with MAPLE values of the binary components CdO and the high-pressure modification B_2O_3-II [82]. The calculated value (26282 kJ·mol^{-1}) for CdB_2O_4 and the MAPLE value obtained from the sum of the binary oxides (26074 kJ·mol^{-1}) tally well (deviation: 0.8 %).

4.1.8 The Borates $M_3B_{11}O_{19}OH$ (M = Fe, Co)

4.1.8.1 Syntheses

The new high-pressure phases $M_3B_{11}O_{19}OH$ (M = Fe, Co) were prepared under high-pressure/high-temperature conditions of 7.5 GPa and 1100 °C (Fe)/ 880 °C (Co) according to Equation 4.9. The origin of hydrogen in the compound $M_3B_{11}O_{19}OH$ (M = Fe, Co) can be found in the partially hydrolysis of the starting material B_2O_3. To simplify the reaction the following equation was written with H_2O instead of the hydrolysis product $B(OH)_3$.

$$3\,M_2O_3 + 11\,B_2O_3 + H_2O \xrightarrow[1100\ °C/880\ °C]{7.5\ GPa} 2\,M_3B_{11}O_{19}OH + 1.5\,O_2 \tag{4.9}$$

Starting materials were the binary oxides M_2O_3 (M = Fe: Sigma-Aldrich Chemie Gmbh, Munich, Germany, 99.9%, Co: Merck KGaA, Darmstadt, Germany, *p.a.*) and B_2O_3 (Strem Chemicals, Newburyport, USA, 99.9%). The stoichiometric mixtures were ground up and filled into boron nitride crucibles (Henze BNP GmbH, HeBoSint® S10, Kempten, Germany). The crucibles were placed inside of 18/11-assemblies. The assemblies were compressed to 7.5 GPa during 3 h, then heated to 1100 (Fe) and 880 °C (Co) in 10 min and kept there for 5 (Fe) and 13 min (Co), respectively. Afterwards, the samples were cooled down to 750 (Fe) and 880 °C (Co) in 15 min and then quenched to room temperature by switching off the heating. After a decompression period of 9 h, the recovered experimental MgO-octahedra were cracked and the samples carefully separated from the surrounding crucible. $Fe_3B_{11}O_{19}OH$ was obtained as colourless, $Co_3B_{11}O_{19}OH$ as violet crystals (see Figure 4.56). During the synthesis of $Fe_3B_{11}O_{19}OH$ several other phases such as the normal-pressure iron oxide borate vonsenite $Fe_2Fe(BO_3)O_2$ or a cubic iron borate "$Fe_3B_7O_{12}N$" (a = 1222.4 pm, see section 4.1.9) occured. $Fe_3B_{11}O_{19}OH$ could not be synthesized as a pure sample until now. In the case of $Co_3B_{11}O_{19}OH$ higher temperatures led to a new phase with the composition β-CoB_4O_7 (see Figure 4.56 and section 4.1.4) [261]. Using lower temperatures, the trigonal phase "$Co_3B_8O_{13}(OH)_4$" was synthesized (see section 4.1.10).

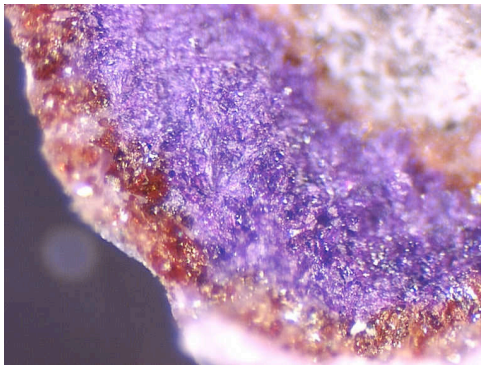

Figure 4.56: Crystals of $Co_3B_{11}O_{19}OH$ (violet) with crystals of β-CoB_4O_7 (red).

4.1.8.2 Crystal Structure Analyses

The powder diffraction patterns of $M_3B_{11}O_{19}OH$ (M = Fe, Co) were obtained in transmission geometry from flat samples using a STOE Stadi P powder diffractometer with monochromatized $MoK_{\alpha 1}$ radiation (λ = 71.073 pm). The diffraction patterns could not be indexed because the samples were mixtures of different phases, that could not be separated. Figures 4.57 and 4.58 show the experimental (top) and the simulated powder diagram (bottom) of $Fe_3B_{11}O_{19}OH$ and $Co_3B_{11}O_{19}OH$, respectively. $Fe_3B_{11}O_{19}OH$ is impurified by vonsenite $Fe_3(BO_3)O_2$. The corresponding reflections are marked in red in Figure 4.57, bottom. In the case of $Co_3B_{11}O_{19}OH$ the trigonal phase "$Co_3B_8O_{13}(OH)_4$" can be found in the diffraction pattern as a by-product.

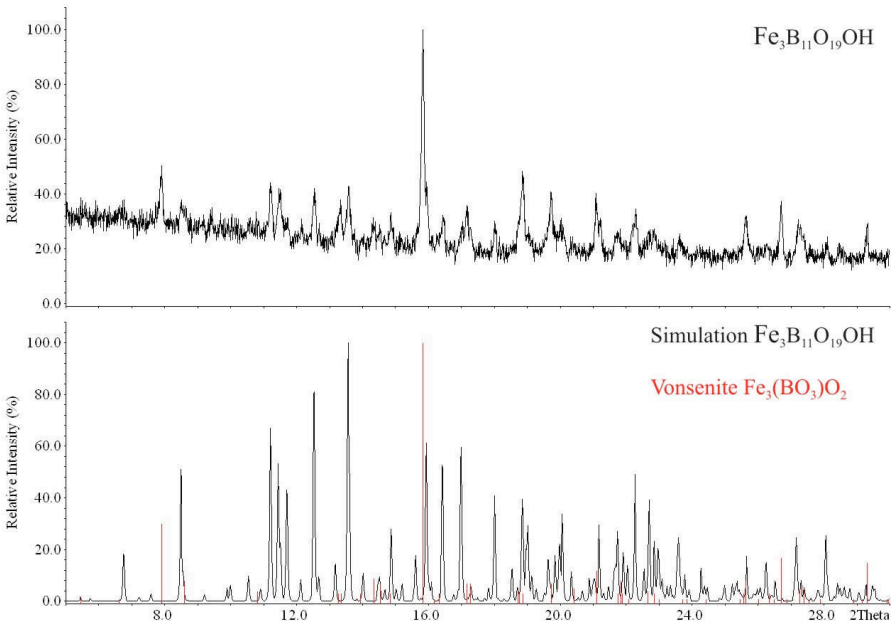

Figure 4.57: Measured (top) and simulated (single crystal data) (bottom) powder diffraction patterns of $Fe_3B_{11}O_{19}OH$. Reflections of vonsenite $Fe_3(BO_3)O_2$ are highlighted in red (bottom).

Small single crystals of the isotypic phases $M_3B_{11}O_{19}OH$ (M = Fe, Co) were isolated by mechanical fragmentation and examined through a Buerger camera, equipped with an image plate system (Fujifilm BAS-2500) in order to check suitability for an intensity data collection. The single crystal intensity data were collected at room temperature using an Enraf-Nonius Kappa CCD diffractometer with MoK_α (λ = 71.073 pm, graded multilayer x-ray optics) radiation. A multi-scan absorption correction (SCALEPACK [133]) was applied to the intensity data. According to the systematic extinction $h0l$ with $h+l \neq 2n$, the orthorhombic space groups $Pmn2_1$ (No. 31) and $Pmnm$ (No. 59) were derived. The noncentrosymmetric space group $Pmn2_1$ (No. 31) could be assigned during the refinement. The ADDSYM routine of the program PLATON [139] and a violation of the

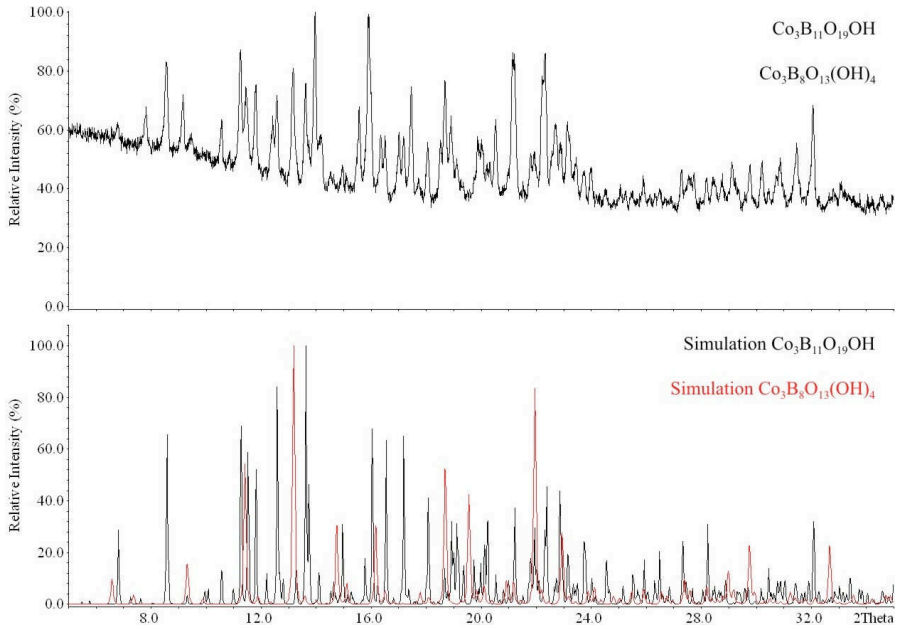

Figure 4.58: Measured (top) and simulated (single crystal data) (bottom) powder diffraction patterns of $Co_3B_{11}O_{19}OH$ which is impurified with the trigonal phase "$Co_3B_8O_{13}(OH)_4$".

systematic extinctions for $0kl$ with $l \neq 2n$ and $0k0$ with $k \neq 2n$ by weak reflections, would lead to the space group $Pbnm$ ($\equiv Pnma$, No. 62). However a close examination of the structure of $M_3B_{11}O_{19}OH$ (M = Fe, Co) disproved the centrosymmetry due to the atoms O24, O25, and B11. Therewith non-centrosymmetric space group $Pmn2_1$ (No. 31) was used to describe the structure. Figure 4.59 (see page 113) clarifies the non-centrosymmetry of the crystal structure, which is described later. Structure solution and parameter refinement were successfully performed using the SHELX-97 software suite [135, 136]. The length of the oxygen-hydrogen bond was restrained to 98.2 pm in accordance to the bond-length between oxygen and hydrogen in borax (98.2(3) pm) [320]. In Table 4.39 the relevant details of the data collection and evaluation are listed. The positional parameters of the refinements, anisotropic displacement parameters, and interatomic distances are listed in Tables 4.40 – 4.47.

Table 4.39: Crystal data and structure refinement of $M_3B_{11}O_{19}OH$ (M = Fe, Co) (standard deviations in parentheses).

Empirical Formula	$Fe_3B_{11}O_{19}OH$	$Co_3B_{11}O_{19}OH$
Molar mass/g·mol^{-1}	606.46	615.70
Crystal system	orthorhombic	
Space group	$Pmn2_1$	
Single crystal diffractometer	Enraf-Nonius Kappa CCD	
Radiation	MoK$_\alpha$ (λ = 71.073 pm)	
Single crystal data		
a/pm	771.9(2)	770.1(2)
b/pm	823.4(2)	817.6(2)
c/pm	1768.0(4)	1746.9(4)
Volume/nm^3	1123.7(4)	1099.9(4)
Formula units per cell	Z = 4	
Temperature/K	293(2)	
Calculated density/g·cm^{-3}	3.588	3.721
Crystal size/mm^3	0.06 × 0.05 × 0.03	0.14 × 0.12 × 0.08
Absorption coefficient/mm^{-1}	3.984	4.638
F (000)/e	1177	1186
θ range/°	3.4 – 35.0	3.4 – 37.8
Range in hkl	± 12, ± 13, ± 28	± 12, -13/+14, -30/+29
Total no. reflections	17098	15885
Independent reflections	5240 (R_{int} = 0.0514)	6000 (R_{int} = 0.0688)
Reflections with I > 2σ(I)	4458 (R_σ = 0.0447)	5256 (R_σ = 0.0732)
Data/parameters	5240/335	6000/335
Absorption correction	multi-scan (SCALEPACK [133])	
Goodness-of-fit (F^2)	1.049	1.013
Final R indices (I > 2σ(I))	R1 = 0.0356	R1 = 0.0401
	wR2 = 0.0885	wR2 = 0.0885
R indices (all data)	R1 = 0.0479	R1 = 0.0516
	wR2 = 0.0930	wR2 = 0.0954
Largest diff. peak, deepest hole/e·Å^{-3}	1.336/-0.804	1.170/-1.039

Table 4.40: Atomic coordinates and equivalent isotropic displacement parameters U_{eq} / Å^2 of $Fe_3B_{11}O_{19}OH$ (space group $Pmn2_1$). U_{eq} is defined as one third of the trace of the orthogonalized U_{ij} tensor (standard deviations in parentheses).

Atom	Wyckoff Position	x	y	z	U_{eq}
Fe1	2*a*	1/2	0.32788(9)	0.34022(4)	0.0106(2)
Fe2	2*a*	0	0.04483(9)	0.70213(4)	0.0124(2)
Fe3	2*a*	0	0.15228(9)	0.25675(4)	0.0098(2)
Fe4	2*a*	0	0.76891(9)	0.13064(4)	0.0099(2)
Fe5	2*a*	1/2	0.73311(8)	0.46030(4)	0.0089(2)
Fe6	2*a*	0	0.5561(2)	0.39836(4)	0.0142(2)
B1	4*b*	0.1648(5)	0.2102(4)	0.4111(2)	0.0051(6)
B2	4*b*	0.3292(5)	0.972(4)	0.3458(2)	0.0063(6)
B3	4*b*	0.3317(6)	0.3981(4)	0.4987(2)	0.0058(7)
B4	4*b*	0.1629(5)	0.9150(4)	0.4614(2)	0.0056(6)
B5	4*b*	0.1681(5)	0.6473(4)	0.5385(2)	0.0045(7)
B6	4*b*	0.3348(6)	0.8526(4)	0.0576(2)	0.0064(7)
B7	4*b*	0.3324(5)	0.8966(4)	0.5950(2)	0.0048(6)
B8	4*b*	0.1672(6)	0.4990(4)	0.2515(3)	0.0097(7)
B9	4*b*	0.3306(5)	0.2871(4)	0.1843(2)	0.0062(7)
B10	4*b*	0.1624(5)	0.4132(4)	0.6345(2)	0.0055(6)
B11	4*b*	0.1683(6)	0.7682(6)	0.2694(3)	0.0254(9)
H	2*a*	1/2	0.649(7)	0.308(2)	0.023
O1	4*b*	0.3046(4)	0.3238(3)	0.4249(2)	0.0071(5)
O2	4*b*	0.1888(4)	0.1242(3)	0.7766(2)	0.0116(5)
O3	4*b*	0.1953(4)	0.1700(3)	0.1708(2)	0.0060(5)
O4	2*a*	0	0.4204(4)	0.2474(2)	0.0086(6)
O5	2*a*	0	0.7937(4)	0.6856(2)	0.0065(6)
O6	2*a*	1/2	0.0635(4)	0.3394(2)	0.0098(7)
O7	2*a*	0	0.1047(4)	0.5918(2)	0.0057(6)
O8	4*b*	0.3061(3)	0.3838(3)	0.2518(2)	0.0070(4)
O9	2*a*	0	0.6014(4)	0.5086(2)	0.0067(6)
O10	4*b*	0.3086(4)	0.8809(3)	0.4118(2)	0.0080(5)
O11	2*a*	1/2	0.8552(4)	0.5640(2)	0.0068(7)
O12	4*b*	0.3015(3)	0.5722(3)	0.4946(2)	0.0065(4)
O13	2*a*	0	0.2969(4)	0.4082(2)	0.0057(6)
O14	4*b*	0.1933(3)	0.1116(3)	0.3431(2)	0.0055(4)
O15	4*b*	0.1753(4)	0.6160(3)	0.3150(2)	0.0105(5)
O16	4*b*	0.1941(4)	0.6269(3)	0.1861(2)	0.0095(5)
O17	2*a*	0	0.6410(4)	0.0306(2)	0.0056(6)
O18	4*b*	0.1945(4)	0.9279(3)	0.0993(2)	0.0066(5)
O19	4*b*	0.1668(4)	0.0931(3)	0.4782(2)	0.0054(4)
O20	4*b*	0.1968(4)	0.8290(3)	0.5390(2)	0.0062(5)
O21	4*b*	0.1776(4)	0.5905(3)	0.6182(2)	0.0068(5)
O22	4*b*	0.1939(3)	0.3279(3)	0.5574(2)	0.0056(5)
O23	2*a*	0	0.8655(4)	0.4305(2)	0.0065(7)
O24	2*a*	0	0.8431(5)	0.2520(2)	0.0195(7)
O25	2*a*	1/2	0.5912(5)	0.3551(2)	0.0194(8)
O26	2*a*	0	0.3688(4)	0.6663(2)	0.0058(6)

Table 4.41: Atomic coordinates and equivalent isotropic displacement parameters U_{eq} / Å^2 of $Co_3B_{11}O_{19}OH$ (space group $Pmn2_1$). U_{eq} is defined as one third of the trace of the orthogonalized U_{ij} tensor (standard deviations in parentheses).

Atom	Wyckoff Position	x	y	z	U_{eq}
Co1	2*a*	1/2	0.32686(7)	0.34190(3)	0.0104(2)
Co2	2*a*	0	0.03967(7)	0.70361(3)	0.0113(2)
Co3	2*a*	0	0.14219(7)	0.25648(3)	0.0108(2)
Co4	2*a*	0	0.77081(7)	0.12879(3)	0.0099(2)
Co5	2*a*	1/2	0.73419(7)	0.45880(3)	0.00928(9)
Co6	2*a*	0	0.56100(8)	0.39936(3)	0.0151(2)
B1	4*b*	0.1650(3)	0.2115(4)	0.4096(2)	0.0082(5)
B2	4*b*	0.3272(4)	0.9728(4)	0.3424(2)	0.0097(5)
B3	4*b*	0.3319(3)	0.3997(4)	0.4990(2)	0.0082(5)
B4	4*b*	0.1629(3)	0.9154(4)	0.4608(2)	0.0088(4)
B5	4*b*	0.1683(4)	0.6500(4)	0.5391(2)	0.0080(5)
B6	4*b*	0.3357(4)	0.8513(4)	0.0576(2)	0.0086(5)
B7	4*b*	0.3323(3)	0.8989(4)	0.5954(2)	0.0088(5)
B8	4*b*	0.1650(3)	0.4940(4)	0.2536(2)	0.0109(5)
B9	4*b*	0.3307(4)	0.2852(4)	0.1858(2)	0.0086(5)
B10	4*b*	0.1617(3)	0.4137(4)	0.6348(2)	0.0086(5)
B11	4*b*	0.1695(4)	0.7602(4)	0.2637(2)	0.0167(6)
H	2*a*	1/2	0.624(7)	0.307(2)	0.016
O1	4*b*	0.3063(2)	0.3238(3)	0.4242(2)	0.0093(3)
O2	4*b*	0.1933(2)	0.1246(3)	0.7726(2)	0.0113(3)
O3	4*b*	0.1949(2)	0.1668(3)	0.1723(2)	0.0096(4)
O4	2*a*	0	0.4140(3)	0.2477(2)	0.0091(5)
O5	2*a*	0	0.7950(4)	0.6855(2)	0.0092(5)
O6	2*a*	1/2	0.0603(4)	0.3344(2)	0.0114(5)
O7	2*a*	0	0.1061(4)	0.5933(2)	0.0080(4)
O8	4*b*	0.3068(2)	0.3817(3)	0.2548(2)	0.0084(3)
O9	2*a*	0	0.6037(4)	0.5091(2)	0.0093(5)
O10	4*b*	0.3086(2)	0.8808(3)	0.4114(2)	0.0096(3)
O11	2*a*	1/2	0.8550(3)	0.5636(2)	0.0090(5)
O12	4*b*	0.3019(2)	0.5743(3)	0.4937(2)	0.0096(3)
O13	2*a*	0	0.3006(4)	0.4063(2)	0.0092(5)
O14	4*b*	0.1909(2)	0.1108(3)	0.3418(2)	0.0085(3)
O15	4*b*	0.1728(2)	0.6179(3)	0.3159(2)	0.0106(3)
O16	4*b*	0.1936(2)	0.6302(3)	0.1886(2)	0.0102(4)
O17	2*a*	0	0.6395(3)	0.0320(2)	0.0090(5)
O18	4*b*	0.1934(2)	0.9256(2)	0.0988(2)	0.0084(3)
O19	4*b*	0.1654(2)	0.0939(3)	0.4778(2)	0.0081(3)
O20	4*b*	0.1955(2)	0.8302(2)	0.5393(2)	0.0080(3)
O21	4*b*	0.1808(2)	0.5912(2)	0.6196(2)	0.0085(3)
O22	4*b*	0.1945(2)	0.3300(2)	0.5574(2)	0.0080(3)
O23	2*a*	0	0.8623(4)	0.4295(2)	0.0085(5)
O24	2*a*	0	0.8368(4)	0.2493(2)	0.0124(5)
O25	2*a*	1/2	0.5896(4)	0.3586(2)	0.0137(5)
O26	2*a*	0	0.3713(4)	0.6673(2)	0.0093(5)

Table 4.42: Anisotropic displacement parameters of $Fe_3B_{11}O_{19}OH$ (standard deviations in parentheses).

Atom	U_{11}	U_{22}	U_{33}	U_{23}	U_{13}	U_{12}
Fe1	0.0087(4)	0.0141(3)	0.0088(3)	-0.0012(2)	0	0
Fe2	0.0140(4)	0.0146(3)	0.0086(3)	-0.0037(3)	0	0
Fe3	0.0065(3)	0.0166(3)	0.0063(3)	-0.0003(2)	0	0
Fe4	0.0076(4)	0.0102(3)	0.0120(3)	-0.0001(2)	0	0
Fe5	0.0078(4)	0.0079(3)	0.0110(3)	0.0006(2)	0	0
Fe6	0.0144(4)	0.0202(4)	0.0080(3)	0.0036(3)	0	0
B1	0.004(2)	0.006(2)	0.005(2)	-0.000(2)	0.000(2)	-0.001(2)
B2	0.006(2)	0.009(2)	0.004(2)	0.001(2)	0.001(2)	0.002(2)
B3	0.007(2)	0.004(2)	0.006(2)	0.001 (2)	0.001(2)	-0.001 (2)
B4	0.006(2)	0.006(2)	0.005(2)	0.000(2)	-0.002(2)	0.001(2)
B5	0.001(2)	0.006(2)	0.006(2)	-0.002(2)	0.000(2)	0.000(2)
B6	0.009(2)	0.004(2)	0.006(2)	0.003(2)	0.001(2)	-0.001(2)
B7	0.003(2)	0.006(2)	0.006(2)	-0.001(2)	-0.000(2)	-0.000(2)
B8	0.007(2)	0.007(2)	0.015(2)	-0.003(2)	-0.000(2)	0.000(2)
B9	0.006(2)	0.007(2)	0.005(2)	0.001(2)	-0.001(2)	0.002(2)
B10	0.005(2)	0.005(2)	0.006(2)	-0.001(2)	-0.002(2)	0.001(2)
B11	0.016(2)	0.026(2)	0.034(2)	0.011(2)	-0.007(2)	-0.004(2)
O1	0.007(2)	0.008(2)	0.007(2)	-0.0010(7)	-0.0002(9)	-0.0027(8)
O2	0.018(2)	0.011(2)	0.006(2)	0.0023(8)	-0.0044(9)	-0.004(2)
O3	0.004(2)	0.008(2)	0.006(2)	-0.0008(7)	0.0016(9)	-0.0017(8)
O4	0.004(2)	0.010(2)	0.013(2)	0.000(2)	0	0
O5	0.007(2)	0.003(2)	0.010(2)	0.001(2)	0	0
O6	0.005(2)	0.011(2)	0.014(2)	0.008(2)	0	0
O7	0.006(2)	0.007(2)	0.005(2)	-0.002(2)	0	0
O8	0.005(2)	0.008(2)	0.008(2)	-0.0004(9)	-0.002(2)	0.0010(8)
O9	0.004(2)	0.008(2)	0.009(2)	-0.003(2)	0	0
O10	0.009(2)	0.007(2)	0.008(2)	0.0020(8)	0.0024(9)	0.0021(9)
O11	0.005(2)	0.009(2)	0.006(2)	-0.003(2)	0	0
O12	0.006(2)	0.0058(9)	0.008(2)	0.0011(8)	0.0035(9)	0.0008(8)
O13	0.002(2)	0.008(2)	0.007(2)	0.000(2)	0	0
O14	0.007(2)	0.0054(9)	0.004(2)	-0.0010(8)	0.0009(9)	0.0018(8)
O15	0.011(2)	0.010(2)	0.011(2)	-0.0020(8)	0.0018(9)	-0.0000(9)
O16	0.004(2)	0.013(2)	0.011(2)	0.0057(9)	0.0028(9)	0.0023(9)
O17	0.003(2)	0.008(2)	0.006(2)	0.000(2)	0	0
O18	0.008(2)	0.0025(9)	0.009(2)	-0.0000(8)	0.0022(9)	0.0006(8)
O19	0.008(2)	0.0047(8)	0.003(2)	0.0024(7)	0.0002(8)	0.0000(8)
O20	0.010(2)	0.004(2)	0.005(2)	0.0023(7)	-0.001(2)	-0.0015(8)
O21	0.008(2)	0.0053(9)	0.007(2)	0.0001(8)	0.0018(9)	-0.0009(7)
O22	0.004(2)	0.006(2)	0.006(2)	0.0013(8)	0.0021(9)	0.0000(8)
O23	0.005(2)	0.007(2)	0.008(2)	-0.002(2)	0	0
O24	0.018(2)	0.026(2)	0.014(2)	-0.007(2)	0	0
O25	0.015(2)	0.025(2)	0.018(2)	-0.006(2)	0	0
O26	0.004(2)	0.008(2)	0.0058(2)	0.001(2)	0	0

Table 4.43: Anisotropic displacement parameters of $Co_3B_{11}O_{19}OH$ (standard deviations in parentheses).

Atom	U_{11}	U_{22}	U_{33}	U_{23}	U_{13}	U_{12}
Co1	0.0065(2)	0.0151(2)	0.0096(2)	-0.0012(2)	0	0
Co2	0.0100(2)	0.0141(2)	0.0099(2)	-0.0009(2)	0	0
Co3	0.0062(2)	0.0175(3)	0.0086(2)	-0.0005(2)	0	0
Co4	0.0055(2)	0.0129(2)	0.0114(2)	-0.0010(2)	0	0
Co5	0.0056(2)	0.0126(2)	0.0097(2)	-0.0002(2)	0	0
Co6	0.0133(2)	0.0233(3)	0.0088(2)	0.0013(2)	0	0
B1	0.003(2)	0.011(2)	0.011(2)	0.001(2)	-0.0013(9)	0.0000(8)
B2	0.007(2)	0.014(2)	0.008(2)	0.003(2)	0.0014(9)	-0.0004(8)
B3	0.006(2)	0.011(2)	0.008(2)	0.0024(9)	-0.0008(8)	-0.0008(9)
B4	0.007(2)	0.012(2)	0.008(2)	0.001(2)	0.0005(8)	0.0004(8)
B5	0.006(2)	0.010(2)	0.009(2)	-0.0007(9)	-0.0012(8)	-0.0007(8)
B6	0.005(2)	0.012(2)	0.009(2)	-0.0001(9)	0.0010(9)	0.0007(8)
B7	0.005(2)	0.014(2)	0.008(2)	0.002(2)	-0.0017(8)	-0.0008(9)
B8	0.005(2)	0.015(2)	0.013(2)	-0.003(2)	-0.0019(9)	0.0014(9)
B9	0.009(2)	0.010(2)	0.007(2)	0.0017(9)	0.0001(9)	-0.0009(9)
B10	0.006(2)	0.011(2)	0.010(2)	-0.0007(9)	0.0000(8)	-0.0002(8)
B11	0.011(2)	0.019(2)	0.020(2)	0.003(2)	-0.001(2)	-0.002(2)
O1	0.0055(7)	0.0135(9)	0.0090(8)	-0.0017(7)	0.0009(6)	-0.0030(6)
O2	0.0094(7)	0.0147(9)	0.0098(8)	0.0014(7)	-0.0015(6)	-0.0005(7)
O3	0.0058(7)	0.0145(9)	0.0085(8)	-0.0004(7)	0.0004(6)	-0.0012(6)
O4	0.0055(9)	0.010(2)	0.012(2)	-0.001(2)	0	0
O5	0.0028(9)	0.011(2)	0.014(2)	-0.001(2)	0	0
O6	0.0041(9)	0.015(2)	0.015(2)	0.003(2)	0	0
O7	0.0031(9)	0.012(2)	0.009(2)	0.0000(9)	0	0
O8	0.0052(7)	0.0118(9)	0.0084(8)	-0.0012(7)	0.0001(6)	0.0014(6)
O9	0.0052(9)	0.013(2)	0.010(2)	-0.0024(9)	0	0
O10	0.0054(7)	0.0135(9)	0.0099(8)	0.0008(7)	0.0020(6)	0.0008(6)
O11	0.004(2)	0.014(2)	0.009(2)	-0.0014(9)	0	0
O12	0.0087(7)	0.0105(8)	0.0095(8)	0.0007(7)	0.0034(6)	0.0004(6)
O13	0.006(2)	0.013(2)	0.009(2)	-0.001(2)	0	0
O14	0.0057(7)	0.0119(9)	0.0080(8)	0.0006(7)	0.0005(6)	0.0017(6)
O15	0.0090(7)	0.0127(9)	0.0100(8)	-0.0020(7)	0.0010(6)	0.0005(6)
O16	0.0060(8)	0.016(2)	0.0090(8)	0.0019(7)	0.0009(6)	0.0007(6)
O17	0.005(2)	0.012(2)	0.010(2)	-0.0004(9)	0	0
O18	0.0052(7)	0.0093(8)	0.0109(8)	0.0003(7)	0.0023(6)	-0.0003(6)
O19	0.0075(7)	0.0097(8)	0.0071(7)	0.0009(6)	0.0004(5)	0.0005(6)
O20	0.0067(8)	0.0102(9)	0.0072(8)	0.0001(6)	-0.0012(6)	-0.0009(6)
O21	0.0081(7)	0.0111(9)	0.0064(8)	0.0008(7)	0.0003(6)	0.0000(5)
O22	0.0043(7)	0.0101(9)	0.0094(8)	0.0003(6)	0.0004(6)	0.0001(6)
O23	0.0020(9)	0.014(2)	0.010(2)	-0.0011(9)	0	0
O24	0.0078(9)	0.017(2)	0.012(2)	-0.001(2)	0	0
O25	0.011(2)	0.015(2)	0.015(2)	-0.001(2)	0	0
O26	0.007(2)	0.012(2)	0.009(2)	0.0009(9)	0	0

4.1.8.3 Crystal Structure Description

Figure 4.59 gives a view of the non-centrosymmetric crystal structure of $M_3B_{11}O_{19}OH$ (M = Fe, Co) along [100]. The high-pressure phase is built up from corrugated multiple layers, consisting of corner-sharing BO_4-tetrahedra. Figure 4.60 shows one layer along the [001]-direction. The layers are interconnected

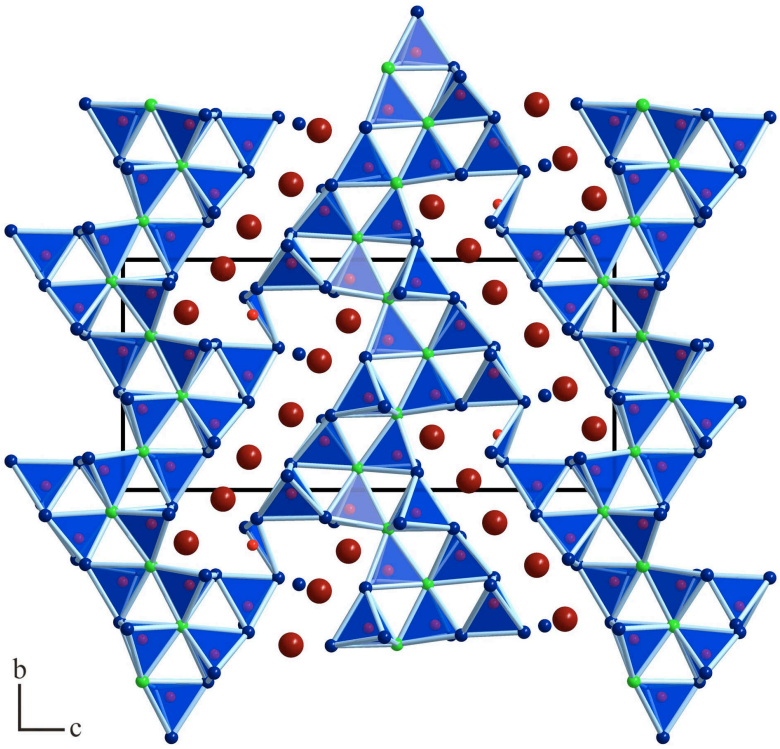

Figure 4.59: Crystal structure of $M_3B_{11}O_{19}OH$ (M = Fe, Co) along [100], exhibiting corrugated multiple layers of corner-sharing BO_4-tetrahedra. The layers are linked *via* BO_3-groups. $O^{[2]}$: blue spheres, $O^{[3]}$: green spheres, B: red spheres, M: dark red spheres.

to a network structure *via* non-planar, flat pyramidal BO_3-groups, generating Z-

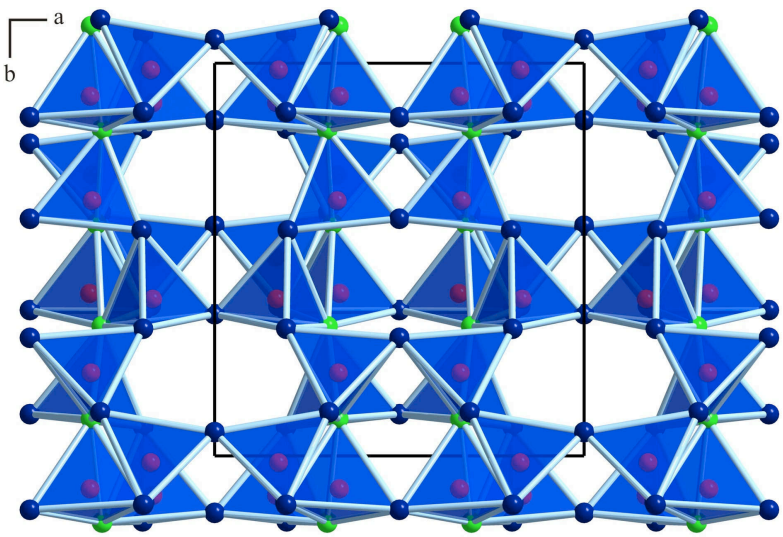

Figure 4.60: One layer in the structure of $M_3B_{11}O_{19}OH$ (M = Fe, Co) along [001]. Blue spheres represent $O^{[2]}$, green spheres $O^{[3]}$, and red spheres B^{3+}.

shaped channels in which the cations are arranged (Figure 4.59). The orientation of these connecting BO_3-groups clarifies the non-centrosymmetry of this structure, because all boron atoms B11 are deflected in the $[00\bar{1}]$-direction. The non-planar BO_3-groups (B11) can be considered as a transition state between a planar BO_3-group and a tetrahedral BO_4-group, because there exists one additional oxygen atom (O16) at a distance to B11 $<$ 190 pm (ECoN values: Co: 0.259, Fe: 0.026). Figure 4.61 shows one of these transition state borate groups, together

with the adjacent BO_4-tetrahedron. The thermal ellipsoids (drawn with 50% probability) of B11 and O16 show that both atoms swing parallel to their connecting line b, which strengthens the assumption of a transition state between a planar BO_3-group and a BO_4-tetrahedron. Table 4.44 lists the distances B11–O16 in comparison to the distance B8–O16 inside of the adjacent BO_4-group as well as the deflection **c** of B11 from the trigonal plane spanned by O2, O15, and O24. Such non-planar BO_3-groups can also be found in several other borates, *e.g.* $M_3(BO_3)_2$ (M = Mn, Mg, Co, Ni) [321] or CaB_2O_4–III [322]. It is noteworthy that the distance between O16 and B8 in the adjacent BO_4-tetrahedron is larger than the average B–O bond-length of 147.6 pm [232, 233] as well, thus building an extremly distorted tetrahedron.

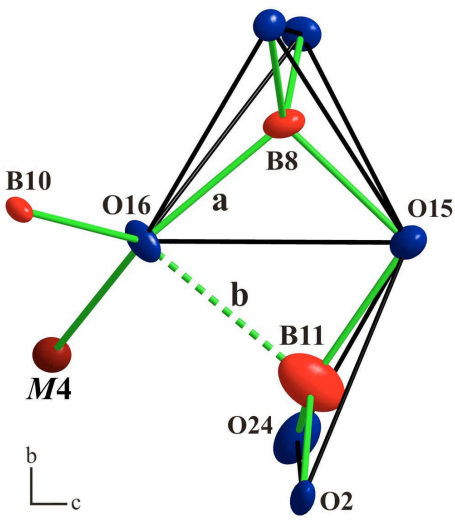

Figure 4.61: Coordination spheres of boron atoms B11, B8 and oxygen atom O16 along [100] drawn with 50% thermal ellipsoids. Distances **a** and **b** see Table 4.44.

Table 4.44: Interatomic distances/pm of O16 to B8 (**a**) and B11 (**b**) and the deflection/pm of B11 from the plane of oxygen-atoms O2, O15, O24 (**c**) in $M_3B_{11}O_{19}OH$ (M = Fe, Co) (see Figure 4.61).

	a	**b**	**c**
$Fe_3B_{11}O_{19}OH$	157.7(6)	188.7(6)	54.2(6)
$Co_3B_{11}O_{19}OH$	160.5(5)	169.8(5)	47.6(5)

Comparably large B–O-distances to the additional fourth oxygen-atom, as observed at the B11–O16-bond in $M_3B_{11}O_{19}OH$ (M = Fe, Co), can only be found in boracites at the fourfold coordinated oxygen atom (Figure 4.62, page 115). Table 4.45 lists these $B{-}O^{[4]}$-distances as well as the deflection of the boron atom from the trigonal plane in some cubic boracites. In $M_3B_{11}O_{19}OH$ (M = Fe, Co) the according oxygen-atom O16, participating at the long B–O-distances, is also surrounded by four atoms (B8, B10, B11, $M4$; Figure 4.61).

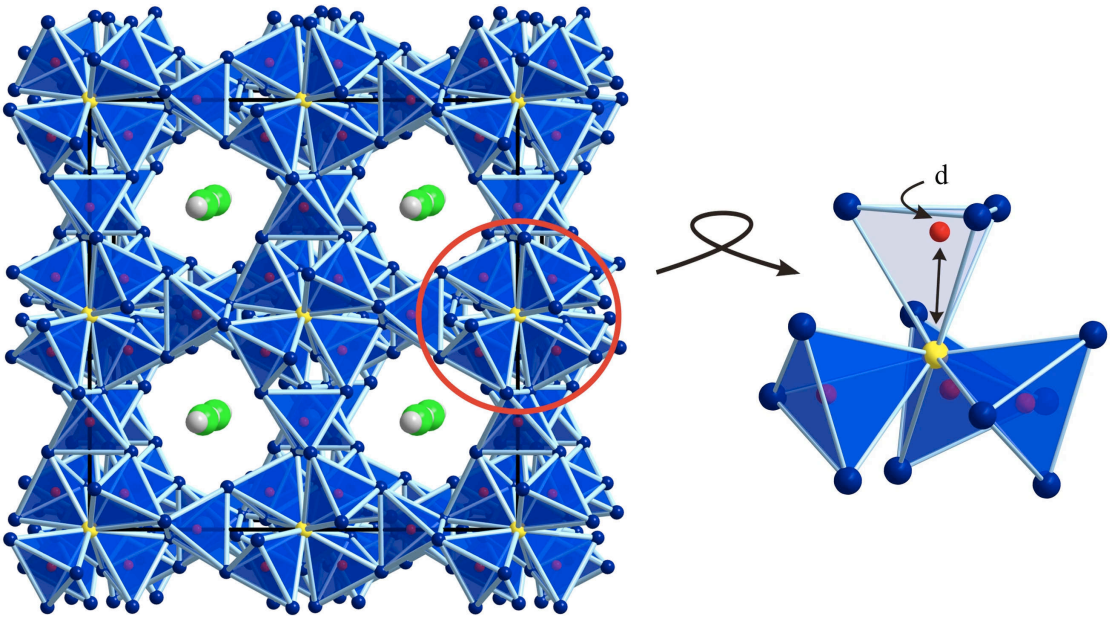

Figure 4.62: Crystal structure of cubic boracite $Mg_3B_7O_{13}Cl$ (left) and an enlarged starlike shaped building block (right). White spheres represent Mg^{2+}, green spheres Cl^-, red spheres B^{3+}, blue spheres $O^{[2]}$, and yellow spheres $O^{[4]}$.

Table 4.45: B-$O^{[4]}$-distances/pm and deflection from the plane **d**/pm in some cubic boracites ($F\bar{4}3c$) [323] (see Figure 4.62).

	B-$O^{[4]}$	**d**
$Mg_3[B_7O_{13}]Cl$	169.3	41.1
$Cr_3[B_7O_{13}]Cl$	168.1	40.6
$Ni_3[B_7O_{13}]Cl$	167.5	38.9

Comparing these B–$O^{[4]}$ distances of boracites to the here described phases, one can notice that the distance between B11 and O16 in $Co_3B_{11}O_{19}OH$ (169.8 pm) is comparable to the B–$O^{[4]}$ bond length in $Mg_3B_7O_{13}Cl$ (169.3 pm). In the Fe-phase however, the B11–O16 distance is about 20 pm longer (188.7 pm). Factoring the ECoN values of this "bond" into the discussion, it is conspicuous that the value of $Co_3B_{11}O_{19}OH$ is nearly 10 times the size of the value of $Fe_3B_{11}O_{19}OH$ (Co: 0.259, Fe: 0.026). This may indicate that the transition state borate group in $Co_3B_{11}O_{19}OH$ tends more to a BO_4-group than in $Fe_3B_{11}O_{19}OH$.

In this sense the flat pyramidal BO_3-group can be described as distorted tetrahedron, whereby an edge-sharing B_2O_6-unit is created. These units are linked to adjacent B_2O_6-units by common edges, forming "Vierer" rings (consisting of four tetrahedral centres) [39] (Figure 4.63). Such a structural element was not observed in borate chemistry before.

The hydrogen atom is presumably located at oxygen atom O25, because this atom shows a reduced value in the bond-length/bond-strength calculation. The

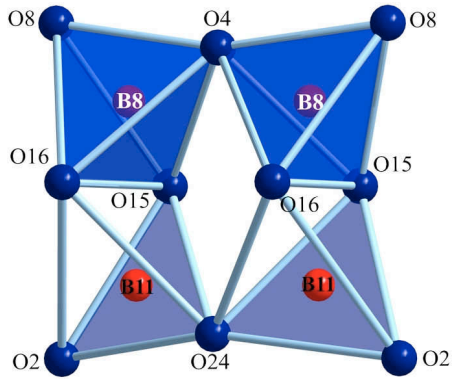

Figure 4.63: BO_3-group (B11) shown as edge-sharing BO_4-group resulting in a "Vierer" ring consisting of two pairs of edge-sharing tetrahedra.

O–H bond in $M_3B_{11}O_{19}OH$ (M = Fe, Co) is located at oxygen-atom O25 with a distance of 98(2) (Co) and 95(2) pm (Fe) (Figure 4.64). O25 shows no bonds to boron-atoms but is coordinated by $M1$ and $M5$ (M = Fe, Co). Furthermore hydrogen bridges can be assumed between the H-atom and adjacent O-atoms. In the case of $Co_3B_{11}O_{19}OH$, the next O^{2-} ion is O26 with a distance of 243.6 pm (green dashed line in Figure 4.64 right). The distances to the oxygen ions O2 show a value of 254.1 pm (red dashed lines in Figure 4.64 right). The hydrogen bridges in $Fe_3B_{11}O_{19}OH$ reveal values of 243.6 pm for H···O2 and 251.8 pm for the distance H···O26. Comparable distances of hydrogen bridges can be found in $Co(OH)_2$ (244.58 pm) [324]. Figure 4.64 clarifies the location of the hydrogen atom.

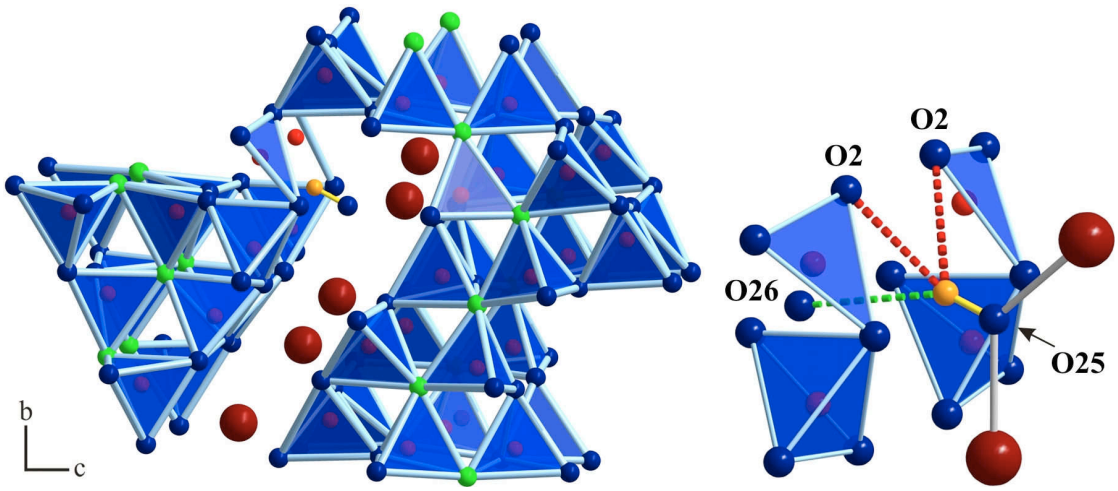

Figure 4.64: Position of the hydrogen-atom in $M_3B_{11}O_{19}OH$ (M = Fe, Co). $O^{[2]}$: blue spheres, $O^{[3]}$: green spheres, B: red spheres, and H: orange sphere. **Left**: View along [100]. **Right**: View along [001]. Red dashed lines represent hydrogen bridges.

The B–O bond-lengths for B1 to B10 in $M_3B_{11}O_{19}OH$ (M = Fe, Co) vary between 142.1 and 159.5 pm in $Fe_3B_{11}O_{19}OH$ and 141.2 – 160.5 pm in $Co_3B_{11}O_{19}OH$ with average B–O bond-lengths of 148.0 pm for $Fe_3B_{11}O_{19}OH$ and 147.8 pm for $Co_3B_{11}O_{19}OH$. This is consistent with the known average value of 147.6 pm for borates [232, 233]. The B–O-distances in the flat pyramidal arrange-

ment for B11 amount 142.0(5), 147.1(5), and 149.1(5) pm with a mean value of 146.1 pm for $Fe_3B_{11}O_{19}OH$. In the case of $Co_3B_{11}O_{19}OH$ distances of 142.4(4), 147.0(3), and 147.8(4) pm are found with a mean value of 145.7 pm. The longer distance to O16 shows values of 188.7(6) pm in $Fe_3B_{11}O_{19}OH$ and 169.8(4) pm in $Co_3B_{11}O_{19}OH$. The mean B–O-distances for the pyramidal BO_3-groups are much longer than the average B–O-bond-length in BO_3-groups of 137.0 pm [323] pm. The O–B–O angles in the 10 crystallographically independent BO_4-tetrahedra for B1 to B10 range between 96.6 and 114.0° with a mean value of 109.4° in $Fe_3B_{11}O_{19}OH$ and between 92.3 and 114.0° with a mean value of 109.4° in $Co_3B_{11}O_{19}OH$. The angles in the transition state borate groups of B11 go from 116.3 to 119.8° and from 113.3 to 117.2° for the model of the flat pyramid, and from 84.3 to 119.8° and 89.0 to 117.2° for the model of the distorted tetrahedral arrangement in $Fe_3B_{11}O_{19}OH$ and $Co_3B_{11}O_{19}OH$, respectively. 2/3 of the metal ions are coordinated octahedrally by six oxygen-atoms ($M1$, $M3$, $M4$, $M5$; M = Fe, Co) (Figure 4.65 right) and 1/3 are surrounded by four oxygen-atoms in a distorted tetrahedral way ($M2$, $M6$; M = Fe, Co) (Figure 4.65 left) with an additional fifth long contact to O6 ($M2$; ECoN values 0.161, Fe: 0.059) and O23 ($M6$; ECoN values Co: 0.071, Fe: 0.043) (Figure 4.66). This can also be noticed in CoB_4O_7 [200]. The Fe–O distances for

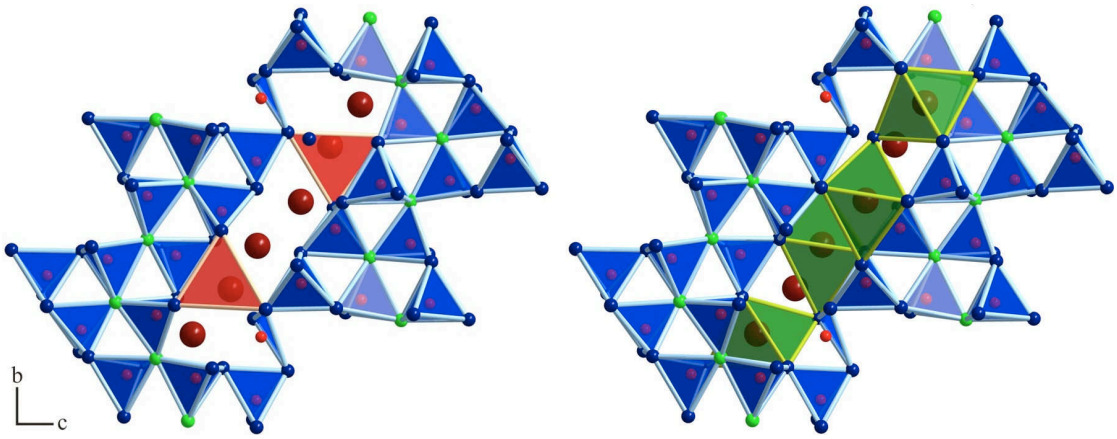

Figure 4.65: Left: Tetrahedral coordination spheres of $M2$ and $M6$ in $M_3B_{11}O_{19}OH$ (M = Fe, Co). **Right**: Octahedral coordination spheres of $M1$, $M3$, $M4$, and $M5$ in $M_3B_{11}O_{19}OH$ (M = Fe, Co).

the sixfold coordinated metal cations range from 205.8(4) to 254.7(4) pm with a mean value of 216.0 pm. This value is slightly higher than the average Fe–O distance of sixfold coordinated iron atoms in $Fe^{II}Fe_2^{III}(BO_4)O_2$ (203.8 pm) [193, 194] or in $FeBO_3$ (202.8 pm) [170]. For the fourfold coordinated Fe atoms, the Fe–O bond-lengths range from 198.5(4) to 214.1(4) pm with a mean value of 206.1 pm. This is longer than the mean Fe–O-bond distance of 199.3 pm in $Fe_2^{II}Mo_3^{IV}O_8$ exhibiting $Fe^{II}O_4$-tetrahedra as well [325]. In the Co-compound the bond-lengths of the sixfold coordinated cations vary from 200.3(3) to 250.0(3) pm with an average

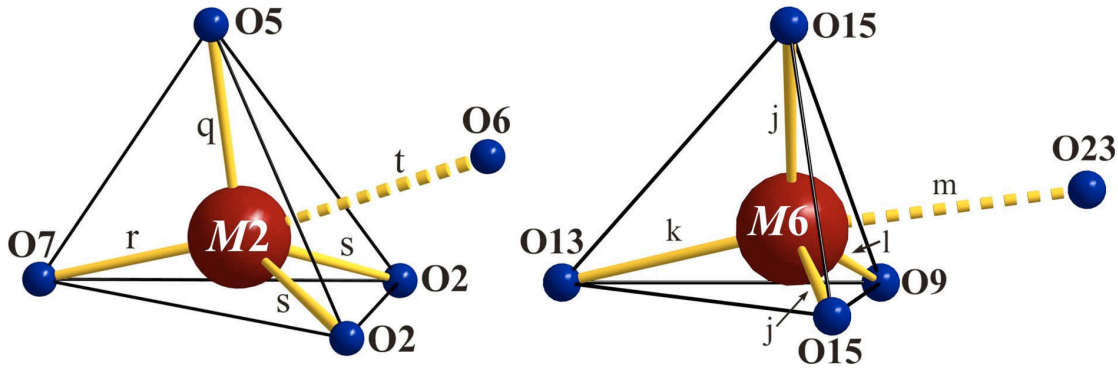

Figure 4.66: Coordination spheres of the M^{2+} ions $M2$ and $M6$ in $M_3B_{11}O_{19}OH$ (M = Fe, Co) with an additional fifth oxygen atoms. Distances **q**, **r**, **s**, **t**, **j**, **k**, **l**, **m**: see Tables 4.46 and 4.47.

value of 212.8 pm. This value is in agreement with the average Co^{2+}–O distance of sixfold coordinated cobalt atoms of 212.2 pm found in $Co_2B_2O_5$ [200]. In the tetrahedral coordination polyhedra, the Co–O distances range from 194.8(3) to 213.3(3) pm with a mean value of 203.0 pm. This agrees to the average Co–O distances of 202.7 pm in CoB_4O_7 [200] and is slightly higher than the average value of 198.4 pm in $Co_4(BO_2)_6O$ [200], which both reveal Co^{2+} in fourfold coordination.

Table 4.46: Interatomic distances/pm in $Fe_3B_{11}O_{19}OH$ (space group $Pmn2_1$) calculated with the single crystal lattice parameters (standard deviations in parentheses). Distances **q**, **r**, **s**, **t**, **j**, **k**, **l**, **m**: see Figure 4.66.

Fe1-O1	2×	212.5(3)	Fe2-O7 (**r**)		201.2(4)	Fe3-O3	2× 214.5(3)
Fe1-O6		217.7(3)	Fe2-O2 (**s**)	2×	207.0(3)	Fe3-O14	2× 216.0(3)
Fe1-O25		218.4(4)	Fe2-O5 (**q**)		208.9(3)	Fe3-O4	221.4(4)
Fe1-O8	2×	221.3(3)			Ø =206.0	Fe3-O24	254.7(4)
		Ø = 217.3	Fe2-O6 (**t**)		258.6(4)		Ø = 222.9
Fe4-O17		205.8(4)	Fe5-O11		209.2(4)	Fe6-O9 (**l**)	198.5(4)
Fe4-O18	2×	206.8(3)	Fe5-O10	2×	209.7(3)	Fe6-O15 (**j**)	2× 206.1(3)
Fe4-O16	2×	213.9(3)	Fe5-O12	2×	211.4(3)	Fe6-O13 (**k**)	214.1(4)
Fe4-O24		223.0(4)	Fe5-O25		219.7(4)		Ø = 206.2
		Ø = 211.7			Ø= 211.9	Fe6-O23 (**m**)	261.1(4)

Table 4.47: Interatomic distances/pm in $Co_3B_{11}O_{19}OH$ (space group $Pmn2_1$) calculated with the single crystal lattice parameters (standard deviations in parentheses). Distances **q**, **r**, **s**, **t**, **j**, **k**, **l**, **m**: see Figure 4.66.

Co1-O1	2×	207.2(2)	Co2-O7 (**r**)		200.1(3)	Co3-O14	2× 210.8(2)
Co1-O25		216.8(3)	Co2-O5 (**q**)		202.5(3)	Co3-O3	2× 211.1(2)
Co1-O8	2×	217.6(2)	Co2-O2 (**s**)	2×	203.7(2)	Co3-O4	222.7(3)
Co1-O6		218.3(3)			Ø = 202.5	Co3-O24	250.0(3)
		Ø = 214.1	Co2-O6 (**t**)		242.6(3)		Ø = 219.4
Co4-O17		200.3(3)	Co5-O10	2×	207.3(2)	Co6-O9 (**l**)	194.8(3)
Co4-O18	2×	202.3(2)	Co5-O11		208.0(3)	Co6-O15 (**j**)	2× 202.8(2)
Co4-O16	2×	215.3(2)	Co5-O12	2×	209.9(2)	Co6-O13 (**k**)	213.3(3)
Co4-O24		217.3(3)	Co5-O25		211.3(3)		Ø = 203.4
		Ø = 208.8			Ø = 209.0	Co6-O23 (**m**)	252.0(3)

4.1.8.4 Theoretical Calculations

Additionally, we calculated bond-valence sums for $M_3B_{11}O_{19}OH$ (M = Fe, Co) with the help of the bond-length/bond-strength concept (Tables 4.48 and 4.49) [164, 165]. The CHARDI concept [167] could not be used, because there was no program available for handling more than 20 anions. The formal ionic charges of the atoms, acquired by X-ray structure analysis, were in agreement within the limits of the concept, with exception of O25, to which the hydrogen is bound to. Due to not knowing the real O–H distance, it is not possible to generate the exact bond-valence sum. The undersized value may indicate that the chosen O–H-distance might be to long.

Table 4.48: Charge distribution in $Fe_3B_{11}O_{19}OH$ calculated with the bond-length/bond-strength concept.

Fe1	Fe2	Fe3	Fe4	Fe5	Fe6			H1				
+1.84	+1.76	+1.67	+2.16	+2.13	+1.67			+0.98				
B1	B2	B3	B4	B5	B6	B7	B8	B9	B10	B11[4]	B11[3]	
+3.02	+2.96	+2.94	+2.96	+3.08	+3.07	+3.00	+2.98	+3.04	+2.96	+2.61	+2.36	
O1	O2	O3	O4	O5	O6	O7	O8	O9	O10	O11	O12	O13
-1.95	-1.92	-1.93	-1.91	-1.93	-1.84	-2.07	-1.94	-2.12	-1.96	-2.02	-2.01	-1.91
O14	O15	O16	O17	O18	O19	O20	O21	O22	O23	O24	O25	O26
-1.85	-1.89	-1.92	-2.02	-2.00	-2.12	-1.90	-2.08	-1.86	-1.71	-1.90	-1.56	-1.74

Furthermore, we calculated the MAPLE values (Madelung Part of Lattice Energy) [161–163] for $M_3B_{11}O_{19}OH$ (M = Fe, Co) in order to compare them with MAPLE values of the high-pressure modification B_2O_3-II, H_2O, and the binary components FeO (Wuestit) and CoO, respectively. The foundation therefore is the additive potential of the MAPLE values, by which it is possible to calculate hypothetical values for $M_3B_{11}O_{19}OH$ (M = Fe, Co), starting from the binary oxides. Resultant we obtained a value of 137379 kJ·mol^{-1} for $Fe_3B_{11}O_{19}OH$ in comparison

Table 4.49: Charge distribution in $Co_3B_{11}O_{19}OH$ calculated with the bond-length/bond-strength concept.

Co1	Co2	Co3	Co4	Co5	Co6			H1				
+1.79	+1.75	+1.63	+2.08	+2.04	+1.71			+0.93				
B1	B2	B3	B4	B5	B6	B7	B8	B9	B10	B11[4]	B11[3]	
+3.03	+2.93	+2.97	+2.99	+3.10	+3.10	+3.02	+2.97	+3.05	+2.98	+2.79	+2.38	
O1	O2	O3	O4	O5	O6	O7	O8	O9	O10	O11	O12	O13
-1.96	-1.94	-1.93	-1.93	-1.98	-1.89	-2.03	-1.93	-2.12	-1.94	-1.96	-1.97	-1.85
O14	O15	O16	O17	O18	O19	O20	O21	O22	O23	O24	O25	O26
-1.86	-1.88	-1.93	-2.03	-2.03	-2.15	-1.95	-2.10	-1.92	-1.68	-1.92	-1.53	-1.79

to 136634 kJ·mol^{-1} (deviation: 0.5%), starting from the binary oxides (3 × FeO (4489 kJ·mol^{-1}) + 5.5 × B_2O_3-II (21938 kJ·mol^{-1}) + 0.5 H_2O (hexagonal ice) [326] (5017 kJ·mol^{-1})). For $Co_3B_{11}O_{19}OH$ we received a value of 137848 kJ·mol^{-1} in comparison to 136848 kJ·mol^{-1} (deviation: 0.07%), starting from the binary oxides (3 × CoO (4560 kJ·mol^{-1}) + 5.5 × B_2O_3-II (21938 kJ·mol^{-1}) + 0.5 H_2O (hexagonal ice) [326] (5017 kJ·mol^{-1})).

4.1.9 The Borate "$Fe_3B_7O_{12}N$"

4.1.9.1 Synthesis

The synthesis of "$Fe_3B_7O_{12}N$" raises a big problem, since it is still not clear under which conditions the phase can be obtained. In the majority of cases it appeared as a by-product during the synthesis of other iron borates. The lack of knowledge of the explicit formula, concerning the O and N content, pointed another problem to solve. Specific trials of the preparation of "$Fe_3B_7O_{12}N$" led to the application of different reagents as BN, NaN_3, or $FeCl_2$. The best result was obtained by adding $FeCl_2$ to the oxide mixture in the ratio Fe_2O_3 : B_2O_3 : $FeCl_2$ = 2.5 : 7 : 1 utilizing a high-pressure/high-temperature reaction (7.5 GPa, 1100 °C). As no chlorine could be found in the crystals of "$Fe_3B_7O_{12}N$", it is assumed that $FeCl_2$ acts as a flux. Presumably the BN-crucible is the nitrogen source in this synthesis. For the synthesis of "$Fe_3B_7O_{12}N$", the 18/11 assembly was compressed to 7.5 GPa within 180 min. After reaching this pressure the sample was heated up to 1100 °C at constant pressure during the following 10 min. Having stayed at this temperature for 5 min, the sample was cooled down to ca. 750 °C in another 15 min and then quenched to room temperature by switching off the heating, followed by a decompression period of 540 minutes. Afterwards, the recovered MgO-octahedron was cracked and the sample carefully separated from the surrounding boron nitride crucible. The compound "$Fe_3B_7O_{12}N$" was obtained in form of air- and water-resistant, light blue crystals. Figure 4.67 shows the sample of "$Fe_3B_7O_{12}N$" , which was synthesized with $FeCl_2$ as flux.

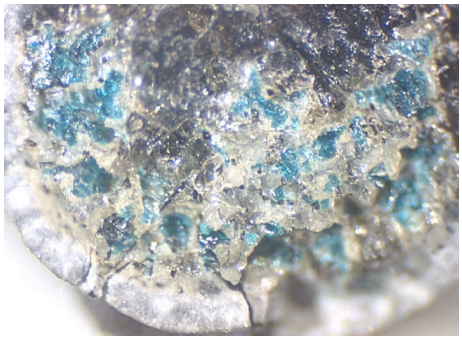

Figure 4.67: Blue crystals of "$Fe_3B_7O_{12}N$".

4.1.9.2 Crystal Structure Analysis

A light blue, cubic crystal of "$Fe_3B_7O_{12}N$" was isolated by mechanical fragmentation and examined by means of a Buerger camera, equipped with an image plate system (Fujifilm BAS-2500) in order to check its suitability for intensity data collection. Single crystal intensity data of "$Fe_3B_7O_{12}N$" were measured with a STOE IPDS I area detector diffractometer (MoK_α, λ = 71.073 pm). A numerical absorption correction was applied (HABITUS [132]).

The determination of the metrics yielded a cubic F centred unit cell. The Laue symmetry $m\bar{3}m$ and systematically absent reflections hhl with $h,l = 2n$ indicated

the possible space groups $F\overline{4}3c$ and $Fm\overline{3}c$. As no solution could be obtained by *Direct methods*, the structure was solved by trial and error. Taking into account the multiplicity of the Wyckoff positions in an F centred unit cell with $m\overline{3}m$ Laue symmetry it is clear that the maximum multiplicity of an iron site can be 24 as otherwise an unreasonably high density of > 4 g/cm^3 would result. Placing Fe on the $24c$ site $(0\ \frac{1}{4}\ \frac{1}{4})$ in $F\overline{4}3c$ yielded an R1 value of ≈ 0.25, and light atoms could be located from subsequent Fourier and difference Fourier syntheses. However, the displacement parameter of Fe indicated a strong deviation from the $24c$ site. Assuming a half occupied split position $48g$ $(\mathrm{x}\ \frac{1}{4}\ \frac{1}{4})$ with x ≈ 0.03 reduced the R values significantly. No additional symmetry could be found and the structure is clearly acentric, so that $Fm\overline{3}c$ can be excluded.

Details of the data collection and structure refinement are listed in Table 4.52. The positional parameters, anisotropic displacement parameters, interatomic distances, and interatomic angles are given in Tables 4.50–4.54.

Table 4.50: Atomic coordinates and equivalent isotropic displacement parameters $U_{\mathrm{eq}}/\mathrm{Å}^2$ of "$Fe_3B_7O_{12}N$" (space group $F\overline{4}3m$). U_{eq} is defined as one third of the trace of the orthogonalized U_{ij} tensor (standard deviations in parentheses).

Atom	Wyckoff-Position	x	y	z	Ueq
Fe	$48g$	0.0309(2)	3/4	3/4	0.0261(8)
B1	$24d$	0	3/4	0	0.011(2)
B2	$32e$	0.9208(6)	x	0.0792(6)	0.023(2)
O	$96h$	0.9770(2)	0.6821(2)	0.9035(2)	0.0146(8)
N	$8a$	0	0	0	0.018(2)

Table 4.51: Anisotropic displacement parameters of "$Fe_3B_7O_{12}N$" (standard deviations in parentheses).

Atom	U_{11}	U_{22}	U_{33}	U_{23}	U_{13}	U_{12}
Fe	0.036(2)	0.020(2)	0.022(2)	-0.004(2)	0	0
B1	0.010(2)	0.011(3)	0.010(2)	0	0	0
B2	0.023(2)	0.023(2)	0.023(2)	-0.013(3)	-0.013(3)	0.013(3)
O	0.016(2)	0.011(2)	0.017(2)	-0.003(2)	0.006(2)	-0.006(2)
N	0.018(2)	0.018(2)	0.018(2)	0	0	0

Table 4.52: Crystal data and structure refinement of "$Fe_3B_7O_{12}N$" (standard deviations in parentheses).

Empirical Formula	$Fe_3B_7O_{12}N$
Molar mass/g·mol^{-1}	449.23
Crystal System	cubic
Space group	$F\bar{4}3c$
Single crystal diffractometer	STOE IPDS-I
Radiation	MoK$_\alpha$ (λ = 71.073 pm)
Single crystal data	
a/pm	1222.4(2)
V/nm^3	1.826(4)
Formula units per cell	Z = 8
Temperature/K	293(2)
Calculated density/g·cm^{-3}	3.267
Crystal size/mm^3	0.068 × 0.096 × 0.122
Detector distance/mm	50.0
Exposure time/min	15.0
Absorption coefficient/mm^{-1}	4.785
F(000)/e	1728
θ range/°	4.7 – 30.2
Range in hkl	-7/+17, -17/+11, ±17
Total no. reflections	1928
Independent reflections	237 (R_{int} = 0.0357)
Reflections with I > 2σ(I)	211 (R_σ = 0.0192)
Data/parameters	237/22
Goodness-of-fit (F^2)	1.136
Final R indices (I > 2σ(I))	R1 = 0.0643
	wR2 = 0.1671
R indices (all data)	R1= 0.0643
	wR2 = 0.1699
Flack-parameter	-0.1(2)
Largest diff. peak, deepest hole/e·Å^{-3}	3.181/-0.713

4.1.9.3 Crystal Structure Description

The new phase "$Fe_3B_7O_{12}N$" is built up from starlike shaped units, consisting of four slightly distorted BO_3N-tetrahedra sharing one common edge. The bridging, fourfold coordinated position is presumably occupied by nitrogen, which is coordinated by four boron atoms in a tetrahedral way. These starlike shaped units are connected *via* additional, undistorted BO_4-tetrahedra to form a network structure. Figure 4.68 shows the cubic unit cell of "$Fe_3B_7O_{12}N$" along [100] with the starlike shaped unit highlightened in red and the connecting BO_4-tetrahedra in violet. The

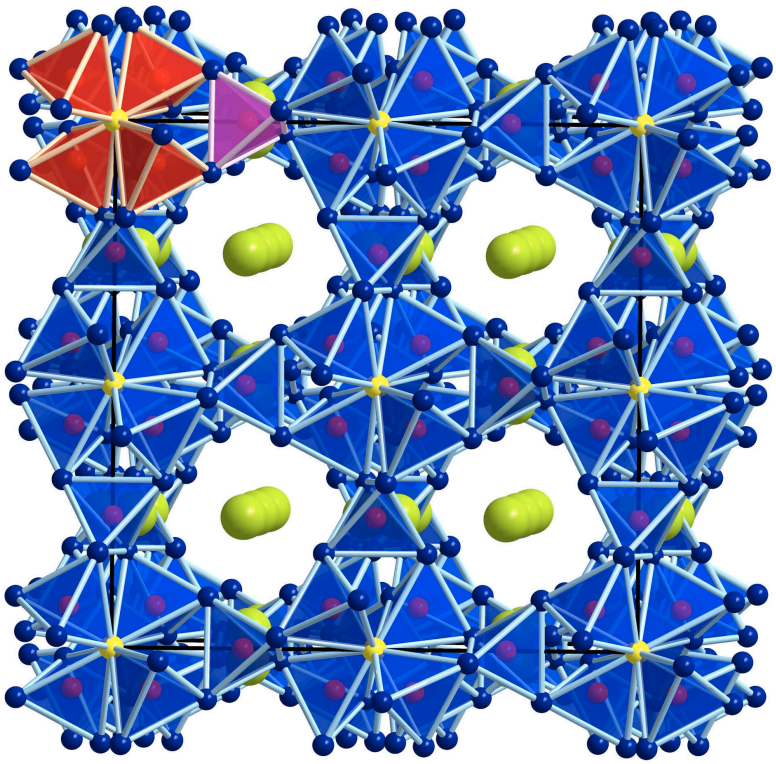

Figure 4.68: Unit cell of "$Fe_3B_7O_{12}N$" with view along [100]. Starlike shaped units are highlightened in red, connecting BO_4-tetrahedra in violet. Green spheres: Fe^{2+}, blue spheres: O^{2-}, yellow spheres: N^{3-}, red spheres: B^{3+}.

structure is crossed by channels built up of "Achter"-rings (rings consisting of eight tetrahedral centres) [39] in which the Fe cations are arranged. These channels have a diameter of ca. 410 pm and run along all three spatial directions, whereas a porous network is generated (Figure 4.68). The iron cations are located on a split position. This might be due to multiple pseudo-merohedral twinning, however, trial refinements did not yield a more satisfactory solution so far. Figure 4.69 points up the split position of Fe^{2+} (view along [011]) by colouring one iron cation on the split position green and the other one orange. Within the substance class of borates, the only compound revealing starlike shaped units is α- or high-boracite (space group $F\bar{4}3c$). In this case the fourfold position in the centre of the starlike building block is occupied by oxygen. Fourfold coordinated oxygen-atoms are very rare. The starlike shaped units in high-boracite are interconnected *via* additional BO_4-tetrahedra, thus showing the identical network of tetrahedra as

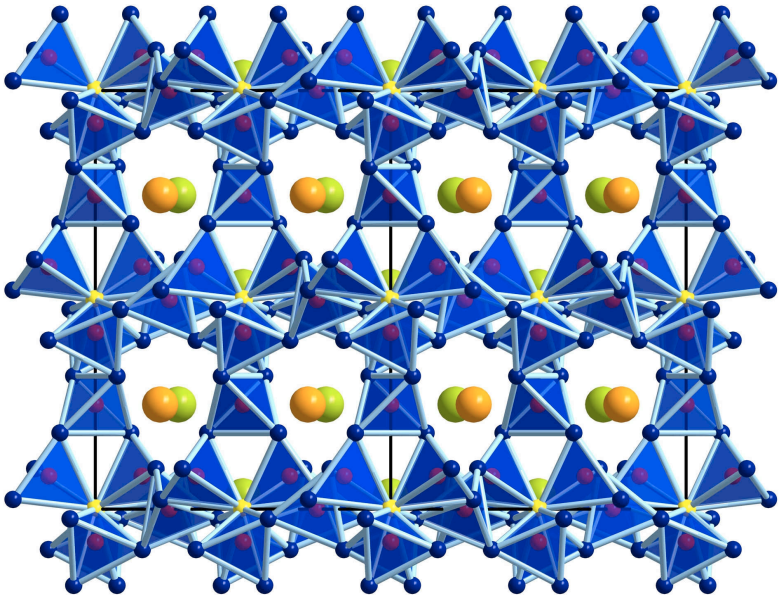

Figure 4.69: View of the crystal structure of "$Fe_3B_7O_{12}N$" along [110]. The iron cations on the split positions are coloured in green and orange.

found in "$Fe_3B_7O_{12}N$". Figure 4.70 shows the crystal structure of high-boracite. The notation boracite, which is actually used for more than 25 compounds, can be attributed to the mineral boracite $Mg_3B_7O_{13}Cl$ [327]. The general formula of boracite can be depicted as $M_3B_7O_{13}X$ with M = Mg, Cr, Fe, Co, Ni, Cu, Zn, Cd, and X = Cl, Br, I [327]. Occasionally, X could be OH, S, Se, Te, or F. Since cubic boracites are usually synthesized in closed quartz ampoules at elevated temperatures [327, 328], the assumption stands to reason, if cubic boracite might be a high-pressure phase. High-boracite even reveals the same space group as "$Fe_3B_7O_{12}N$", namely $F\bar{4}3c$, but shows a smaller cell volume of 1.772 nm^3. In accord with this, the diameter of the channels is a little bit smaller (405 pm) as well. In both compounds the cations are positioned inside of the channels, whereas in boracite also Cl^- anions are arranged in the channels. These chlorides could not be detected in "$Fe_3B_7O_{12}N$", but would be thinkable.

Besides this very interesting and unique structure, boracites even reveal pyroelectricity [327, 329] (*e.g.* orthorhombic $Mg_3B_7O_{13}Cl$ [328]), piezoelectricity (e.g. cubic $Mg_3B_7O_{13}Cl$ [328]), dielectricity ($Cr_3B_7O_{13}Cl$ [330]), ferroelectricity, ferroelasticity, and partially ferromagnetism ($Fe_3B_7O_{13}I$ below 30 K [331]). Boracites have recieved special attention due to their unusual physical properties, that make them have potential applications: as optic stopper due to the modification in birefringence produced by the application of a mechanical strain, electric fields, electron beam, and/or a change in temperature [327, 332]; ferroelectric nonvolatile memory (ferroelectric random access memory, or FRAM) because of the reorientation of its ferroelectric domains [327, 333]; infrared (IR) detection due to the intrinsic pyroelectricity of the boracite [327, 334, 335].

Additionally, there also exist low-temperature modifications of boracite, which

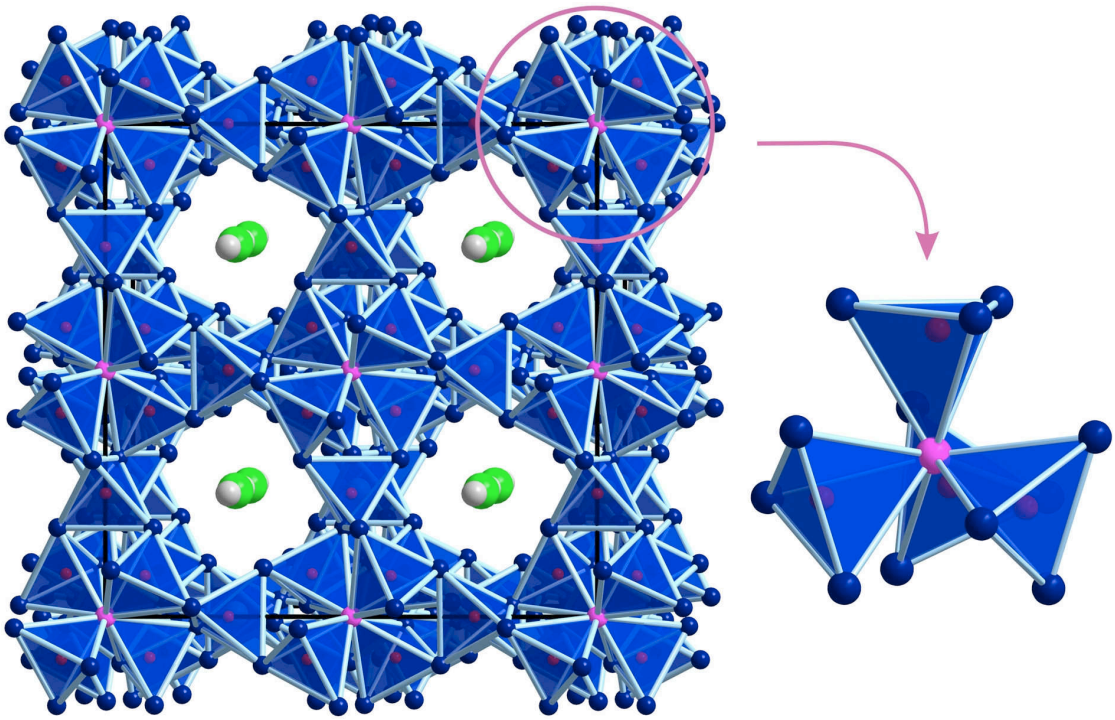

Figure 4.70: Crystal structure of high-boracite $Mg_3B_7O_{13}Cl$ along [100]. Mg^{2+} is shown as grey, Cl^- as green, $O^{[2]}$ as blue, $O^{[4]}$ as pink, and B^{3+} as red spheres.

reveal either orthorhombic (*e.g.* low- or β-$Mg_3B_7O_{13}Cl$, $Pca2_1$ [336]), trigonal (*e.g.* $Fe_3B_7O_{13}Cl$, $R3c$ [336, 337]), tetragonal (*e.g.* $Cr_3B_7O_{13}Cl$ [330], $P\bar{4}2_1c$), or monoclinic symmetry (*e.g.* $Fe_3B_7O_{13}I$ below 30 K [331]) depending on the elemental composition and the temperature. The crystal structure of orthorhombic boracites can be described on the basis structure of the cubic boracites. One of the four boron atoms, coordinating one common oxygen atom (O1), shifts from a tetrahedrally to a triangularly coordination (see Figure 4.71). This shift involves displacements of about 50 pm [338]. Concerning the trigonal boracites the displacement of the cubic can be described as follows: The fourfold coordinated oxygen atom (O1), one boron atom, and chlorine atoms lie on and are displaced along the one cubic threefold axis which is preserved in the trigonal structure. The metal cations lie on and are displaced along the cubic [100] directions, but the resultant of their displacement is along the threefold axis [336].

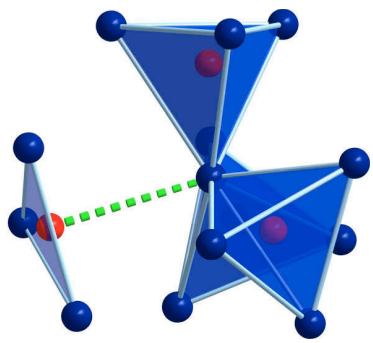

Figure 4.71: Structural element of orthorhombic $Mg_3B_7O_{13}Cl$.

Sueno *et al.* [338] considered the structure of high-temperature cubic boracite as an "average" of the orthorhombic structure variant. They discussed three models: 1) The cubic structure might be a true high-temperature structure with located atoms at distinctive positions with high thermal motion. 2) The cubic structure

might be a disordered space-time average of the different ferroelectric orientations of the orthorhombic structure. 3) A combination of 1) and 2). This model assumes the borate framework to have the normal elevated temperature vibrations with a stable configuration, whereas the metal cations and chlorine atoms are affected by disordering. The authors prefer the latter model because the only appreciable drop in the residual factor comes with splitting the Cl and Mg atoms, just as in "$Fe_3B_7O_{12}N$". Further on, it is described by different authors, that boracites crystals are obtained as twins. Ito *et al.* describe the crystal of low-$Mg_3B_7O_{13}Cl$, which they used for their powder diffraction experiments, as tiny, optically diversely orientated laminae and it was almost impossible to obtain a homogeneous slip free from twinning [339]. Their measurements permit an easy and perfect indexing on the basis of a cubic lattice. The transformation matrix from the cubic to orthorhombic (direct) axes were assigned to $\begin{pmatrix} \frac{1}{2} & \frac{1}{2} & 0 \\ \frac{1}{2} & \frac{1}{2} & 0 \\ 0 & 0 & 1 \end{pmatrix}$. Friedel described low-$Mg_3B_7O_{13}Cl$ as mimetic twin, composed of several individuals of varying shape and size [339] and Schmid observed two twinning "laws": head-head (tail-tail) domains with $\{110\}_{cub}$ as composition plane and head-tail domains with $\{100\}_{cub}$ as composition plane [340]. Considering this, our crystals of "$Fe_3B_7O_{12}N$" have to be examined very closely.

In "$Fe_3B_7O_{12}N$" iron is coordinated by four oxygen atoms nearly squarish planar or by an extremely distorted tetrahedron (see Figure 4.72). In this connection it is noteworthy that between the Fe^{2+} cations a big cavity is located, wich remains empty in the proposed structure (see Figure 4.73). In high-boracite the Cl^- ions are arranged at this position. In "$Fe_3B_7O_{12}N$" at this position a high electron density remains in the structure refinement, but no atom could be placed at this position. The Fe–O-distances range between 205.4(3) to 215.5(3) pm with a mean value of 210.5 pm, which is slightly higher than the average Fe–O distance of sixfold coordinated iron atoms found in $Fe^{II}Fe_2^{III}(BO_4)O_2$ (203.8 pm) or in $FeBO_3$ (202.8 pm). The B2–O-distance in the BO_3N-tetrahedra is 144.9(5) pm, whereas the B1–O-distance in the bridging BO_4-tetrahedra adds up to 147.0(3) pm, which agrees to the known average value of 147.6 pm for borates [232, 233]. Obviously, the B2–O bond-length inside the BO_3N-groups is smaller than the distances inside the BO_4-groups. The

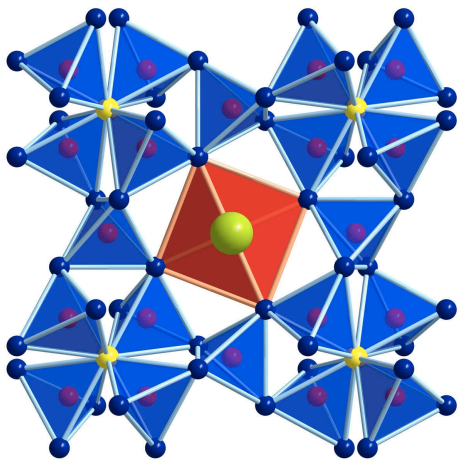

Figure 4.72: Coordination sphere of the Fe^{2+} cations in "$Fe_3B_7O_{12}N$" . Green spheres: Fe^{2+}, blue spheres: O^{2-}, yellow spheres: N^{3-}, red spheres: B^{3+}.

B2–N bond-length inside of the BO_3N-tetrahedra adds up to 168.0(2) pm, which is drastically longer than the B–O-distances inside of the same tetrahedra (see Table

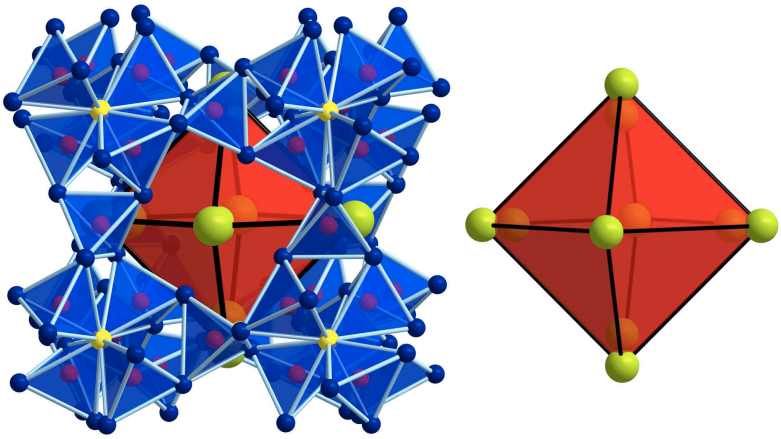

Figure 4.73: View of the cavity spanned by the Fe^{2+} cations inside of the crystal structure of "$Fe_3B_7O_{12}N$".

4.53). The B–N-distance in c-BN (cubic ZnS structure) shows a value of 156.5 pm [341], which is considerably shorter than the B–N-distance in "$Fe_3B_7O_{12}N$". Thereby it has to be considered that c-BN is composed of regular BN_4-tetrahedra, whereas "$Fe_3B_7O_{12}N$" possesses distorted BO_3N-tetrahedra. The O–B–O and O–B–N angles inside the tetrahedra show mean values of 109.9 and 109.3 °, respectively (Table 4.54). Drawing a comparison to cubic high-boracite $Mg_3B_7O_{13}Cl$, one can see slight differences in the bond-lengths inside the starlike shaped unit, whereas the bond distances inside bridging BO_4-groups coincide in both structures. The B2–O$^{[4]}$ ($Mg_3B_7O_{13}Cl$) distance accounts 169.3 pm [338] and the B2–N$^{[4]}$ bond length ("$Fe_3B_7O_{12}N$") adds up to 168.0 pm. Considering the B2–O$^{[2]}$ distances, also a small difference can be discovered ($Mg_3B_7O_{13}Cl$: 143.7 pm [338], "$Fe_3B_7O_{12}N$" : 144.9 pm). This tendency of smaller X–N$^{[4]}$ in comparison to X–O$^{[4]}$ distances was also observed by Schleid *et al.* in the related phases $La_4NS_3Cl_3$ [342] and $La_4OS_4Cl_2$ [343] with tetrahedrally La_4N and La_4O units, respectively. This is a known trend, also observed in other nitridosulfides and -oxides, showing the same coordination number of the O^{2-} and N^{3-} ions [342]. This appears to be feasable, due to the lower oxidation state (higher charge) of N^{3-}, but disagrees with the ionic radii given by Shannon ($r(O^{2-})$ = 138 pm, $r(N^{3-})$ = 146 pm for C.N. = 4) [344].

Table 4.53: Interatomic distances/pm in "$Fe_3B_7O_{12}N$" (space group $F\bar{4}3c$) calculated with the single crystal lattice parameters (standard deviations in parentheses).

Fe-Oa	205.4(3)	2 ×	B2-O	144.9(5)	3 ×
Fe-Ob	215.5(3)	2 ×	B2-N	168.0(2)	1 ×
	Ø = 210.5			Ø = 150.7	
B1-O	147.0(3)	4 ×	N-B2	167.0(2)	4 ×

Table 4.54: Interatomic angles/° in "$Fe_3B_7O_{12}N$" calculated with the single crystal lattice parameters (standard deviations in parentheses).

O-B1-O	108.6(2)	3 ×	O-B2-O	110.3(4)	3 ×
O-B1-O	111.2(2)	3 ×	O-B2-N	108.2(5)	3 ×
	Ø = 109.9			Ø = 109.3	

EDX measurements could prove the presence of iron, boron, and oxygen; the occurence of nitrogen could not be clearly evidenced though. Therefore future EELS measurements of this phase are essential to prove or disprove the presumed composition "$Fe_3B_7O_{12}N$".

Recently Stephanie Neumaier was able to synthesize "$Fe_3B_7O_{12}N$" nearly phase pure at conditions of 3 GPa and ca. 950 °C. The impurity consists simply of boron oxide, which is not detected in the diffraction pattern because of its amorphism. No other crystalline compound could be found in the sample. Comparing the powder diffractogram to other boracite like structures, one finds a clear accordance between the measured diffractogram and the diagram of $Fe_3B_7O_{13}Cl$. This compound formes red crystals [345], in contrast to the here investigated phase, which formes blue crystals.

4.1.9.4 Vibrational Spectroscopic Investigations

The Raman-spectrum of "$Fe_3B_7O_{12}N$" was measured at a single crystal with a Raman-microscope Horiba Jobin yvon HR800 (x50LWD), using a green laser (Melles Griot ion laser) with a wavelength of 514 nm (Figure 4.74).

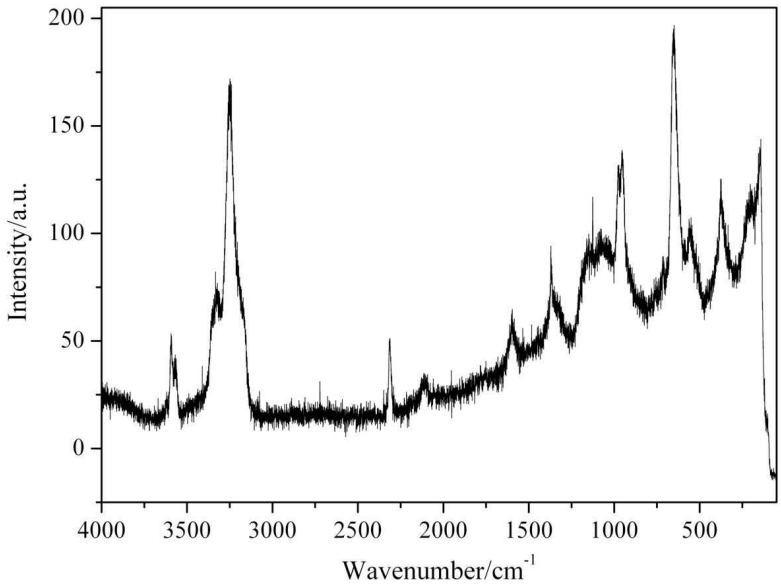

Figure 4.74: Raman-spectrum of "$Fe_3B_7O_{12}N$".

Due to the lack of knowledge concerning the real crystal structure the assignement of the bands could not be carried out until yet. Further investigations are still going on.

4.1.10 The Borate "$Co_3B_8O_{13}(OH)_4$"

4.1.10.1 Synthesis

Starting materials for the synthesis of "$Co_3B_8O_{13}(OH)_4$" were mixtures of B_2O_3 (Strem Chemicals, Newburyport, U.S.A., 99.9%) and Co_2O_3. The non-stoichiometric mixture, with ratio $B_2O_3 : Co_2O_3 = 11 : 3$, was filled into a boron nitride crucible of an 18/11 assembly. The origin of hydrogen in the compound "$Co_3B_8O_{13}(OH)_4$" can be found in the partially hydrolysis of the starting material B_2O_3. To simplify the reaction Equation 4.10 was written with H_2O instead of the hydrolysis product $B(OH)_3$.

$$3\,Co_2O_3 + 8\,B_2O_3 + 4\,H_2O \xrightarrow[800\ °C]{7.5\ GPa} 2\,Co_3B_8O_{13}(OH)_4 + 1.5\,O_2 \tag{4.10}$$

The assembly was compressed within 3 h to 7.5 GPa and heated to 800 °C in the following 10 min. After staying at this temperature for 5 min, the sample was cooled down to 500 °C in another 15 min. The sample was then quenched to room temperature by switching off the heating. After a decompression period of 9 h, the recovered octahedron was cracked, and the sample carefully separated from the surrounding boron nitride. "$Co_3B_8O_{13}(OH)_4$" was sustained as a coarsely crystalline, pink solid. The phase was obtained as a by-product in combination with violet $Co_3B_{11}O_{19}OH$ (section 4.1.8). "$Co_3B_8O_{13}(OH)_4$" is formed in the middle of the crucible, as shown in Figure 4.75. Therefore, it is presumed that pure "$Co_3B_8O_{13}(OH)_4$" can be synthesized at lower temperatures.

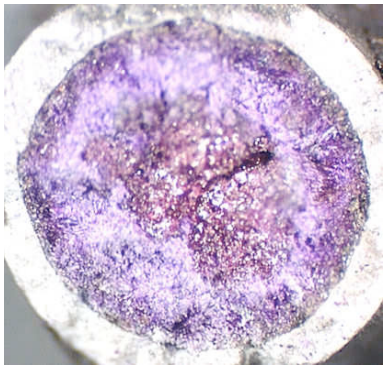

Figure 4.75: BN-crucible with violet $Co_3B_{11}O_{19}OH$ and pink "$Co_3B_8O_{13}(OH)_4$".

4.1.10.2 Crystal Structure Analysis

The powder diffraction pattern was obtained from a flat sample, utilizing a STOE Stadi P powder diffractometer with monochromated $MoK_{\alpha 1}$ radiation (λ = 71.073 pm). Due to the lack of phase purity of the sample, the powder diagram (Figure 4.76) could not be indexed. Reflections marked with asterisks could not be clearly assigned to any known phase in the system Co–B–O. Figure 4.76 shows a comparison of the experimental powder pattern to the pattern derived from single crystal data.

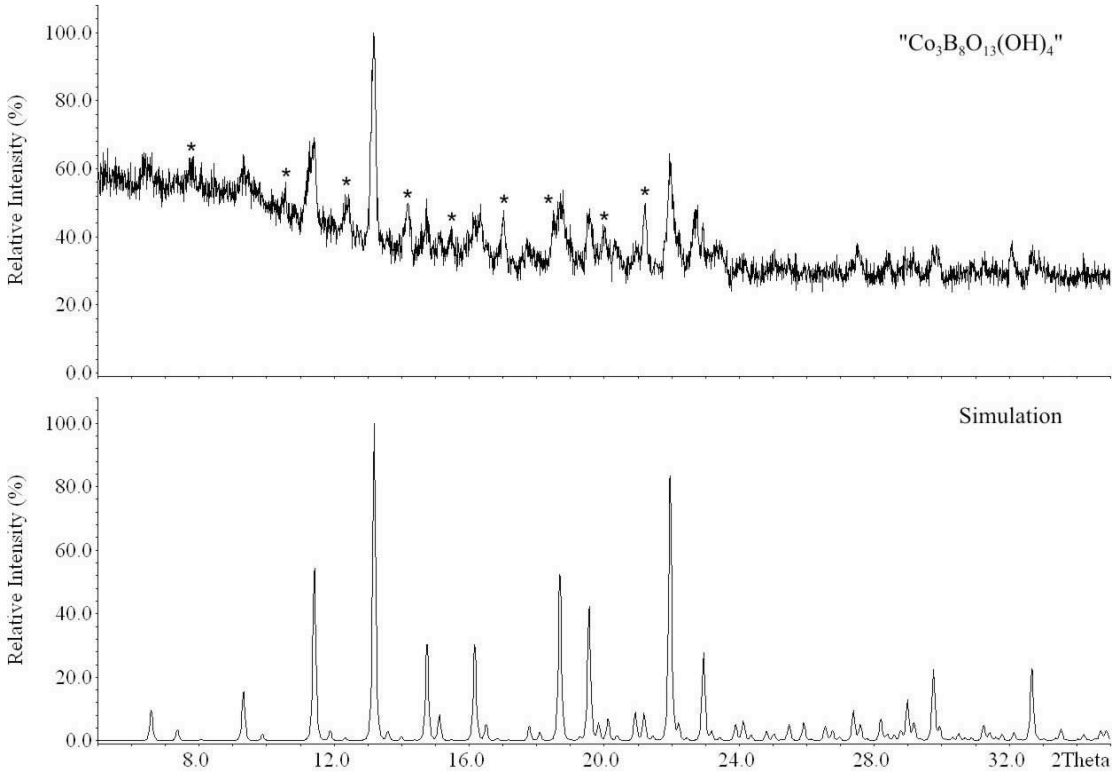

Figure 4.76: Measured (top) and simulated (single crystal data) (bottom) powder diffraction patterns of "$Co_3B_8O_{13}(OH)_4$".

Single crystals of "$Co_3B_8O_{13}(OH)_4$" were isolated by mechanical fragmentation and examined by means of Laue photographs on a Buerger camera equipped with an image plate system (Fujifilm BAS-2500) in order to check their suitability for intensity data collection. Single crystal intensity data of "$Co_3B_8O_{13}(OH)_4$" were measured with an Enraf-Nonius Kappa CCD diffractometer (MoK_α, λ = 71.073 pm) with graded multilayer X-ray optics. A semi empirical absorption correction was applied to the data (SCALEPACK [133]). The determination of the metrics yielded a cubic F centred unit cell. The Laue symmetry $m\overline{3}m$ and systematically absent reflections hhl with $h,l = 2n$ indicated the possible space groups $F\overline{4}3c$ and $Fm\overline{3}c$. As no structure solution could be obtained by direct methods or charge flipping, the structure was solved in $P1$ using SIR 2004 [137]. The approximate refinement provided a R1-value of 18%. The ADDSYM routine of the program PLATON revealed the space group Cc. As the Laue symmetry is $m\overline{3}m$, the corresponding structure model must be refined taking into account a twin with twelve twin domains. The refinement led to a residual of R1 = 5%. A repeated search for higher symmetry displayed $R3c$ to be the correct space group. The structure could then be refined in $R3c$ with the help of a twin consisting of four twin domains. Electrostatic considerations suggest the presence of hydrogen, leading to the presumed formula "$Co_3B_8O_{13}(OH)_4$". Bond-valence calculations suggest that hydrogen bonds to the oxygen atoms of isolated BO_4-tetrahedra. The structural data

will be elaborated in the following sections. The lengths of the oxygen-hydrogen bonds were restrained to 88 pm in accordance to the bond-length between oxygen and hydrogen in $[B(OH)_4]^-$ of teepleite $Na_2[B(OH)_4]Cl$ (88(5) pm) [346]. Details of the data collections and structure refinements are listed in Table 4.55. The positional parameters, anisotropic displacement parameters, interatomic distances, and interatomic angles are given in Tables 4.56 – 4.59.

Table 4.55: Crystal data and structure refinement of "$Co_3B_8O_{13}(OH)_4$" (standard deviations in parentheses).

Empirical Formula	"$Co_3B_8O_{13}(OH)_4$"
Molar mass/g·mol^{-1}	539.17
Crystal system	trigonal
Space group	$R3c$
Single crystal diffractometer	Enraf-Nonius Kappa CCD
Radiation	MoK$_\alpha$ (λ = 71.073 pm)
Single crystal data	
a/pm	1747.4(2)
c/pm	2140.1(2)
Volume/nm^3	5.659
Formula units per cell	Z = 24
Temperature/K	293
Calculated density/g·cm^{-3}	3.798
Crystal size/mm^3	0.11 × 0.09 × 0.07
Detector distance/mm	40.0
Scan time per degree/min	4.0
Absorption coefficient/mm^{-1}	5.360
F (000)/e	261
θ range/°	3.30 – 34.96
Range in hkl	±28, ±28, ±34
Total no. reflections	16466
Independent reflections	2768
Reflections with I > 2σ(I)	14085 (R$_\sigma$ = 0.0675)
Data/parameters	2768/360
Absorption correction	multi-scan (SCALEPACK)
Goodness-of-fit (F^2)	0.975
Final R indices (I > 2 σ(I))	R1 = 0.0586
	wR2 = 0.1398
R indices (all data)	R1 = 0.0761
	wR2 = 0.1509
Largest diff. peak/ deepest hole/e·Å^{-3}	1.602/-0.982

Table 4.56: Atomic coordinates and equivalent isotropic displacement parameters $U_{eq}/Å^2$ of "$Co_3B_8O_{13}(OH)_4$" (space group $R3c$). U_{eq} is defined as one third of the trace of the orthogonalized U_{ij} tensor (standard deviations in parentheses).

Atom	Wyckoff Position	x	y	z	U_{eq}
Co1	18*b*	0.23781(5)	0.24455(5)	0.07209(4)	0.0123(2)
Co2	18*b*	0.23231(5)	0.49339(6)	0.07808(3)	0.0145(2)
Co3	18*b*	0.07332(8)	0.1635(2)	0.24580(4)	0.0351(3)
Co4	18*b*	0.99478(6)	0.24825(5)	0.09020(4)	0.0135(2)
B1	6*a*	0	0	0.9748(5)	0.014(2)
B2	18*b*	0.0454(3)	0.1003(3)	0.1051(3)	0.0101(8)
B3	18*b*	0.3386(4)	0.4230(4)	0.9975(4)	0.0060(8)
B4	18*b*	0.2243(3)	0.2864(3)	0.9373(3)	0.0079(7)
B5	18*b*	0.1652(4)	0.3328(4)	0.1629(4)	0.0107(8)
B6	18*b*	0.2255(3)	0.4367(3)	0.9356(3)	0.0086(8)
B7	18*b*	0.3329(3)	0.1762(4)	0.1680(3)	0.0072(8)
B8	18*b*	0.4169(4)	0.3420(4)	0.1623(4)	0.006(2)
B9	18*b*	0.1671(3)	0.0921(4)	0.1597(3)	0.0050(9)
B10	18*b*	0.3613(3)	0.4336(3)	0.1128(3)	0.0080(7)
B11	18*b*	0.0781(4)	0.1649(4)	0.9935(3)	0.0102(9)
B12	6*a*	1/3	2/3	0.9953(6)	0.012(2)
H1	18*b*	0.131(2)	0.386(4)	0.188(3)	0.023
H2	18*b*	0.250(4)	0.370(2)	0.183(3)	0.021
H3	18*b*	0.064(5)	0.287(4)	0.211(2)	0.024
H4	18*b*	0.155(4)	0.333(4)	0.069(3)	0.027
H5	18*b*	0.219(4)	0.567(4)	0.985(2)	0.022
H6	6*a*	1/3	2/3	0.886(2)	0.059
O1	18*b*	0.1822(3)	0.3207(3)	0.0985(2)	0.023(2)
O2	18*b*	0.0732(3)	0.2711(3)	0.1732(2)	0.0197(8)
O3	6*a*	0	0	0.0891(3)	0.012(2)
O4	18*b*	0.1910(2)	0.3422(2)	0.9076(2)	0.0071(5)
O5	18*b*	0.4254(2)	0.4309(2)	0.9891(2)	0.0107(7)
O6	18*b*	0.1056(2)	0.1516(2)	0.0541(2)	0.0085(6)
O7	18*b*	0.4104(2)	0.2560(2)	0.1466(2)	0.0074(6)
O8	18*b*	0.9749(2)	0.1207(2)	0.1106(2)	0.0093(6)
O9	18*b*	0.3622(2)	0.3549(2)	0.1142(2)	0.0087(6)
O10	18*b*	0.3790(2)	0.4828(2)	0.1670(2)	0.0105(6)
O11	18*b*	0.3349(2)	0.4597(2)	0.0606(2)	0.0097(6)
O12	18*b*	0.1753(2)	0.4273(2)	0.9932(2)	0.0092(6)
O13	18*b*	0.2149(2)	0.4894(2)	0.8887(2)	0.0099(6)
O14	18*b*	0.3202(2)	0.4727(2)	0.9506(2)	0.0096(6)
O15	18*b*	0.2699(2)	0.3274(2)	0.995(2)	0.0092(6)
O16	18*b*	0.0955(2)	0.1147(2)	0.1628(2)	0.0089(6)
O17	18*b*	0.2857(2)	0.2801(2)	0.8937(2)	0.0103(6)
O18	18*b*	0.2515(2)	0.1695(2)	0.1427(2)	0.0096(6)
O19	18*b*	0.9992(2)	0.0782(2)	0.9713(2)	0.0095(6)
O20	18*b*	0.1478(2)	0.1970(2)	0.9469(2)	0.0087(6)
O21	18*b*	0.1836(2)	0.4221(2)	0.1736(2)	0.0194(8)
O22	18*b*	0.2484(2)	0.5977(2)	0.0161(2)	0.0187(8)
O23	18*b*	0.2229(3)	0.3165(2)	0.2017(2)	0.0172(7)
O24	6*a*	1/3	2/3	0.9268(4)	0.049(3)

Table 4.57: Anisotropic displacement parameters of "$Co_3B_8O_{13}(OH)_4$" (standard deviations in parentheses).

Atom	U_{11}	U_{22}	U_{33}	U_{23}	U_{13}	U_{12}
Co1	0.0137(3)	0.0082(3)	0.0130(3)	0.0003(2)	-0.0029(3)	0.0039(3)
Co2	0.0129(3)	0.0195(4)	0.0136(3)	-0.0034(3)	-0.0027(3)	0.0101(3)
Co3	0.0264(5)	0.0692(7)	0.0256(5)	-0.0272(4)	-0.0141(4)	0.0358(5)
Co4	0.0192(4)	0.0091(3)	0.0131(4)	0.0021(2)	0.0036(2)	0.0078(3)
B1	0.010(2)	0.010(2)	0.023(5)	0	0	0.005(2)
B2	0.005(2)	0.011(2)	0.009(2)	0.003(2)	0.002(2)	-0.000(2)
B3	0.004(2)	0.006(2)	0.002(2)	0.000(2)	0.001(2)	-0.001(2)
B4	0.009(2)	0.008(2)	0.005(2)	-0.002(2)	-0.001(2)	0.003(2)
B5	0.017(3)	0.008(2)	0.009(3)	0.001(2)	0.001(3)	0.008(3)
B6	0.009(2)	0.008(2)	0.011(2)	0.004(2)	0.005(2)	0.005(2)
B7	0.007(2)	0.009(2)	0.006(2)	0.002(2)	-0 .002(2)	0.004(2)
B8	0.006(2)	0.005(2)	0.008(2)	0.002(2)	0.004(2)	0.003(2)
B9	0.004(2)	0.005(2)	0.006(2)	0.0004(8)	-0.0009(8)	0.0021(9)
B10	0.007(2)	0.004(2)	0.010(2)	-0.000(2)	-0.001(2)	0.001(2)
B11	0.008(3)	0.015(3)	0.006(3)	-0 .003(2)	-0.002(2)	0.004(2)
B12	0.014(3)	0.014(3)	0.010(4)	0	0	0.007(2)
O1	0.033(3)	0.035(2)	0.011(2)	-0.001(2)	0.001(2)	0.025(2)
O2	0.013(2)	0.019(2)	0.024(2)	-0.004(2)	-0.002(2)	0.006(2)
O3	0.011(2)	0.011(2)	0.013(4)	0	0	0.0055(8)
O4	0.0067(9)	0.0046(8)	0.0073(9)	0.0003(7)	-0.0024(7)	0.0008(7)
O5	0.006(2)	0.012(2)	0.017(2)	-0.003(2)	-0.000(2)	0.007(2)
O6	0.007(2)	0.011(2)	0.007(2)	0.001(2)	0.001(2)	0.003(2)
O7	0.006(2)	0.005(2)	0.010(2)	0.002(2)	-0.001(2)	0.002(2)
O8	0.008(2)	0.008(2)	0.014(2)	0.000(2)	0.002(2)	0.006(2)
O9	0.006(2)	0.009(2)	0.012(2)	-0.001(2)	-0.002(2)	0.004(2)
O10	0.015(2)	0.009(2)	0.007(2)	-0.004(2)	-0.003(2)	0.006(2)
O11	0.012(2)	0.010(2)	0.012(2)	-0.000(2)	-0.001(2)	0.010(2)
O12	0.012(2)	0.009(2)	0.008(2)	-0.000(2)	-0.001(2)	0.006(2)
O13	0.009(2)	0.007(2)	0.012(2)	0.003(2)	0.004(2)	0.003(2)
O14	0.008(2)	0.008(2)	0.014(2)	-0.000(2)	-0.002(2)	0.005(2)
O15	0.009(2)	0.006(2)	0.010(2)	0.004(2)	0.002(2)	0.002(2)
O16	0.013(2)	0.010(2)	0.006(2)	0.001(2)	0.002(2)	0.008(2)
O17	0.005(2)	0.015(2)	0.011(2)	-0.002(2)	-0.003(2)	0.004(2)
O18	0.006(2)	0.009(2)	0.011(2)	0.000(2)	0.000(2)	0.002(2)
O19	0.007(2)	0.008(2)	0.012(2)	0.001(2)	0.000(2)	0.003(2)
O20	0.007(2)	0.006(2)	0.009(2)	0.002(2)	0.000(2)	0.001(2)
O21	0.012(2)	0.012(2)	0.031(2)	-0.004(2)	-0.005(2)	0.005(2)
O22	0.010(2)	0.008(2)	0.034(2)	-0.003(2)	0.003(2)	0.001(2)
O23	0.027(2)	0.015(2)	0.015(2)	-0.004(2)	-0.006(2)	0.015(2)
O24	0.065(4)	0.065(4)	0.016(4)	0	0	0.033(2)

4.1.10.3 Crystal Structure Description

"$Co_3B_8O_{13}(OH)_4$" contains trigonal BO_3 and tetrahedral BO_4-groups, condensed to a network structure. The trigonal units are linked *via* twofold coordinating oxygen atoms ($O^{[2]}$). The tetrahedral BO_4-groups are connected by oxygen atoms that share either two ($O^{[2]}$) or three ($O^{[3]}$) common corners. Additionally in "$Co_3B_8O_{13}(OH)_4$" there are isolated $B(OH)_4$-tetrahedra. The structural element of isolated $[B(OH)_4]^-$ anions can be found only in a few other borates, *e.g.* bandylite ($Cu_2[B(OH)_4]_2Cl_2$) [347, 348], $Ba[B(OH)_4]_2 \cdot H_2O$ [349], teepleite ($Na_2[B(OH)_4]Cl$) [346], or henmilite ($Ca_2Cu(OH)_4[B(OH)_4]_2$) [350]. Figure 4.77 shows the structure

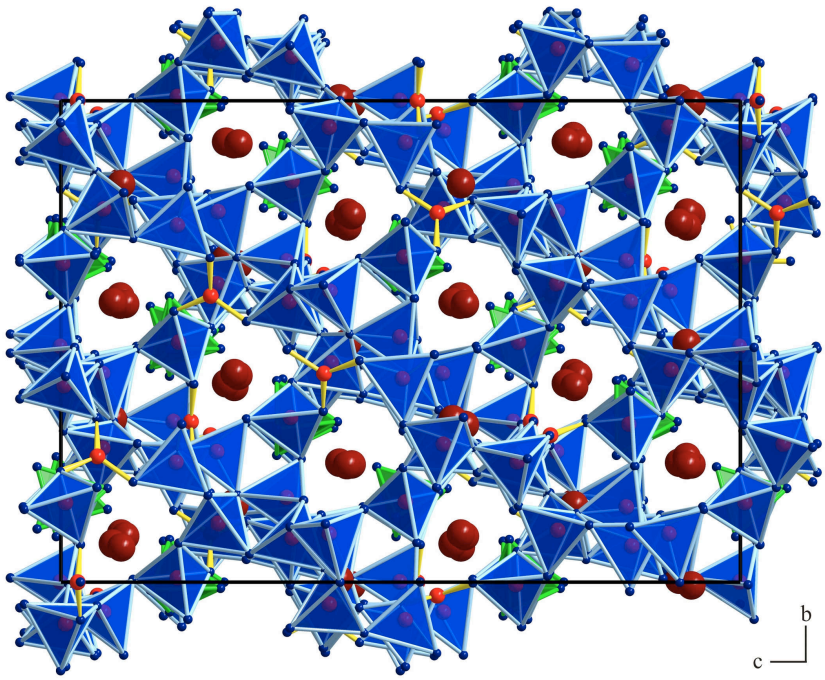

Figure 4.77: Crystal structure of "$Co_3B_8O_{13}(OH)_4$" with view along [$\bar{1}$00]. Co^{2+} ions are shown as dark red, O^{2-} ions as blue, and B^{3+} as red spheres. Green tetrahedra represent isolated $B(OH)_4$-groups, whereas blue ones represent Q^2 or Q^3 tetrahedra.

of "$Co_3B_8O_{13}(OH)_4$" along [$\bar{1}$00], exhibiting drop-shaped channels running along the a- and b-direction. The vertices of these asymmetric channels point all in the same direction, which illustrates the non-centrosymmetry of the structure. Figure 4.78 gives a view of the crystal structure along [101], showing a network with channels incorporating the isolated $B(OH)_4$-tetrahedra and a part of Co^{2+}.

The channels are built up by different "Achter" rings [39], composed either of eight tetrahedra, of seven tetrahedral and one trigonal unit, or of six tetrahedra and two trigonal BO_3-groups. Figure 4.79 demonstrates the different types of rings along [101]. Inside of each ring, the Co^{2+} ions are located, which are either coordinated by six oxygen ions in a strongly distorted octahedral way (Co1, Co2, Co4) or by seven oxygen anions (Figure 4.80).

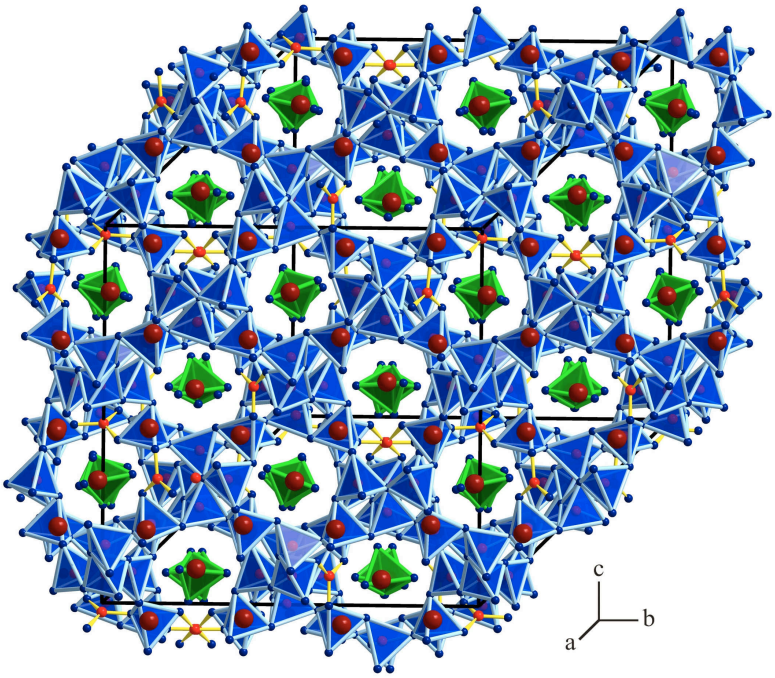

Figure 4.78: Crystal structure of "$Co_3B_8O_{13}(OH)_4$" with a view along [101]. Co^{2+} ions are shown as dark red, O^{2-} ions as blue, and B^{3+} as red spheres. Green tetrahedra represent isolated $B(OH)_4$-groups, whereas blue ones represent Q^2 or Q^3 tetrahedra.

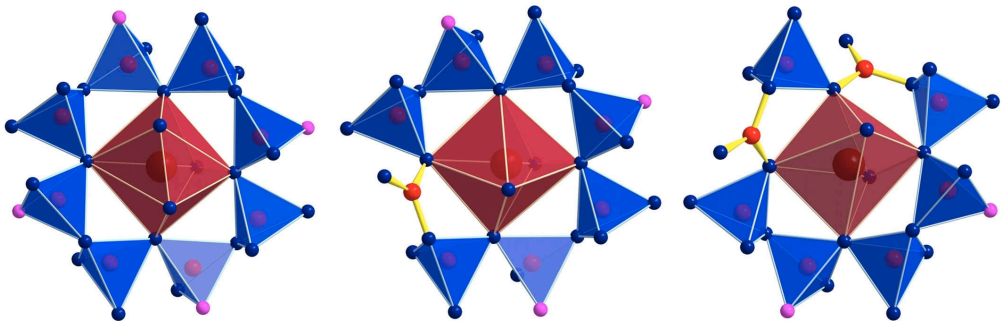

Figure 4.79: Left: "Achter" ring composed of eight BO_4-tetrahedra. **Middle**: "Achter" ring composed of seven BO_4-tetrahedra and one trigonal BO_3-group. **Right**: "Achter" ring composed of six BO_4-tetrahedra and two trigonal BO_3-groups. All rings are shown with a CoO_6-octahedron inside of them.

The Co-polyhedra are interconnected by the isolated $B(OH)_4$-tetrahedra resulting in a chain, composed of tetrahedra, CoO_6-octahedra (Co1, Co2, Co4), and CoO_7-polyhedra (Co3). Figure 4.81 demonstrates the different chains of $B(OH)_4$- and Co-polyhedra, surrounded by "Achter" rings, and the linkage of the different polyhedra. On the left hand side the chain is composed of B5, B12, Co2, and Co3 as well as "Achter" rings alternating built up either from eight tetrahedra or seven tetrahedra and one trigonal unit. The middle chain consists of B5 and Co4. The rings consisting of seven tetrahedral and one trigonal planar borate group are rotated against each other by approximately 180°. The chain pictured on the right hand side exhibits B5 and Co4 atoms. The corresponding rings are not rotated

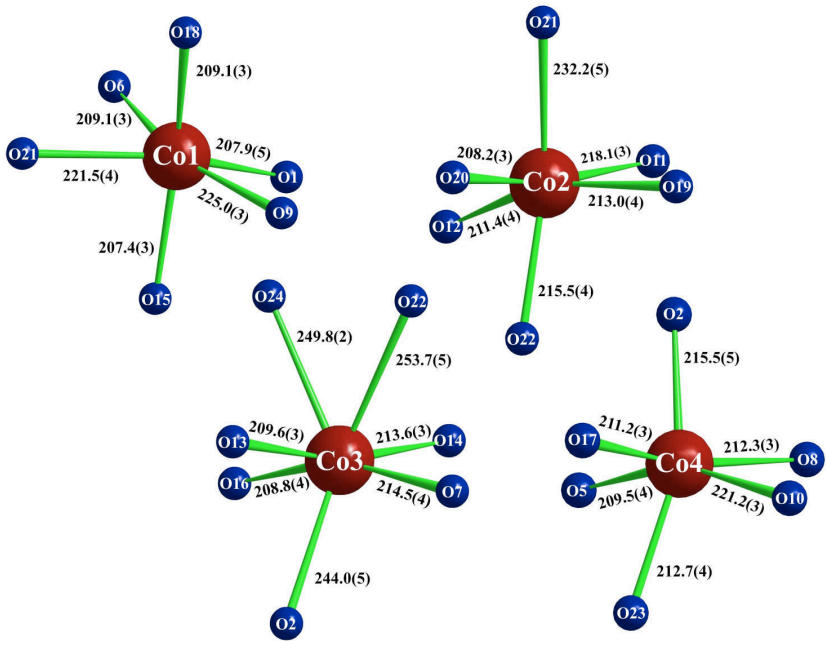

Figure 4.80: Coordination spheres of Co^{2+} in "$Co_3B_8O_{13}(OH)_4$". Distances are given in pm.

along the [101]-direction, the BO_3-groups are situated on top of each other. The occurence of different chains inside the crystal structure of "$Co_3B_8O_{13}(OH)_4$" is 2:1:1 (Figure 4.81 from left to right). The remaining Co^{2+} ions are positioned between the rings in a way that four Co cations are located between two rings along [101] on a level with the $B(OH)_4$-tetrahedra. The Co^{2+} ions Co1, Co2, and Co4 are coordinated in a distorded octahedral way, whereas Co3 is coordinated by seven O^{2-} ions (Figure 4.80). These coordination numbers are obtained by ECoN calculations (Effective Coordination Numbers according to Hoppe) [161–163].

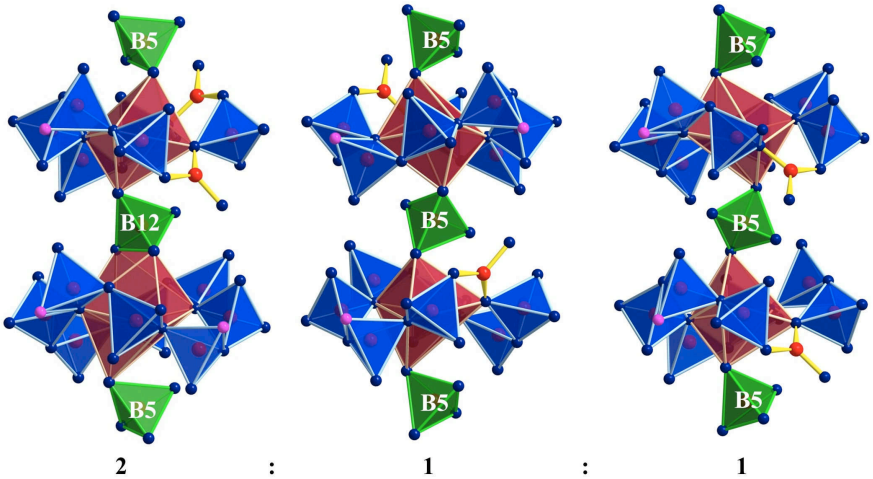

Figure 4.81: Three types of chains composed of $B(OH)_4$- and Co-polyhedra, surrounded by "Achter" rings.

The "Achter" rings are interconnected *via* strings of BO_4-tetrahedra running along [101]. These strings are built up from $[(BO_3)O^{[3]}]$ units, consisting of three tetrahedra linked by one common corner ($O^{[3]}$). The units are connected among

each other by additional tetrahedra. Figure 4.82 demonstrates the three different types of strings appearing in "$Co_3B_8O_{13}(OH)_4$". The left and right types of strings reveal only O4, whereas the middle type exhibits alternating O3 and O4 on the position of $O^{[3]}$. Threefold coordinated oxygen atoms $O^{[3]}$ can also be

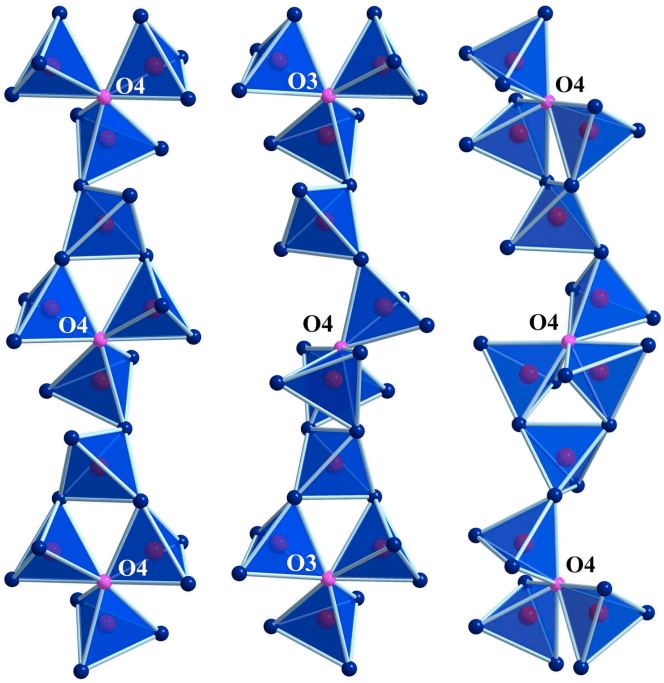

Figure 4.82: Three types of strings connecting "Achter" rings to a network structure.

found in other borates, *e.g.* β-MB_4O_7 (M = Mn [261], Co, Ni [261], Cu [261], Zn [171]), β-$RE(BO_2)_3$ (RE = Nd, Sm, Gd–Lu) [262–264], γ-$RE(BO_2)_3$ (RE = La–Nd) [265, 266], and minerals like tunnelite ($SrB_6O_9(OH)_2{\cdot}3H_2O$), strontioginorite ($(Sr,Ca)_2B_{14}O_{20}(OH)_6{\cdot}6H_2O$) [267], aristarainite ($Na_2Mg[B_6O_8(OH)_4]_2{\cdot}4H_2O$) [268], and the high-pressure modification of B_2O_3 [82].

For clarity, the hydrogen atoms are not shown in the previous Figures, but Figure 4.83 demonstrates the two crystallographically distinguishable $B(OH)_4$-tetrahedra with the positions of the hydrogen atoms. Reduced values in the bond-valence calculations for oxygen atoms O1, O2, O21, O22, O23, and O24 led to the suggestion that hydrogen bonds to these oxygen atoms beeing part of the isolated BO_4-tetrahedra.

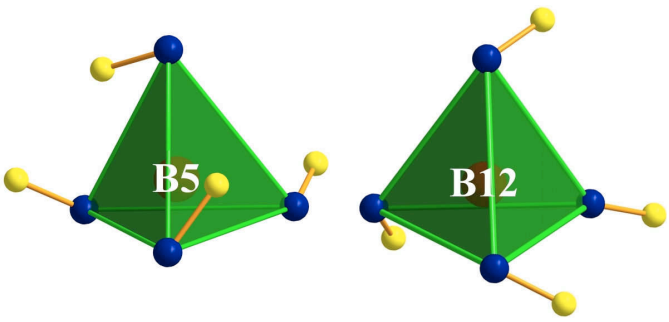

Figure 4.83: The two crystallographically distinguishable $B(OH)_4$-tetrahedra. Red spheres represent B^{3+}, blue spheres O^{2-}, and yellow spheres H^+.

The bond-lengths B–O for B1 and B10 (BO_3) in "$Co_3B_8O_{13}(OH)_4$" (Table 4.58) vary between 137.2 and 138.4 pm, with an average bond-length B–O of 137.8 pm. They are in good accordance with the mean value known for triangular BO_3-groups (137.0 pm) [323]. The B–O bond-distances in the remaining 10 crystallographically independent BO_4-tetrahedra (Table 4.58) range between 143.5 and 157.7 pm with an average of 147.5 pm, which fits the known average value of 147.6 pm for borates [232, 233]. As expected, the bonds to threefold coordinated oxygen atoms $O^{[3]}$ are significantly longer (150.2–157.7 pm) than the average, with partial compensation by shortening of other bonds. Longer bonds can also be found in the borates MB_4O_7 (M = Sr [174, 175], Pb [175, 176], Eu [177]) and β-MB_4O_7 (M = Ca [173], Hg [172]), as well as in β-MB_4O_7 (M = Mn [261], Co, Ni [261], Cu [261], Zn [171]). The O–B–O angles in the 10 crystallographically independent BO_4-tetrahedra vary between 104.6 and 114.1° (Table 4.59). These strong deviations from the ideal tetrahedron angle are not exceptional for borates, synthesized under extreme conditions. Examples for such strongly distorted tetrahedra in BO_4-networks can be found *e.g.* in the high-pressure phases α-$RE_2B_4O_9$ (RE = Eu-Tb [74–76]) with O–B–O angles varying between 99.5 and 118.9° for α-$Eu_2B_4O_9$, 99.4–119.0° for α-$Gd_2B_4O_9$, and 99.4–119.4° for α-$Tb_2B_4O_9$. The BO_3-groups (B1, B10) are nearly planar, exhibiting O–B–O-angles between 119.0 and 121.3° with an average of 119.8°.

Table 4.58: Interatomic distances/pm in "$Co_3B_8O_{13}(OH)_4$" (space group $R3c$) calculated with the single crystal lattice parameters (standard deviations in parentheses).

B2-O8	144.7(6)	B5-O2	143.5(7)	B8-O12	146.5(7)
B2-O16	146.1(7)	B5-O23	143.9(7)	B8-O17	147.6(9)
B2-O6	147.0(6)	B5-O21	144.5(7)	B8-O7	148.8(7)
B2-O3	155.9(5)	B5-O1	144.8(9)	B8-O9	149.5(7)
	Ø = 148.4		Ø = 144.2		Ø = 148.1
B3-O5	146.3(6)	B6-O13	143.5(6)	B9-O18	146.3(6)
B3-O14	146.5(8)	B6-O12	147.6(6)	B9-O8	147.5(7)
B3-O15	149.2(6)	B6-O14	148.2(6)	B9-O16	149.0(6)
B3-O11	151.0(8)	B6-O4	156.6(6)	B9-O13	150.1(7)
	Ø = 148.3		Ø = 149.0		Ø = 148.2
B4-O15	145.5(7)	B7-O7	144.9(6)	B11-O6	144.1(7)
B4-O17	146.6(7)	B7-O5	145.3(7)	B11-O20	145.1(7)
B4-O20	147.8(6)	B7-O18	147.0(6)	B11-O10	150.3(7)
B4-O4	150.2(6)	B7-O4	157.7(7)	B11-O19	152.8(7)
	Ø = 147.5		Ø = 148.7		Ø = 148.1
B1-O19	137.6(3) 3×	B10-O11	137.2(6)	B12-O22	143.7(5) 3×
		B10-O10	138.2(6)	B12-O24	147.0(2)
		B10-O9	138.4(5)		Ø = 144.5
			Ø = 137.9		
O3-B2	155.9(5) 3×	O4-B4	150.2(6)		
		O4-B6	156.6(6)		
		O4-B7	157.7(7)		
			Ø = 154.8		

Table 4.59: Interatomic angles/° in "$Co_3B_8O_{13}(OH)_4$" calculated with the single crystal lattice parameters (standard deviations in parentheses).

O8-B2-O3	106.1(3)	O2-B5-O1	105.7(6)	O7-B8-O9	105.3(5)
O16-B2-O3	107.7(4)	O23-B5-O1	107.7(4)	O12-B8-O17	106.3(5)
O6-B2-O3	109.2(4)	O23-B5-O21	108.8(6)	O17-B8-O7	109.3(5)
O16-B2-O6	109.8(4)	O2-B5-O21	110.4(4)	O12-B8-O9	110.6(5)
O8-B2-O6	110.4(4)	O21-B5-O1	110.9(5)	O12-B8-O7	111.3(4)
O8-B2-O16	113.6(4)	O2-B5-O23	113.3(5)	O17-B8-O9	114.1(4)
	Ø = 109.5		Ø = 109.5		Ø = 109.5
O14-B3-O11	106.9(4)	O14-B6-O4	106.9(3)	O18-B9-O8	107.1(5)
O5-B3-O15	108.5(4)	O13-B6-O4	107.8(4)	O18-B9-O13	108.6(4)
O15-B3-O11	108.8(5)	O12-B6-O4	108.0(3)	O8-B9-O16	109.3(4)
O5-B3-O11	109.4(5)	O12-B6-O14	110.0(4)	O16-B9-O13	109.9(5)
O14-B3-O15	110.5(5)	O13-B6-O14	110.8(4)	O8-B9-O13	110.9(4)
O14-B3-O5	112.6(5)	O13-B6-O12	113.3(4)	O18-B9-O16	111.0(4)
	Ø = 109.5		Ø = 109.5		Ø = 109.5
O20-B4-O4	107.8(3)	O18-B7-O4	104.6(4)	O10-B11-O19	106.4(4)
O17-B4-O4	108.4(4)	O5-B7-O4	107.0(4)	O6-B11-O10	108.4(5)
O17-B4-O20	108.6(4)	O7-B7-O4	108.9(4)	O6-B11-O19	109.2(4)
O15-B4-O4	109.6(4)	O7-B7-O18	111.2(4)	O20-B11-O10	109.6(4)
O15-B4-O17	109.7(4)	O7-B7-O5	112.3(4)	O20-B11-O19	109.7(5)
O15-B4-O20	112.6(4)	O5-B7-O18	112.4(4)	O6-B11-O20	113.4(4)
	Ø = 109.5		Ø = 109.4		Ø = 109.5
O19-B1-O19 3×	119.7(2)	O11-B10-O10	119.0(4)	O22-B12-O24 3×	108.1(5)
		O10-B10-O9	119.4(4)	O22-B12-O22 3×	110.8(5)
		O11-B10-O9	121.3(4)		Ø = 109.5
			Ø = 119.9		

4.1.10.4 Theoretical Calculations

Bond-valence sums were calculated for "$Co_3B_8O_{13}(OH)_4$" with the help of the bond-length/bond-strength concept (Table 4.60) [164, 165]. The CHARDI concept [167] could not be used, because there was no program available for handling more than 20 anions. The formal ionic charges of the atoms, calculated from the results of X-ray structure analysis, were in agreement within the limits of the concept, with exception of O1, O2, O21, O22, O23, and O24, to which hydrogen is bound. Due to the unknown O–H distances, it is not possible to generate the exact bond-valence sum.

Table 4.60: Charge distribution in "$Co_3B_8O_{13}(OH)_4$" calculated with the bond-length/bond-strength concept.

Co1	Co2	Co3	Co4			H1	H2	H3	H4	H5	H6
+1.84	+1.70	+1.84	+1.80			+1.21	+1.19	+1.24	+1.32	+1.14	+1.22
B1	B2	B3	B4	B5	B6	B7	B8	B9	B10	B11	B12
+2.96	+2.96	+2.96	+3.02	+3.30	+2.93	+2.95	+2.97	+2.96	+2.93	+2.99	+3.28
O1	O2	O3	O4	O5	O6	O7	O8	O9	O10	O11	O12
-2.02	-2.03	-1.81	-1.86	-1.91	-1.93	-1.83	-1.88	-1.90	-1.91	-1.95	-1.85
O13	O14	O15	O16	O17	O18	O19	O20	O21	O22	O23	O24
-1.88	-1.82	-1.87	-1.85	-1.85	-1.88	-1.95	-1.90	-2.06	-2.15	-1.97	-1.99

Furthermore, we calculated the MAPLE values (Madelung Part of Lattice Energy) [161–163] for "$Co_3B_8O_{13}(OH)_4$" in order to compare them with MAPLE values of the binary components CoO and the high-pressure modification B_2O_3-II. The foundation therefore is the additive potential of the MAPLE values, by which it is possible to calculate hypothetical values for "$Co_3B_8O_{13}(OH)_4$", starting from the binary oxides. Resultant we obtained a value of 109485 kJ·mol^{-1} for "$Co_3B_8O_{13}(OH)_4$" in comparison to 111466 kJ·mol^{-1} (deviation: 1.8%), starting from the binary oxides (3 × CoO (4560 kJ·mol^{-1}) + 4 × B_2O_3-II (21938 kJ·mol^{-1}) + 2 H_2O (hexagonal ice [326]) (5017 kJ·mol^{-1})).

4.1.11 Closing Remarks to the Chapter Transition Metal Borates

In the former chapters 4.1.3 – 4.1.10, the phases β-MB$_2$O$_5$ (M = Hf [230], Zr [231]), β-MB$_4$O$_7$ (M = Mn, Co, Ni, Cu [261]), α-FeB$_2$O$_4$ [285], HP-NiB$_2$O$_4$ [286], CdB$_2$O$_4$ [292], M_3B$_{11}$O$_{19}$OH (M = Fe, Co), "Fe$_3$B$_7$O$_{12}$N", and "Co$_3$B$_8$O$_{13}$(OH)$_4$" were presented. The results of β-MB$_2$O$_5$ (M = Hf [230], Zr [231]), β-MB$_4$O$_7$ (M = Mn, Co, Ni, Cu [261]), α-FeB$_2$O$_4$ [285], HP-NiB$_2$O$_4$ [286], and CdB$_2$O$_4$ [292] are published in the meantime, whereas the phases "Fe$_3$B$_7$O$_{12}$N" and "Co$_3$B$_8$O$_{13}$(OH)$_4$" are still under investigation. M_3B$_{11}$O$_{19}$OH (M = Fe, Co) will be published in the near future.

In the second part of this thesis, a summary concerning applications and properties of main metal borates. Subsequently, a survey of barium, bismuth, and tin borates is given. Afterwards, the results of the high-pressure investigations regarding the mentioned systems are discussed.

4.2 Main Group Metal Borates

4.2.1 Introduction

Due to their superior NLO (Non Linear Optics) properties, borates are very interesting materials used to generate new laser sources of frequencies, that cannot be obtained directly from available lasers [351]. In contrast to other commonly used NLO materials, such as KH_2PO_4 (KDP; Figure 4.84 left), $KTiOPO_4$ (KTP), and $LiNdO_3$, borates reveal improved features *e.g.* in UV and even VUV (vacuum UV) applications because of their high UV transmittance at wavelengths down to 155 nm [351], combined with a high damage threshold. The most common borates for NLO applications can be found among the main group borates, namely β-BaB_2O_4 (BBO) [13–15], LiB_3O_5 (LBO) [16–19], α-BiB_3O_6 (BIBO, Figure 4.84 middle) [20–22], and $CsLiB_6O_{10}$ (CLBO; Figure 4.84 right) [23–26].

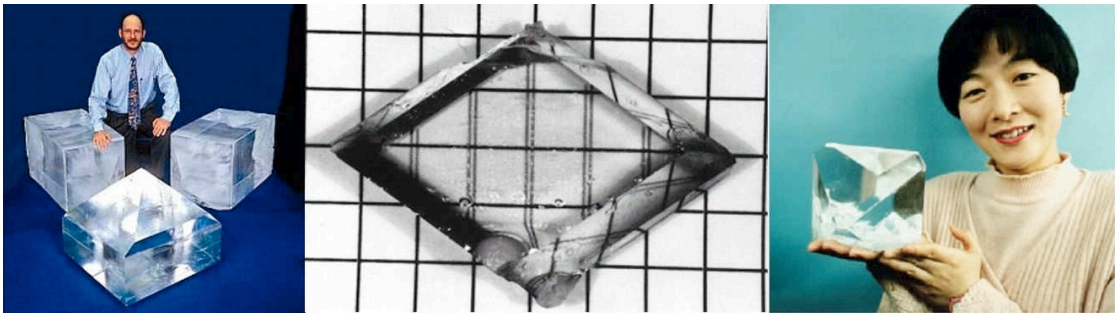

Figure 4.84: Crystals of KDP (left) [352], BIBO grown by Becker *et al.* (middle) [22], and single crystal of CLBO grown by Mori *et al.* (right) [23].

There are also other main group borates, which are not that popular, exhibiting excellent NLO properties. Examples are CsB_3O_5 (CBO) [353], $YCa_4(BO_3)_3O$ (YCOB) [354], $GdCa_4(BO_3)_3O$ [355, 356], $Gd_xY_{1-x}CaO(BO_3)_3$ (GdYCOB) [26, 357, 358], $K_2Al_2B_2O_7$ (KABO), $Li_2B_4O_7$ (LTB or LB4) [359], $KB_5O_8 \cdot 4\,H_2O$ (KB5, the first described NLO borate) [360, 361], KBe_2BO_3F (KBBF), or $Sr_2Be_2B_2O_7$ (SBBO). The well known phases SrB_4O_7 (SBO) [174, 175, 362] and PbB_4O_7 (PBO) [175, 176, 363] are also attractive compounds for NLO applications. Unfortunately, they are characterized by small birefringence, which makes phase-matching (and therefore second harmonic generation) impossible. SBO shows a unique transmission in the UV region down to 130 nm, which makes it suitable for UV applications. Because of its lack in phase-matching, SBO can be used under waveguide mode synchronism or quasi-synchronism conditions [362]. PBO shows higher optical nonlinearity and higher refractive indices relative to borates such as BBO or LBO, what makes it a promising candidate for high-power electro-optic Q-switches or modulators [363]. There is still high demand for new NLO materials, why much

effort is made in this research area. For example the borate $BaBiBO_4$ was recently synthesized by Barbier *et al.* [364] showing second harmonic generation efficiency about five times larger than KDP [365].

Further on, borates like $Li_2B_4O_7$:Cu [366] and MgB_4O_7:Dy,Na [367] show thermally stimulated luminescence (TSL) and are therefore used *e.g.* as phosphors in thermoluminescence dosimetry. Also BaB_4O_7 was investigated regarding its TSL by different researchers in the last years [368–370]. The characteristics of BaB_4O_7:Ce, reported by Yazici *et al.* [369], indicate that the material may be a new promising phosphor for the use in ionizing radiation dosimetry. Li *et al.* introduced a Dy-doped variant, namely BaB_4O_7:Dy, and proposed its potential as a material for γ-ray thermoluminescence dosimeter for clinical dosimetry [370].

Having this backround, we enlarged our research into the fields of main metal borates, whereas basic research initially was the centre of our attention. Within this work, the systems Ba–B–O, Bi–B–O, and Sn–B–O were investigated. In the following a small introduction in this three systems is given.

Regarding former high-pressure/high-temperature studies on phase formation and crystal chemistry of the alkaline earth tetraborates α-CaB_4O_7 [371] and SrB_4O_7 [174, 175], we focused on the synthesis of a high-pressure phase of BaB_4O_7 [372] (in the following designated as α-BaB_4O_7) (Figure 4.85). In the case of Ca^{2+}, we gained the high-pressure phase β-CaB_4O_7 [173], whereas for Sr^{2+} no high-pressure phase could be synthesized until now. Under ambient pressure, following barium borates have been structurally well-characterized up to now: α-BaB_4O_7 ($P2_1/c$) [372], α-BaB_2O_4 ($R\bar{3}c$, high-temperature form) [373], β-BaB_2O_4 ($R3$, low-temperature form) [13], and $Ba_5(BO_3)_2(B_2O_5)$ ($P2_12_12_1$) [374]. The following compositions are mentioned in the literature as well, but are not specified structurally: $Ba_3B_2O_6$ [375], $Ba_4B_2O_7$ [376], $Ba_2B_{10}O_{17}$ [376], $Ba_2B_2O_5$ [376], and BaB_8O_{13} [377].

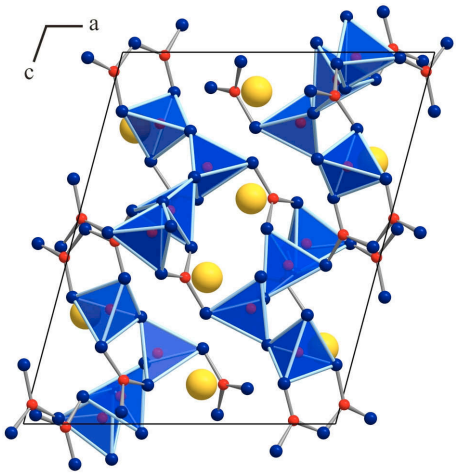

Figure 4.85: Crystal structure of α-BaB_4O_7.

In the system Bi–B–O, primarily determined by Levin and McDaniel in 1962 [378], the crystalline compounds $Bi_{12}BO_{20}$ (correctly $Bi_{24}B_2O_{39}$ [379] (boron-sillenite)), $Bi_4B_2O_9$, $Bi_3B_5O_{12}$, BiB_3O_6, and $Bi_2B_8O_{15}$ were found. Later on,

$BiBO_3$ was added as a metastable compound [380, 381]. The most prominent compound in this system is bismuth triborate, BiB_3O_6 [20–22] (BIBO), due to its exceptional nonlinear optical properties [382], which raised the interest of many research groups around the world. Meanwhile, BiB_3O_6 is already well-established as a nonlinear optical material with outstanding physical properties and furthermore characterized in detail concerning its piezoelectric, pyroelectric, dielectric, elastic, and thermoelastic properties [383]. Recently, Li *et al.* synthesized two new polymorphs of BiB_3O_6 under autogenous pressure at 240 °C in Teflon autoclaves (50 cm^3 volume) [384]. For clarity, the authors renamed bismuth triborate as α-BiB_3O_6 (Figure 4.86 top) and the two new modifications as β- (Figure 4.86 bottom left) and γ-BiB_3O_6 (Figure 4.86 bottom right). In contrast to the α-phase, which crystallizes in the non-centrosymmetric, monoclinic space group $C2$, these modifications crystallize with centrosymmetric symmetry in the space group $P2_1/n$.

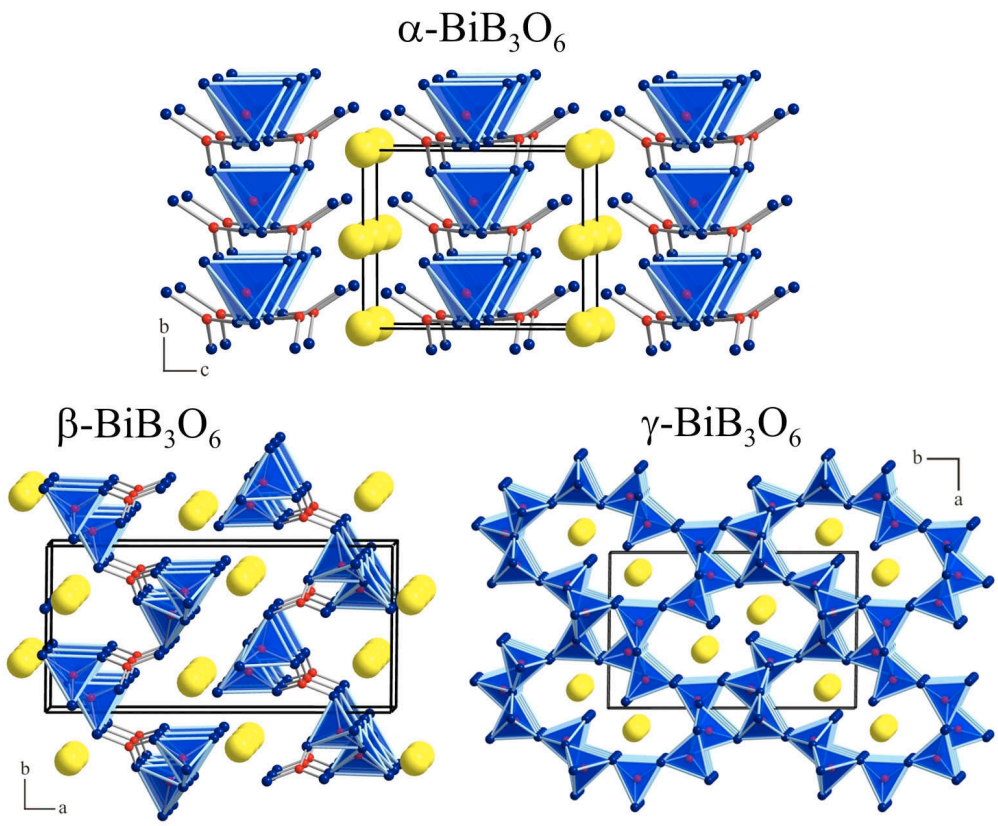

Figure 4.86: The three known modifications of BiB_3O_6.

Further on, several investigations were performed in the ternary system Sn–B–O as a simplified variant of the tin-based amorphous composite oxides (TCO). This material is used as negative electrodes of lithium ion rechargeable batteries. All compounds in this system are glasses, so the synthesis of crystalline approximands for a more detailed structural investigation would be favourable. In 1997, Idota *et*

al. reported about a tin-based amorphous oxide, that could replace the carbon-based lithium intercalation materials currently in use as negative electrodes of lithium ion rechargeable batteries [27]. This tin-based amorphous composite oxide (TCO) has the complex composition $SnB_{0.56}P_{0.40}Al_{0.42}O_{3.6}$, showing twice the gravimetry and four times the volumetric capacity of carbon based materials. Unfortunately, this outstanding performance is counterbalanced by a large irreversible capacity, which is lost during the first electrochemical cycle. Since the reasons are not yet fully understood, several groups tried to clarify the mechanisms at simplified variants of the TCO glasses. For example, Holland *et al.* investigated the borate anomaly of the Sn(II) environment in tin borate glasses of the general composition $xSnO(1\text{-}x)B_2O_3$, using ^{11}B and ^{119}Sn nuclear magnetic resonance (NMR) spectroscopy [28]. In this system, the introduction of SnO into the boroxol ring structure of B_2O_3 converts one symmetrically coordinated boroxol ring boron to a BO_4–tetrahedron, accompanied by changes of the environment of the neighbouring threefold coordinated atoms. Due to the structural chemistry of Sn(II), which is dominated by the steric activity of a lone pair, trigonal pyramidal SnO_3 polyhedra can be found with the lone pair at one vertex, leading to a pseudo tetrahedron. The authors showed that the increase of SnO leads to less symmetrical threefold-coordinated boron atoms, while the symmetry of the tin atoms becomes more axial. Hayashi *et al.* investigated the structures of $SnO–B_2O_3$ glasses by various spectroscopic measurements, using solid-state NMR and X-ray photoelectron spectroscopy [29]. Additionally, they successfully prepared $xSnO(100\text{-}x)B_2O_3$ ($0 \leq x \leq 80$) glasses by mechanical milling [30]. These investigations showed that the composition dependence of T_g for the milled glasses was similar to that of the corresponding melt-quenched glasses. Geijke *et al.* presented a neutron diffraction study of SnB_2O_4 glass, including a reverse Monte Carlo modelling, in which an average 3–3.5 fold coordination of boron gave an excellent agreement with the experimental structure factors [31]. Concerning SnO, the authors suggested the role of a network glass former (bridging between two neighboring borate units) than simply as a network modifier. Another study on $SnB_{2.2}O_{4.3}$, using diffuse reflectance infrared spectroscopy, led to the conclusion, that this compound is mainly built up from meta-borate groups, forming a network [32]. Furthermore, Gejke *et al.* investigated the effect of lithium insertion/extraction in/out of SnB_2O_4 and $Sn_2B_3O_{6.5}$ glass electrodes by *in situ* ^{119}Sn Mößbauer measurements [33]. They were able to show that there was some disruption of the glass network during the first cycle, which was responsible for a major part of the capacity loss. Recapitulating, several investigations have been performed until now in the ternary system Sn–B–O as a simplified variant of the original TCO glass, in which all known compositions are glasses without any exception. Although glasses are only

partly comparable to crystalline compounds, the knowledge about possible structural building blocks and models of linkage inside the glasses can be enhanced by crystalline approximands. Therefore, we started our investigations into the system Sn–B–O, aiming at a crystalline tin borate by use of the parameter "pressure". In principle, pressure can induce amorphization or crystallization, depending on the applied parameters in a specific chemical system [34, 35, 385–390]. Several reasons for amorphization like thermodynamic melting and mechanical instabilities were quoted. Meanwhile, it is established that the pressure-induced amorphization leads to a kinetically preferred amorphous state in most systems. The progress of the transformation to the high-pressure equilibrium state is presumably impeded by a lack of thermal energy. Recently, the assumption of an intermediate state between two thermodynamically stable states was confirmed by Zhang *et al.*, showing that the final equilibrium phases are independent of the starting materials [390].

As elaborated above, a lot of research activity was carried out concerning the huge family of main metal borates. Noticably no investigations within the scope of high-pressure experiments were conducted in this field of chemisty. Therefore we concentrated our attention on the high-pressure behaviour of the systems Ba–B–O, Bi–B–O, and Sn–B–O, which led us to the first high-pressure phases within these systems. In the case of the elemental combination Sn–B–O we were even able to synthesize the first crystalline ternary compound. In the following the synthesis, structural charactarization, and description of the new high-pressure phases β-BaB_4O_7, δ-BiB_3O_6, and β-SnB_4O_7 are discussed.

4.2.2 Starting Materials

The starting materials for the adjacent syntheses were all air- and humidity-resistant. The characterization of the crystalline materials was carried out *via* powder diffraction followed by a comparison with the ICSD-database, whereas only crystalline impurities with a concentration over 3 % can be detected. The used substances are listed in Table 4.61.

Table 4.61: List of used substances.

Substance	State	Source of Supply	Purity	ICSD-PDF
B_2O_3	Granulate	Strem Chemicals, Newburyport, USA	99.9	amorphous
"BaO"	Powder	Fluka Chemie AG, Buchs, Switzerland	*p.a.*	[26-154],$Ba(OH)_2 \cdot H_2O$ [33-153], $Ba(OH)_2 \cdot 3\,H_2O$
Bi_2O_3	Powder	Merck, Darmstadt	extra pure	[45-1344], [71-465]
SnO	Powder	Strem Chemicals, Newburyport, USA	99	[72-1012]

4.2.3 The Borate β-BaB_4O_7

4.2.3.1 Synthesis

To synthesize the compound β-BaB_4O_7 [391], high-pressure/high-temperature conditions of 7.5 GPa and 1100 °C were applied (Equation 4.11), starting from stoichiometric mixtures of $Ba(OH_2)$ (hydrolyzed oxide BaO; Fluka Chemie AG, Buchs, Switzerland, *p.a.*) and B_2O_3 (Strem Chemicals, Newburyport, USA, 99.9 %). The starting materials were ground up and filled into a boron nitride crucible of an 18/11 assembly. At 1100 °C, ware is completely lost from the reaction mixture, so the reaction can be formulated as follows:

$$\mathrm{Ba(OH_2)} + 2\,\mathrm{B_2O_3} \xrightarrow[1100\ ^\circ\mathrm{C}]{7.5\ \mathrm{GPa}} \beta\text{-}\mathrm{BaB_4O_7} + \mathrm{H_2O} \tag{4.11}$$

The assembly was compressed to 7.5 GPa in 3 h and heated up to 1100 °C in the following 10 min, kept there for 10 min, and cooled down to 500 °C in 90 min at constant pressure. Then, the sample was quenched to room temperature by switching off the heating, followed by a decompression period of 9 h. After this, the recovered octahedral pressure medium was broken apart and the sample carefully separated from the surrounding graphite and boron nitride. β-BaB_4O_7 was obtained as a colourless, air- and water-resistant, crystalline solid.

4.2.3.2 Crystal Structure Analysis

The powder diffraction pattern of β-BaB_4O_7 was obtained in transmission geometry from a flat sample using a STOE Stadi P powder diffractometer with monochromatized $CuK_{\alpha 1}$ radiation (λ = 154.051 pm). The diffraction pattern was indexed with the program TREOR [122–124] on the basis of an orthorhombic unit cell. The lattice parameters (Table 4.62) were calculated from least-squares fits of the powder data. The correct indexing of the pattern of β-BaB_4O_7 was confirmed by intensity calculations, taking the atomic positions from the structure refinement [121]. The lattice parameters, determined from the powder data and single crystal data, fit well. Figure 4.87 compares the experimental powder diagram to the powder pattern derived from the single crystal data. No additional reflections, indicating a crystalline impurity, were found. Small single crystals of β-BaB_4O_7 were isolated by mechanical fragmentation and examined through a Buerger camera, equipped with an image plate system (Fujifilm BAS-2500). Single crystal intensity data of β-BaB_4O_7 were measured by means of an Enraf-Nonius Kappa CCD with graded multilayer X-ray optics (MoK_α radiation, λ = 71.073 pm). Afterwards, a multi-scan absorption correction was applied to the data (SCALEPACK [133]). According to the systematic extinctions $0kl$ with $k + l \neq 2n$, $hk0$ with

$h \neq 2n$, $h00$ with $h \neq 2n$, $0k0$ with $k \neq 2n$, $00l$ with $l \neq 2n$, the orthorhombic space group *Pmnb* (No. 62) was derived. Structure solution and parameter refinement (full-matrix least squares against F^2) were successfully performed using the SHELX-97 software suite [135, 136]. Details of the data collection and structure refinement are listed in Table 4.62. The positional parameters, anisotropic displacement parameters, interatomic distances, and interatomic angles are given in Tables 4.63–4.66.

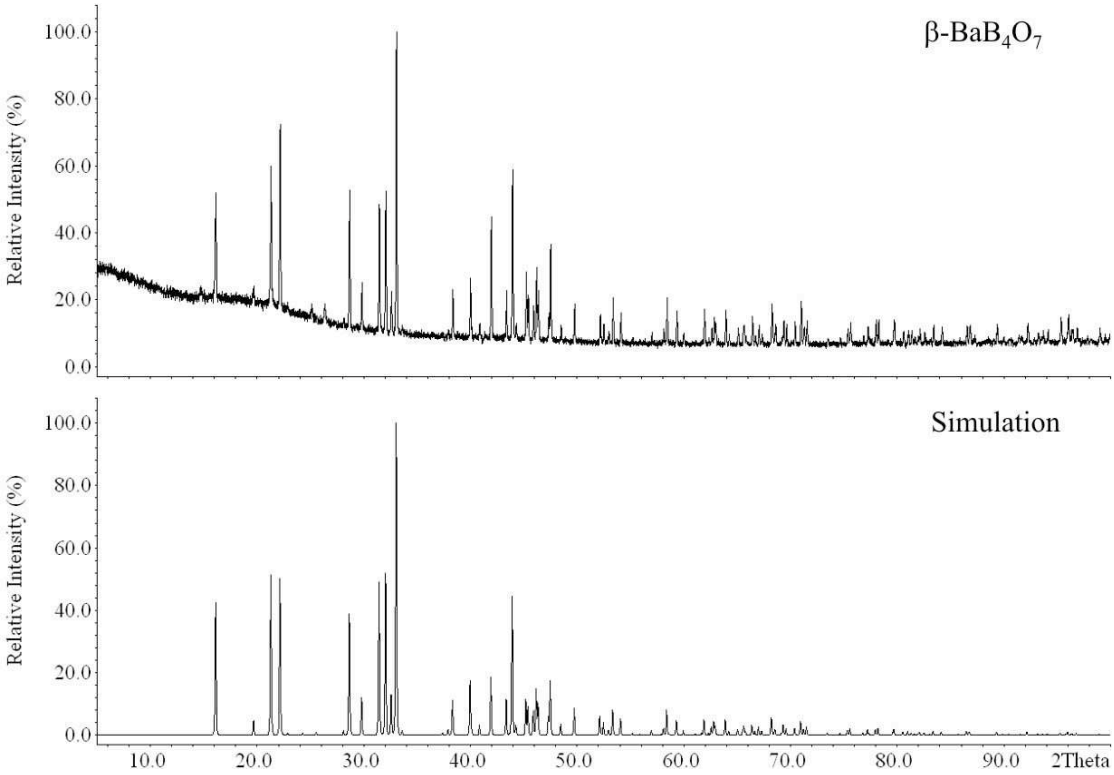

Figure 4.87: Measured (top) and simulated (single crystal data) (bottom) powder diffraction patterns of β-BaB_4O_7.

Table 4.62: Crystal data and structure refinement of β-BaB_4O_7 (standard deviations in parentheses).

Empirical formula	BaB_4O_7
Molar mass/g·mol^{-1}	292.58
Crystal system	orthorhombic
Space group	*Pmnb*
Powder diffractometer	STOE Stadi P
Radiation	$CuK_{\alpha 1}$ (λ = 154.051 pm)
Lattice parameters from powder data	
a/pm	1098.45(4)
b/pm	900.85(3)
c/pm	430.34(2)
V/nm^3	0.426
Single crystal diffractometer	Enraf-Nonius Kappa CCD
Radiation	MoK_α (λ = 71.073 pm)
Single crystal data	
a/pm	1099.4(2)
b/pm	901.7(2)
c/pm	430.73(9)
V/nm^3	0.427
Formula units per cell	Z = 2
Temperature/K	293(2)
Calculated density/g·cm^{-3}	4.55
Crystal size/mm^3	0.04 × 0.02 × 0.02
Detector distance/mm	30
Scan time per degree/min	50
Absorption coefficient/mm^{-1}	9.28
F(000)/e	528
θ range /°	3.7–40.2
Range in hkl	±19, -16/+14, ±7
Total no. reflections	6549
Independent reflections	1377
Reflections with I > 2σ(I)	1273
Data/parameters	1377/59
Absorption correction	multi-scan (SCALEPACK [133])
Goodness-of-fit (F^2)	1.075
Final R indices (I > 2σ(I))	R1 = 0.0173
	wR2 = 0.0395
R indices (all data)	R1 = 0.0199
	wR2 = 0.0406
Extinction coefficient	0.0055(4)
Largest diff. peak, deepest hole/e·Å^{-3}	1.708/-1.447

Table 4.63: Atomic coordinates and equivalent isotropic displacement parameters $U_{eq}/Å^2$ of β-BaB_4O_7 (space group *Pmnb*). U_{eq} is defined as one third of the trace of the orthogonalized U_{ij} tensor (standard deviations in parentheses).

Atom	Wyckoff Position	x	y	z	U_{eq}
Ba	4*c*	1/4	0.35283(2)	0.23024(3)	0.00641(4)
B1	8*d*	0.4995(2)	0.3425(2)	0.7207(3)	0.0050(2)
B2	8*d*	0.3738(2)	0.5894(2)	0.7942(3)	0.0051(2)
O1	8*d*	0.46252(9)	0.1952(2)	0.8764(2)	0.0053(2)
O2	4*c*	1/4	0.1345 (2)	0.7864(3)	0.0056(2)
O3	8*d*	0.39475(9)	0.4362(2)	0.7049(2)	0.0057(2)
O4	8*d*	0.3936(1)	0.6085(2)	0.1268(2)	0.0058(2)

Table 4.64: Anisotropic displacement parameters of β-BaB_4O_7 (standard deviations in parentheses).

Atom	U_{11}	U_{22}	U_{33}	U_{23}	U_{13}	U_{12}
Ba	0.00689(6)	0.00611(6)	0.00622(6)	0.00017(3)	0	0
B1	0.0052(5)	0.0047(6)	0.0050(5)	0.0000(4)	0.0001(4)	-0.0005(4)
B2	0.0052(5)	0.0046(5)	0.0054(5)	-0.0001(4)	-0.0001(4)	0.0001(4)
O1	0.0065(4)	0.0051(4)	0.0041(3)	0.0010(3)	-0.0010(3)	-0.0014(3)
O2	0.0030(5)	0.0065(5)	0.0072(5)	-0.0012(4)	0	0
O3	0.0056(4)	0.0042(4)	0.0074(4)	-0.0006(3)	-0.0006(3)	0.0012(3)
O4	0.0062(4)	0.0074(4)	0.0038(3)	-0.0004(3)	-0.0007(3)	-0.0016(3)

4.2.3.3 Crystal Structure Description

The crystal structure of β-BaB_4O_7 is composed of corner-sharing BO_4-tetrahedra, interconnected to a network isotypic to the mineral barylite $BaBe_2Si_2O_7$ [392]. 2/7 of the oxygen atoms link three tetrahedra ($O^{[3]}$), while 5/7 connect two tetrahedra ($O^{[2]}$). Figure 4.88 gives a view of β-BaB_4O_7 along [00$\bar{1}$], showing the network structure, which is crossed by channels along [001]. These channels are built up from "Vierer" and "Sechser" rings (a ring with four and six tetrahedral centres, respectively) [39]. Inside of the "Sechser" ring channels, the cations are located, while the "Vierer" ring channels

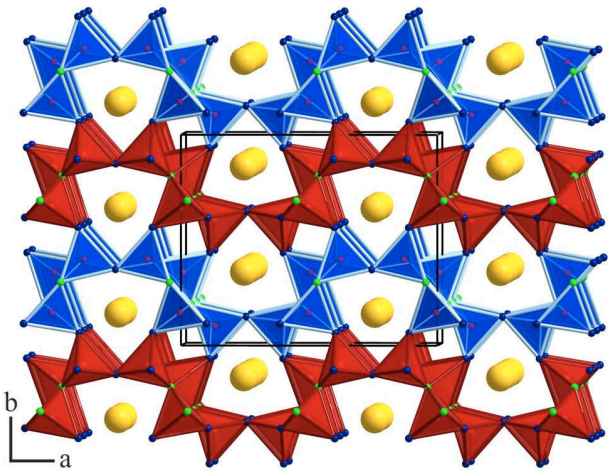

Figure 4.88: Crystal structure of β-BaB_4O_7 with view along [00$\bar{1}$]. Ba^{2+}: yellow, B^{3+}: red, $O^{[2]}$: blue, $O^{[3]}$: green.

remain empty. The structure is closely related to the orthorhombic high-pressure phases β-MB$_4$O$_7$ (M = Ca [173], Hg [172], Sn [393]) and the ambient-pressure phases MB$_4$O$_7$ (M = Sr [174, 175], Pb [175, 176], Eu [177]), but shows a different orientation of the tetrahedra. Figure 4.89 shows a comparison of the crystal structures of β-BaB$_4$O$_7$ (left), β-MB$_4$O$_7$ (M = Ca [173], Hg [172], Sn [393]), and MB$_4$O$_7$ (M = Sr [174, 175], Pb [175, 176], Eu [177]) (right) along [100]. In the latter compounds, all tetrahedra point towards the left hand side ([00$\bar{1}$] direction). This illustrates clearly that the structure of β-MB$_4$O$_7$ (M = Ca [173], Hg [172],

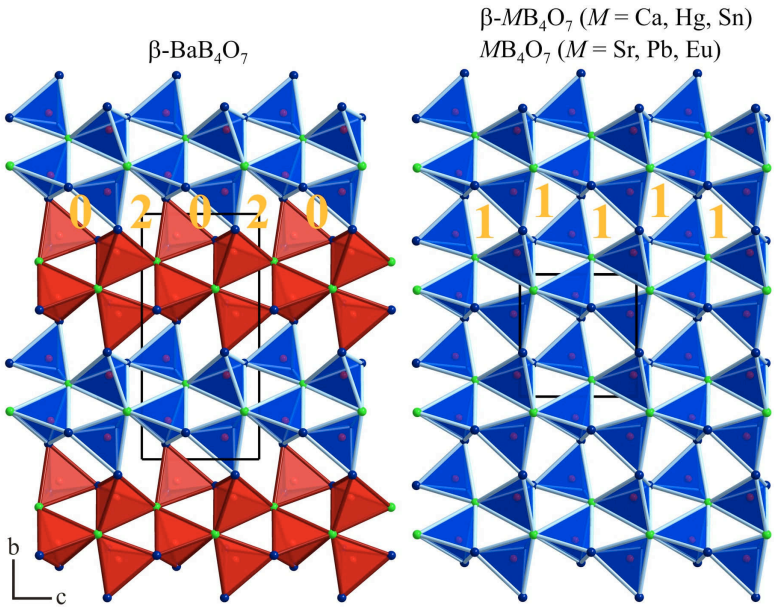

Figure 4.89: View of the crystal structure of β-BaB$_4$O$_7$ along [100] (left) in comparison to the crystal structure of β-MB$_4$O$_7$ (M = Ca, Hg, Sn) and MB$_4$O$_7$ (M = Sr, Pb, Eu) along [100] (right). "Vierer" rings are labeled with their number of O$^{[3]}$ atoms.

Sn [393]) and MB$_4$O$_7$ (M = Sr [174, 175], Pb [175, 176], Eu [177]) is acentric. By contrast, the BO$_4$-network in β-BaB$_4$O$_7$ can be divided into layers, spreading along the ac-plane, consisting of tetrahedra pointing either in the [00$\bar{1}$] or in the [001] direction (Figure 4.89: different colours). The layers can be transformed into one another by a centre of inversion. This can be considered as chemical twinning. In this sense, β-BaB$_4$O$_7$ can be regarded as the first centrosymmetric variant of the compounds β-MB$_4$O$_7$ (M = Ca [173], Hg [172], Sn [393]) and MB$_4$O$_7$ (M = Sr [174, 175], Pb [175, 176], Eu [177]). An examination of the linkage of the layers leads to a different connection between the borate-layers. The generated "Vierer" rings (a ring with four tetrahedral centres) [39] show unequal numbers of three-fold coordinated oxygen atoms O$^{[3]}$. Thus, β-BaB$_4$O$_7$ reveals "Vierer" rings, which alternating exist of two and zero O$^{[3]}$ atoms, whereas β-MB$_4$O$_7$ (M = Ca [173], Hg [172], Sn [393]) and the ambient-pressure phases MB$_4$O$_7$ (M = Sr [174, 175], Pb [175, 176], Eu [177]) show only rings with one O$^{[3]}$ atom. In Figure 4.89 the

rings are marked with the quantity of threefold coordinated oxygen atoms (orange numbers). Interestingly, the both polymorphs of $BaBe_2Si_2O_7$ barylite [392] and clinobarylite [394] show the same relationship as exist between β-BaB_4O_7 and β-MB_4O_7 (M = Ca [173], Hg [172], Sn [393]) as well as MB_4O_7 (M = Sr [174, 175], Pb [175, 176], Eu [177]). This is another impressive example for the chemical connection between borates and silicates.

Figure 4.90 gives a view of the coordination of the barium cations along [100], which are positioned inside of the "Sechser" ring channels. The Ba cations are coordinated by 16 oxygen atoms in the range of 270–338 pm with a mean value of 297.6 pm. This is in accordance with the pressure-coordination rule, considering the coordination numbers of 10 for Ba1 (261–334 pm) and 11 for Ba2 (272 – 340 pm) in α-BaB_4O_7 [372]. These coordination numbers are derived by ECoN calculations (Effective Coordination Numbers according to Hoppe) [161, 162] calculated with the program MAPLE [163]. The coordination numbers published by Block and Perloff [372] are not consistent with those received through ECoN calculations. Block and Perloff considered the coordinative spheres to be 9 for Ba1 and 10 for Ba2. The 10th and 11th oxygen atoms in the coordination spheres of Ba1 and Ba2, respectively, exhibit a difference in their Ba–O distance to the former oxygen atom of ca. 25 pm (Ba1) and 28 pm (Ba2). This is remarkably larger than the other differences in the Ba–O bond lengths, which range between ca. 1 and 12 pm. However, the 10th oxygen atom bonding to Ba1 and 11th oxygen atom bonding to Ba2 show contributions of 0.126 and 0.224 in the ECoN calculation, respectively. A consideration of the next oxygen atoms in the coordination spheres reveals differences in the Ba–O distances of 35 pm for the 11th atom bonding to Ba1 and 68 pm for the 12th atom bonding to Ba2. A comparison of the coordination of the cations in β-BaB_4O_7 and β-CaB_4O_7 discloses the different coordination numbers of 16 for Ba and 15 for Ca. This is caused by the different orientation of the BO_4-tetrahedra in the crystal structures of both compounds. The difference gets visible in Figure 4.90, where the regarded Ba–O bond is marked in red.

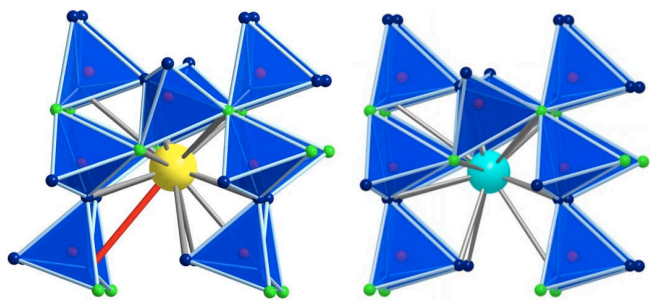

Figure 4.90: Coordination of Ba^{2+} (left) and Ca^{2+} (right) in β-BaB_4O_7 and β-CaB_4O_7, respectively. Red spheres represent B, blue spheres $O^{[2]}$ and green spheres $O^{[3]}$.

The other well characterized barium borates show smaller coordination numbers for the Ba atoms. In α-BaB_2O_4, as well as in β-BaB_2O_4 [13], Ba^{2+} is coordinated by 8 oxygen atoms in the range of 261–303 pm and 249–367 pm, respectively. $Ba_5(BO_3)_2(B_2O_5)$ [374] exhibits Ba^{2+} in seven-

and eightfold coordination, with a distance range between 251–310 pm. In the two crystallographically distinguishable BO_4-groups inside of the structure of β-BaB_4O_7, the B–O distances vary between 142–158 pm with an average value of 148.6 pm, which is slightly higher than the known average value of 147.6 pm for B–O bonds in tetrahedral BO_4-groups [232, 233]. This is caused by the linkage of the BO_4-tetrahedra *via* threefold coordinated oxygen atoms. The B–O[3] distances reveal a mean value of 156 pm, which is in agreement with the distances in other borates, revealing threefold coordinated oxygen atoms, *e.g.* β-MB_4O_7 (M = Mn [261], Co, Ni [261], Cu [261], Zn [171]), β-$RE(BO_2)_3$ (RE = Nd, Sm, Gd–Lu) [262–264], γ-$RE(BO_2)_3$ (RE = La–Nd) [265, 266], and minerals like tunnelite ($SrB_6O_9(OH)_2{\cdot}3H_2O$), strontioginorite ($(Sr,Ca)_2B_{14}O_{20}(OH)_6{\cdot}6H_2O$) [267], aristarainite ($Na_2Mg[B_6O_8(OH)_4]_2{\cdot}4H_2O$) [268], and the high-pressure modification of B_2O_3 [82]. The angles O–B–O range from 106.4 to 120.4° with a mean value of 109.5°.

Table 4.65: Interatomic distances/pm in β-BaB_4O_7 (space group *Pmnb*) calculated with the single crystal lattice parameters (standard deviations in parentheses).

Ba-O3	269.8(1) 2×	B1-O4	141.7(2)	B2-O3	145.2(2)
Ba-O2	274.4(2)	B1-O3	143.0(2)	B2-O4	145.9(2)
Ba-O4	278.0(2) 2×	B1-O1a	154.2(2)	B2-O2	146.2(2)
Ba-O4	283.0(2) 2×	B1-O1b	157.8(2)	B2-O1	155.0(2)
Ba-O3	286.7(2) 2×		Ø = 149.2		Ø = 148.1
Ba-O2	310.0(2)				
Ba-O1	313.1(2) 2×	O1-B1a	154.2(2)		
Ba-O1	325.2(2) 2×	O1-B2	155.0(2)		
Ba-O2	328.4(2)	O1-B1b	157.8(2)		
Ba-O2	337.7(2)		Ø = 155.7		
	Ø = 297.6				

Table 4.66: Interatomic angles/° in β-BaB_4O_7 calculated with the single crystal lattice parameters (standard deviations in parentheses).

O4-B1-O1a	106.4(2)	O4-B2-O1	107.4(2)	B2-O1-B1a	118.7(1)
O4-B1-O1b	106.6(1)	O2-B2-O1	107.6(2)	B1b-O1-B2	119.3(1)
O1a-B1-O1b	107.0(1)	O4-B2-O2	109.8(2)	B1a-O1-B1b	121.65(8)
O3-B1-O1a	107.2(1)	O3-B2-O4	110.4(2)	Ø = 119.9	
O3-B1-O1b	108.5(2)	O3-B2-O2	110.5(2)		
O4-B1-O3	120.4(2)	O3-B2-O1	111.1(2)		
Ø = 109.4		Ø = 109.5			

4.2.3.4 Thermal Behaviour

In situ X-ray powder diffraction experiments were performed on a STOE Stadi P powder diffractometer ($MoK_{\alpha 1}$ radiation (λ = 71.073 pm)) with a computer controlled STOE furnace. The sample was enclosed in a silica capillary and heated

from room temperature to 500 °C in 100 °C steps, and from 500 °C to 1100 °C in 50 °C steps. The heating rate was set to 40 °C/min. Afterwards, the sample was cooled down to 500 °C in 50 °C steps, and from 500 °C to room temperature in 100 °C steps (heating rate: 50 °C/min). After each heating step, a diffraction pattern was recorded over the angular range 6°≤ 2θ ≤ 30°. Figure 4.91 shows that β-BaB_4O_7 is stable up to a temperature of 800 °C and transforms into an X-ray amorphous phase between 800 and 850 °C.

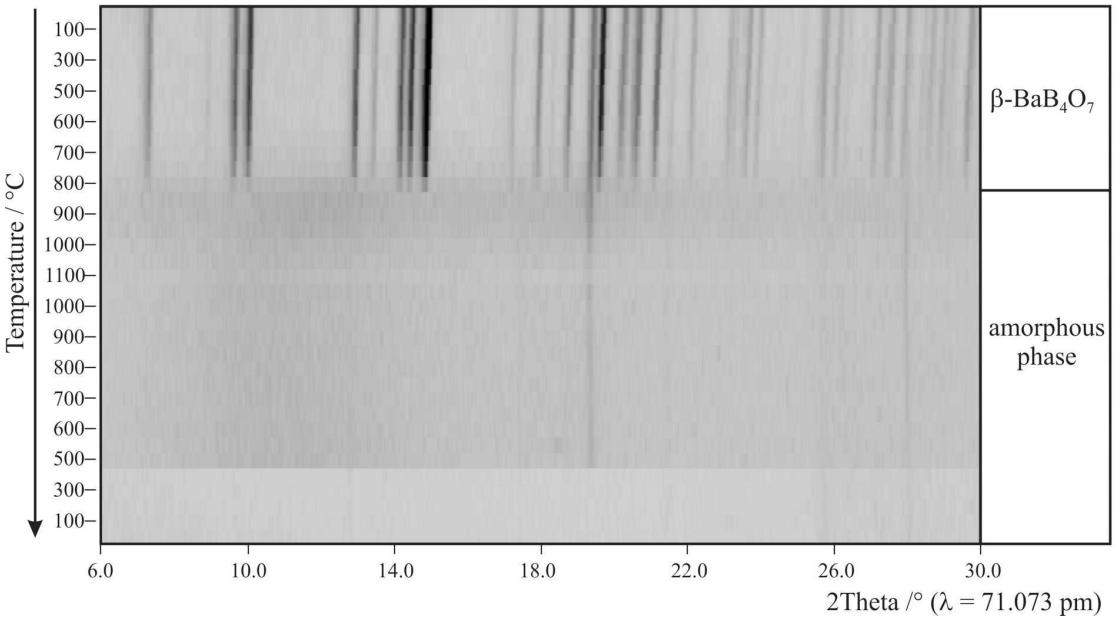

Figure 4.91: *In situ* X-ray powder patterns of β-BaB_4O_7.

4.2.3.5 Theoretical Calculations

Bond-valence sums for β-BaB_4O_7 were calculated with the help of bond-length/bond-strength [164, 165] and CHARDI (ΣV) [167] concepts (see Table 4.67). The formal ionic charges of the atoms, acquired by X-ray structure analysis, were in agreement within the limits of both concepts, except for the threefold coordinated oxygen atom O1 and Ba^{2+}. The oxygen atom O1 shows a reduced value of -1.71 (ΣQ) in the CHARDI concept. Similar deviating values for $O^{[3]}$ atoms are obtained in β-SnB_4O_7 (-1.92 (ΣV); -1.93 (ΣQ)) [393], β-CaB_4O_7 (-1.92 (ΣV); -1.77 (ΣQ)) [173], β-HgB_4O_7 (-2.06 (ΣV); -1.83 (ΣQ)) [172], and β-ZnB_4O_7 (1.83 (ΣV); 1.67 (ΣQ)) [171]. Ba^{2+} shows a heightened value of +2.96 (ΣQ) in the bond-length/bond-strength concept. This presumably results in the high coordination (C. N. = 16) of the barium cation. On the other hand, the CHARDI calculation for Ba^{2+} with $\Sigma Q = +1.95$ fits well to the expected value of +2.

Furthermore, we calculated the MAPLE values (Madelung Part of Lattice Energy) [161–163] for β-BaB_4O_7 in order to compare the results with MAPLE values

Table 4.67: Charge distribution in β-BaB_4O_7 calculated with the bond-length/bond-strength concept (ΣV) and the CHARDI concept (ΣQ).

	Ba	B1	B2	O1	O2	O3	O4
ΣV	+ 2.96	+ 2.94	+ 2.99	- 2.01	- 2.09	- 2.20	- 2.17
ΣQ	+ 1.95	+ 3.04	+ 2.99	- 1.71	- 1.95	- 2.15	- 2.16

of the binary components BaO ($Fm\overline{3}m$ [395]) and the high-pressure modification B_2O_3-II [82]. The calculated value (47599 kJ·mol^{-1}) for β-BaB_4O_7 and the MAPLE value obtained from the sum of the binary oxides (47396 kJ·mol^{-1}) tally well (deviation 0.4 %). A comparison to the α-modification of BaB_4O_7 provides a MAPLE value of 47496 kJ·mol^{-1} (deviation 0.2 %).

4.2.3.6 DFT Calculations

Structural optimizations, total energies, and properties were calculated within density functional theory (DFT) [154], for which the Vienna *ab-initio* Simulation Package (VASP) was used. It combines the total energy pseudopotential method with a plane-wave basis set [155–157]. The electron exchange and correlation energy is treated within the general gradient approximation (GGA) [158] to approximate the electron exchange and correlation energy. The utilized pseudopotentials were based on the projector-augmented-wave (PAW) method [159]. The cut-off energy for the expansion of the wave function into the plane wave basis set was 500 eV. Residual forces were converged below $5{\cdot}10^{-3}$ eV/Å. The Brillouin-Zone integration was carried out *via* the Monkhorst-Pack scheme [160].

The choice of the GGA functional is based on the experience that it significantly better describes relative energies of structures with different coordination of the atoms. Since our target is to study structures and structural transformations at high pressures, it is the better choice in comparison to the local density approximation (LDA). Therefore, though we controlled all our calculations within the LDA as well, all enthalpy differences and transition pressures given are based on GGA calculations. Structure optimizations for α-BaB_4O_7 [372], β-BaB_4O_7, and BaB_4O_7 in the β-CaB_4O_7 [173] structure were done by relaxing all internal parameters as well as cell parameters and the unit cell volume. The unit cell of α-BaB_4O_7 contains 96 atoms (8 formula units). The structure was computed using the conventional unit cell and a k-point mesh of 4×4×4. The unit cell of β-BaB_4O_7 contains 48 atoms (4 formula units). A k-point mesh of 4×4×8 was used for optimization. The unit cell of β-CaB_4O_7 comprises 24 atoms (2 formula units). Calculations were done in the conventional unit cell. A k-point mesh of 4×8×8 was employed.

To obtain the bulk modulus, the volume is varied around the zero pressure volume V_0 and the calculated energies are fitted to Murnaghans, Birchs, and Vinets

Equation of State (EOS) [396–399]. The E-V diagrams can be transformed easily to give enthalpy versus pressure diagrams. To get the pressure p from the E-V graph a simple numerical differentiation of a spline fit and Murnaghans, Birchs, and Vinets EOS is employed: $p = -\partial E/\partial V$. After conversion into H-p data the obtained data from different fitting procedures resulted in virtually the same transition pressures. For reasons of simplicity, all figures and values given in this work are derived from evaluation by Murnaghans EOS.

The enthalpy H is calculated *via* $H = E + pV$. In equilibrium a system will adopt the structure with the lowest free energy G. A phase transformation is therefore governed by the difference of free enthalpy: $\Delta G = \Delta E + p\Delta V - T\Delta S$. The contribution of the entropy is usually neglected, due to the small difference in entropy between solid state crystal structures and the comparably larger changes of ΔH within 1 GPa of pressure change. Therefore, $\Delta H = \Delta E + p\Delta V$ is a good measure to compare the relative stability of solid state structures under pressure.

The calculated unit cell parameters and equilibrium volumes for α-BaB_4O_7 as well as for β-BaB_4O_7 accord well with the experimental values. No particular bond lengths or any significant distortion of the structure have been observed. Detailed data on structure optimizations of α-BaB_4O_7 and β-BaB_4O_7 compared to experimental data are given in Table 4.68.

Table 4.68: Structure optimization of α-BaB_4O_7 and β-BaB_4O_7.

	α-BaB_4O_7	GGA	β-BaB_4O_7	GGA
Space group	$P2_1/c$ (No. 14, monoclinic)		*Pmnb* (No. 62, orthorhombic)	
a / pm	1056(1)	1072.24	1099.4(2)	1110.25
b / pm	820(1)	839.06	901.7(2)	909.38
c / pm	1301(1)	1313.73	430.73(9)	434.50
β / °	104.95(17)	104.80		
V / 10^6 pm^3	1088(20)	1142.69	427	438.69
V f.u. / 10^6 pm^3	136	142.84	107	109.67
δ / g·cm^{-3}	3.57	3.40	4.55	4.43

The structure of β-CaB_4O_7 [173] was also considered as a candidate for BaB_4O_7. The Ca^{2+} ions in β-CaB_4O_7 are coordinated by 15 oxygen ions, whereas the Ba^{2+} ions for the hypothetical BaB_4O_7 in the β-CaB_4O_7 structure are coordinated by 16 oxygen atoms (coordination numbers for M^{2+} confirmed by ECoN [162], calculated with MAPLE [163]). A comparison of the lattice parameters of β-CaB_4O_7 and BaB_4O_7 in the β-CaB_4O_7 structure is given in Table 4.69. The calculated bond lengths for BaB_4O_7 in the β-CaB_4O_7 structure are all in the range of those in α- and β-BaB_4O_7 (Table 4.70).

A comparison of the densities and ground state energies of the three considered BaB_4O_7 structures shows that – as expected – the ambient pressure phase α-BaB_4O_7 has the lowest density (δ = 3.57 g·cm^{-1} (experimental); 3.40 g·cm^{-1}

Table 4.69: Structure optimization of BaB_4O_7 in the β-CaB_4O_7 structure.

	β-CaB_4O_7	BaB_4O_7 GGA
space group	$Pmn2_1$ (No. 31, orthorhombic)	
a / pm	1058.4(1)	1105.54
b / pm	436.94(10)	455.88
c / pm	419.35(10)	434.34
V / 10^6 pm^3	193.93(7)	218.90
V f.u. / 10^6 pm^3	96.97	109.45
δ / g·cm^{-3}	3.34	4.44

Table 4.70: Bond lengths/pm in BaB_4O_7 in the β-CaB_4O_7 structure compared to values of α- and β-BaB_4O_7.

α-BaB_4O_7		β-BaB_4O_7		β-CaB_4O_7 structure BaB_4O_7 GGA	
$Ba^{[10,11]}$-O	260.9–340.3	$Ba^{[16]}$-O	269.8–337.7	$Ba^{[16]}$-O	268.96–346.23
$B^{[3,4]}$-O	129.6–153.1	$B^{[4]}$-O	141.7–157.8	$B^{[4]}$-O	142.22–159.33
$O^{[3]}$-B	/	$O^{[3]}$-B	154.2–157.8	$O^{[3]}$-B	155.94–159.33
$O^{[2]}$-B	129.6–153.1	$O^{[2]}$-B	141.7–146.2	$O^{[2]}$-B	142.22–147.06

(calculated)) and energy (-95.4121 eV per formula unit). The next denser structure is that of β-BaB_4O_7 (δ = 4.55 g·cm^{-1} (experimental); 4.43 g·cm^{-1} (calculated)), with an energy per formula unit of -95.1080 eV. BaB_4O_7 in the β-CaB_4O_7 structure comes out even denser (δ = 4.44 g·cm^{-1} (calculated)). The energy of BaB_4O_7 in the β-CaB_4O_7 structure in its ground state is 0.3146 eV per formula unit higher with respect to α-BaB_4O_7 and 0.0105 eV with respect to β-BaB_4O_7. However, while the difference in density and energy for α-BaB_4O_7 and β-BaB_4O_7 is quite large (0.3041 eV), it is very small for β-BaB_4O_7 and BaB_4O_7 in the β-CaB_4O_7 structure, coming up against limiting factors of accuracy attainable for energy differences. The bulk modulus of α-BaB_4O_7 has been calculated to 51 GPa, of β-BaB_4O_7 to 159 GPa and of BaB_4O_7 in the β-BaB_4O_7 structure to 154 GPa.

In Figures 4.92 and 4.93, the E-V curves of the three structures of BaB_4O_7 are shown, from which the enthalpy as a function of pressure is extracted, as depicted in Figure 4.94. Accordingly, the transition pressure of α-BaB_4O_7 to β-BaB_4O_7 is calculated to 1.5 GPa. At 7.5 GPa the enthalpy of BaB_4O_7 in the β-CaB_4O_7 structure becomes more favourable than that of β-BaB_4O_7, so that we tentatively propose BaB_4O_7 in the β-CaB_4O_7 structure as its second high-pressure phase.

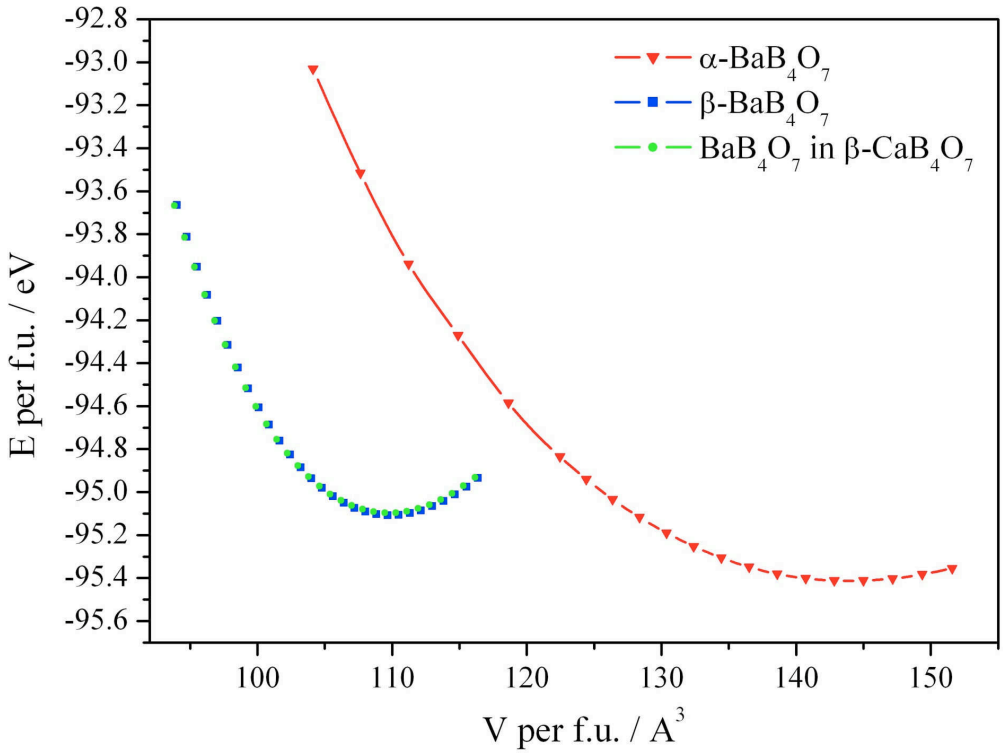

Figure 4.92: E-V diagram for all three considered phases of BaB_4O_7 (Red curve: α-BaB_4O_7, blue curve: β-BaB_4O_7, green curve: BaB_4O_7 in the β-CaB_4O_7 structure).

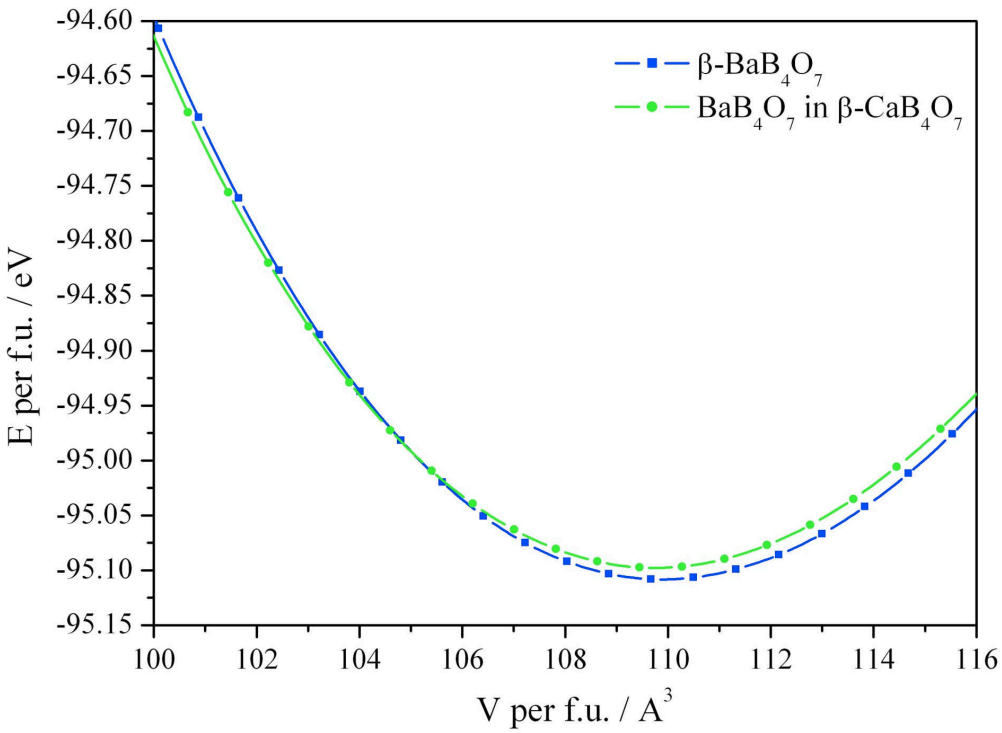

Figure 4.93: Zoom in on the two curves of β-BaB_4O_7 and BaB_4O_7 in the β-CaB_4O_7 structure.(Blue curve: β-BaB_4O_7, green curve: BaB_4O_7 in the β-CaB_4O_7 structure).

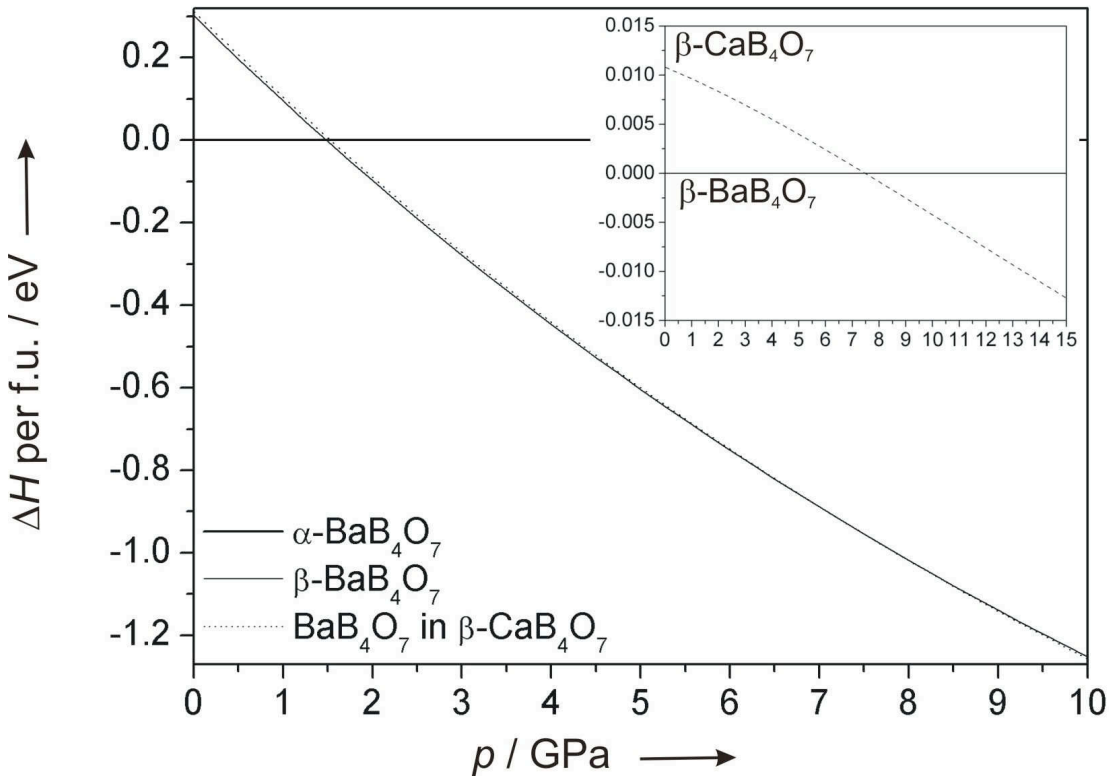

Figure 4.94: Enthalpy-pressure diagram for the transition of α-BaB_4O_7 into β-BaB_4O_7 (p_t = 1.5 GPa) and of β-BaB_4O_7 into BaB_4O_7 in the β-CaB_4O_7 structure (p_t = 7.5 GPa)(Murnaghan EOS evaluation).

4.2.4 The Borate δ-BiB_3O_6

4.2.4.1 Synthesis

According to Equation 4.12, the starting materials for the synthesis of δ-BiB_3O_6 [400] were stoichiometric mixtures of Bi_2O_3 (Merck, Darmstadt, extra pure) and B_2O_3 (Strem Chemicals, Newburyport, USA, 99.9%).

$$Bi_2O_3 + 3\,B_2O_3 \xrightarrow[820\ ^\circ C]{5.5\ GPa} 2\,\delta{-}BiB_3O_6 \tag{4.12}$$

The mixture (∼120 mg) was filled into a cylindrical boron nitride crucible of an 18/11 assembly. The arrangement was compressed within 120 min to 5.5 GPa and heated to 820 °C in the following 10 min. After holding this temperature for 5 min, the sample was cooled down to 500 °C in another 15 min and then quenched to room temperature by switching off the heating. After decompression (6 h), the recovered experimental octahedron was ruptured and the sample carefully separated from the surrounding boron nitride. The air- and humidity-resistant compound δ-BiB_3O_6 was obtained as a coarsely-crystalline, colourless solid. Systematic investigations of the minimal pressure for the synthesis of δ-BiB_3O_6 revealed a value of 3 GPa. Therefore, it should be experimentally possible, to grow large single crystals under high-pressure conditions for a detailed characterization of their nonlinear optical properties.

4.2.4.2 Crystal Structure Analysis

Powder diffraction was accomplished by a STOE Stadi P powder diffractometer with monochromatized $CuK_{\alpha 1}$ radiation in transmission geometry (flat sample). The diffraction diagram was indexed with the program TREOR [122–124] on the basis of an orthorhombic unit cell. Based on least-squares fits of the powder data, the lattice parameters (Table 4.71) were calculated. The correct indexing of the pattern was confirmed by intensity calculations [121], taking the atomic positions from the refined crystal structure data. The lattice parameters derived from the powder data and single crystal data accord. Figure 4.95 shows the experimental diffraction pattern of δ-BiB_3O_6, compared to the theoretical pattern calculated with the single crystal data. Additional reflections, marked with asterisks in Figure 4.95, belong to (an) undefined byproduct(s). Variation of temperature or pressure did not succeed in pure samples until now.

Single crystals of δ-BiB_3O_6 were isolated by mechanical fragmentation and examined through a Buerger camera, equipped with an image plate system (Fujifilm BAS-2500) in order to check suitability for an intensity data collection. Single crystal intensity data of δ-BiB_3O_6 were measured with an Enraf-Nonius Kappa

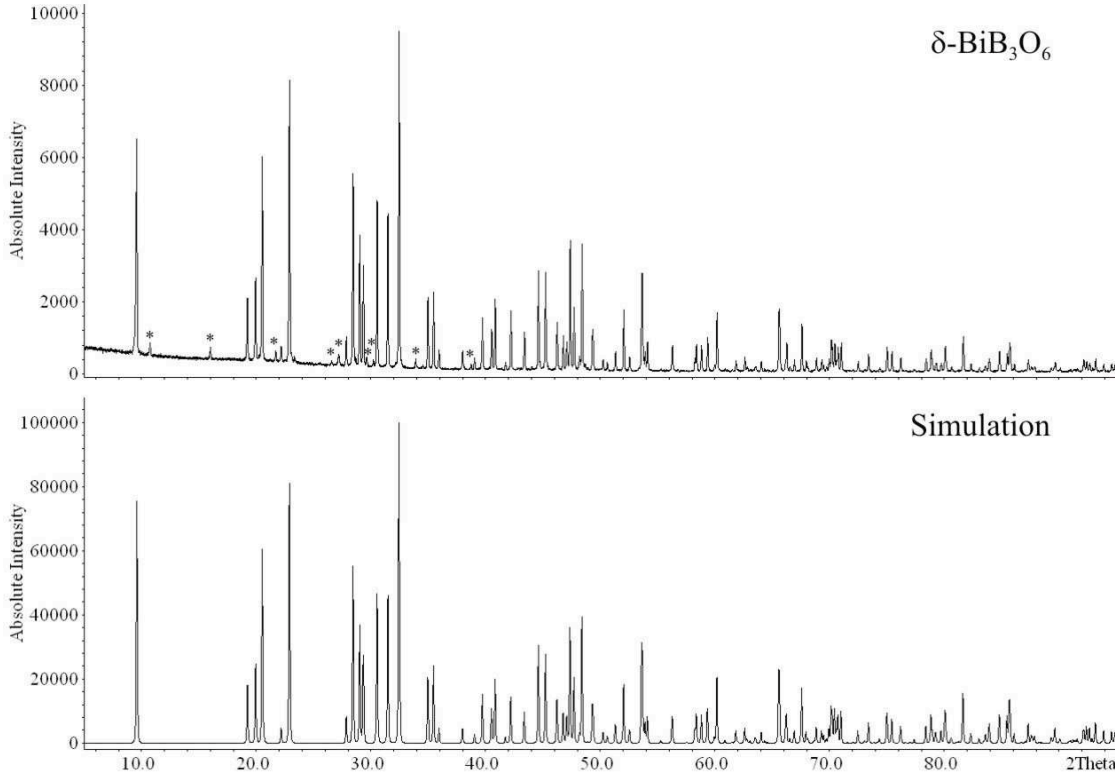

Figure 4.95: Experimental and simulated (single crystal data) powder diffraction patterns of δ-BiB_3O_6. Reflections of unknown byproduct(s) are marked with asterisks.

CCD diffractometer (MoK_α; λ = 71.073 pm). A multi-scan absorption correction was applied to the data (SCALEPACK [133]). According to the systematic extinctions $h0l$ with $h = l \neq 2n$, $h00$ with $h \neq 2n$, and $00l$ with $l \neq 2n$, the space groups $Pca2_1$ (No. 29) and $Pbcm$ (No. 57) were derived. The non-centrosymmetric group $Pca2_1$ was found to be correct during the refinement. This was confirmed with the ADDSYM routine of the program PLATON [139]. Supplemental, an ungraded powder sample of δ-BiB_3O_6 was subjected to a qualitative powder SHG measurement, using the method reported by Kurtz & Perry [401]. KDP (grain size 125 – 185 µm) was used as reference material. The observed intensities of the second harmonics generated by δ-BiB_3O_6 and by KDP were nearly equal, thus corroborating the non-centrosymmetry of δ-BiB_3O_6 and signalizing a considerable SHG effect of the measured sample [402]. Structure solution and parameter refinement (full-matrix least squares against F^2) were successfully performed using the SHELX-97 software suite [135, 136]. Table 4.71 lists details of the data collection and structure refinement. The positional parameters, anisotropic displacement parameters, interatomic distances, and interatomic angles are given in Tables 4.72–4.75.

Table 4.71: Crystal data and structure refinement of δ-BiB_3O_6 (standard deviations in parentheses).

Empirical Formula	BiB_3O_6
Molar mass/g·mol^{-1}	337.41
Crystal system	orthorhombic
Space group	$Pca2_1$
Powder diffractometer	STOE Stadi P
Radiation	$CuK_{\alpha 1}$ (λ = 154.051 pm)
Powder data	
a/pm	1844.56(5)
b/pm	444.79(2)
c/pm	427.81(2)
V/nm^3	0.351
Single crystal diffractometer	Enraf-Nonius Kappa CCD
Radiation	MoK_α (λ = 71.073 pm)
Single crystal data	
a/pm	1844.8(4)
b/pm	444.95(9)
c/pm	428.06(9)
V/nm^3	0.352(2)
Formula units per cell	Z = 4
Temperature/K	293(2)
Calculated density/g·cm^{-3}	6.378
Crystal size/mm^3	0.042 × 0.03 × 0.021
Detector distance/mm	30
Exposure time per plate/min	70
Absorption coefficient/mm^{-1}	50.11
F (000)/e	584
θ range/°	3.134–37.785
Range in hkl	±3, ±7, ±7
Total no. reflections	6356
Independent reflections	1866 (R_{int} = 0.0605)
Reflections with I > 2σ(I)	1736 (R_σ = 0.0467)
Data/parameters	1866/92
Flack-Parameter	-0.01(2)
Absorption correction	multi-scan (SCALEPACK [133])
Goodness-of-fit (F^2)	1.057
Final R indices (I > 2 σ(I))	R1 = 0.0276
	wR2 = 0.0643
R indices (all data)	R1 = 0.0304
	wR2 = 0.0664
Extinction coefficient	0.0076(5)
Largest diff. peak, deepest hole/e·Å^{-3}	4.078/-4.180

Table 4.72: Atomic coordinates and equivalent isotropic displacement parameters $U_{eq}/Å^2$ of δ-BiB_3O_6 (space group $Pca2_1$; all Wyckoff site $4a$). U_{eq} is defined as one third of the trace of the orthogonalized U_{ij} tensor (standard deviations in parentheses).

Atom	x	y	z	U_{eq}
Bi	0.837945(8)	0.15740(3)	0.7024(2)	0.00650(7)
B1	0.7883(2)	0.3102(7)	0.1578(8)	0.0061(7)
B2	0.9277(3)	0.673(2)	0.146(2)	0.0044(9)
B3	0.0023(3)	0.176(2)	0.114(2)	0.0055(9)
O1	0.7883(2)	0.3102(7)	0.1578(8)	0.0061(7)
O2	0.9394(2)	0.3611(8)	0.070(2)	0.0068(6)
O3	0.8543(2)	0.7597(9)	0.0338(8)	0.0051(5)
O4	0.7242(2)	0.7487(8)	0.9867(9)	0.0057(6)
O5	0.0679(2)	0.2639(9)	0.9753(9)	0.0070(6)
O6	0.9821(2)	0.8705(7)	0.9726(9)	0.0048(6)

Table 4.73: Anisotropic displacement parameters of δ-BiB_3O_6 (standard deviations in parentheses).

Atom	U_{11}	U_{22}	U_{33}	U_{23}	U_{13}	U_{12}
Bi	0.00793(9)	0.00577(9)	0.00581(9)	0.0003(2)	0.0008(2)	-0.00012(4)
B1	0.005(2)	0.002(2)	0.003(3)	0.002(15)	-0.001(2)	-0.000(2)
B2	0.005(2)	0.006(2)	0.002(2)	-0.000(2)	-0.002(2)	-0.001(2)
B3	0.005(2)	0.007(2)	0.005(2)	0.001(2)	-0.001(2)	-0.002(2)
O1	0.009(2)	0.005(2)	0.004(2)	-0.001(2)	0.002(2)	0.0002(9)
O2	0.009(2)	0.005(2)	0.007(2)	-0.002(2)	-0.002(2)	0.000(2)
O3	0.004(2)	0.007(2)	0.005(2)	-0.001(2)	-0.001(2)	0.002(2)
O4	0.004(2)	0.009(2)	0.005(2)	-0.002(2)	0.001(2)	0.001(2)
O5	0.008(2)	0.009(2)	0.005(2)	0.001(2)	0.001(2)	0.000(2)
O6	0.008(2)	0.004(2)	0.003(2)	-0.001(2)	0.002(2)	-0.000(2)

4.2.4.3 Crystal Structure Description

The crystal structure of δ-BiB_3O_6 is exclusively built up of BO_4-tetrahedra sharing common corners to form layers (Figure 4.96, blue polyhedra), that are shifted by a c-glide plane. These layers are interconnected *via* zigzag chains of BO_4-groups (red polyhedra in Figures 4.96 and 4.97), forming a network structure with channels of "Sechser" rings along [010] and "Zehner"- rings [39] along [001], containing the metal cations. Inside of the layers, the green spheres represent threefold-coordinated oxygen atoms ($O^{[3]}$; 1/6 of all oxygen atoms). Within the zigzag chains, only twofold coordinated oxygen atoms are found. This structure type was recently discovered by Huppertz *et al.*, realized in the high-pressure compounds γ-$RE(BO_2)_3$ (RE = La–Nd) [265, 266]. Drawing a comparison to other borate phases, a similarity to the well characterized high-pressure phases β-CaB_4O_7 [173], β-HgB_4O_7 [172], and β-SnB_4O_7 [393], as well as to the ambient-pressure phases SrB_4O_7 [174, 175], PbB_4O_7 [175, 176], and EuB_4O_7 [177] can be found. Both structure types exhibit topologically identical borate layers, but a different connection of them. While the layers are directly linked in MB_4O_7 (M =

Sr [174, 175], Pb [175, 176], Eu [177]), and β-MB_4O_7 (M = Ca [173], Hg [172], Sn [393]) through a mirror plane, the layers in γ-$RE(BO_2)_3$ (RE = La–Nd) [265, 266] are associated *via* zigzag chains.

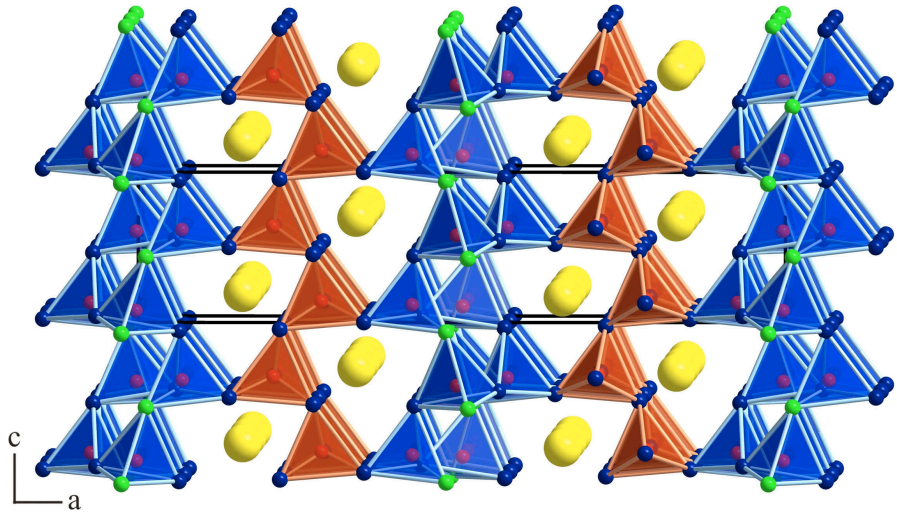

Figure 4.96: Crystal structure of δ-BiB_3O_6 with a view along [010]. Blue tetrahedra show layers connected *via* zigzag chains (red tetrahedra). Yellow spheres represent Ba^{2+}, red spheres B^{3+}, blue spheres $O^{[2]}$, and green spheres $O^{[3]}$.

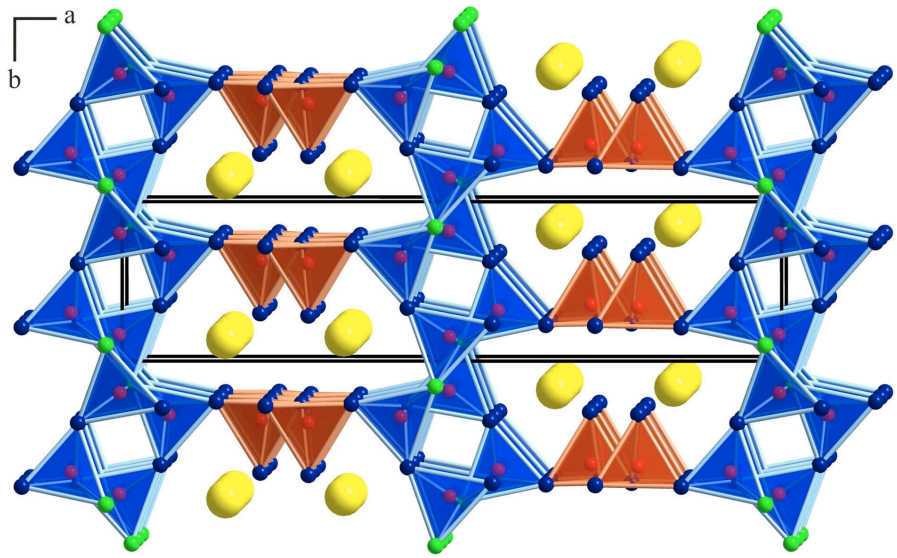

Figure 4.97: Crystal structure of δ-BiB_3O_6 with view along [001]. Blue tetrahedra show layers connected via zigzag chains (red tetrahedra). Yellow spheres represent Bi^{3+}, red spheres B^{3+}, blue spheres ($O^{[2]}$), and green spheres ($O^{[3]}$).

Although the topology of the BO_4-tetrahedra is nearly identical, a remarkable difference in the coordination of the metal cations exists. For example in γ-$Ce(BO_2)_3$, the Ce^{3+} ions are coordinated by 10 oxygen atoms (239 – 303 pm), while the Bi^{3+} ions in δ-BiB_3O_6 exhibit only a seven-fold coordination (226 – 273 pm) (Figure 4.98). To point out the difference in the coordination inside the

structures of the mentioned phases, the bonds representing the difference are highlighted red in Figure 4.98 (right). The reason for the different coordination of the Bi^{3+} ions, compared to the Ce^{3+} ions, is the sterically active lone pair localized at Bi^{3+}.

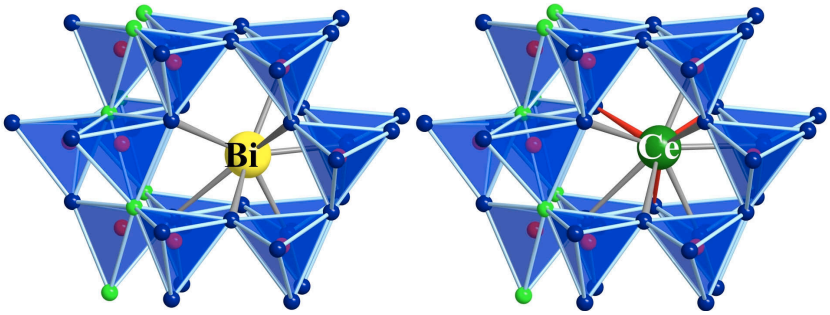

Figure 4.98: Comparison of the coordination of the cations in δ-BiB_3O_6 and γ-$Ce(BO_2)_3$.

A comparison between α-, β-, and γ-BiB_3O_6 shows an increasing density (α: 5.033; β: 5.411; γ: 6.177 g·cm^{-3}), which runs parallel with a transformation of BO_3 into BO_4 groups. In α-BiB_3O_6, the ratio of BO_3:BO_4 is 2:1, changing to 1:2 in β-BiB_3O_6, followed by the exclusive occurrence of BO_4-tetrahedra in γ-BiB_3O_6. As expected, the new high-pressure phase δ-BiB_3O_6 exhibits a denser structure (6.378 g·cm^{-3}), compared to the γ-modification prepared under autogenous pressure at 240 °C in Teflon autoclaves (50 cm^3 volume)[384]. As the coordination of the oxygen atoms is identical in both structures (fraction of $O^{[3]}$: 1/6), the bismuth coordination was examined. In fact, ECoN calculations (Effective Coordination Numbers according to Hoppe) [161–163] for δ-BiB_3O_6 exhibit sevenfold coordinated Bi^{3+} ions (226–273 pm) in contrast to sixfold coordinated Bi^{3+} ions in γ-BiB_3O_6 (216–267 pm).

Table 4.74: Interatomic distances/pm in δ-BiB_3O_6 (space group $Pca2_1$) calculated with the single crystal lattice parameters (standard deviations in parentheses).

Bi-O1a	225.9(4)	B1-O1	145.4(6)	B3-O5	140.5(7)
Bi-O3	228.8(4)	B1-O4a	146.8(7)	B3-O2	143.7(7)
Bi-O4	234.0(4)	B1-O3	147.1(7)	B3-O6a	153.4(6)
Bi-O1b	243.3(4)	B1-O4b	148.1(7)	B3-O6b	157.4(7)
Bi-O1c	259.5(4)		Ø = 146.9		Ø = 148.8
Bi-O2	260.6(4)	B2-O2	144.1(6)	O6-B3a	152.6(7)
Bi-O5	273.4(4)	B2-O5	144.1(6)	O6-B2	153.4(6)
	Ø = 246.5	B2-O3	148.8(7)	O6-B3b	157.4(7)
		B2-O6	152.6(7)		Ø = 154.5
			Ø = 147.4		

Table 4.75: Interatomic angles/° in δ-BiB_3O_6, calculated with the single crystal lattice parameters (standard deviations in parentheses).

O4a-B1-O4b	105.2(4)	O3-B2-O6	107.1(4)	O2-B3-O6a	105.0(4)
O3-B1-O4a	109.3(4)	O2-B2-O3	108.2(4)	O5-B3-O6a	106.8(4)
O1-B1-O4a	109.4(4)	O5-B2-O3	108.4(4)	O5-B3-O6b	107.0(4)
O1-B1-O3	110.3(4)	O5-B2-O6	109.1(4)	O6a-B3-O6b	108.3(4)
O4b-B1-O3	110.9(4)	O2-B2-O6	110.3(4)	O2-B3-O6a	110.7(4)
O1-B1-O4b	111.6(4)	O5-B2-O2	113.6(4)	O5-B3-O2	118.7(4)
	Ø = 109.5		Ø = 109.5		Ø = 109.4

4.2.4.4 Thermal Behaviour

Thermoanalytical investigations, using temperature-programmed X-ray powder diffraction patterns of δ-BiB_3O_6, showed that the compound is stable up to 700 °C. Between 700 and 750 °C, the phase transforms into an X-ray amorphous compound (Figure 4.99).

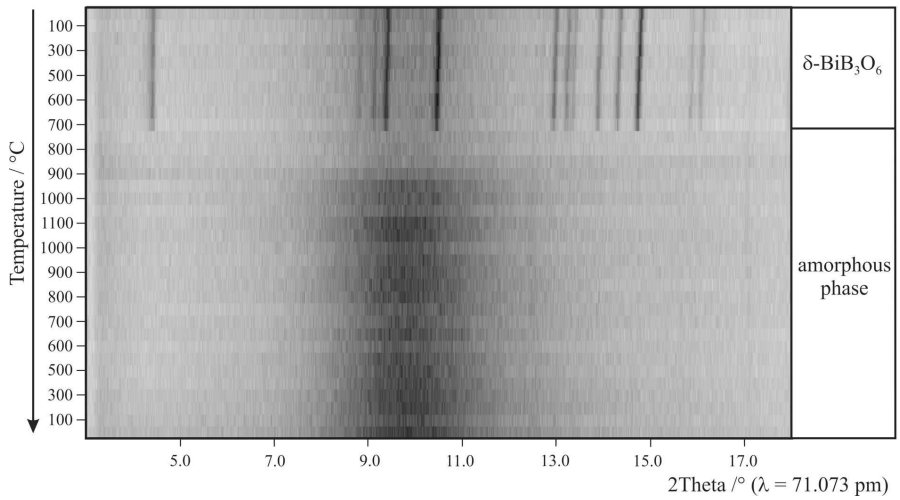

Figure 4.99: Temperature-programmed diffraction patterns of δ-BiB_3O_6, showing the transformation into an X-ray amorphous phase.

These results are in agreement with the DTA-TG measurements, which exhibit a broad endothermic effect with an onset of 709 °C (Figure 4.100). Subsequent cooling to room temperature did not succeed in obtaining any crystalline phase under ambient pressure conditions.

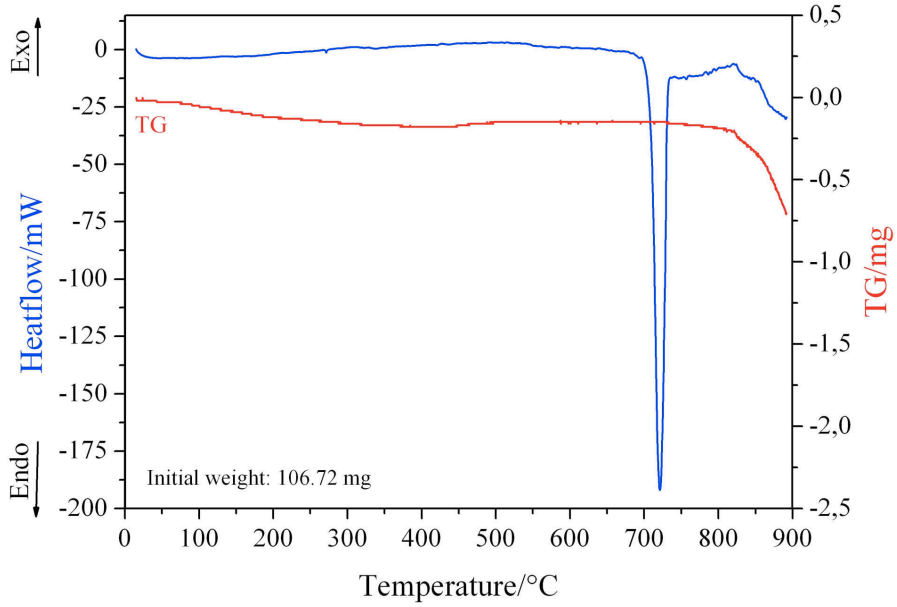

Figure 4.100: DTA-TG curves of δ-BiB_3O_6.

4.2.4.5 Vibrational Spectroscopic Investigations

A FTIR spectrum of δ-BiB_3O_6 was obtained at room temperature by using a Bruker IFS 66v/S spectrometer with DTGS detector. The sample was thoroughly mixed with dried KBr (5 mg of the sample, 500 mg of KBr). The preparation procedure was performed in a glovebox under dried argon atmosphere. The spectrum was collected in a range from 400 to 4000 cm^{-1} with a resolution of 2 cm^{-1}. During the measurement, the sample chamber was evacuated. Figure 4.101 shows the section 400–4000 cm^{-1} of the infrared spectrum of δ-BiB_3O_6 (green) and the spectrum of the isotypic high-pressure phase γ-CeB_3O_6 (blue). A comparison of the two spectra confirms the strong structural similarities of both phases, because the absorptions of both compounds are nearly identical. The spectra show strong absorptions of the BO_4-tetrahedra between 800 and 1150 cm^{-1} as in YBO_3, $GdBO_3$, or $TaBO_4$ [403–405]. Additionally, a strong absorption at 1261 cm^{-1} was observed, which is typical for triangular BO_3-groups as in $LaBO_3$ [406, 407] or $Eu_2B_4O_9$ [408]. Since BO_3-groups are missing in δ-BiB_3O_6, the ab-

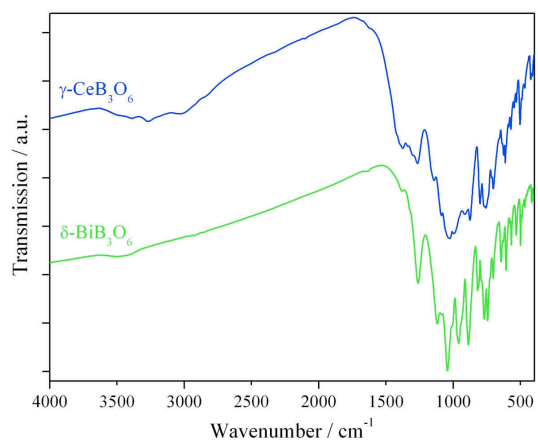

Figure 4.101: Infrared spectra of γ-CeB_3O_6 (blue) and δ-BiB_3O_6 (green).

sorptions can be assigned to the corresponding OB_3-vibrations. Analogous geometrics and similar force parameters in the OB_3-group recommend this assignment, because it is also valid *e.g* for β-ZnB_4O_7 [171], β-CaB_4O_7 [173], and the high-pressure phase B_2O_3-II [82]. The existence of three crystallographically independent BO_4-units in the network structure of δ-BiB_3O_6 in combination with OB_3-groups renders a detailed assignment of the broad bands difficult. Vibrational bands due to OH groups or water were not detectable.

4.2.4.6 DFT Calculations

Self-consistent DFT band structure calculations were performed by the LMTO-method in its scalar-relativistic version (program TB-LMTO-ASA). Detailed descriptions are given in [149, 150]. Reciprocal space integrations were performed with the tetrahedron method [151], employing 273 irreducible k-points from 845 (grid $5 \times 13 \times 13$). The basis set consisted of Bi-6s/6p/{6d/5f}, B-2s/2p{3d}, and O-{2s}2p{3d}. Orbitals given in parentheses were downfolded [409]. In order to achieve space filling within the atomic sphere approximation, interstitial spheres were introduced. A three dimensional grid of the charge density and electron localization function (ELF) [152, 153] were calculated. In the density functional theory, ELF depends on the excess of local kinetic energy due to the Pauli principle as compared to a bosonic system. High values of ELF appear in regions of space, where the Pauli principle does not increase the local kinetic energy and thus pairing of electrons plays an important role. These regions can be assigned either to covalent bonds or to lone pairs.

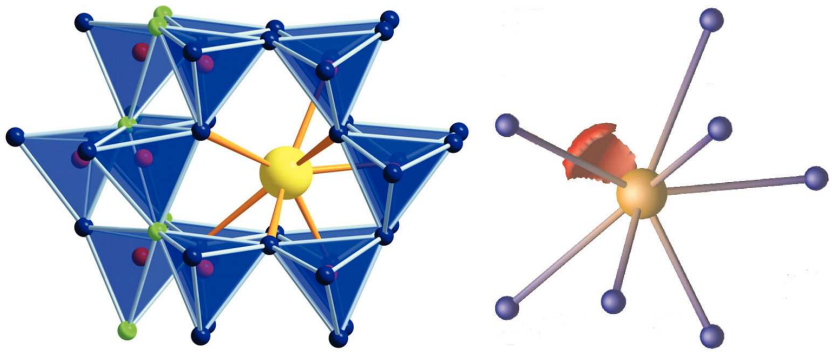

Figure 4.102: Left: Coordination sphere of Bi^{3+} in the crystal structure of δ-BiB_3O_6; right: the lone pair at the Bi^{3+} ion visualized by the electron localization function (ELF) (Isosurface value ELF = 0.9).

In order to analyze the conspicuous lone pair behaviour of δ-BiB_3O_6, we calculated the band structure and the electron density distribution. Figure 4.102 displays the coordination of the bismuth atoms in δ-BiB_3O_6, decorated with an ELF isosurface of ELF = 0.9. The lone pair at the bismuth atom is clearly visible and points toward the "empty" space above the atom.

4.2.4.7 Theoretical Calculations

Calculation of bond-valence sums for δ-BiB_3O_6 with the help of bond-length/bond-strength (ΣV) [164, 165] and CHARDI (ΣQ) [167] concepts confirmed the formal ionic charges (Table 4.76), acquired by the X-ray structure analysis, except the threefold coordinated oxygen atom O6, which shows a reduced value of -1.7 (ΣQ) in the CHARDI-concept. Similar deviating values for the $O^{[3]}$ atoms are obtained in β-CaB_4O_7 (-1.92 (ΣV); -1.77 (ΣQ))[173] β-HgB_4O_7 (-2.06 (ΣV); -1.83 (ΣQ))[172], and β-ZnB_4O_7 (-1.83 (ΣV); -1.67 (ΣQ) [171]). Remarkably, in all these cases the deviation was only observed in the CHARDI-calculations (ΣQ), whereas the bond-length/bond-strength values (ΣV) corresponded to the expected values.

Table 4.76: Charge distribution in δ-BiB_3O_6 calculated with the bond-length/bond-strength concept (ΣV) and the CHARDI concept (ΣQ).

	Bi	B1	B2	B3	O1	O2	O3	O4	O5	O6
ΣV	+2.6	+3.1	+3.0	+3.0	-2.2	-1.9	-2.0	-2.0	-1.9	-1.9
ΣQ	+2.8	+2.9	+3.1	+3.2	-2.0	-2.1	-2.2	-2.0	-2.0	-1.7

Then, we calculated the MAPLE values (Madelung Part of Lattice Energy) [161–163] for δ-BiB_3O_6 in order to compare them with MAPLE values of the binary oxides Bi_2O_3 and the high-pressure modification B_2O_3-II. We obtained a value of 40313 kJ·mol^{-1} in comparison to 40174 kJ·mol^{-1} (deviation: 0.3 %), starting from the binary compounds (0.5 × Bi_2O_3 (14533 kJ·mol^{-1}) + 1.5 × B_2O_3-II (21938 kJ·mol^{-1})).

4.2.5 The Borate β-SnB_4O_7

4.2.5.1 Synthesis

According to Equation 4.13, the starting materials for the synthesis of β-SnB_4O_7 [393] were stoichiometric mixtures of B_2O_3 (Strem Chemicals, Newburyport, U.S.A., 99.9%) and SnO (Strem Chemicals, Newburyport, USA, 99%). The mixture (≈ 65 mg) was filled into a boron nitride crucible of an 18/11 assembly.

$$\mathrm{SnO} + 2\,\mathrm{B_2O_3} \xrightarrow[1100\ ^\circ\mathrm{C}]{7.5\ \mathrm{GPa}} \beta\text{-}\mathrm{SnB_4O_7} \tag{4.13}$$

The assembly was compressed within 3 h to 7.5 GPa and heated to 1100 °C in the following 10 minutes. After holding this temperature for 5 minutes, the sample was cooled down to 750 °C in another 15 min and after that quenched to room temperature by switching off the heating. After decompression, the recovered experimental octahedron was cracked, and the sample carefully separated from the surrounding boron nitride. The air- and humidity-resistant compound β-SnB_4O_7 was obtained as a single-phase, coarsely-crystalline, colourless solid.

All experiments at pressures beyond 7 GPa led exclusively to crystalline β-SnB_4O_7. Attempts to produce SnB_4O_7 as glass under high-pressure conditions, using high cooling rates (quenching), did not succeed in any amorphous phase. The cooling rate in our high-pressure assembly was too low for the production of glass with the composition SnB_4O_7, as it was possible for other borates under these conditions. In contrast, experiments in the pressure range 1-2 GPa resulted only in amorphous phases (see Figure 4.103). *E.g.*, the synthesis of "SnB_4O_7", following equation 4.13 performed at a pressure of 1 GPa and a temperature of 650 °C, including a slow decrease of temperature (0.8 °C/min) to 350 °C, led to an X-ray amorphous product, showing reflections of metallic tin, which originate from the reducing character of the hexagonal boron nitride capsule during long heating periods. Moreover, the elongation of the reaction times destabilized the assemblies resulting in distorted capsules, due to which an isolation of a product was difficult. Presumably, the destabilization occurred from a molten sample, wherefore the stability of the assembly was affected during long reaction times at low pressure. Furthermore, we observed that a higher temperature (700 °C) at 1 GPa in combination with slow cooling rates caused an increasing amount of metallic tin in the product. Shortening the reaction time and lowering

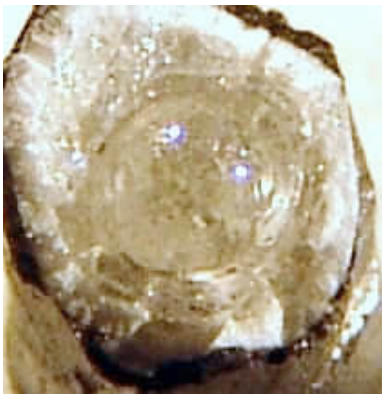

Figure 4.103: BN-crucible with glassy tin borate.

the temperature (heating to 500 °C in 6 min, followed by quenching) led to an amorphous phase as well.

4.2.5.2 Crystal Structure Analysis

The powder diffraction pattern was obtained from a 0.2 mm Mark capillary, filled with β-SnB_4O_7, using a STOE Stadi P powder diffractometer with monochromatized $CuK_{\alpha 1}$ radiation (λ = 154.051 pm). The diffraction pattern was indexed with the program ITO [125] on the basis of an orthorhombic unit cell. The lattice parameters (Table 4.77) were calculated from least-squares fits of the powder data. The correct indexing of the pattern of β-SnB_4O_7 was confirmed by intensity calculations, taking the atomic positions from the structure refinement [121]. The lattice parameters, determined from the powder and single crystal data, tally well. Figure 4.104 shows a comparison of the experimental powder pattern to the pattern simulated from single crystal data.

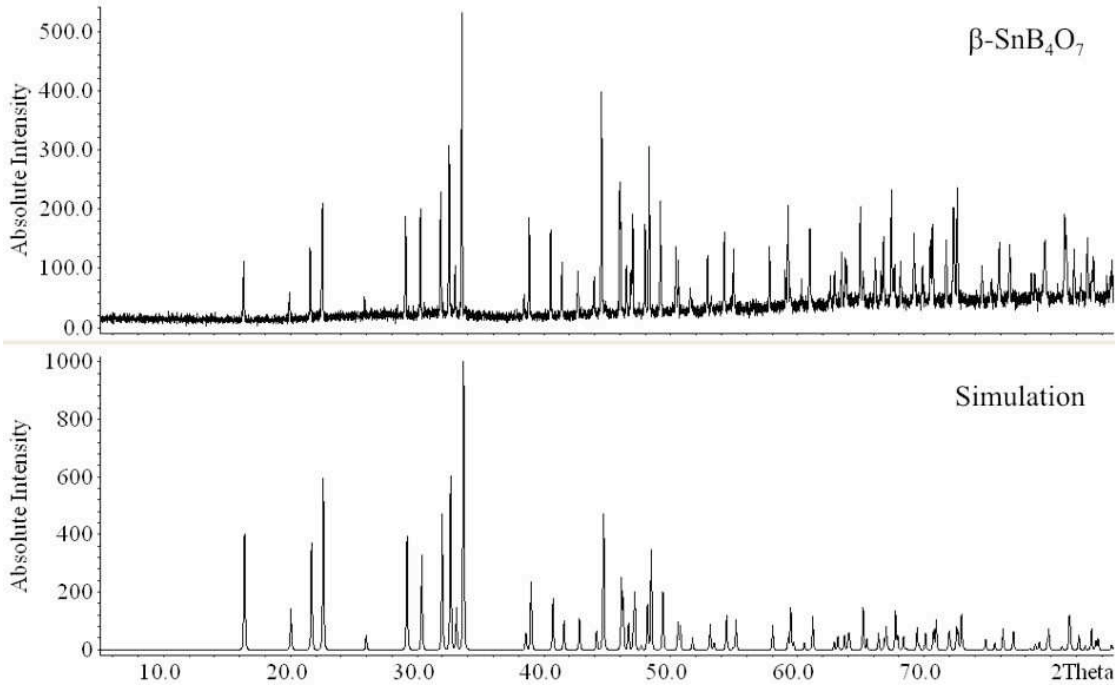

Figure 4.104: Measured (top) and simulated (single crystal data) (bottom) powder diffraction patterns of β-SnB_4O_7.

Small single crystals of β-SnB_4O_7 were isolated by mechanical fragmentation and examined through a Buerger camera, equipped with an image plate system (Fujifilm BAS-2500) in order to check their suitability for an intensity data collection. Single crystal intensity data of β-SnB_4O_7 were measured with a STOE IPDS I area detector diffractometer (MoK_α (λ = 71.073 pm)). A numerical absorption correction was applied to the data (HABITUS [132]). According to the systematic extinctions $h0l$ with $h = l \neq 2n$, $h00$ with $h \neq 2n$, and $00l$ with $l \neq$

$2n$, the space groups $Pmn2_1$ (No. 31) and $Pmnm$ (No. 59) were derived. The non-centrosymmetric group $Pmn2_1$ was found to be correct during the refinement. This was confirmed with the ADDSYM routine of the program PLATON [139]. Additionally, a powder sample of β-SnB_4O_7 was subjected to a qualitative powder SHG measurement, using the method reported by Kurtz & Perry [401]. The observed intensities of the second harmonic, generated by β-SnB_4O_7, signalized an SHG effect, thus corroborating the non-centrosymmetry of β-SnB_4O_7 [402]. Structure solution and parameter refinement (full-matrix least squares against F^2) were successfully performed using the SHELX-97 software suite [135, 136]. Details of the data collections and structure refinements are listed in Table 4.77. The positional parameters, anisotropic displacement parameters, interatomic distances, and interatomic angles are given in Tables 4.78–4.81.

Table 4.77: Crystal data and structure refinement of β-SnB_4O_7 (standard deviations in parentheses).

Empirical Formula	SnB_4O_7
Molar mass/g·mol^{-1}	273.93
Crystal system	orthorhombic
Space group	$Pmn2_1$ (No. 31)
Powder diffractometer	STOE Stadi P
Radiation	$CuK_{\alpha 1}$ (λ = 154.051 pm)
Powder data	
a/pm	1085.34(4)
b/pm	444.84(3)
c/pm	423.43(3)
V/nm^3	0.2044(1)
Single crystal diffractometer	STOE IPDS I
Radiation	MoK_α (λ = 71.073 pm)
Single crystal data	
a/pm	1086.4(2)
b/pm	444.80(9)
c/pm	423.96(8)
V/nm^3	0.2049(1)
Formula units per cell	Z = 2
Temperature/K	293(2)
Calculated density/g·cm^{-3}	4.44
Crystal size/mm^3	0.08 × 0.08 × 0.03
Detector distance	40.0
Exposure time per plate/min	16.0
Absorption coefficient/mm^{-1}	6.2
F (000)/e	252
θ range/°	4.6 – 28.7
Range in hkl	±14, ±6, ±5
Total no. reflections	2027
Independent reflections	600 (R_{int} = 0.0218)
Reflections with I > 2σ(I)	581 (R_σ = 0.0182)
Flack parameter	0.00(3)
Data/parameters	600/59
Absorption correction	empirical (X-PREP [134])
Transm. ratio (min/max)	0.689/0.844
Goodness-of-fit (F^2)	1.064
Final R indices (I > 2σ(I))	R1 = 0.0145
	wR2 = 0.0322
R indices (all data)	R1 = 0.0155
	wR2 = 0.0324
Extinction coefficient	0.019(2)
Largest differ. peak, deepest hole/e·Å^{-3}	0.763/-0.550

Table 4.78: Atomic coordinates and equivalent isotropic displacement parameters $U_{eq}/Å^2$ of β-SnB_4O_7 (space group $Pmn2_1$). U_{eq} is defined as one third of the trace of the orthogonalized U_{ij} tensor (standard deviations in parentheses).

Atom	Wyckoff Position	x	y	z	U_{eq}
Sn	2*a*	0	0.82402(5)	0.89554(5)	0.0086(2)
B1	4*b*	0.1225(3)	0.3272(6)	0.444(2)	0.004(2)
B2	4*b*	0.2481(3)	0.1749(6)	0.9742(7)	0.0022(6)
O1	4*b*	0.2197(2)	0.1298(4)	0.6188(5)	0.0032(4)
O2	4*b*	0.1422(2)	0.6426(4)	0.5237(5)	0.0042(4)
O3	4*b*	0.1372(2)	0.2733(5)	0.1116(5)	0.0040(4)
O4	2*a*	0	0.2309(6)	0.5541(6)	0.0029(5)

Table 4.79: Anisotropic displacement parameters of β-SnB_4O_7 (standard deviations in parentheses).

Atom	U_{11}	U_{22}	U_{33}	U_{23}	U_{13}	U_{12}
Sn	0.0075(2)	0.0116(2)	0.0066(2)	0.0016(2)	0	0
B1	0.004(2)	0.0019(9)	0.006(4)	-0.000(2)	-0.001(2)	-0.0003(9)
B2	0.004(2)	0.002(2)	0.000(2)	0.0000(8)	0.0001(8)	0.000(2)
O1	0.005(2)	0.0021(8)	0.0022(8)	-0.0002(7)	-0.0010(8)	0.0015(7)
O2	0.005(2)	0.0025(8)	0.0051(7)	-0.0009(7)	0.0010(7)	0.0005(7)
O3	0.004(2)	0.0053(8)	0.0024(9)	-0.0010(6)	-0.0005(7)	0.0015(7)
O4	0.002(2)	0.003(2)	0.004(2)	0.0028(9)	0	0

4.2.5.3 Crystal Structure Description

β-SnB_4O_7 is assembled solely of corner-sharing BO_4-tetrahedra, being isotypic to the mineral clinobarylite $BaBe_2Si_2O_7$ [394], to the known high-pressure phases β-CaB_4O_7 [173] and β-HgB_4O_7 [172], as well as to the ambient-pressure phases SrB_4O_7 [174, 175], PbB_4O_7 [175, 176], and EuB_4O_7 [177]. Figure 4.105 (right) shows the crystal structure of β-SnB_4O_7 along [001], exhibiting a network of corner-sharing BO_4-tetrahedra, forming channels along [001], which are composed of "Vierer" and "Sechser" rings (rings with four and six tetrahedral centres, respectively) [39]. The tin cations lie in the "Sechser" ring channels, while the "Vierer" ring channels remain empty. Figure 4.105 (left) illustrates the highly condensed layers along [100] partially built up by threefold coordinated oxygen atoms $O^{[3]}$ (green spheres), which are also found in other borates, *e.g.* β-MB_4O_7 (M = Mn [261], Co, Ni [261], Cu [261], Zn [171]), β-$RE(BO_2)_3$ (RE = Nd, Sm, Gd–Lu) [262–264], γ-$RE(BO_2)_3$ (RE = La–Nd) [265, 266], and minerals like tunnelite ($SrB_6O_9(OH)_2{\cdot}3H_2O$), strontioginorite ($(Sr,Ca)_2B_{14}O_{20}(OH)_6{\cdot}6H_2O$) [267], aristarainite ($Na_2Mg[B_6O_8(OH)_4]_2{\cdot}4H_2O$) [268], and the high-pressure modification of B_2O_3 [82]. Figure 4.105 shows that all tetrahedra point towards the $[00\bar{1}]$ direction, confirming the non-centrosymmetric structure of β-SnB_4O_7.

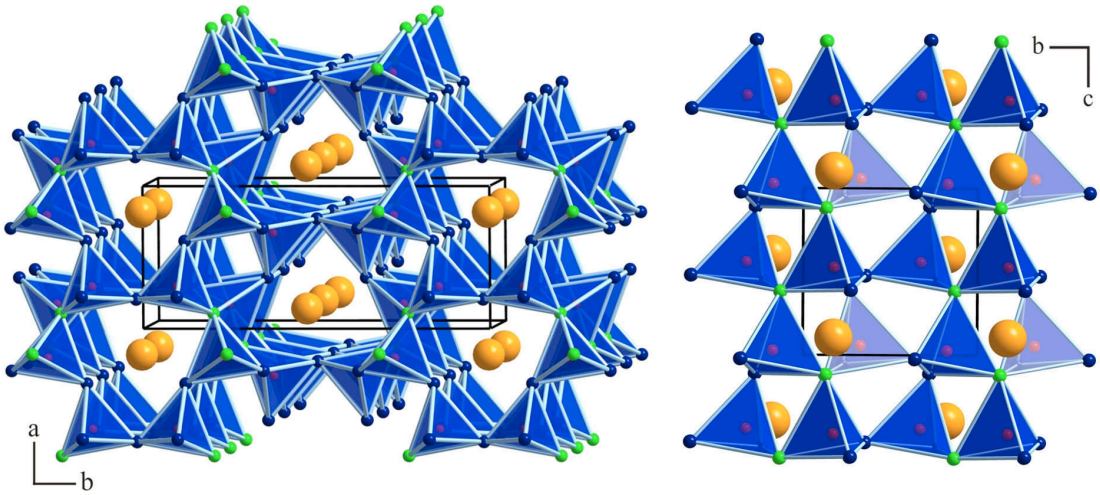

Figure 4.105: Crystal structure β-SnB_4O_7 along [001] (left) and along [$\bar{1}$00] (right). Orange spheres: Sn^{2+}, red spheres: B^{3+}, blue spheres: $O^{[2]}$, green spheres: $O^{[3]}$.

The B–O bond–lengths in β-SnB_4O_7 (Table 4.80) vary between 141 and 156 pm with an average B–O bond-length of 148.5 pm, which is slightly larger than the known average value of 147.6 pm for borates [232, 233]. As expected, the bonds to threefold coordinated oxygen atoms $O^{[3]}$ are significantly longer (153–156 pm) than the average, with partial compensation by the shortening of other bonds. Longer bonds can also be found in the borates MB_4O_7 (M = Sr [174, 175], Pb [175, 176], Eu [177]) and β-MB_4O_7 (M = Ca [173], Hg [172]), as well as in β-MB_4O_7 (M = Mn [261], Co, Ni [261], Cu [261], Zn [171]). The O–B–O angles in the two crystallographically independent BO_4-tetrahedra vary between 104.4 and 117.8° (Table 4.81). These strong deviations from the ideal tetrahedron angle are not exceptional for borates, synthesized under extreme conditions. Examples for such strongly distorted tetrahedra in BO_4-networks can be found *e.g.* in the high-pressure phases α-$RE_2B_4O_9$ (RE = Eu-Tb [74–76]) with O–B–O angles varying between 99.5 and 118.9° for α-$Eu_2B_4O_9$, 99.4–119.0° for α-$Gd_2B_4O_9$, and 99.4–119.4° for α-$Tb_2B_4O_9$. The
B-$O^{[3]}$-B angles inside of the OB_3-group are 117.3, 117.6, and 121.6° with a mean value of 118.8° (Table 4.81). The slight distortion of the OB_3-group is understandable, because the Sn^{2+} ions lie in the direct neighborhood of the OB_3-group with an $O^{[3]}$···Sn distance of 298.7 pm (Table 4.80). The coordinative contribution of $O^{[3]}$ leads to a deflection of these atoms from the plane into the direction of the Sn^{2+} ions. Similar distortions inside the $O^{[3]}B_3$-group can be found in other borates, such as β-MB_4O_7 (M = Mn [261], Co, Ni [261], Cu [261], Zn [171]). In contrast to the isotypic high-pressure phases β-CaB_4O_7 [173] and β-HgB_4O_7 [172], where the M^{2+} ions are coordinated by 15 oxygen atoms (β-CaB_4O_7: 242–316 pm, β-HgB_4O_7: 237–315 pm), the coordination number in β-SnB_4O_7 can be described

as a 10 + 5 coordination. The Sn–O distances vary between 232 and 301 pm for the 10 nearest oxygen atoms (Table 4.80). Five oxygen atoms can be found in a distance of 318 pm (2×), 320 pm (2×), and 333 pm, which make only a negligible coordinative contribution to the Sn^{2+} ion. ECoN calculations (Effective Coordination Numbers according to Hoppe) [161–163] for the Sn^{2+} ions confirm the coordination number of 10 in β-SnB_4O_7, if values of δ-ECoN smaller than 0.05 are neglected. Figure 4.106 displays the different coordination spheres in β-SnB_4O_7 and β-CaB_4O_7. The reason for the different coordination of the Sn^{2+} ions, com-

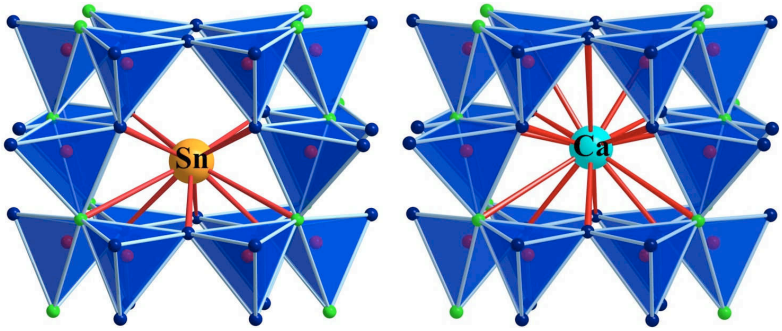

Figure 4.106: Coordination sphere of tin in the crystal structure of β-SnB_4O_7 with sterically active lone pair at Sn^{2+} (left) compared to the coordination sphere of Ca^{2+} in the crystal structure of β-CaB_4O_7 (right).

pared to the Ca^{2+} and Hg^{2+} ions, may be the sterically active lone pair localized at Sn^{2+}. Bohatý *et al.* presented a detailed comparison of the coordination surroundings of Pb^{2+} and Sr^{2+} ions in PbB_4O_7 and SrB_4O_7, respectively [410]. The comparison signalized a slight off-center shift of Pb^{2+} within its coordination compared to Sr^{2+}, caused in a moderate influence of the lone pair, which is present in PbB_4O_7. This effect is much stronger in β-SnB_4O_7.

Table 4.80: Interatomic distances/pm in β-SnB_4O_7 (space group $Pmn2_1$) calculated with the single crystal lattice parameters (standard deviations in parentheses).

Sn-O4a	231.8(3)	B1-O3	143.6(4)	B2-O3	140.8(4)	O1-B2a	152.8(4)
Sn-O2	235.0(2) 2×	B1-O2	145.9(3)	B2-O2	145.7(4)	O1-B2b	155.1(4)
Sn-O3a	265.6(2) 2×	B1-O4	147.5(4)	B2-O1a	152.8(4)	O1-B1	156.1(4)
Sn-O1	298.7(2) 2×	B1-O1	156.1(4)	B2-O1b	155.1(4)		Ø = 154.7
Sn-O4b	300.9(3)		Ø = 148.3		Ø = 148.6		
Sn-O3b	301.0(2) 2×						
	Ø = 273.3						

Table 4.81: Interatomic angles/° in β-SnB_4O_7 calculated with the single crystal lattice parameters (standard deviations in parentheses).

O4-B1-O1	107.2(3)	O2-B2-O1a	104.4(2)	B2a-O1-B2b	117.3(2)
O3-B1-O1	107.3(2)	O3-B2-O1b	105.8(2)	B2a-O1-B1	117.6(2)
O2-B1-O1	109.3(3)	O3-B2-O1a	107.8(2)	B2b-O1-B1	121.6(2)
O2-B1-O4	109.7(3)	O1a-B2-O1b	108.7(2)		Ø = 118.8
O3-B1-O4	111.3(3)	O2-B2-O1b	112.0(2)		
O3-B1-O2	111.9(3)	O3-B2-O2	117.8(2)		
	Ø = 109.5		Ø = 109.4		

4.2.5.4 Thermal Behaviour

In situ X-ray powder diffraction experiments were performed on a STOE Stadi P powder diffractometer (MoK_α radiation (λ = 71.073pm)) with a computer controlled STOE furnace. The sample was enclosed in a silica capillary and heated from room temperature to 500 °C in 100 °C steps, and from 500 °C to 1100 °C in 50 °C steps. After that, the sample was cooled down to 500 °C in 50 °C steps, and below 500 °C in 100 °C steps. At each temperature a diffraction pattern was recorded from 7° to 22° in 2θ.

Figure 4.107 illustrates the temperature-programmed X-ray powder diffraction patterns of β-SnB_4O_7, showing a transformation of the high-pressure phase into an X-ray amorphous phase after heating to 500–550 °C. Further heating up to 1100 °C and subsequent cooling to room temperature did not succeed in any crystalline phase under ambient pressure conditions. Thermoanalytical investigations

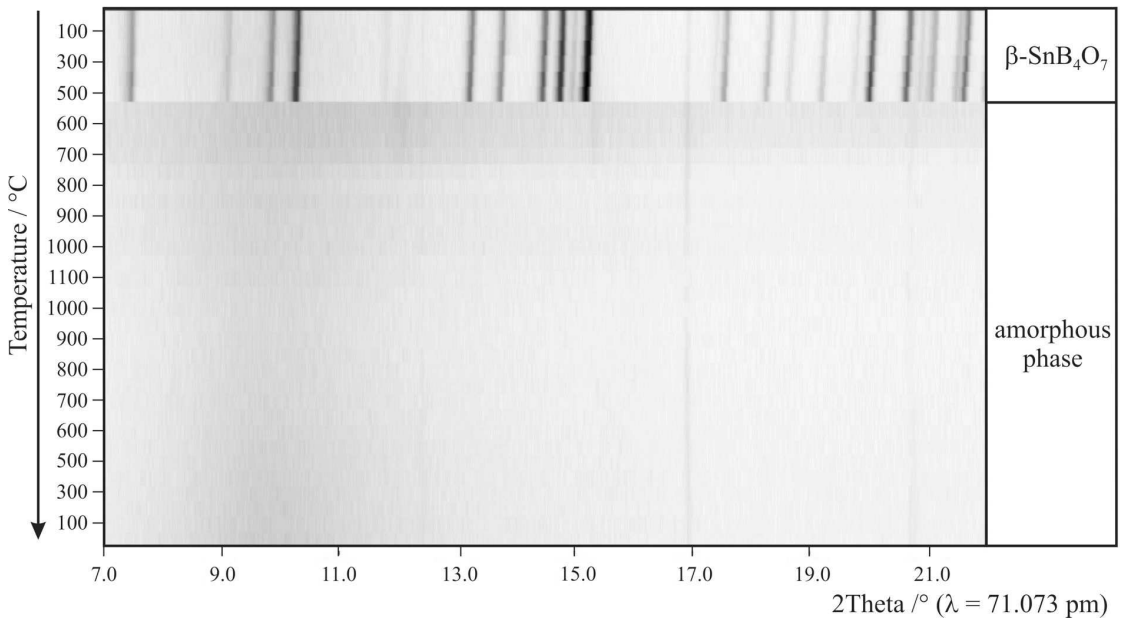

Figure 4.107: *In situ* X-ray powder patterns of β-SnB_4O_7.

were carried out utilzing a Setaram TGA 92-2400 DTA-TG-thermobalance. The DTA-TG curve of β-SnB_4O_7 was recorded between room temperature and 600 °C with a heating rate of 10 °C·min^{-1}. The results of the temperature-programmed powder diffraction patterns are in agreement with the DTA measurements (Figure 4.108). During the heating of β-SnB_4O_7, a broad endothermic effect occurred in the DTA between 520 and 580 °C, owing to a melting process of the compound. A small weight loss (2%) could be observed in the thermogravimetrical measurement between 100 and 350 °C, which can be attributed to a loss of water and boric acid.

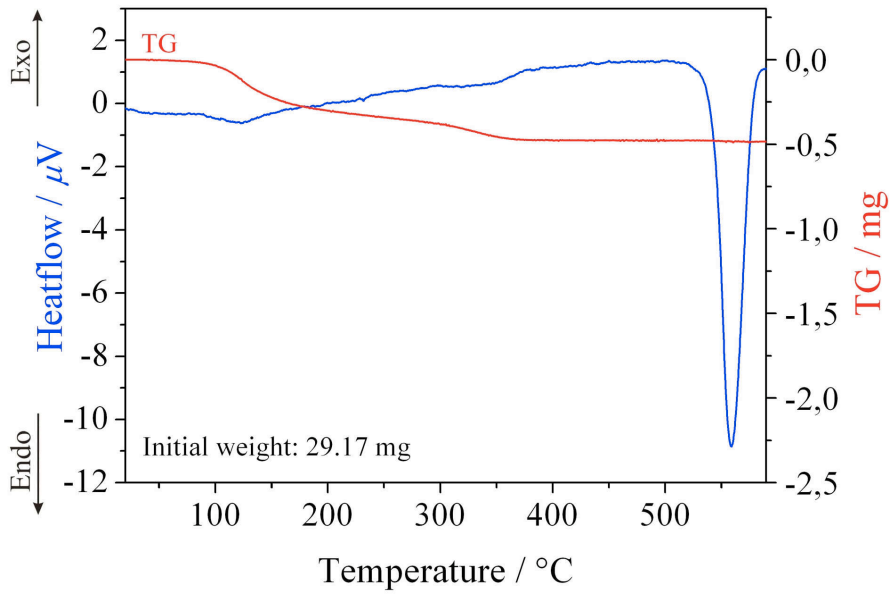

Figure 4.108: DTA-TG curves of β-SnB_4O_7.

4.2.5.5 Vibrational Spectroscopic Inverstigations

A FTIR spectrum of β-SnB_4O_7 was obtained at room temperature by using a Bruker IFS 66v/S spectrometer with DTGS detector. The sample was thoroughly mixed with dried KBr (5 mg of the sample, 500 mg of KBr). The preparation procedure was performed in a glovebox under dried argon atmosphere. The spectrum was collected in a range from 400 to 4000 cm^{-1} with a resolution of 2 cm^{-1}. During the measurement, the sample chamber was evacuated.

Figure 4.109 shows the section 400–2000 cm^{-1} of the infrared spectrum of β-SnB_4O_7 (red) in comparison to the spectra of the isotypic high-pressure phase β-CaB_4O_7 (blue) and the amorphous ambient-pressure tin borate "SnB_4O_7" (black). A first comparison of the three spectra confirms that β-SnB_4O_7 is isotypic to β-CaB_4O_7, as the absorptions of both compounds are nearly identical. In

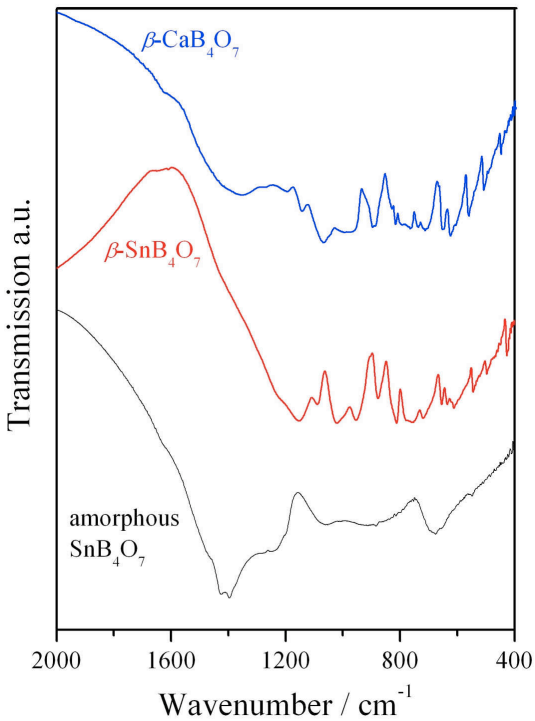

Figure 4.109: Infrared spectra of β-CaB_4O_7 (blue), β-SnB_4O_7 (red), and amorphous SnB_4O_7 (black).

contrast, the spectrum of the amorphous ambient-pressure phase "SnB_4O_7" is completely different. In the spectra of β-SnB_4O_7 and β-CaB_4O_7, the absorption peaks between 800 and 1100 cm^{-1} are those typical for the tetrahedral borate group BO_4 as in YBO_3, $GdBO_3$, or $TaBO_4$ [403–405]. Between 1100 and 1450 cm^{-1}, and below 800 cm^{-1}, we observe absorptions typical for triangular BO_3-groups as in $LaBO_3$ [406, 407] and $Eu_2B_4O_9$ [408]. Since BO_3-groups are missing in β-SnB_4O_7, the absorptions can be assigned to the corresponding OB_3-vibrations. Analogous geometrics and similar force parameters in the OB_3-group recommend this assignment, because it is also valid *e.g.* for β-ZnB_4O_7 [171], β-CaB_4O_7 [173], and the high-pressure phase B_2O_3-II [82]. The existence of two crystallographically independent BO_4-units in the network structure of β-SnB_4O_7 in combination with OB_3-groups renders a detailed assignment of the broad bands difficult. The spectrum of the amorphous "SnB_4O_7" exhibits a strong absorption around 1400 cm^{-1}, which is typical for BO_3-groups in borates. Around 1000 cm^{-1}, also characteristic BO_4-absorption bands can be observed. From these results, we conclude that the amorphous ambient-pressure phase "SnB_4O_7" exhibits both BO_3- and BO_4- groups in contrast to its high-pressure modification. Moreover, absorptions in the range 3100–3600 cm^{-1} show the presence of OH/H_2O, indicating no pure "SnB_4O_7". Up to now, it has not been possible to synthesize a defined, reproduceable glass with the composition SnB_4O_7.

4.2.5.6 Mößbauer Spectroscopic Investigations

^{119}Sn Mößbauer spectroscopy is a sensitive tool to investigate the coordination environment of tin in tin borate glasses. The spectra of β-SnB_4O_7 at 77 K and room temperature are presented in Figure 4.110 together with transmission integral fits. The fitting parameters are listed in Table 4.82. Both spectra show a main signal at an isomer shift of 4.09(1) $mm{\cdot}s^{-1}$ and a line width of 0.88(1) $mm{\cdot}s^{-1}$, compatible with divalent tin. A small impurity component (ca. 5% of the total area) around 0 $mm{\cdot}s^{-1}$ results most likely from a minor SnO_2 content [411] of the sample. Due to the low site symmetry of the tin site (m), the spectra show quadrupole splitting of 0.71(3) and 0.78(3) $mm{\cdot}s^{-1}$ at room temperature and 77 K, respectively.

It is worthwhile to note that the ^{119}Sn Mössbauer spectrum of a SnB_2O_4 glass [412] shows a smaller isomer shift (between 3.09 and 3.17 $mm{\cdot}s^{-1}$) and a much higher quadrupole splitting parameter, clearly indicating different tin coordinations in the SnB_2O_4 glass than in the crystalline material β-SnB_4O_7.

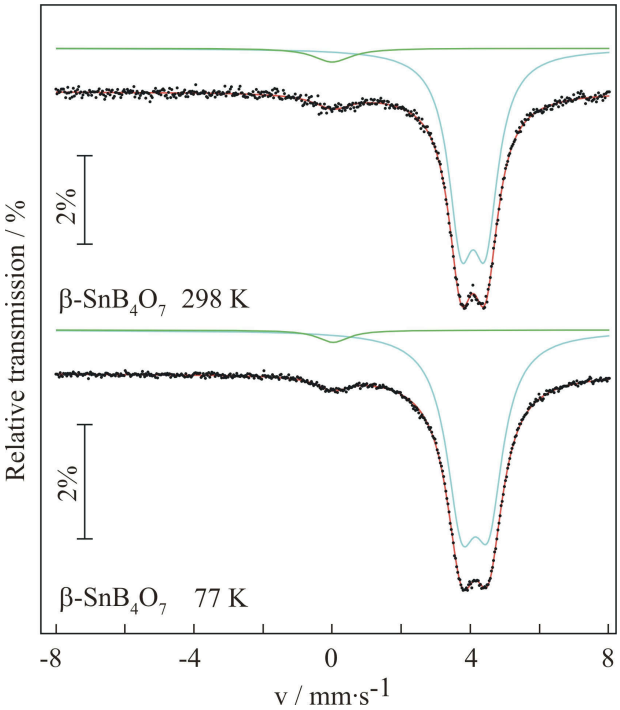

Figure 4.110: Experimental (green: Sn^{4+}, blue: Sn^{2+}) and simulated (black) ^{119}Sn spectra of β-SnB_4O_7 at 77 K and room temperature.

Table 4.82: Fitting parameters for the ^{119}Sn Mössbauer spectra of β-SnB_4O_7 at room temperature and 77 K. (δ = isomer shift; Γ = experimental line width; ΔE_Q = electric quadrupole interaction.)

T/K	δ_1/mm·s^{-1}	Γ_1/mm·s^{-1}	ΔE_Q/mm·s^{-1}	δ_2/mm·s^{-1}	Γ_2/mm·s^{-1}
298	4.09(1)	0.88(1)	0.71(3)	0.01(1)	1.3(1)
77	4.14(1)	1.06(1)	0.78(3)	0.03(3)	1.1(1)

4.2.5.7 Solid State NMR Investigations

The NMR experiments on β-SnB_4O_7 were carried out on a Bruker Avance DSX spectrometer, equipped with standard 2.5 mm and 4.0 mm MAS NMR probe tubes. The magnetic field strength was 11.75 T, corresponding to ^{117}Sn and ^{11}B resonance frequencies of 178.03 and 160.50 MHz, respectively. A commercially available pneumatic control unit was used to limit MAS frequency variations to a 2 Hz interval during the experiment. Samples were spun at 10 and 25 kHz, respectively. The chemical shift values refer to $Sn(CH_3)_4$ and $BF_3 \cdot Et_2O$ as external chemical shift references for ^{117}Sn and ^{11}B. The repetition rates of the experiments were 300 and 50 s, respectively. The ^{117}Sn MAS spectrum was obtained from 200 accumulated transients. The ^{11}B MQMAS spectrum was obtained, using a triple-quantum 3 pulse sequence with a z-filter [144]. The SOQE parameters and isotropic chemical shift values were determined from the moment analysis [144, 145] of the sheared MQMAS spectrum. Simulations of the ^{117}Sn chemical shift parameters were done by minimizing the squared difference between experiment and simulation, using the Simpson Minuit routines [146], and the chemical

shift conventions implemented in SIMPSON [147].

In agreement with the diffraction results, one tin and two boron positions were resolved in the solid-state NMR experiments (Figure 4.111). The ^{117}Sn chemical shift parameters were δ_{iso} = -1284.7 ppm, δ_{aniso} = -334 ppm, and η = 0.1, which were determined from an ^{117}Sn MAS NMR spectrum. Zero asymmetry parameters η are found, when the tin atoms have a point group with a 3-fold axis element or higher. Slight distortions as in the structure of β-SnB_4O_7 result in small but

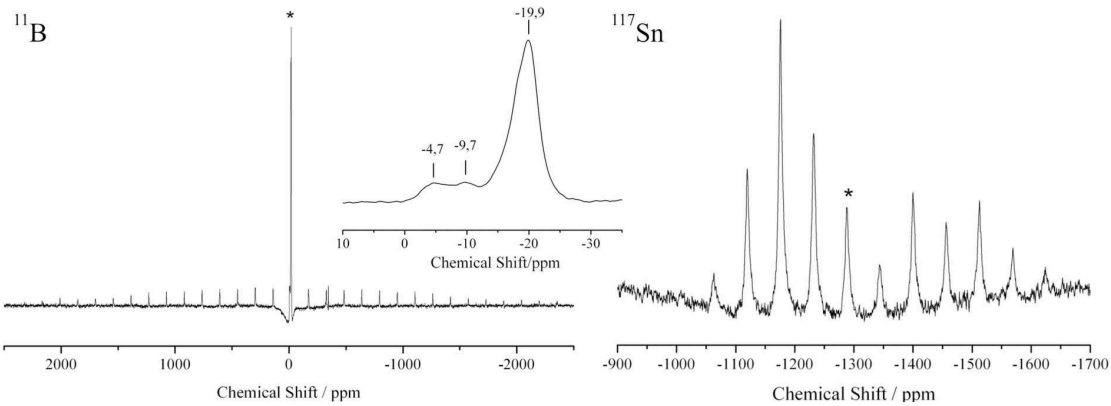

Figure 4.111: ^{11}B (left) and ^{117}Sn (right) MAS NMR spectra of β-SnB_4O_7. The isotropic sidebands are marked by an asterisk.

non-zero asymmetry parameters. Since the high-pressure phase β-SnB_4O_7 is an extreme example for a highly coordinated tin atom, we compared the observed chemical shift parameters with literature values [413–418]. Prior work [417, 418] on thiostannates indicates that it is impossible to distinguish Sn^{2+} and Sn^{4+} on the basis of $^{117/119}$Sn NMR, due to the mutual overlap of anisotropic and isotropic chemical values for Sn^{2+} and Sn^{4+}. In fact, the situation is more favourable for tin coordinated to oxygen. The values of the anisotropic and isotropic chemical shifts span a space, in which Sn^{2+} and Sn^{4+} atoms are well separated from each other (Figure 4.112). Obviously the chemical shift parameters of thiostannates are much more difficult to understand, due to the higher electronic polarizability of sulphur compared to oxygen. The resolution power of $^{117/119}$Sn MAS NMR experiments might be

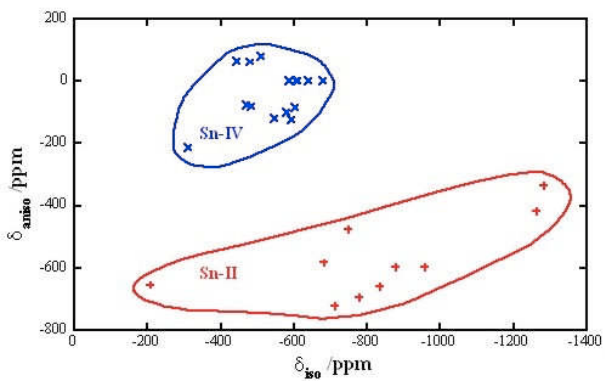

Figure 4.112: Chemical shift parameters of Sn^{2+} and Sn^{4+} in oxygen-based, crystalline model compounds (references [413–416] and β-SnB_4O_7); some δ_{aniso} values were too small to be determined experimentally and were assumed to be zero for this diagram.

useful to determine oxidation states spectroscopically in various amorphous and crystalline inorganic materials. From the ^{11}B MQMAS (Figure 4.113), the chemical shift and quadrupole coupling parameters were determined to be δ_{iso} = 3.4 and 4.6 ppm and SOQE = 0.7 and 1.1 MHz, respectively. The determined SOQE and the isotropic chemical shift parameters are typical for tetrahedrally coordinated boron atoms [419].

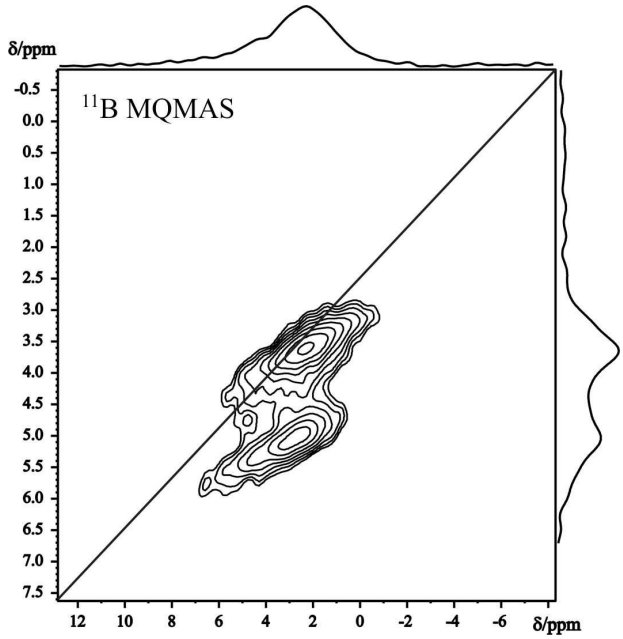

Figure 4.113: ^{11}B MQMAS NMR spectrum of crystalline β-SnB_4O_7; two crystallographically independent positions are resolved δ_{iso} = 3.4 and 4.6 ppm, SOQE = 0.7 and 1.1 MHz, respectively.

4.2.5.8 DFT Calculations

Self-consistent DFT band structure calculations were performed by the LMTO-method in its scalar-relativistic version (program TB-LMTO-ASA). Detailed descriptions are given elsewhere [149, 150]. Reciprocal space integrations were performed with the tetrahedron method [151], employing 273 irreducible k-points. The basis set consisted of Sn-5s/5p/{5d/4f}, B-2s/2p{3d}, and O-{2s}2p{3d}. Orbitals given in parentheses were downfolded [409]. In order to achieve space filling within the atomic sphere approximation, interstitial spheres were introduced. A three dimensional grid of the charge density and electron localization function (ELF) [152, 153] were calculated. In the density functional theory, ELF de-

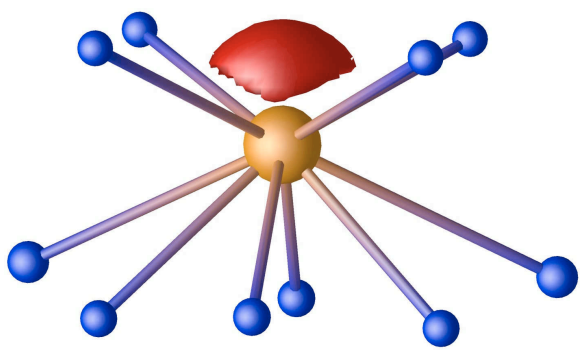

Figure 4.114: The lone pair at the Sn^{2+} ion in β-SnB_4O_7 visualized by the electron localization function (ELF) (isosurface value ELF = 0.93).

pends on the excess of local kinetic energy due to the Pauli principle as compared to a bosonic system. High values of ELF appear in regions of space, where the Pauli principle does not increase the local kinetic energy and thus pairing of electrons plays an important role. These regions can be assigned either to covalent bonds or to lone pairs.

In order to analyze the conspicuous lone pair behaviour of PbB_4O_7 and β-SnB_4O_7, we have calculated the band structure of both compounds and the electron density distribution of β-SnB_4O_7. The electron localization function ELF is a useful tool to discover regions with paired spins, as expected for covalent bonds or lone pairs. Figure 4.114 displays the coordination of the tin atoms in β-SnB_4O_7, decorated with an ELF isosurface of ELF = 0.93. The lone pair at the tin atom is clearly visible and points toward the "empty" space above the tin atom. Thus, the DFT calculations support the existence of the stereochemically active lone pair of Sn^{2+} in β-SnB_4O_7, but it is not yet clear, why the isostructural lead compound shows no distinctive asymmetry, as reported in reference [410].

In recently published papers [420, 421] it is shown that the reason for lone pair formation in tin- and lead-chalcogenides mainly lies in the antibonding Sn(5s)-O(2p) interactions, which decrease the energy separation of the Sn(5s)-Sn(5p) states and allow s-p mixing. So, the more s-p mixed levels occur near the Fermi energy (ϵ_F), the stronger is the tendency to form a lone pair at the tin (or lead) site. Figure 4.115 shows the partial density of states (PDOS) for the s- and p-orbitals of Sn^{2+} in β-SnB_4O_7, of Pb^{2+} in "PbB_4O_7" with off-center Pb (structure of β-SnB_4O_7), and finally of Pb in the experimental structure with a nearly symmetric environment [175].

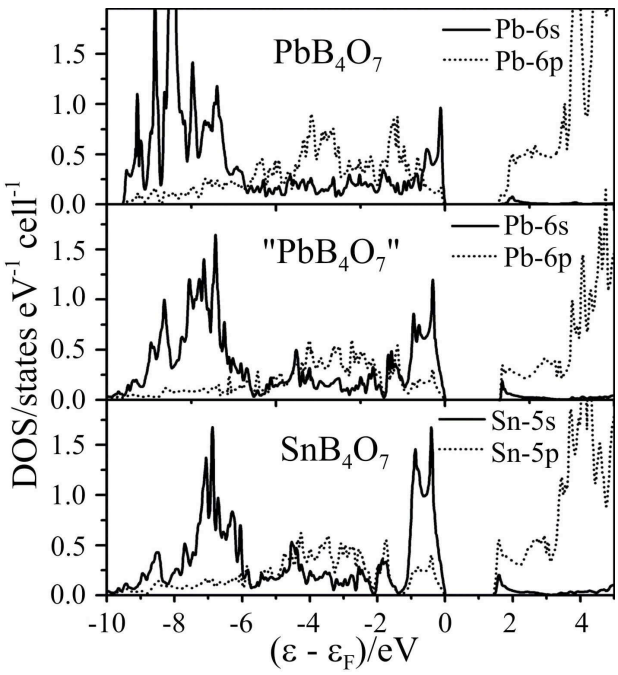

Figure 4.115: Partial density-of-states (PDOS) diagrams of s- and p-orbitals in β-SnB_4O_7 (bottom), "PbB_4O_7" with β-SnB_4O_7 structure (middle), and experimental PbB_4O_7 (top).

Strong s-orbital contributions discern between ϵ_F and -2 eV for β-SnB_4O_7, which are significantly reduced by ∼25% in "PbB_4O_7" with the same structure. These s-levels mix with p-orbitals (dotted lines) in the same energy range and form the lone pair at the tin or lead site. But this tendency is much stronger in the tin compound than in "PbB_4O_7". The lead atoms in the experimental structure of PbB_4O_7 are much more symmetrically coordinated. Consequently, the s-p contribution near ϵ_F is very low (upper part of Figure 4.115), and almost no indication of lone pair formation is discernible in the PDOS of PbB_4O_7, in agreement with the experimental data. Our analysis supports the conclusion drawn in reference [421], that the lone pair is not a result of chemically inert s-orbitals (equally present in Sn^{2+} and Pb^{2+}), but rely on the electronic interaction with the coordinated anions. Thus, the asymmetric oxygen coordination drives to the formation of the lone pair, and vice versa. The unit cell volumes of β-SnB_4O_7 and PbB_4O_7 differ only 0.3%, and the available space for Sn^{2+} and Pb^{2+} within the coordination polyhedra is almost the same. But the ionic radius for Pb^{2+} (1.29 Å) [238] is larger than for Sn^{2+} (1.22 Å). Therefore, lead is well coordinated (almost) in the centre of the oxygen polyhedron, but the smaller tin ion shifts significantly off-center, so the lone pair results from this asymmetric oxygen environment.

4.2.5.9 Theoretical Calculations

Additionally, we calculated bond-valence sums for β-SnB_4O_7 with the bond-length/bond-strength (ΣV) [164, 165] and CHARDI concepts (ΣQ) (Table 4.83) [167]. As bond-valence parameters for the bond-length/bond-strength concept we used R_{ij} = 137.1 for B-O bonds and R_{ij} = 198.4 for Sn-O bonds. The formal ionic charges of the atoms, acquired by X-ray structure analysis, were in agreement within the limits of the concepts, except the threefold coordinated oxygen atom O1, which shows a reduced value of -1.70 (ΣQ) in the CHARDI-concept. Similar deviating values for the $O^{[3]}$ atoms are obtained in β-CaB_4O_7 (-1.92 (ΣV); -1.77 (ΣQ))[173] β-HgB_4O_7 (-2.06 (ΣV); -1.83 (ΣQ))[172], and β-ZnB_4O_7 (-1.83 (ΣV); -1.67 (ΣQ) [171]). Remarkably, in all these cases the deviation was only observed in the CHARDI-calculations (ΣQ), whereas the bond-length/bond-strength values (ΣV) corresponded to the expected values.

Table 4.83: Charge distribution in β-SnB_4O_7 calculated with the bond-length/bond-strength (ΣV) and the CHARDI concept (ΣQ).

	Sn	B1	B2	O1	O2	O3	O4
ΣV	+1.79	+2.98	+2.97	-1.93	-1.95	-1.97	-1.98
ΣQ	+1.90	+2.95	+3.09	-1.70	-2.14	-2.12	-2.09

Then, we calculated the MAPLE values (Madelung Part of Lattice Energy) [161–

163] for β-SnB_4O_7 in order to compare them with MAPLE values of the binary components SnO and the high-pressure modification B_2O_3-II. Their foundation is the additive potential of the MAPLE-values, by which it is possible to calculate hypothetical values for β-SnB_4O_7, starting from the binary oxides. For β-SnB_4O_7 we obtained a value of 47755 kJ·mol^{-1} in comparison to 47638 kJ·mol^{-1} (deviation: 0.2%) starting from the binary oxides [1 × SnO (3762 kJ·mol^{-1}) + 2 × B_2O_3-II (21938 kJ·mol^{-1})].

4.2.6 Closing Remarks to the Chapter Main Group Borates

The phases β-BaB_4O_7, δ-BiB_3O_6, and β-SnB_4O_7 could be prepared and characterized within the scope of this thesis (chapters 4.2.3 – 4.2.5). Each of the three compounds represents the first high-pressure phase in the according system. In the case of β-SnB_4O_7 we even were able to synthesize the first crystalline phase in the ternary system Sn-B-O. The results of these investigations are already published in the References [391, 393, 400].

5 Prospects

Within this thesis the family of high-pressure borates, which was explored in detail by Huppertz and Emme concerning rare-earth borates, could be successfully enlarged into the fields of transition metal and main group metal borates. Systematic research activities, primary for the elements Mn – Cu, led to a couple of new compounds, which not only showed fascinating crystal structures, but revealed interesting properties as well.

In the range of iron borates, which show a huge diversity under ambient-pressure conditions, several high-pressure borates could be realized in this work. A very attractive compound can be found in the boracite-analogous phase "$Fe_3B_7O_{12}N$", which presumably exhibits nitrogen on a fourfould coordinated position. One of the essential ambitions concerning this phase is to approve the supposed formula "$Fe_3B_7O_{12}N$". For this purpose futher investigations, such as EELS studies, are still going on. Boracites show promising material features, *e.g.* pyroelectricity, piezoelectricity, dielectricity, ferroelectricity, ferroelasticity, or partially ferromagnetism. Therefore the crystal structure of "$Fe_3B_7O_{12}N$", which could not be solved in a satisfactory way so far, as well as its properties should be investigated in detail.

With the phases "$M_3B_{11}O_{19}OH$" (M = Co, Fe) another remarkable crystal structure was discovered. The interesting building block within this structure type constitutes a transition state borate group that ranges between a trigonal BO_3- and a tetrahedral BO_4-group.

The trigonal high-pressure phase "$Co_3B_8O_{13}(OH)_4$" shows another notable cobalt borate with a new crystal structure as well as a new composition. The crystal structure exhibits BO_3- and BO_4-groups connected *via* common corners, as well as the rare motif of isolated $[B(OH)_4]$-tetrahedra. For both mentionend boratehydroxides ($M_3B_{11}O_{19}OH$ with M = Co, Fe and "$Co_3B_8O_{13}(OH)_4$") a proof of the existence of hydrogen should be provided in future works.

The extraordinary structural building block of edge-sharing BO_4-tetrahedra, found in the two phases $RE_4B_6O_{15}$ (RE = Dy, Ho) and α-$RE_2B_4O_9$ (RE = Sm –Tb, Ho), could be realized again in the high-pressure borate HP-NiB_2O_4. The striking feature in this compound is that every BO_4-tetrahedron reveals a common edge to an adjacent tetrahedron, which was not observed in borate chemistry before. Due

to the isotypy of the nickel borate β-NiB_4O_7 to the zinc borate β-ZnB_4O_7, one could assume futher correlations between both systems. In this connection, the question came up if there may exist an isotypic Zn-phase to the remarkable nickel borate HP-NiB_2O_4 as well. Experiments, applying pressures up to 12.2 GPa to the system Zn–B-O always led to the product β-ZnB_4O_7. Since β-NiB_4O_7 and HP-NiB_2O_4 were both prepared under a pressure of 7.5 GPa, but at different reaction temperatures, "HP-ZnB_2O_4" may be synthesized at a different temperature as β-ZnB_4O_7. The demand for a diamagnetic compound with edge-sharing tetrahedra, that can be investigated by solid-state NMR (which would be the case for "HP-ZnB_2O_4"), still remains. Additionally, the research activities should be enlarged into the fields of alkaline- or earth alkaline metal borates as well.

A fundamental aim of our research is to increase the coordination number of the boron atoms from four to five, or maybe six, in extreme conditions. For this purpose, HP-NiB_2O_4 is an excellent candidate for *in situ* investigations inside a laser-heated diamond anvil cell. In this connection the copper borate $CuBO_2$ has to be mentioned. Snure and Tiwari reported the synthesis of a borate with the quoted formula $CuBO_2$ in 2007. The compound is described to be isotypic to the Cu delafossites CuMO_2 (M = Al, Ga, In), which represent transparent conductive oxides that find application in transparent light emitting diodes, UV detectors, or solar cells. The isotypy was postulated on the basis of three concurrent reflections of an X-ray powder diffraction pattern of $CuBO_2$ with the powder pattern of CuMO_2 delafossite (the name refers to the mineral delafossite $CuFeO_2$, trigonal structure, $P\overline{3}m$). The crystal structure of copper delafossite is composed of linear arranged Cu^+ and M^{3+} ions coordinated octahedrally by oxygen, while the octahedra build planar layers. This means that $CuBO_2$ would comprise boron in an octahedral coordination, which would be a revolutionary discovery, because until today the maximum coordination number of boron in borates is four. Due to this it seems to be most doubtful, if $CuBO_2$ truly adopts the delafossite structure. Thus, it has to be a main intention to investigate this compound in the near future.

In the section of silicate-analogous borates several discoveries were made within the scope of this work. First of all the phases β-MB_2O_5 (M = Hf, Zr) have to be referred to. An intensive literature research revealed the analogy to minerals of the gadolinite group (gadolinite-(Y): $Y_2Be_2FeSi_2O_8O_2$). Recently another representative of this structure type could be synthesized by S. Herdlicka, namely the borate $Y_2Fe_{0.4}Mg_{0.6}B_4O_{10}$. But also the related structures β-BaB_4O_7 and MB_4O_7 (M = Sr, Pb, Eu, β-Ca, β-Hg), show isotypy to the polymorphs of $BaBe_2Si_2O_7$ barylite and clinobarylite, respectively. On the basis of these results, the increase of the coordination number at boron atoms in analogy to silicon, as it was found in the silicon dioxide modification stishovite, might be possible. Presumably, the pres-

sure needed for this will exceed our preparative possibilities, why the experiments should be conducted inside a laser-heated diamond anvil cell.

Furthermore, the transition metals, which were not investigated in this thesis, should be implicated in prospective studies. High-pressure experiments of A. Haberer already led to the new transition metal borate $Ti_5B_{12}O_{26}$, which is composed of $B_{12}O_{26}$-clusters arranged as the atoms in the Zintl-phase NaTl. Not only experiments with other cations are very promising, but also syntheses accomplished with reaction conditions differing from the standard conditions of 7.5 GPa, used in the context of this work. Pressures below 5 GPa already showed respectable results within the range of rare-earth borates. With the preparation of $Pr_4B_{10}O_{21}$ [422, 423] a new structure type displaying a new composition could be realized at a pressure of about 3.5 GPa. Additionally, the pressure range beyond 7.5 GPa should be implicated as well.

Future research activities could also be enlarged in the fields of doped borates, because those materials often reveal remarkable material features in the area of fluorescence. Another promising branch could be the enhancement of borate systems towards hydroxyborates, fluoroborates, or even oxonitridoborates. Initial studies concerning this systems, except for fluoroborates, were exemplarily conducted within this thesis with the compounds $M_3B_{11}O_{19}OH$ (M = Co, Fe), "$Co_3B_8O_{13}(OH)_4$", and "$Fe_3B_7O_{12}N$".

6 Summary

6.1 High-Pressure/High-Temperature Synthesis

The high-pressure route establishes a versatile tool for new synthetic possibilities in long known borate systems by applying extreme reaction conditions. Especially the increase of the coordination number of boron from three to four in high-pressure borates allows the synthesis of denser borates with structural analogies to *e.g.* aluminates, gallates, silicates, and nitridophosphates. But also the increase of the coordination of the metal cations forces the formation of new crystal structures with new compositions.

Under normal-pressure conditions, glasses are often the favored reaction products in oxoborate chemistry. As demonstrated in this thesis, high-pressure/high-temperature conditions can force the formation of a crystalline product. This is supported by the preparation of β-SnB_4O_7, the first crystalline borate in the system Sn–B–O.

All summarized experiments were conducted by means of an octahedral multianvil system, which represents the best combination of realizable pressures and sample size, in combination with a 1000 t press. These experiments reflect the variety of borate chemistry in combination with a powerful preparative method.

6.2 Transition Metal Borates

β-MB_2O_5(M = Hf, Zr) (Chapter 4.1.3, page 43)

The new high-pressure phases β-HfB_2O_5 and β-ZrB_2O_5 show analogies to the silicate minerals of the gadolinite group. The crystal structure is composed of BO_4-tetrahedra interconnected to layers, which are built up from "Achter" and "Vierer" rings. The cations are located between the "Achter" rings. Starting with a stoichiometric mixture of the comparing oxides, the phases were synthesized in an 18/11-assembly, which was compressed up to 7.5 GPa and heated to 1100 °C. Single crystal structure analysis revealed the monoclinic space group $P2_1/c$ with Z = 4, a = 438.43(3), b = 690.48(6), c = 897.27(6) pm, β = 90.76(1)°,

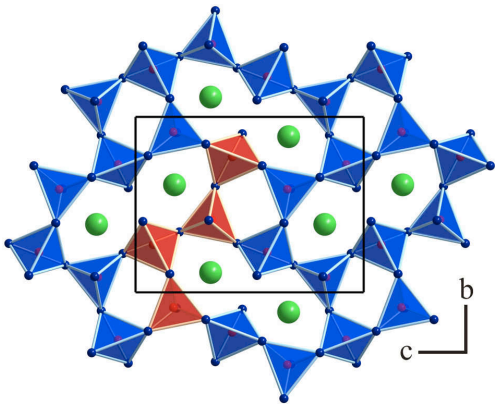

Figure 6.1: View on one borate layer in β-MB_2O_5 (M = Hf, Zr).

R1 = 0.0210, and wR2 = 0.0502 (all data) for β-HfB_2O_5 and a = 440.21(2), b = 693.15(3), c = 899.24(3) pm, β = 90.93(1)°, R1 = 0.0379, and wR2 = 0.0576 (all data) for β-ZrB_2O_5. The application of Liebau's nomenclature for silicates to the arrangement of tetrahedra in the structure of β-MB_2O_5 (M = Hf, Zr) leads to the formula $M\{\mathrm{uB}, 1^2_\infty\}[^4\mathrm{B}_2\mathrm{O}_5]$, representing an unbranched "Vierer" single layer. Figure 6.1 demonstates one borate sheet with the "Vierer" single-chain highlighted in red.

β-MB_4O_7 (M = Mn, Co, Ni, Cu) (Chapter 4.1.4, page 56)

High-pressure/high-temperature syntheses with conditions of 7.5 GPa and temperatures of 1000 °C (Mn)/ 1250 °C (Co)/ 1150 °C (Ni)/ 550 °C (Cu) led to the phases β-MB_4O_7 (M = Mn, Co, Ni, Cu), which are isotypic to β-ZnB_4O_7. Single crystal structure analysis led to the orthorhombic space group *Cmcm* with the representative parameters for β-MnB_4O_7 of Z = 4, a = 1088.5(2), b = 663.3(2), c = 518.7(2) pm, R1 = 0.0209, and wR2 = 0.0553 (all data). The structure is unexceptionally composed of BO_4-tetrahedra, linked *via* common corners forming a network structure. 2/5 of the oxygen atoms bridge three boron atoms ($O^{[3]}$), while 3/5 connect two boron atoms ($O^{[2]}$). Along c, the structure shows channels of "Vierer" and "Sechser" rings, with the cations positioned inside the "Sechser" ring channels. The differences inside the structures of β-MB_4O_7 (M = Mn, Co, Ni, Cu, Zn) are due to the varying ionic radii and electronic configurations of the M^{2+} ions and becomes manifest in a differing distortion of the square-pyramidal coordination spheres of the cations. Figure 6.2 shows the crystal structure of β-MB_4O_7 (M = Mn, Co, Ni, Cu) with a view along $[00\bar{1}]$.

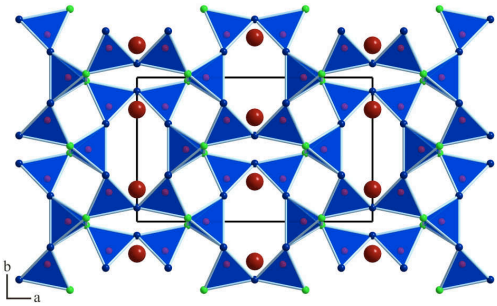

Figure 6.2: Crystal structure of β-MB_4O_7 (M = Mn, Co, Ni, Cu).

α-FeB_2O_4 (Chapter 4.1.5, page 76)

The new iron borate α-FeB_2O_4 was prepared by means of a high-pressure/high-temperature synthesis of 7.5 GPa and 1100 °C in an 18/11-assembly. The monoclinic compound crystallizes in the space group $P2_1/c$ with four formula units and the lattice parameters of a = 715.2(2), b = 744.5(2), c = 862.3(2) pm, β = 94.71(3)°, R1 = 0.0350, and wR2 = 0.0532 (all data) (Figure 6.3, top). The high-pressure phase exclusively exhibits corner-sharing BO_4-tetrahedra, which are interconnected to "Sechser" rings with the topology UUDUDD (U = up, D = down) (Figure 6.3 bottom). These rings condense to borate layers, linked among each other to form a framework. The cations are arranged in channels composed of "Sechser" rings. α-FeB_2O_4 is isotypic to the compounds β-$SrGa_2O_4$, $CaAl_2O_4$-II, and $CaGa_2O_4$. All mentioned compounds can be understood as stuffed derivates of the tridymite (SiO_2) framework-structure.

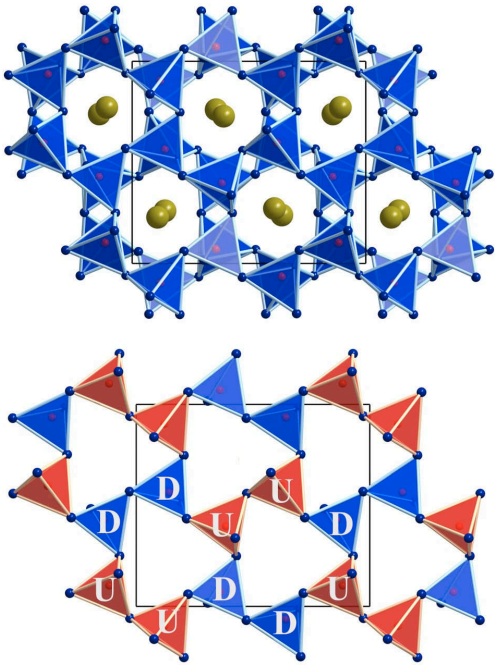

Figure 6.3: Crystal structure (top) and single layer (bottom) of α-FeB_2O_4.

HP-NiB_2O_4 (Chapter 4.1.6, page 84)

Edge-sharing BO_4-tetrahedra are a very rare structural feature, which could only be realized in the compounds $RE_4B_6O_{15}$ (RE = Dy, Ho), α-$RE_2B_4O_9$ (RE = Sm –Tb, Ho). Now it was possible to synthesize a third structure type represented in the new high-pressure phase HP-NiB_2O_4. Whereas in both rare-earth compounds only some of the tetrahedra are linked *via* one common edge, in HP-NiB_2O_4 every BO_4-group shares one common edge with the adjacent BO_4-unit. This is unique in borate chemistry. The edge-sharing dimer building blocks are linked to "Sechser" rings, interconnected to planar layers, which are connected by strings of edge-sharing NiO_6-octahedra. The crystal structure was solved on the basis of sin-

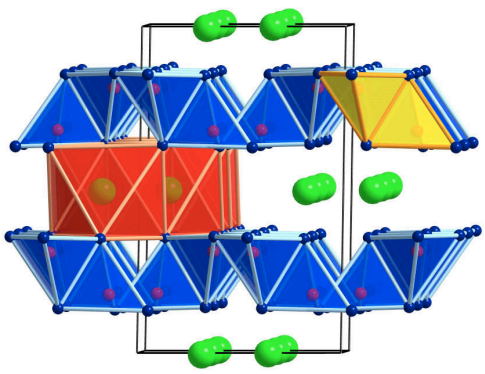

Figure 6.4: Crystal structure HP-NiB_2O_4.

gle crystal data and revealed the space group $C2/c$ with four formula units and the lattice parameters of a = 924.7(2), b = 552.3(2), c = 442.88(9) pm, β = 108.30(3)°, R1 = 0.0314, and wR2 = 0.0542 (all data). Figure 6.4 demonstrates the crystal structure of HP-NiB_2O_4 along $[00\bar{1}]$. One dimer building block is highlighted in yellow and one string of edge-sharing NiO_6-octahedra is drawn in red. Similar layers composed of edge-sharing tetrahedra were observed in the compounds β-$Ca_3[Al_2N_4]$, $Ca_3[Al_2As_4]$, $Sr_3[Al_2P_4]$, $Ba_3[In_2P_4]$, and α-$Ca_3[Ga_2N_4]$. In contrast, the layers in all these compounds are corrugated and the metal content between the layers is three times as high as in HP-NiB_2O_4, leading to a different crystal structure.

CdB_2O_4 (Chapter 4.1.7, page 94)

CdB_2O_4 was synthesized at conditions of 7.5 GPa and 1100 °C starting from the binary oxides CdO and B_2O_3. Its network structure consists of corner-sharing BO_4-tetrahedra, interconnected to layers. The layers consist of "Sechser" rings, showing two types of tetrahedra orientation: an UDUDUD topology and an UUUDDD topology (U = up, D = down) in the ration 1 : 3. Figure 6.5 gives a view of the crystal structure of the cadmium borate and displays the two arrangements inside of a layer as well. Due to single crystal structure investigations, including the consideration of twinning by merohedry and the introduction of a twofold rotation axis, the hexagonal structure ($P6_3$, Z = 8) could be refined with the parameters a = 886.64(3), c = 717.38(3) pm, R1 = 0.0178, and wR2 = 0.0388 (all data). The structure of CdB_2O_4 is closely related to the structure type of the compounds $BaGa_2O_4$, $KAlSiO_4$, $KGeAlO_4$, $KCoPO_4$, CaP_2N_4, and SrP_2N_4. Except for CdB_2O_4 all mentioned compounds form a superstructure, which means that CdB_2O_4 is the first representative, showing a threefold smaller basic cell. This is confirmed by electron diffraction experiments.

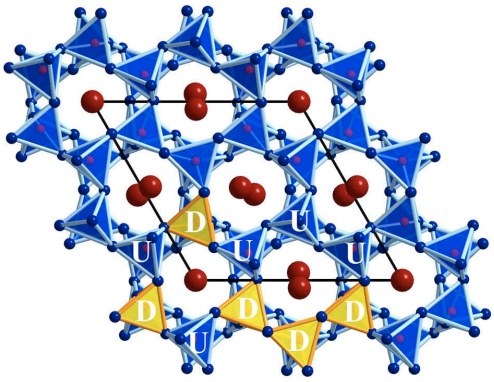

Figure 6.5: Crystal structure of CdB_2O_4.

$M_3B_{11}O_{19}OH$ (M = Fe, Co) (Chapter 4.1.8, page 105)

The non-centrosymmetric borates $M_3B_{11}O_{19}OH$ (M = Fe, Co) were obtained at 7.5 GPa and 1100 °C (Fe)/ 880 °C (Co). The crystal structures were solved on the basis of orthorhombic unit cells in the space group $Pmn2_1$ with the parameters a = 771.9(2), b = 823.4(2), c = 1768.0(4) pm, R1 = 0.0479, and wR2 = 0.0930

(all data) for $Fe_3B_{11}O_{19}OH$ and a = 770.1(2), b = 817.6(2), c = 1746.9(4) pm, R1 = 0.0516, and wR2 = 0.0954 for $Co_3B_{11}O_{19}OH$. The length of the oxygen-hydrogen bond was restrained to 98.2 pm in accordance to the bond-length between oxygen and hydrogen in borax (98.2(3) pm). The phases are built up from corrugated multiple layers, composed of BO_4-tetrahedra. The layers are interconnected to a network structure *via* non-planar, flat pyramidal BO_3-groups, generating Z-shaped channels in which the cations are arranged. Figure 6.6 demonstrates the crystal structure of $M_3B_{11}O_{19}OH$ (M = Fe, Co) and zooms in on one transition state borate group. The non-planar BO_3-groups (B11) represent a transition state between a planar BO_3-group and a tetrahedral BO_4-group, because comparably large B–O-distances, can also be found in boracites, which exclusively consist of BO_4-tetrahedra.

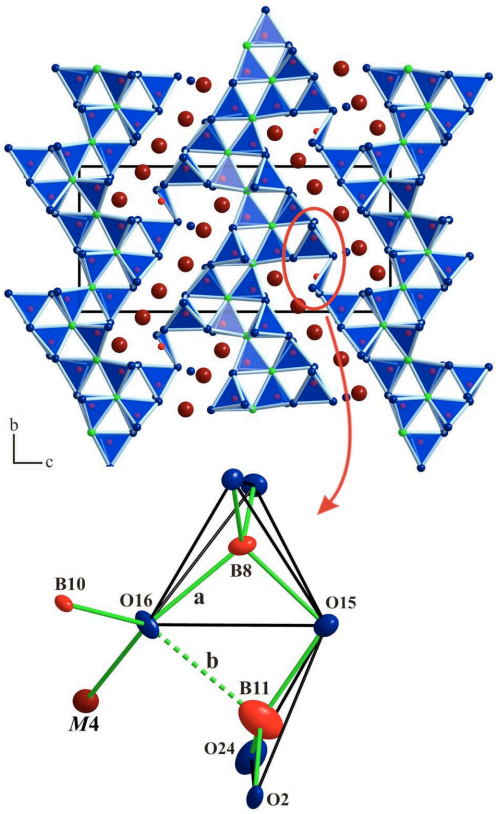

Figure 6.6: Crystal structure of the high-pressure borates $M_3B_{11}O_{19}OH$ (M = Fe, Co) with an enlargement of the transition state borate group.

"$Fe_3B_7O_{12}N$" (Chapter 4.1.9, page 121)

A pressure of 7.5 GPa and a temperature of 1100 °C led to the high-pressure phase "$Fe_3B_7O_{12}N$". The structure could not be solved using *Direct methods*, why the structure was solved by trial and error. The best results were achieved in the space group $F\overline{4}3c$ and the parameters Z = 8, a = 1222.4(2) pm, R1= 0.0643, and wR2 = 0.1699 (all data). The new phase is built up from starlike shaped units, consisting of four BO_3N-tetrahedra linked *via* one common edge. The bridging, fourfold coordinated position is presumably occupied by nitrogen, which is coordinated by four boron atoms in a tetrahedral way. These starlike shaped units are linked over additional BO_4-tetrahedra to form a network struc-

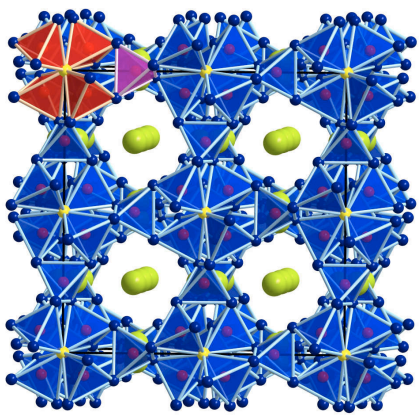

Figure 6.7: Crystal structure of the high-pressure borate "$Fe_3B_7O_{12}N$".

ture analogous to cubic boracite. Figure 6.7 represents the crystal structure of "$Fe_3B_7O_{12}N$" with one starlike shaped building block highlighted in red and one bridging tetrahedron shown in violet. The network is crossed by channels, consisting of "Achter"-rings in which the Fe^{2+} ions are arranged. The iron cations are located on a split position, which might be due to multiple pseudo-merohedral twinning. However, trial refinements did not yield a more satisfactory solution so far.

"$Co_3B_8O_{13}(OH)_4$" (Chapter 4.1.10, page 130)

"$Co_3B_8O_{13}(OH)_4$" was synthesised *via* the high-pressure/high-temperature route at 7.5 GPa and 800 °C in an 18/11-assembly. The crystal structure could be solved on the basis of single crystal data and was then refined in the space group $R3c$ with the help of a twin based on four twin domains (Z = 24, a = 1747.4(2), b = 2140.1(2) pm, R1 = 0.0761, and wR2 = 0.1509 for all data). The complex network structure is assembled of trigonal BO_3- and tetrahedral BO_4-groups, being linked *via* twofold coordinated oxygen atoms ($O^{[2]}$) as well as threefold coordinated oxygen atoms ($O^{[3]}$). Additionally, there exist isolated $B(OH)_4$-tetrahedra, which are positioned in channels that cross the borate network. The channels are built up by different "Achter" rings, composed either of eight tetrahedra, of seven tetrahedral and one trigonal unit, or of six tetrahedra and two trigonal BO_3-groups. The rings are interconnected *via* strings consisting of $[(BO_3)O^{[3]}]$ units, linked among each other by additional tetrahedra. Inside of each ring, the Co^{2+} ions are located, which either are coordinated in a strongly distorted octahedral way or by seven oxygen anions. These Co-polyhedra are interconnected by the isolated $B(OH)_4$-tetrahedra resulting in chains.

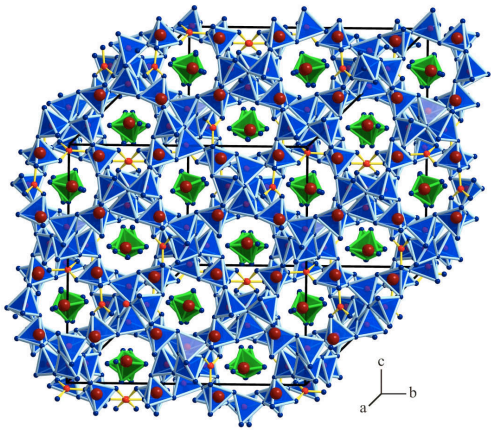

Figure 6.8: Crystal structure of "$Co_3B_8O_{13}(OH)_4$".

6.3 Main Group Borates

β-BaB_4O_7 (Chapter 4.2.3, page 150)

The new barium borate β-BaB_4O_7 was prepared under high-pressure/high-temperature conditions of 7.5 GPa and 1100 °C. The orthorhombic phase crystallizes in the space group $Pmnb$ with the lattice parameters a = 1099.4(2),

b = 901.7(2), c = 430.73(9) pm, Z = 2, R1 = 0.0199, and wR2 = 0.0406 (all data). The network structure is composed of corner-sharing BO_4-tetrahedra isotypic to the mineral barylite $BaBe_2Si_2O_7$. The framework is crossed by channels built up from "Vierer" and "Sechser" rings. Inside of the "Sechser" ring channels, the cations are located, while the "Vierer" ring channels remain empty. The structure is closely related to the orthorhombic high-pressure phases β-MB_4O_7 (M = Ca, Hg, Sn) and the ambient-pressure phases MB_4O_7 (M = Sr, Pb, Eu), but shows a different orientation of the tetrahedra. Figure 6.9 demonstrates the crystal structure of the orthorhombic barium borate, whereas differently orientated tetrahedra are highlighted in blue and red. β-BaB_4O_7 can be regarded as the first centrosymmetric variant of the compounds β-MB_4O_7 (M = Ca, Hg, Sn) and MB_4O_7 (M = Sr, Pb, Eu). Interestingly the orthorhombic phases are isotypic to the mineral clinobarylite $BaBe_2Si_2O_7$, which is polymorphic to barylite. DFT calculations led to the assumption that BaB_4O_7 in the β-CaB_4O_7 structure might be a second high-pressure phase above 7.5 GPa.

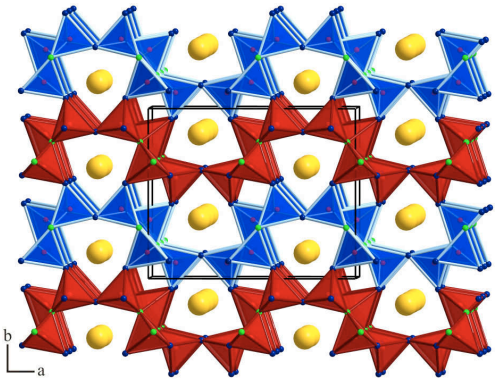

Figure 6.9: Crystal structure of β-BaB_4O_7.

δ-BiB_3O_6 (Chapter 4.2.4, page 163)

To synthesize the compound δ-BiB_3O_6, high-pressure/high-temperature conditions of 5.5 GPa and 820 °C were applied. Single crystal structure analysis revealed the non-centrosymmetric space group $Pca2_1$ and the parameters a = 1844.8(4), b = 444.95(9), c = 428.06(9) pm, Z = 4, R1 = 0.0304, and wR2 = 0.0664 (all data). The structure of the new high-pressure polymorph of the important NLO material BIBO (α-BiB_3O_6) consists of corner-sharing BO_4-tetrahedra condensed to layers, that are shifted by a c-glide plane. These layers are interconnected *via* zigzag chains of BO_4-groups (red polyhedra in Figure 6.10), forming a network structure with channels of "Sechser"- and "Zehner"-rings, containing the metal cations. In contrast

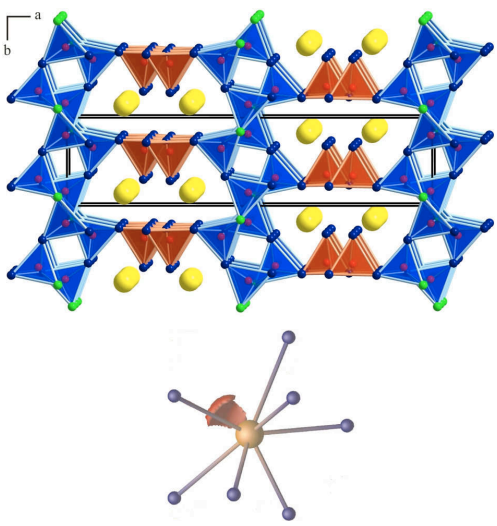

Figure 6.10: Crystal structure of δ-BiB_3O_6 with lone pair at Bi^{3+}.

to the compounds γ-$RE(BO_2)_3$ (RE = La–Nd), which are isotypic to δ-BiB_3O_6, the bismuth phase shows a different coordination of Bi^{3+}. The reason for this is a sterically active lone pair localized at Bi^{3+}. DFT calculations confirmed the existence of a lone pair which points toward the "empty" space above the bismuth atom.

β-SnB_4O_7 (Chapter 4.2.5, page 173)

High-pressure/high-temperature conditions of 7.5 GPa and 1100 °C succeeded in the synthesis of the first crystalline tin borate β-SnB_4O_7. The crystal structure was solved on the basis of single crystal data in the space group $Pmn2_1$ with two formula units per unit cell and was refined to the parameters a = 1085.34(4), b = 444.84(3), c = 423.43(3) pm, R1 = 0.0155, wR2 = 0.0324 (all data). The non-centrosymmetric crystal structure is solely composed of corner-sharing BO_4-tetrahedra and is isotypic to the mineral clinobarylite $BaBe_2Si_2O_7$, to the high-pressure phases β-CaB_4O_7 and β-HgB_4O_7, as well as to the ambient-pressure phases SrB_4O_7, PbB_4O_7, and EuB_4O_7. The network is crossed by channels, which consist of "Vierer" and "Sechser" rings, whereas the tin cations are arranged in the "Sechser" ring channels, while the "Vierer" ring channels remain empty. The main difference between the isotypic phases consists in the coordination of the Sn^{2+} ions, compared to the other cations. The reason for this, may be the sterically active lone pair localized at Sn^{2+}. DFT calculations support the existence of the this active lone pair in β-SnB_4O_7, but it is not yet clear why the isostructural lead compound shows no distinctive asymmetry.

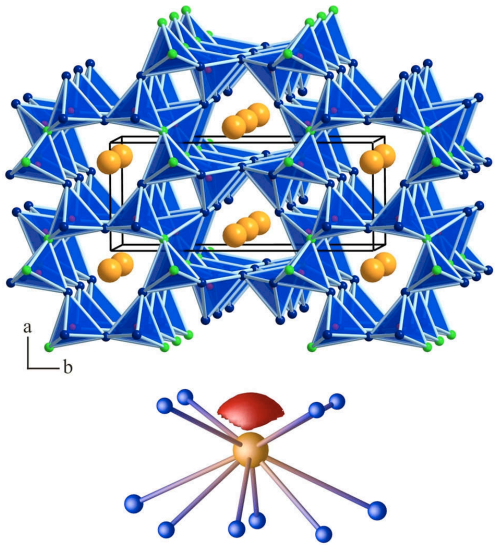

Figure 6.11: Crystal structure of δ-BiB_3O_6 and vizualization of the sterically active lone pair at Sn^{2+}.

7 Appendix

7.1 Abbreviations

Ø	Average	C.N.	Coordination number
kbar	Kilobar	kHz	Kilohertz
°C	Degree Celsius	kJ	Kilojoule
Å	Ångstrøm	kV	Kilovolt
δ	Chemical shift parameter	LMTO	Linear Muffin-Tin Orbital
η	Asymmetry parameter	MAS	Magic Angle Spinning
λ	Wave length	mg	Milligramme
μ_B	Effective Bohr magneton	MHz	Megahertz
ρ	Density	min	Minute
χ	Magnetic susceptibility	mm	Millimetre
ca., $\sim$	circa	MQMAS	Multi-Quantum Magic-Angle Spinning
CCD	Charge Coupled Device	NIR	Near Infra Red
cm	Centimetre	NLO	Non Linear Optics
cm^{-1}	Wavenumber	nm	Nanometer
d	Distance	NMR	Nuclear Magnetic Resonance
DFT	Density Functional Theory	NP	Normal Pressure
EDX	Energy Dispersive X-Ray Analysis	PDOS	Partial density-of-states
e.g.	Exempli gratia	PET	Polyethylen
EELS	Electron Energy Loss Spectroscopy	pm	Picometer
ELF	Electron Localization Function	ppm	Parts per million
et al.	Et alii	PSD	Position Sensitive Detector
Fa.	Firma, engl. company	PTFE	Polytetrafluoroethylene
g	Gramme	*RE*	Rare Earth
GPa	Gigapascal	s	Second
Goof	Goodness of Fit	SEM	Scanning Electron Microscope
h	Hour	SOQE	Second Order Quadrupole Effect
HP	High Pressure	t	Ton
I	Intensity	T	Tesla
ICSD	Inorganic Crystal Structure Database	UV	Ultraviolet
IR	Infra Red	V	Volume
K	Kelvin	Z	Formula Units

7.2 Curriculum Vitae

Personal Information	
	Johanna Sibille Knyrim
24/09/1979	Born in Regensburg (Bavaria), Germany
	Second child of Brigitte Knyrim (Teacher, Galerist) and Helmut Knyrim (Teacher, Artist)
	Nationality: German
	Family status: Single
Education	
since 11/2005	PhD Studies in the group of Univ.-Prof. Dr. H. Huppertz at the Department of Chemistry – Ludwig-Maximilians-Universität München; PhD thesis entitled *"Synthetic Investigations into Main Group and Transition Metal Borates at Extreme Conditions"*
12/2007	Römer-Award (Dr. Klaus Römer-Foundation; URL: http://www.cup.uni-muenchen.de/roemer/index.php)
09/2005	Diploma thesis in the group of Univ.-Prof. Dr. H. Huppertz at the Department of Chemistry – Ludwig-Maximilians-Universität München with the title *"Synthesis and Characterization of the New Oxoborates HP-SnB_4O_7 and HP-HfB_2O_5"*
10/2000–09/2005	Basic and advanced chemistry courses at the Ludwig-Maximilians-Universität München
10/1999–09/2000	Basic courses in process engineering at the University of Applied Sciences Regensburg
06/1999	Abitur at the Goethe-Gymnasium Regensburg
1985 – 1999	Secondary education: Goethe-Gymnasium Regensburg
1985 – 1989	Primary education: Kreuzschule Regensburg

7.3 Publications

Most of the here pesented results are already published. The following lists all conference contributions and papers.

7.3.1 Conference contributions

4. Felix W. Roeßner, Johanna S. Knyrim, Hubert Huppertz
   HP-NiB_2O_4: The first borate presenting edge-sharing at all BO_4–tetrahedra
   Joint 21st AIRAPT and 45th EHPRG International Conference on High Pressure Science and Technology, Catania (Italy), 17/09 – 21/09/2007.

3. Johanna S. Knyrim
   Die Hochdruckphasen FeB_2O_4 und CdB_2O_4 (Talk)
   Festkörper-Seminar Hirschegg, Hirschegg (Austria), 07/06 – 10/06/2007.

2. Johanna S. Knyrim, Hubert Huppertz
   Hochdrucksynthese und Kristallstruktur des neuen Eisenborates FeB_2O_4 (Poster)
   15. Jahrestagung der Deutschen Gesellschaft für Kristallographie, Bremen, 05/03 – 09/03/2007.

1. Johanna S. Knyrim, Hubert Huppertz
   Hochdrucksynthese und Kristallstruktur des silicat-ähnlichen Hafniumborates β-HfB_2O_5 (Poster)
   14. Jahrestagung der Deutschen Gesellschaft für Kristallographie, Freiburg, 03/04 – 06/04/2006.

7.3.2 Papers

9. *High-pressure Synthesis and Characterization of the Alkaline Earth Borate β-BaB_4O_7*
   Johanna S. Knyrim, S. Rebecca Römer, Wolfgang Schnick, and Hubert Huppertz
   Solid State Sci. 10 (**2008**) in press.

8. *Synthesis and Crystal Structure of the High-Pressure Iron Borate α-FeB_2O_4*
   Johanna S. Knyrim and H. Huppertz
   J. Solid State Chem. 181 (**2008**) 2092-2098.

7. *Synthesis and Crystal Structure of the New High-Pressure Phase CdB_2O_4*
Johanna S. Knyrim, Holger Emme, Markus Döblinger, Oliver Oeckler, Matthias Weil, and Hubert Huppertz
Chem. Eur. J. 14 (**2008**) 6149-6154.

6. *High-Pressure Synthesis, Crystal Structure, and Properties of the First Ternary Zirconium Borate β-ZrB_2O_5*
Johanna S. Knyrim and Hubert Huppertz
Z. Naturforsch. B 63 (**2008**) 707-712.

5. *High-pressure Syntheses and Characterization of the Transition Metal Borates β-MB_4O_7 ($M = Mn^{2+}$, Ni^{2+}, Cu^{2+})*
Johanna S. Knyrim, Jana Friedrichs, Stephanie Neumair, Felix Roeßner, Yvonne Floredo, Stefanie Jakob, Dirk Johrendt, Robert Glaum, and Hubert Huppertz
Solid State Sci. 10 (**2008**) 168-176.

4. *Exclusive Formation of Edge-Sharing BO_4 Tetrahedra in the High-Pressure Borate HP-NiB_2O_4*
Johanna S. Knyrim, Felix Roeßner, Stefanie Jakob, Dirk Johrendt, Isabel Kinski, Robert Glaum, and Hubert Huppertz
Angew. Chem. 119 (**2007**) 9256-9259; *Angew. Chem. Int. Ed.* 46 (**2007**) 9097-9100.

3. *High-Pressure Synthesis, Crystal Structure, and Properties of the First Ternary Hafniumborate β-HfB_2O_5*
Johanna S. Knyrim and Hubert Huppertz
J. Solid State Chem. 180 (**2007**) 742-748.

2. A New Non-Centrosymmetric Modification of BiB_3O_6
Johanna S. Knyrim, Petra Becker, Dirk Johrendt, and Hubert Huppertz
Angew. Chem. 118 (**2006**) 8419-8421; *Angew. Chem. Int. Ed.* 45 (**2006**) 8239-8241.

1. *Pressure-Induced Crystallization and Characterization of the Tin-Borate β-SnB_4O_7*
Johanna S. Knyrim, Falko M. Schappacher, Rainer Pöttgen, Jörn Schmedt auf der Günne, Dirk Johrendt, and Hubert Huppertz
Chem. Mater. 19 (**2007**) 254-262.

7.4 CSD-Numbers

The CIF-files (Crystallographic Information File) of the following compounds were deposited at the Fachinformationszentrum Karlsruhe, 76344 Eggenstein Leopoldshafen, Germany.

β-HfB_2O_5	CSD-417031
β-ZrB_2O_5	CSD-418931
β-SnB_4O_7	http://pubs.acs.org
CdB_2O_4	CSD-419180
α-FeB_2O_4	CSD-419183
β-BaB_4O_7	CSD-419469
β-MnB_4O_7	CSD-391409
β-NiB_4O_7	CSD-391407
β-CuB_4O_7	CSD-391408
HP-NiB_2O_4	CSD-418385
δ-BiB_3O_6	CSD-416822

Bibliography

[1] D. M. Schubert, *Structure and Bonding* **2003**, *105*, 1.

[2] *http://de.wikipedia.org/wiki/Borax;* **07.07.2008**.

[3] *http://pt.wikipedia.org/wiki/Kernite;* **02.07.2008**.

[4] *http://jburkhart.com/ulexite.html;* **02.07.2008**.

[5] *http://www.gc.maricopa.edu/earthsci/imagearchive/colemanite.htm;* **02.07.2008**.

[6] *http://webplaza.pt.lu/public/andre/turmalin_kristalle/heisteine_ polychrom_ Turmalin.jpg* **02.07.2008**.

[7] Y. Kaup, M. Schmid, A. Middleton, U. Weser, *J. Inorg. Biochem.* **2003**, *94*, 214.

[8] *http://www.mindat.org/min-4003.html;* **07.07.2008**.

[9] *http://www.gwbasic.at/chemie;* **02.07.2008**.

[10] E. Riedel, *Anorganische Chemie*, 4. Auflage, Walter de Gruyter Gmbh & Co.KG, Berlin, **1999**.

[11] *Inorganic Crystal Structure Database v1.0.0 Fachinformationszentrum Karlsruhe* **July 2008**.

[12] *http://www.britannica.com;* **08.07.2008**.

[13] D. Xue, S. J. Zhang, *Acta Crystallogr. B* **1998**, *54*, 652.

[14] J. Liebertz, S. Stähr, *Z. Kristallogr.* **1983**, *165*, 91.

[15] C. Chen, B. Wu, A. Jiang, G. You, *Sci. Sin. B* **1985**, *28*, 235.

[16] C. Mazzetti, F. D. Carli, *Chim. Ital.* **1926**, *56*, 23.

[17] B. S. R. Sastry, F. A. Hummel, *J. Am. Ceram. Soc.* **1958**, *41*, 7.

[18] H. König, R. Hoppe, *Z. Anorg. Allg. Chem.* **1978**, *41*, 7.

[19] C. Chen, B. Wu, A. Jiang, B. Wu, G. You, R. Li, S. Lin, *J. Opt. Soc. Am. B* **1989**, *6*, 616.

[20] J. Liebertz, *Z. Kristallogr.* **1982**, *158*, 319.

[21] R. Fröhlich, L. Bohatý, J. Liebertz, *Acta Crystallogr. C* **1984**, *40*, 343.

[22] P. Becker, J. Liebertz, L. Bohatý, *J. Cryst. Growth* **1999**, *203*, 149.

[23] Y. Mori, I. Kuroda, S. Nakajiama, T. Sasaki, S. Nakai, *Appl. Phys. Lett.* **1995**, *67*, 1818.

[24] G. Ryu, C. S. Yoon, T. P. J. Han, H. G. Gallagher, *J. Cryst. Growth* **1998**, *191*, 492.

[25] Y. Mori, Y. K. Yap, T. Kamimura, M. Yoshimura, T. Sasaki, *Opt. Mater.* **2002**, *19*, 1.

[26] T. Sasaki, Y. Mori, M. Yoshimura, *J. Nonlinear Opt. Phys. Mater.* **2001**, *2*, 249.

[27] Y. Idota, T. Kubota, A. Matsufuji, Y. Maekawa, T. Miyasaka, *Science* **1997**, *276*, 1395.

[28] D. Holland, M. E. Smith, A. P. Howes, T. Davies, L. Barrett, *Phys. Chem. Glasses* **2003**, *44*, 59.

[29] A. Hayashi, M. Nakai, M. Tatsumisago, T. Minami, Y. Himei, Y. Miura, M. Katada, *J. Non-Cryst. Solids* **2002**, *306*, 227.

[30] A. Hayashi, M. Nakai, H. Morimoto, T. Minami, M. Tatsumisago, *J. Mater. Sci.* **2004**, *39*, 5361.

[31] C. Geijke, J. Swenson, R. G. Delaplané, L. Börjesson, *Phys. Rev. B* **2002**, *65*, 212201.

[32] C. Geijke, E. Zanghellini, J. Svenson, L. J. Börjesson, *Power Sources* **2003**, *119-121*, 576.

[33] C. Geijke, E. Nordström, L. Fransson, K. Edström, L. Häggström, L. Börjesson, *J. Mater. Chem.* **2002**, *12*, 2965.

[34] O. Mishima, L. D. Calvert, E. Whalley, *Nature* **1984**, *310*, 393.

[35] R. J. Hemley, A. P. Jephcoat, H. K. Mao, L. C. Ming, M. H. Manghnani, *Nature* **1988**, *334*, 52.

[36] K. Landskron, H. Huppertz, J. Senker, W. Schnick, *Angew. Chem* **2001**, *113*, 2713; *Angew. Chem. Int. Ed. Engl.*, **2001**, *40*, 2643.

[37] F. Karau, W. Schnick, *Angew. Chem.* **2006**, *118*, 4617; *Angew. Chem. Int. Ed. Engl.*, **2006** , *632*, 2093.

[38] S. Sedlmair, *Personal Communication* **07.07.2008**.

[39] F. Liebau, *Structural Chemistry of Silicates*, Springer-Verlag, Berlin, **1985**.

[40] A. Zerr, G. Miehe, G. Serghiou, M. Schwarz, E. Kroke, R. Riedel, H. Fuess, P.Kroll, R. Boehler, *Nature* **1999**, *400*, 340.

[41] E. Soignard, M. Somayazulu, J. Dong, O. F. Sankey, P. McMillan, *J. Phys.: Condens. Matter* **2001**, *13*, 557.

[42] H. He, T. Sekine, T. Kobayashi, H. Hirosaki, I. Suzuki, *Phys. Rev. B* **2000**, *62*, 11412.

[43] M. Schwarz, G. Miehe, E. Zerr, A.and Kroke, B. T. Poe, H. Fuess, R. Riedel, *Adv. Mater.* **200**, *12*, 883.

[44] W. Schnick, *Angew. Chem.* **1999**, *111*, 3511; *Angew. Chem. Int. Ed. Engl.*, **1999**, *38*, 3309.

[45] P. Kroll, J. Appen, *Phys. Stat. Sol. B* **2001**, *1*, R6.

[46] I. Higashi, K. Kobayashi, T. Takabatake, M. Kasaya, *J. Alloys Compd.* **1993**, *193*, 300.

[47] C. Routsi, J. K. Yakinthos, E. Gamari-Seale, *J. Magn. Magn. Mater.* **1992**, *110*, 317.

[48] R. Pöttgen, *Z. Naturforsch. B* **1996**, *51*, 806.

[49] J. Sakurai, K. Kegai, T. Kuwai, Y. Isikawa, K. Nishimura, K. Mori, *J. Magn. Magn. Mater.* **1995**, *140-144*, 875.

[50] F. Canepa, S. Cirafici, *J. Alloys Compd.* **1996**, *232*, 71.

[51] G. Heymann, *PhD Thesis* Ludwig–Maximilians–Universität München, **2007**.

[52] G. Heymann, *Personal Communication* **11.07.2008**.

[53] R. V. Skolozdra, O. E. Koretskaya, Y. K. Gorelenko, *Inorg. Mater.* **1984**, *20*, 604.

[54] T. Takabatake, F. Teshima, H. Fujii, S. Nishigori, T. Suzuki, T. Fujita, Y. Yamaguchi, J.Sakurai, D. Jaccard, *Phys. Rev. B* **1990**, *41*, 9607.

[55] C. B. Shoemaker, D. P. Shoemaker, *Acta Crystallogr.* **1965**, *18*, 900.

[56] P. I. Krypyakevich, V. Y. Markiv, E. V. Melnyk, *Dopov. Akad. Nauk. Ukr. RSR Ser. A* **1967**, 750.

[57] M. F. Zumdick, R.-D. Hoffmann, R. Pöttgen, *Z. Naturforsch. B* **1999**, *54*, 45.

[58] A. E. Dwight, M. H. Mueller, R. A. Conner (Jr.), J. W. Downey, H. Knott, *Trans Met Soc. AIME* **1968**, *242*, 2075.

[59] J. F. Riecken, G. Heymann, T. Soltner, R.-D. Hoffmann, H. Huppertz, D. Johrendt, R. Pöttgen, *Z. Naturforsch. B* **2005**, *60*, 821.

[60] G. Heymann, S. Rayayprol, J. F. Riecken, R.-D. Hoffmann, U. C. Rodewald, H. Huppertz, R. Pöttgen, *Solid State Sci.* **2006**, *8*, 1258.

[61] J. F. Riecken, U. C. Rodewald, G. Heymann, S. Rayaprol, H. Huppertz, R.-D. Hoffmann, R. Pöttgen, *Z. Naturforsch. B* **2006**, *61*, 1477.

[62] G. Heymann, J. F. Riecken, S. Rayaprol, S. Christian, R. Pöttgen, H. Huppertz, *Z. Anorg. Allg. Chem.* **2007**, *633*, 77.

[63] D. Mazzone, D. Rossi, R. Marazza, R. Ferro, *J. Less-Common Met.* **1981**, *80*, P47.

[64] K. Łątka, E. A. Görlich, J. Gurgul, R. Kmieć, *Hyp. Int.* **2000**, *126*, 299.

[65] C. P. Sebastian, S. Rayaprol, R. Pöttgen, *Solid State Commun.* **2006**, *140*, 276.

[66] S. Baran, J. Leciejewicz, N. Stüsser, A. Szytula, A. Zygmunt, Y. Ding, *J. Magn. Magn. Mater.* **1997**, *170*, 143.

[67] A. Adam, J. Sakurai, Y. Yamaguchi, H. Fujiwara, K. Mibu, T. Shinjo, *J. Magn. Magn. Mater.* **1990**, *90 & 91*, 544.

[68] S. Baran, A. Szytula, J. Leciejewicz, N. Stüsser, Y. F. Ding, A. Zygmunt, *Aperiodic'97, Proceedings of the International Conference on Aperiodic Crystals*, Alpe d'Huez, Aug. 27-31 (Eds.: M. de Boissieu, J.-L. Verger-Gaugry, R. Currat), World Scientific, Singapore, **1997**, pp. 599–603.

[69] K. Łątka, R. Kmieć, J. Gurgul, *Mol. Phys. Rep.* **2000**, *30*, 94.

[70] C. P. Sebastian, G. Heymann, B. Heying, U. C. Rodewald, H. Huppertz, R. Pöttgen, *Z. Anorg. Allg. Chem.* **2007**, *633*, 1551.

[71] H. Emme, *PhD Thesis* Ludwig–Maximilians–Universität München, **2005**.

[72] H. Emme, M. Valldor, R. Pöttgen, H. Huppertz, *Chem. Mater.* **2005**, *17*, 2707.

[73] H. Huppertz, B. von der Eltz, *J. Am. Chem. Soc.* **2002**, *124*, 9376.

[74] H. Huppertz, *Z. Naturforsch. B* **2003**, *58*, 278.

[75] H. Huppertz, H. Emme, *Phys.: Condens. Matter* **2004**, *16*, S1283.

[76] H. Emme, H. Huppertz, *Z. Anorg. Allg. Chem.* **2002**, *628*, 2165.

[77] H. Emme, H. Huppertz, *Chem. Eur. J.* **2003**, *9*, 3623.

[78] H. Emme, H. Huppertz, *Acta Crystallogr. C* **2005**, *61*, i29.

[79] A. Weiss, A. Weiss, *Z. Anorg. Allg. Chem.* **1954**, *276*, 95.

[80] A. Neuhaus, *Chimia* **1964**, *18*, 93.

[81] G. E. Gurr, P. W. Montgomery, C. D. Knutson, B. T. Gorres, *Acta Crystallogr. B* **1970**, *26*, 906.

[82] C. T. Prewitt, R. D. Shannon, *Acta Crystallogr. B* **1968**, *24*, 869.

[83] A. Haberer, *Master Thesis* Ludwig–Maximilians–Universität München, **2008**.

[84] H. Huppertz, *Habilitationsschrift* Ludwig–Maximilians–Universität München, **2003**.

[85] W. Wünschheim, H. Huppertz, PRESSCONTROL - A Program for Communication, Calibration and Surveillance of a Hydraulic Press with Heating Device *via* RS232C Interfaces, Ludwig-Maximilians-Universität München, **1999-2003**.

[86] D. Walker, M. A. Carpenter, C. M. Hitch, *Am. Mineral.* **1990**, *75*, 1020.

[87] D. J. Frost, *Personal Communication with H. Huppertz.*

[88] E. Takahashi, H. Yamada, E. Ito, *Geophys. Res. Lett.* **1982**, *9*, 805.

[89] I. C. Getting, G. L. Chen, J. A. Brown, *Pure Appl. Geophys.* **1993**, *141*, 545.

[90] P. W. Bridgman, *Phys. Rev.* **1935**, *48*, 825.

[91] V. E. Bean, S. Akimoto, P. M. Bell, S. Block, W. B. Holzapfel, M. H. Manghnani, M. F. Nicol, S. M. Stishov, *Physica* **1986**, *139 & 140B*, 52.

[92] F. P. Bundy, *Natl. Bur. Stand. Sp. Publ.* **1971**, *326*, 263.

[93] P. W. Bridgman, *Phys. Rev.* **1935**, *48*, 893.

[94] A. A. Giardini, G. A. Samara, *J. Phys. Chem. Solids* **1965**, *26*, 1523.

[95] M. J. Duggin, *J. Phys. Chem. Solids* **1972**, *33*, 1267.

[96] A. Yoneda, S. Endo, *J. Appl. Phys.* **1980**, *51*, 3216.

[97] J. H. Chen, H. Iwasaki, T. Kikegawa, *High Press. Res.* **1996**, *15*, 143.

[98] E. C. Lloyd, C. W. Becket, F. R. Boyd (Jr.), *Accurate Characterization of the High-Pressure Environment*, (ed. E. C. Lloyd), (Washington, DC: *Natl. Bur. Stand. (US) Sp. Publ.*, **1971**, *326* 1).

[99] H. G. Drickamer, *Rev. Sci. Instr.* **1970**, *41*, 1667.

[100] C. G. Homan, *J. Phys. Chem. Solids* **1975**, *36*, 1249.

[101] M. I. McMahon, O. Degtyareva, R. J. Nelmes, *Phys. Rev. Let.* **2000**, *85*, 4896.

[102] K. Kusaba, L. Galoisy, Y. Wang, M. T. Vaughan, D. J. Weidner, *Pure Appl. Geophys.* **1993**, *141*, 643.

[103] J. Camacho, I. Loa, A. Cantarero, K. Syassen, *J. Phys.: Condens. Matter* **2002**, *14*, 739.

[104] A. S. Miguel, A. Polian, M. Gautier, J. P. Itie, *Phys. Rev. B* **1993**, *48*, 8683.

[105] R. J. Nelmes, M. I. McMahon, N. G. Wright, D. R. Allan, *J. Phys. Chem. Solids* **1995**, *56*, 545.

[106] R. J. Nelmes, M. I. McMahon, N. G. Wright, D. R. Allan, *Phys. Rev. Lett.* **1994**, *73*, 1805.

[107] R. Herman, C. A. Swenson, *J. Chem. Phys.* **1958**, *29*, 398.

[108] A. K. Singh, *High Temp.-High Pressures* **1980**, *12*, 47.

[109] R. A. Stager, H. G. Drickamer, *Phys. Rev. B* **1964**, *133*, A830.

[110] L. F. Vereshchagin, E. V. Zubova, V. A. Stupnikov, *High Temp.-High Pressures* **1975**, *7*, 149.

[111] A. S. Balchan, H. G. Drickamer, *Rev. Sci. Instr.* **1961**, *32*, 308.

[112] R. A. Stager, H. G. Drickamer, *Phys. Rev.* **1963**, *131*, 2524.

[113] S. Akimoto, T. Yagi, , Y. Ida, K. Inoue, *High Temp.-High Pressures* **1975**, *7*, 287.

[114] M. J. Walter, Y. Thibault, K. Wei, R. W. Luth, *Can. J. Phys.* **1995**, *73*, 273.

[115] W. Kleber, *Einführung in die Kristallographie*, Verlag Technik Berlin, 17th ed., **1990.**

[116] J. Karle, *Angew. Chem.* **1986**, *98*, 611; *Angew. Chem. Int. Ed.*, **1986**, *25*, 614.

[117] H. Hauptman, *Angew. Chem.* **1986**, *98*, 600; *Angew. Chem. Int. Ed.*, **1986**, *25*, 603.

[118] Y. Amemiya, J. Miyahara, *Nature* **1988**, *336*, 89.

[119] Basread, Raytest Isotopenmessgeräte GmbH, Straubenhardt.

[120] Tina, Vers. 2.10g, Raytest Isotopenmessgeräte GmbH, Straubenhardt, **1993.**

[121] Stoe WinXpow, v1.2, Stoe & CIE GmbH, Darmstadt, Germany, **2001.**

[122] P.-E. Werner, Treor90, Universität Stockholm, **1990.**

[123] P.-E. Werner, *Z. Kristallogr.* **1964**, *120*, 375.

[124] P.-E. Werner, L. Errikson, M. Westdahl, *J. Appl. Crystallogr.* **1985**, *18*, 367.

[125] J. W. Visser, *J. Appl. Crystallogr.* **1969**, *2*, 89.

[126] A. Boultif, D. Louër, *J. Appl. Crystallogr.* **1991**, *24*, 987.

[127] Stoe WinXpow Theo, Vers. 1.18, **2000.**

[128] JCPDS, International Center for Diffraction Data, Swathmore, USA, **1992.**

[129] Stoe X-Red, v1.19, Stoe *Data Reduction Programm*, Stoe & Cie GmbH, Darmstadt, **1999.**

[130] STOE X-RED32, v1.03, STOE *Data Reduction Program*, STOE & Cie GmbH, Darmstadt, **2002.**

[131] STOE X-SHAPE, Vers. 1.05, *Crystal Optimisation for Numerical Absorption Correction*, STOE & Cie GmbH, Darmstadt, **1999.**

[132] W. Herrendorf, H. Bärnighausen, HABITUS - *Program for Numerical Absorption Correction*, University of Karlsruhe/Giessen, Germany, **1993/1997**.

[133] Z. Otwinowski, W. Minor, *Methods Enzymol.* **1997**, *276*, 307.

[134] G. M. Sheldrick, X-PREP, *Data Preparation & Reciprocal Space Exploration*, v6.12, Siemens Analytical X-ray Instruments, **1996.**

[135] G. M. Sheldrick, SHELXS97 and SHELXL97 - *Program suite for the solution and refinement of crystal structures*, University of Göttingen, Germany, **1997.**

[136] G. M. Sheldrick, *Acta Crystallogr. A* **2008**, *64*, 112.

[137] M. C. Burla, R. Caliandro, M. Camalli, B. Carrozzini, G. L. Cascarano, L. D. Caro, C. Giacovazzo, G. Polidori, R. Spagna, SIR2004, **2004.**

[138] X-STEP32, Revision 1.05b, STOE & Cie GmbH, Darmstadt, **1999.**

[139] L. A. Spek, PLATON - *A Multipurpose Crystallographic Toolpose*, Utrecht University, Netherlands, **2002.**

[140] K. Brandenburg, DIAMOND, *Crystal and Molecular Structure Visualization*, v3.1b, Crystal Impact GbR, Bonn, **2005.**

[141] E. Krausz, *AOS News* **1998**, *12*, 21.

[142] E. Krausz, *Aust. J. Chem.* **1993**, *46*, 1041.

[143] ORIGIN 6.1, v6.1052 (B232), OriginLab Corporation, Northampton, USA, **2000.**

[144] J.-P. Amoureux, C. Fernandez, S. J. Steuernagel, *Magn. Reson.* **1996**, *A123*, 116.

[145] B. Herreros, A. W. Metz, G. S. Harbison, *Solid State Nucl. Magn. Reson.* **2000**, *16*, 141.

[146] T. Vosegaard, A. Malmendal, N. C. Nielsen, *Monatsh. Chem.* **2002**, *133*, 1555.

[147] M. Bak, J. T. Rasmussen, N. C. J. Nielsen, *Magn. Reson.* **2000**, *147*, 296.

[148] INCA v4.02, Oxford Instruments Analytical Ltd., **1998–2002.**

[149] O. K. Andersen, O. Jepsen, Tight-Binding LMTO 4.7c, Max-Planck-Institut für Festkörperforschung, Stuttgart, Germany, **1994.**

[150] O. K. Andersen, O. Jepsen, M. Sob, *Electronic Band Structure and its Applications, Lect. Notes Phys.*, *Vol. 283*, (Ed. M. Yussouff) Springer-Verlag, Berlin, **1987**.

[151] P. E. Blöchl, O. Jepsen, O. K. Andersen, *Phys. Rev. B* **1994**, *49*, 16223.

[152] B. Silvi, A. Savin, *Nature* **1994**, *371*, 683.

[153] A. D. Becke, K. E. J. Edgecomb, *Chem. Phys.* **1990**, *92*, 5397.

[154] P. Hohenberg, W. Kohn, *Phys. Rev. B* **1964**, *136*, 864.

[155] G. Kresse, J. Hafner, *Phys. Rev. B* **1993**, *47*, 558; ibid.*49*, **1994** 14251.

[156] G. Kresse, J. Furthmüller, *Comput. Mat. Sci.* **1996**, *6*, 15.

[157] G. Kresse, J. Furthmüller, *Phys. Rev. B* **1996**, *54*, 11169.

[158] J. P. Perdew, *Electronic Structures of Solids '91*, (Eds.: P. Ziesche and H. Eschrig), Akademie Verlag, Berlin, **1991**.

[159] G. Kresse, J. Joubert, *Phys. Rev. B* **1999**, *59*, 1758.

[160] H. J. Monkhorst, J. D. Pack, *Phys. Rev. B* **1976**, *13*, 5188.

[161] R. Hoppe, *Angew. Chem.* **1966**, *78*, 52; *Angew. Chem. Int. Ed.*, **1966**, *5*, 95.

[162] R. Hoppe, *Angew. Chem.* **1970**, *82*, 7; *Angew. Chem. Int. Ed.*, **1970**, *9*, 25.

[163] R. Hübenthal, MAPLE - *Program for the Calculation of* MAPLE- *Values*, Vers. 4, University of Giessen, Germany, **1993.**

[164] I. D. Brown, D. Altermatt, *Acta Crystallogr. B* **1985**, *41*, 244.

[165] N. E. Brese, M. O'Keeffe, *Acta Crystallogr. B* **1991**, *47*, 192.

[166] A. Trzesowska, R. Kruszynski, T. J. Bartczak, *Acta Cryst. B* **2004**, *60*, 174.

[167] R. Hoppe, S. Voigt, H. Glaum, J. Kissel, H. P. Müller, K. J. Bernet, *J. Less-Common Met.* **1989**, *156*, 105.

[168] R. Hoppe, *Z. Kristallogr.* **1979**, *150*, 23.

[169] L. Pauling, *J. Am. Chem. Soc.* **1947**, *69*, 542.

[170] R. Diehl, *Solid State Comm.* **1975**, *17*, 743.

[171] H. Huppertz, G. Heymann, *Solid State Sci.* **2003**, *5*, 281.

[172] H. Emme, M. Weil, H. Huppertz, *Z. Naturforsch. B* **2005**, *60*, 815.

[173] H. Huppertz, *Z. Naturforsch. B* **2003**, *58*, 257.

[174] F. Pan, G. Shen, R. Wang, X. Wang, D. J. Shen, *Cryst. Growth* **2002**, *241*, 108.

[175] A. Perloff, S. Block, *Acta Crystallogr.* **1966**, *20*, 274.

[176] D. L. Corker, A. M. Glazer, *Acta Crystallogr. B* **1996**, *52*, 260.

[177] K.-I. Machida, G.-Y. Adachi, J. Shiokawa, *Acta Crystallogr. B* **1980**, *36*, 2008.

[178] S. C. Abrahams, J. L. Bernstein, P. Gibart, M. Robbins, R. C. Sherwood, *J. Chem. Phys.* **1974**, *60*, 1899.

[179] H. Bauer, *Z. Anorg. Allg. Chem.* **1963**, *320*, 306.

[180] C. E. Weir, R. A. Schroeder, *J. Res. Nat. Bur. Stand. A* **1964**, *86*, 465.

[181] M. Martinez-Ripoll, S. Martinez-Carrera, S. Garcia-Blanco, *Acta Crystallogr. B* **1971**, *27*, 672.

[182] M. Ihara, J. Krogh-Moe, *Acta Crystallogr.* **1966**, *20*, 132.

[183] A. Utzolino, K. Bluhm, *Z. Naturforsch. B* **1996**, *51*, 1433.

[184] R. Norrestam, M. Kritikos, A. Sjödin, *J. Solid State Chem.* **1995**, *114*, 311.

[185] A. Bergstein, *Czech. J. Phys. B* **1973**, *23*, 777.

[186] J. P. Attfield, A. M. T. Bell, L. M. Rodriguez-Martinez, J. M. Greneche, R. Retoux, M. Leblance, R. J. Cernik, J. F. Clarke, D. A. Perkins, *J. Mater. Chem.* **1998**, *9*, 205.

[187] J. P. Attfield, A. M. T. Bell, L. M. Rodriguez-Martinez, J. M. Greneche, R. J. Cernik, D. A. Perkins, *Nature* **1998**, *369*, 655.

[188] J. P. Attfield, J. F. Clarke, D. A. Perkins, *Physica B* **1992**, *180 & 181*, 581.

[189] M. Mir, J. Janczak, Y. P. Mascarenhas, *J. Appl. Crystallogr.* **2006**, *39*, 42.

[190] M. Federico, *Periodico Mineral.* **1957**, *26*, 191.

[191] J. S. Swinnea, H. Steinfink, *Am. Mineral.* **1983**, *68*, 827.

[192] N. A. Yamnova, M. A. Simonov, N. V. Belov, *Kristallografiya* **1975**, *20*, 156.

[193] J. G. White, A. Miller, R. E. Nielsen, *Acta Crystallogr.* **1965**, *19*, 1060.

[194] R. Diehl, G. Brandt, *Acta Crystallogr. B* **1975**, *31*, 1662.

[195] T. A. Kravchuk, Y. D. Lazebnik, *Russ. J. Inorg. Chem.* **1967**, *12*, 21.

[196] I. M. Rumanova, E. A. Genkina, N. V. Belov, *Latvijas PSR Zinatnu Akademijas Vestis Kimijas Serija* **1981**, *5*, 571.

[197] A. G. Gavriliuk, I. A. Trojan, R. Boehler, M. Ermets, A. Zerr, I. S. Lyubutin, V. A. Sarkisyan, *JETP Lett.* **2002**, *75*, 23.

[198] K. Parlinski, *Eur. Phys. J. B* **2002**, *27*, 283.

[199] H. Effenberger, F. Pertlik, *Z. Kristallogr.* **1984**, *166*, 129.

[200] J. L. C. Rowsell, N. J. Taylor, L. F. Nazar, *J. Solid State Chem.* **2003**, *174*, 189.

[201] S. V. Berger, *Acta Chem. Scand.* **1950**, *4*, 1054.

[202] R. Norrestam, K. Nielsen, I. Sotofte, N. Thorup, *Z. Kristallogr.* **1989**, *189*, 33.

[203] W. Götz, *Naturwissenschaften* **1963**, *50*, 567.

[204] J. Pardo, M. Martinez-Ripoll, S. Garcia-Blanco, *Acta Crystallogr. B* **1974**, *30*, 37.

[205] M. Pompetzki, B. Albert, *Z. Anorg. Allg. Chem.* **2004**, *630*, 2550.

[206] J. L. C. Rowsell, N. J. Taylor, L. F. Nazar, *J. Am. Chem. Soc.* **2002**, *124*, 6522.

[207] T. Yang, G. Li, L. You, J. Ju, F. Liao, J. Lin, *Chem. Comm.* **2005**, 4225.

[208] M. Martinez-Ripoll, S. Martinez-Carrera, S. Garcia-Blanco, *Acta Crystallogr. B* **1971**, *27*, 677.

[209] G. K. Abdullaev, K. S. Mamedov, *J. Struct. Chem.* **1981**, *22*, 637.

[210] H. Behm, *Acta Crystallogr. B* **1982**, *38*, 2781.

[211] H. Behm, *Z. Kristallogr.* **1981**, *154*, 251.

[212] G. A. Petrakovskiĭ, K. A. Sablina, A. M. Vorotynov, O. A. Bayukov, A. F. Bovina, G. V. Bondarenko, *Phys. Solid State* **1999**, *41*, 610.

[213] P. F. Rza-Zade, G. K. Abdullaev, N. A. Éyubova, F. R. Samedov, *Inorg. Mater.* **1971**, *7*, 1872.

[214] M. Snure, A. Tiwari, *Appl. Phys. Lett.* **2007**, *91*, 092123–1.

[215] C. T. Prewitt, R. D. Shannon, D. B. Rogers, *Inorg. Chem.* **1971**, *10*, 719.

[216] B. U. Koehler, M. Jansen, *Z. Anorg. Allg. Chem.* **1986**, *543*, 73.

[217] K. Bluhm, H. Müller-Buschbaum, *J. Less Comm. Met.* **1989**, *147*, 133.

[218] A. Akella, D. A. Keszler, *Inorg. Chem.* **1994**, *33*, 1554.

[219] A. Utzolino, K. Bluhm, *Z. Naturforsch. B* **1995**, *50*, 1653.

[220] V. Hornebecq, P. Gravereau, J. P. Chaminade, E. Lebraud, *Mat. Res. Bull.* **2002**, *37*, 2165.

[221] A. B. Riabov, V. A. Yartys' , B. C. Hauback, P. W. Guegan, G. Wiesinger, I. R. Harris, *J. Alloys Compd.* **1999**, *293*, 93.

[222] K. Bluhm, H. Müller-Buschbaum, *Z. Anorg. Allg. Chem.* **1989**, *575*, 26.

[223] H. Bartl, W. Schuckmann, *Neues Jahrb. Mineral. Monatsh.* **1966**, 142.

[224] M. Weil, *Acta Crystallogr. E* **2003**, *59*, i40.

[225] Y. Laureiro, M. L. Veiga, M. L. Lopez, S. Garcia-Martin, A. Jerez, C. Pico, *Powder Diffraction* **1991**, *6*, 28.

[226] Y.-H. Zhao, X.-A. Chen, X.-A. Chang, J.-L. Zuo, M. Li, *Acta Crystallogr. E* **2007**, *63*, i50.

[227] S. V. Berger, *Acta Chem. Scand.* **1949**, *3*, 660.

[228] M. Weil, *Acta Crystallogr. E* **2003**, *59*, i95.

[229] G. C. Guo, W. D. Cheng, J. T. Chen, J. S. Huang, Q. E. Zhang, *Acta Crystallogr.* **1995**, *51*, 351.

[230] J. S. Knyrim, H. Huppertz, *J. Solid State Chem.* **2007**, *180*, 742.

[231] J. S. Knyrim, H. Huppertz, *Z. Naturforsch. B* **2008**, *63*, 707.

[232] E. Zobetz, *Z. Kristallogr.* **1990**, *191*, 45.

[233] F. C. Hawthorne, P. C. Burns, J. D. Grice, *The Crystal Chemistry of Boron, in Boron: Mineralogy, Petrology and Geochemistry*, *Vol. 33*, (Eds.: E. S. Grew, L. M. Anovitz), Mineralogical Society of America, Washington, 2nd ed., **1996**, p. 41.

[234] J. A. Speer, B. J. Cooper, *Am. Mineral.* **1982**, *67*, 804.

[235] S. Achary, G. Mukherjee, A. Tyagi, B. Godwal, *Phys. Rev. B* **2002**, *66*, 184106–1.

[236] L. W. Finger, *Carnegie Institution of Washington: Yearbook* **1974**, *73*, 544.

[237] R. F. Klevtsova, L. A. Glinskaya, E. S. Zolotova, P. V. Klevtsov, *Sov. Phys. Dokl.* **1989**, *34*, 185.

[238] R. D. Shannon, C. T. Prewitt, *Acta Crystallogr.* **1969**, *25*, 925.

[239] H. Bartl, G. Pfeifer, *Neues Jahrb. Miner. Mh.* **1976**, 58.

[240] P. V. Pavlov, N. V. Belov, *Sov. Phys. Crystallogr.* **1959**, *4*, 300.

[241] R. Miyawaki, I. Nakai, K. Nagashima, *Am. Mineral.* **1984**, *69*, 948.

[242] F. Demartin, A. Minaglia, C. M. Gramaccioli, *Can. Mineral.* **2001**, *39*, 1105.

[243] T. Ito, H. Mori, *Acta Crystallogr.* **1953**, *6*, 24.

[244] F. F. Foit (Jr.), M. W. Phillips, G. V. Gibbs, *Am. Mineral.* **1973**, *58*, 909.

[245] A. K. Pant, D. W. J. Cruickshank, *Z. Kristallogr.* **1967**, *125*, 286.

[246] M. Watanabe, K. Nagashima, *Acta Crystallogr. B* **1972**, *28*, 326.

[247] R. Miyawaki, I. Nakai, K. Nagashima, *Acta Crystallogr.* **1985**, *41*, 13.

[248] A. B. Voloshin, I. A. Pakhomovskii, I. P. Menshikov, *Dokl. Akad. Nauk USSR* **1983**, *270*, 1188.

[249] E. Foord, R. V. Gaines, J. G. Crock, W. B. Simmons (Jr.), C. P. Barbosa, *Am. Mineral.* **1986**, *71*, 603.

[250] R. K. Rastsvetaeva, D. Y. Pushcharovskii, I. V. Pekov, A. V. Voloshin, *Kristallografiya* **1996**, *42*, 217.

[251] T. Nakai, *Bull. Chem. Soc. Jpn.* **1938**, *13*, 591.

[252] J. Ito, *Am. Mineral.* **1967**, *52*, 1523.

[253] J. Ito, S. S. Hafner, *Am. Mineral.* **1974**, *59*, 700.

[254] F. F. Foit (Jr.), G. V. Gibbs, *Zeitschrift für Kristallographie Kristallgeometrie Kristallphysik Kristallchemie* **1975**, *141*, 375.

[255] G. A. Lager, G. V. Gibbs, *Am. Mineral.* **1974**, *59*, 919.

[256] N. Perchiazzi, A. F. Gualtieri, S. Merlino, A. R. Kampf, *Am. Mineral.* **2004**, *89*, 767.

[257] J. Schaefer, K. Bluhm, *Z. Naturforsch. B* **1994**, *50*, 630.

[258] K. Bluhm, A. Wiesch, *Z. Naturforsch. B* **1995**, *51*, 677.

[259] D. M. Burt, *Compositional and phase relations among rare earth element minerals, in Geochemistry and Mineralogy of Rare Earth Elements*, *Vol. 21*, (Eds.: B. R. Lipin, G. A. McKay), Mineralogical Society of America, Washington, **1989**, p. 259.

[260] N. Hirosaki, S. Ogata, C. Kocer, *J. Alloys Compd.* **2003**, *351*, 31.

[261] J. S. Knyrim, J. Friedrichs, S. Neumair, F. Roeßner, Y. Floredo, S. Jakob, D. Johrendt, R. Glaum, H. Huppertz, *Solid State Sci.* **2008**, *10*, 168.

[262] H. Emme, T. Nikelski, Th. Schleid, R. Pöttgen, M. H. Möller, H. Huppertz, *Z. Naturforsch. B* **2004**, *59*, 202.

[263] T. Nikelski, Th. Schleid, *Z. Anorg. Allg. Chem.* **2003**, *629*, 1017.

[264] H. Emme, G. Heymann, A. Haberer, H. Huppertz, *Z. Naturforsch. B* **2007**, *62*, 765.

[265] H. Emme, C. Despotopoulou, H. Huppertz, *Z. Anorg. Allg. Chem.* **2004**, *630*, 1717.

[266] H. Emme, C. Despotopoulou, H. Huppertz, *Z. Anorg. Allg. Chem.* **2004**, *630*, 2450.

[267] J. A. Konnert, J. R. Clark, C. L. Christ, *Am. Mineral.* **1970**, *55*, 1911.

[268] S. Ghose, C. Wan, *Am. Mineral.* **1977**, *62*, 979.

[269] J. P. Chapman, J. P. Attfield, M. Molgg, C. M. Friend, T. P. Beales, *Angew. Chem. Int. Ed. Engl.* **1996**, *35*, 2482.

[270] E. Ketatni, B. Mernari, F. Abraham, O. Mentre, *J. Solid State Chem.* **2000**, *153*, 48.

[271] E. Gutie'rrez-Puebla, M. A. Monge, C. Ruiz-Valero, J. A. Campa, *Chem. Mater.* **1998**, *10*, 3405.

[272] J.-C. Horng, S.-L. Wang, *Acta Crystallogr. C* **1994**, *50*, 488.

[273] N. R. Khasanova, F. Izumi, Z. Hiroi, M. Takano, Q. Huang, A. Santoro, *Acta Crystallogr. C* **1996**, *52*, 2381.

[274] B. Raveau, C. Michel, *Annu. Rev. Mater. Sci.* **1989**, *19*, 319.

[275] K. Maaß, R. Glaum, *Acta Crystallogr. C* **2000**, *56*, 404.

[276] J. M. LeMeins, G. Courbion, *Acta Crystallogr. C* **1999**, *55*, 481.

[277] D. Riou, B. Raveau, *Acta Crystallogr. C* **1991**, *47*, 1708.

[278] B. E. Bali, A. Boukhari, J. Aride, K. Maaß, D. Wald, R. Glaum, F. Abraham, *Solid State Sci.* **2001**, *3*, 669.

[279] A. Moquine, A. Boukhari, L. Elammari, J. Durand, *J. Solid State Chem.* **1993**, *107*, 368.

[280] M. Gerloch, J. Kohl, J. Lewis, W. Urland, *J. Chem. Soc.* **1970**, *1970A*, 3269.

[281] S. Sasaki, K. Fujino, Y. Takeuchi, *Acta Crystallogr. A* **1980**, *36*, 904.

[282] N. C. Tombs, H. P. Rooksby, *Nature* **1950**, *165*, 442,.

[283] H. Taguchi, *Solid State Comm.* **1998**, *108*, 635.

[284] N. G. Schmahl, G. F. Eikerling, *Z. Phys. Chem.* **1968**, *62*, 268.

[285] J. S. Knyrim, H. Huppertz, *J. Solid State Chem.* **2008**, *181*, 2092.

[286] J. S. Knyrim, F. Roeßner, S. Jakob, D. Johrendt, I. Kinski, R. Glaum, H. Huppertz, *Angew. Chem.* **2007**, *119*, 9256; *Angew. Chem. Int. Ed.*, **2007**, *46*, 9097.

[287] V. Kahlenberg, R. X. Fischer, C. S. J. Shaw, *J. Solid State Chem.* **2000**, *153*, 294.

[288] S. Ito, K. Suzuki, M. Iagaki, S. Naka, *Mater. Res. Bull.* **1980**, *15*, 925.

[289] B. Lazic, V. Kahlenberg, J. Konzett, *Z. Kristallogr.* **2007**, *222*, 690.

[290] H. J. Deiseroth, H. Müller-Buschbaum, *Z. Anorg. Allg. Chem.* **1973**, *402*, 201.

[291] W. Leib, H. Müller-Buschbaum, *Z. Anorg. Allg. Chem.* **1986**, *538*, 71.

[292] J. S. Knyrim, H. Emme, M. Döblinger, O. Oeckler, M. Weil, H. Huppertz, *Chem. Eur. J.* **2008**, *14*, 6149.

[293] M. Ludwig, J. Jäger, R. Niewa, R. Kniep, *Inorg. Chem.* **2000**, *39*, 5909.

[294] G. Cordier, E. Czech, M. Jacowski, H. Schäfer, *Rev. Chim. Mineral.* **1981**, *18*, 9.

[295] M. Somer, W. Carrillo-Cabrera, K. Peters, H. G. von Schnering, *Z. Kristallogr. NCS* **1998**, *213*, 230.

[296] M. Somer, W. Carrillo-Cabrera, K. Peters, H. G. von Schnering, *Z. Kristallogr. NCS* **1998**, *213*, 4.

[297] S. J. Clarke, F. J. DiSalvo, *Inorg. Chem.* **1997**, *36*, 1143.

[298] H. Lueken, *Magnetochemie*, B. G. Teubner, Stuttgart, Leipzig, **1999.**

[299] A. B. P. Lever, *J. Chem. Educ.* **1968**, *45*, 711.

[300] K. Maaß, *PhD Thesis* University of Gießen, **2002**.

[301] D. Reinen, M. Atanasov, S.-L. Lee, *Coord. Chem. Rev.* **1998**, *175*, 91.

[302] B. N. Figgis, M. A. Hitchman, *Ligand Field Theory and its Applications*, Wiley-VCH, **2000.**

[303] H. Taguchi, *Solid State Comm.* **1998**, *108*, 635.

[304] Bruker-AXS - Shelxtl, v5.1, Bruker AXS Inc., Madison, Wisconsin, USA, **1997.**

[305] Y. Laureiro, M. L. Veiga, M. L. Lopez, S. Garcia-Martin, A. Jerez, C. Pico, *Powder Diffraction* **1991**, *6*, 28.

[306] V. Kahlenberg, R. X. Fischer, J. B. Parise, *J. Solid State Chem.* **2000**, *154*, 612.

[307] A. P. Khomyakov, G. N. Nechelyustov, E. Sokolova, E. Bonaccorsi, S. Merlino, M. Pasero, *Can. Mineral.* **2002**, *40*, 961.

[308] P. A. Sandomirskii, S. S. Meshalkin, I. V. Rozhdestvenskaya, L. N. Dem'yanets, T. G. Uvarova, *Sov. Phys. Crystallogr.* **1986**, *31*, 522.

[309] R. B. G. Lampert, *Z. Kristallogr. Kristallgeom. Kristallphys. Kristallchem.* **1986**, *176*, 29.

[310] M. Lujan, F. Kubel, H. Schmid, *Z. Naturforsch. B* **1994**, *49*, 1256.

[311] F. Karau, *PhD Thesis* Ludwig–Maximilians–Universität München, **2007**.

[312] F. W. Karau, L. Seyfarth, O. Oeckler, J. Senker, K. Landskron, W. Schnick, *Chem. Eur. J.* **2007**, *13*, 6841.

[313] J. D. Odom, A. J. Zozulin, S. A. Johnston, J. R. Durig, *J. Organom. Chem.* **1980**, *201*, 351.

[314] K. L. Geisinger, G. V. Gibbs, A. Navrotsky, *Phys. Chem. Minerals* **1985**, *11*, 266.

[315] W. H. Baur, T. Ohta, *Acta Crystallogr. B* **1982**, *38*, 390.

[316] Y. I. Smolin, Y. F. Shepelev, A. P. Titov, *Sov. Phys. Crystallogr.* **1973**, *17*, 749.

[317] K. Heidebrecht, M. Jansen, *Z. Anorg. Allg. Chem.* **1982**, *597*, 79.

[318] H. Huppertz, W. Schnick, *Angew. Chem.* **1997**, *36*, 2651.

[319] F. Liebau, *Acta Crystallogr. A Supplement* **1984**, *40*, C254.

[320] H. A. Levy, G. C. Lisensky, *Acta Crystallogr. B* **1978**, *34*, 3502.

[321] H. Effenberger, F. Pertlik, *Z. Kristallogr.* **1984**, *166*, 129.

[322] E. Zobetz, *Z. Kristallogr.* **1982**, *160*, 81.

[323] E. Zobetz, *Z. Kristallogr.* **1982**, *160*, 81.

[324] F. Perlik, *Monatsh. Chem.* **1999**, *130*, 1983.

[325] Y. Kanazawa, A. Sasaki, *Acta Crystallogr. C* **1986**, *42*, 9.

[326] A. Goto, T. Hondoh, S. Mae, *J. Chem. Phys.* **1990**, *93*, 1412.

[327] J. Campa-Molina, S. Ulloa-Godinez, A. Barrera, L. Bucio, J. Mata, *J. Phys.: Condens. Matter* **2006**, *18*, 4827.

[328] H. Schmid, *J. Phys. Chem. Solids* **1965**, *26*, 973.

[329] J. D. Dana, *Dana's System of Mineralogy*, (Eds. C. Palache, H. Berman, C. Frondel) Wiley, New York.

[330] H. K. Mao, F. Kubel, H. Schmid, *Acta Crystallogr. B* **1991**, *47*, 692.

[331] F. Kubel, *Ferroelectrics* **1994**, *160*, 61.

[332] L. Smart, E. Moore, *Solid State Chemistry, An Introduction*, Chapman and Hall, London, **1992.**

[333] S. Matthews, R. Ramesh, *Science* **1997**, *276*, 238.

[334] J. Campa-Molina, A. G. Castellanos-Guzman, *Solid State Commun.* **1994**, *89*, 963.

[335] J. Campa-Molina, O. Blanco, A. Correa-Gomez, M. Czank, A. G. Castellanos-Guzman, *J. Microsc.* **2002**, *208*, 201.

[336] E. Dowty, J. R. Clark, *Solid State Comm.* **1972**, *10*, 543.

[337] M.-E. Mendoza-Alvarez, K. Yvon, W. Depmeier, H. Schmid, *Acta Crystallogr. C* **1985**, *41*, 1551.

[338] S. Sueno, J. R. Clark, J. J. Papike, J. A. Konnert, *Am. Mineral.* **1973**, *58*, 691.

[339] T. Ito, N. Morimoto, R. Sadanaga, *Acta Crystallogr.* **1951**, *4*, 310.

[340] H. Schmid, *Phys. Stat. Sol.* **1970**, *37*, 209.

[341] R. H. J. Wentorf, *J. Chem. Phys.* **1957**, *26*, 956.

[342] F. Lissner, Th. Schleid, *Z. anorg. allg. Chem.* **1994**, *620*, 1998.

[343] Th. Schleid, F. Lissner, *Z. Naturforsch. B* **1994**, *49*, 340.

[344] R. D. Shannon, *Acta Crystallogr. A* **1976**, *32*, 751.

[345] F. Heide, G. Walter, R. Urlau, *Naturwissenschaften* **1961**, *48*, 97.

[346] H. Effenberger, *Acta Crystallogr. B* **1982**, *38*, 82.

[347] R. I. Collin, *Acta Crystallogr.* **1951**, *4*, 204.

[348] Y. Li, P. C. Burns, *Can. Mineral.* **2000**, *38*, 713.

[349] L. Kutschabsky, *Acta Crystallogr. B* **1969**, *25*, 1811.

[350] I. Nakai, H. Okada, K. Masutomi, E. Koyama, K. Nagashima, *Am. Mineral.* **1986**, *71*, 1234.

[351] P. Becker, *Adv. Mater.* **1998**, *10*, 979.

[352] *http://www.clevelandcrystals.com/htm;* **07.05.2008**.

[353] Y. Wu, T. Sasaki, S. Nakai, A. Yokotani, H. Tang, C. Chen, *Appl. Phys. Lett.* **1993**, *21*, 2614.

[354] M. Iwai, T. Kobayashi, H. Furuya, H. Mori, T. Sasaki, *Jpn. J. Appl. Phys.* **1997**, *36*, L276.

[355] G. Aka, A. Kahn-Haradi, D. Vivien, J.-M. Benitez, F. Salin, J. Godard, *Eur. J. Solid State Inorg. Chem.* **1996**, *33*, 727.

[356] G. Aka, A. Kahn-Harari, F. Mougel, D. Vivien, F. Salin, P. Coquelin, P. Colin, D. Pelenc, J. P. Damelet, *J. Opt. Soc. Am. B* **1997**, *14*, 2238.

[357] M. Yoshimura, H. Furuya, T. Kobayashi, M. M. ans Y. Mori, T. Sasaki, *Opt. Lett.* **1999**, *24*, 193.

[358] H. Furuya, M. Yoshimura, T. Kobayashi, K. Murase, Y. Mori, T. Sasaki, *J. Cryst. Growth* **1999**, *198/199*, 560.

[359] J. D. Garret, M. Natarajan, J. E. Greedan, *J. Cryst. Growth* **1977**, *41*, 225.

[360] W. H. Zachariasen, *Z. Kristallogr.* **1937**, *98*, 266.

[361] C. F. Dewey Jr., W. R. Cook (Jr.), R. T. Hodgson, J. J. Wynne, *Appl. Phys. Lett.* **1975**, *26*, 714.

[362] A. I. Zaitsev, A. S. Aleksandrovskii, A. V. Zamkov, A. M. Sysoev, *Inorg. Mater.* **2006**, *42*, 1360.

[363] J. F. H. Nicholls, B. H. T. Chai, D. Russell, B. Henderson, *Opt. Mater.* **1997**, *8*, 185.

[364] J. Barbier, N. Penin, A. Denoyer, L. M. D. Cranswick, *Soliid State Chem.* **2005**, *7*, 1055.

[365] A. H. Reshak, S. Auluck, I. V. Kityk, *J. Solid State Chem.* **2008**, *181*, 789.

[366] A. R. Lakshmanan, B. Chandra, R. C. Bhatt, *Radiat. Prot. Dosim.* **1982**, *2*, 231.

[367] C. Furetta, M. Prokic, R. Salamon, G. Kitis, *Appl. Radiation and Isotopes* **2000**, *52*, 243.

[368] J. Manam, S. K. Sharma, *J. Mater. Sci.* **2004**, *39*, 6203.

[369] A. N. Yazici, M. Doğan, V. E. Kafadar, H. Toktamiş, *Nucl. Instr. and Meth in Phys. Res. B* **2006**, *246*, 402.

[370] J. Li, J. Hao, C. Zhang, Q. Tang, Y. Zhang, Q. Su, S. Wang, *Nucl. Instr. and Meth. in Phys. Res. B* **2004**, *222*, 577.

[371] N. V. Zayakina, A. A. Brovkin, *Kristallografiya* **1977**, *22*, 275.

[372] S. Block, A. Perloff, *Acta Crystallogr.* **1965**, *19*, 297.

[373] R. Fröhlich, *Z. Kristallogr.* **1984**, *168*, 109.

[374] N. G. Furmanova, B. A. Maksimov, V. N. Molchanov, A. E. Kokh, N. G. Kononova, P. P. Fedorov, *Crystallogr. Rep.* **2006**, *51*, 219.

[375] E. H. P. Cordfunke, R. J. M. Konings, R. R. Van der Laan, W. Ouweljes, *J. Chem. Thermodyn.* **1993**, *25*, 343.

[376] K.-H. Hübner, *Neues Jahrb. Mineral. Monatsh.* **1969**, 335.

[377] J. Krogh-Moe, M. Ihara, *Acta Crystallogr. B* **1969**, *25*, 2153.

[378] E. M. Levin, C. L. McDaniel, *J. Am. Ceram. Soc.* **1962**, *45*, 355.

[379] M. Burianek, M. Mühlberg, *Cryst. Res. Technol.* **1997**, *32*, 1023.

[380] M. J. Pottier, *Bull. Soc. Chim. Belg.* **1974**, *83*, 235.

[381] P. Becker, R. Fröhlich, *Z. Naturforsch. B* **2004**, *59*, 256.

[382] H. Hellwig, J. Liebertz, L. Bohatý, *Solid State Commun.* **1998**, *109*, 249.

[383] S. Haussühl, L. Bohatý, P. Becker, *Applied Physics A: Materials Science & Processing* **2006**, *82*, 495.

[384] L. Li, G. Li, Y. Wang, F. Liao, J. Lin, *Inorg. Chem.* **2005**, *44*, 8243.

[385] S. K. Deb, M. Wilding, M. Somayazulu, P. F. McMillan, *Nature* **2001**, *414*, 528.

[386] C. A. Perottoni, H. A. H. Da Jornada, *Science* **1997**, *280*, 886.

[387] J. H. Nguyen, M. B. Kruger, R. Jeanloz, *Phys. Rev. Lett.* **1997**, *78*, 1936.

[388] S. M. Sharma, S. K. Sikka, *Prog. Mater. Sci.* **1996**, *40*, 1.

[389] E. G. Ponyatovsky, O. I. Barkalov, *Mater. Sci. Rep.* **1992**, *8*, 147.

[390] J. Zhang, Y. Zhao, H. Xu, M. V. Zelinskas, L. Wang, Y. Wang, T. Uchida, *Chem. Mater.* **2005**, *17*, 2817.

[391] J. S. Knyrim, S. R. Römer, W. Schnick, H. Huppertz, *Solid State Sci.* **2008**, *10*, in press.

[392] P. D. Robinson, J. H. Fang, *Am. Mineral.* **1977**, *62*, 167.

[393] J. S. Knyrim, F. M. Schappacher, R. Pöttgen, J. Schmedt auf der Günne, D. Johrendt, H. Huppertz, *Chem. Mater.* **2007**, *19*, 254.

[394] S. V. Krivovichev, V. N. Yakovenchuk, T. Armbruster, Y. Mikhailova, Y. A. Pakhomovsky, *N. Jb. Miner. Mh.* **2004**, *8*, 373.

[395] W. Gerlach, *Z. Phys.* **1922**, *9*, 184.

[396] F. D. Murnaghan, *Proc. Nat. Acad. Sci. USA* **1944**, *30*, 244.

[397] F. Birch, *J. Geophys. Res.* **1952**, *57*, 227.

[398] P. Vinet, J. Ferrante, J. R. Smith, J. H. Rose, *Phys. Rev. B* **1987**, *35*, 1945.

[399] P. Vinet, J. H. Rose, J. Ferrante, J. R. Smith, *J. Phys.: Condens. Matter* **1989**, *1*, 1941.

[400] J. S. Knyrim, P. Becker, D. Johrendt, H. Huppertz, *Angew. Chem.* **2006**, *118*, 8419; *Angew. Chem. Int. Ed.* , **2006**, *45*, 8239.

[401] S. K. Kurtz, T. T. Perry, *J. Appl. Phys.* **1968**, *39*, 3798.

[402] P. Becker, *Personal Communication* **2006**.

[403] M. Ren, J. H. Lin, Y. Dong, L. Q. Yang, M. Z. Su, L. P. You, *Chem. Mater.* **1999**, *11*, 1576.

[404] J. P. Laperches, P. Tarte, *Spectrochim. Acta* **1966**, *22*, 1201.

[405] G. Blasse, G. P. M. van den Heuvel, *Phys. Stat. Sol. A* **1973**, *19*, 111.

[406] W. C. Steele, J. C. J. Decius, *Chem. Phys.* **1956**, *25*, 1184.

[407] R. Böhlhoff, H. U. Bambauer, W. Hoffmann, *Z. Kristallogr.* **1971**, *133*, 386.

[408] K. Machida, H. Hata, K. Okuno, G.-Y. Adachi, J. J. Shiokawa, *Inorg. Nucl. Chem.* **1979**, *41*, 1425.

[409] W. R. L. Lambrecht, O. K. Andersen, *Phys. Rev. B* **1986**, *34*, 2439.

[410] L. Bohatý, S. Haussühl, J. Liebertz, P. Becker, W.-D. Stein, Braden, *Kristallogr. Suppl.* **2006**, 93.

[411] P. E. Lippens, *Phys. Rev. B* **1999**, *60*, 4576.

[412] C. Geijke, E. Nordström, L. Fransson, K. Edström, L. Häggström, L. J. Börjesson, *Mater. Chem.* **2002**, *12*, 2965.

[413] P. Amornsakchai, D. C. Apperley, R. K. Harris, P. Hodgkinson, P. C. Waterfield, *Solid State Nucl. Magn. Reson.* **2004**, *26*, 160.

[414] L. P. Cruz, J.-M. Savariault, J. Rocha, J.-C. Jumas, A. Pedrosa de Jesus, J. D. Pedrosa de Jesus, *J. Solid State Chem.* **2001**, *156*, 349.

[415] C. Cossement, J. Darville, J.-M. Gilles, J. B. Nagy, C. Fernandez, J.-P. Amoureux, *Magn. Reson. Chem.* **1992**, *30*, 263.

[416] K. J. D. Mackenzie, M. E. Smith, *Multinuclear Solid-State NMR of Inorganic Solids*, Pergamon, Amsterdam, **2002.**

[417] C. Mundus, G. Taillades, A. Pradel, M. Ribes, *Solid State Nucl. Magn. Reson.* **1996**, *7*, 141.

[418] T. Pietrass, F. Taulelle, *Magn. Reson. Chem.* **1997**, *35*, 363.

[419] S. Kroeker, J. F. Stebbins, *Inorg. Chem.* **2001**, *40*, 6239.

[420] A. Walsh, G. W. J. Watson, *Phys. Chem. B* **2005**, *109*, 18868.

[421] A. Walsh, G. W. J. Watson, *Solid State Chem.* **2005**, *178*, 1422.

[422] A. Haberer, G. Heymann, H. Huppertz, *Z. Anorg. Allg. Chem.* **2006**, *632*, 2079.

[423] A. Haberer, G. Heymann, H. Huppertz, *J. Solid State Chem.* **2007**, *180*, 1595.